DEVELOPMENT OF SUPERCONDUCTING BOLOMETER DEVICE TECHNOLOGY FOR MILLIMETER-WAVE COSMOLOGY INSTRUMENTS

Ernst Otto

New College

A thesis submitted in candidature for the degree of Doctor of Philosophy
at the
University of Oxford

Michaelmas Term 2013

DEVELOPMENT OF SUPERCONDUCTING BOLOMETER DEVICE TECHNOLOGY FOR MILLIMETER-WAVE COSMOLOGY INSTRUMENTS

Ernst Otto

New College

A thesis submitted in candidature for the degree of Doctor of Philosophy
Michaelmas Term 2013

ABSTRACT

The Cold-Electron Bolometer (CEB) is a sensitive detector of millimeter-wave radiation, in which tunnel junctions are used as temperature sensors of a nanoscale normal metal strip absorber. The absorber is fed by an antenna via two Superconductor-Insulator-Normal metal (SIN) tunnel junctions, fabricated at both ends of the absorber. Incoming photons excite electrons, heating the whole electron system. The incoming RF power is determined by measuring the tunneling current through the SIN junctions. Since electrons at highest energy levels escape the absorber through the tunnel junctions, it causes cooling of the absorber. This electron cooling provides electro-thermal feedback that makes the saturation power of a CEB well above that of other types of millimeter-wave receivers. The key features of CEB detectors are high sensitivity, large dynamic range, fast response, easy integration in arrays on planar substrates, and simple readout. The high dynamic range allows the detector to operate under relatively high background levels.

In this thesis, we present the development and successful operation of CEB, focusing on the fabrication technology and different implementations of the CEB for efficient detection of electromagnetic signals. We present the CEB detector integrated across a unilateral finline deposited on a planar substrate. We have measured the finline-integrated CEB performance at 280-315 mK using a calibrated black-body source mounted inside the cryostat. The results have demonstrated strong response to the incoming RF power and reasonable sensitivity. We also present CEB devices fabricated with advanced technologies and integrated in log-periodic, double-dipole and cross-slot antennas. The measured CEB performance satisfied the requirements of the balloon-borne experiment BOOMERANG and could be considered for future balloon-borne and ground-based instruments.

In this thesis we also investigated a planar phase switch integrated in a back-to-back finline for modulating the polarization of weak electromagnetic signals. We examine the switching characteristics and demonstrate that the switching speed of the device is well above the speed required for phase modulation in astronomical instruments. We also investigated the combination of a detector and a superconducting phase switch for modulating the polarization of electromagnetic radiation.

DECLARATION

This thesis is the result of my own work carried out between October 2007 and August 2013 at the University of Oxford, unless otherwise stated.

No part of this thesis has been accepted, or is currently being submitted, for any degree, diploma or any other qualification in this University or elsewhere. The total length of this thesis does not exceed 250 pages.

The fabrication methods described in Chapter 2 were developed by myself only, and the manufacturing was done entirely on my own.

The work presented in Chapter 3 was produced in collaboration with my supervisor Professor Ghassan Yassin, Dr. Paul Grimes and Dr. Boon Kok Tan at Oxford and Dr. Mikhail Tarasov at Chalmers University. I have fabricated all devices at Chalmers University, using procedures I developed myself. The CEB-finline design and testing was done by the author under the guidance of my supervisor and Dr. Paul Grimes.

The work described in Chapter 4 was produced in collaboration with my supervisor Ghassan Yassin, Paul Grimes, Mikhail Tarasov, and Leonid Kuzmin. The devices were fabricated by the author with guidance from Dr. Mikhail Tarasov.

The material in Chapter 5 was done in collaboration with my supervisor Ghassan Yassin, Paul Grimes, Mikhail Tarasov, Leonid Kuzmin and Christopher North. I have developed and fabricated the phase switch devices presented here.

All the work and material above was published, and relevant references are given in the text of each chapter.

ACKNOWLEDGEMENTS

First and foremost, I would like to extend my gratitude to a number of people who have helped me during the time I spent working on this thesis.

I am exceedingly grateful to my supervisor, Professor Ghassan Yassin, for his expertise, support, guidance and explanation. I am especially grateful for his professional advice, financial support and coaching, which all provided me with significant benefits.

In addition, the help, advice and guidance of Paul Grimes, as well as the technical support of Jamie Leech and especially Rik Elliott were much appreciated.

Thanks to Chris North, Boon Kok Tan, Oliver King, Mihran Vardanyan, Yangjun Zhou, and Andre Hector for fruitful collaboration and exciting technical discussions.

I would also like to thank Professor Leonid Kuzmin, my second supervisor, who gave me invaluable help with Cold-electron Bolometer theory and design, while also organising successful and collaborative work with the Quantum Device Physics Group at Chalmers University – MC2. Also, I would like to extend my gratitude to our collaborators and students at Chalmers: Sumedh Mahashabde, Anna Gordeeva, Artem Chekushkin and Daria Kharchenko Nagirnaya for fruitful collaboration, and Tom Yager for interesting discussions. I am especially grateful to Dr. Mikhail Tarasov for his support in fabricating and testing the devices.

Finally, I am extremely grateful to my mother Svetlana and the rest of my family for their support during my time in Oxford. Especial thanks go to my daughter Svetlana, as well as to my sister Anna and my wonderful wife Inna, who both have supported me and helped me to take care of our children Anton, Markus, Gleb, Simona, and Svetlana.

Contents

Chapter 1

Introduction

1.1. Introduction to CMB cosmology

Radio astronomy is perhaps one of the most exciting research areas studied in the last few decades. Very high sensitivities have been achieved using modern technologies and new observation techniques such as radio interferometry and ultra-sensitive detectors. Early observations in radio astronomy were performed at frequencies in the GHz region, while extensive observations at millimeter and sub-millimeter wavelengths became feasible following the development of a new generation of heterodyne detectors. A substantial improvement in the sensitivity was achieved following the development of the Superconductor-Insulator-Superconductor (SIS) detectors that were used as mixers in heterodyne receivers. This invention and the development of coherent receivers enabled very advanced astronomical observations using new high performance millimeter and sub-millimeter telescopes. New instruments were built at sites with very low humidity, enabling, for the first time, astronomical observations from about 100 GHz to 1 THz. Among these sub-

millimeter receivers is HARP-b (Heterodyne Array Receiver Project) which was installed on the largest single-dish sub-mm telescope at that time, the JCMT (James Clerk Maxwell Telescope) [1]. More recently, SIS heterodyne receivers covering the frequency range of 100 GHz to 1 THz have been developed and fabricated for the largest submillimeter telescope ever built which is the Atacama Large Millimeter / submillimeter Array (ALMA) [1, 2].

The performance of sub-millimeter instruments is determined by key components, in particular very sensitive detectors, since the radiation coming from space is extremely weak. In this thesis, we will describe our work on the technology development for sub-millimeter cosmology instrumentation using bolometric devices fabricated by means of newly developed technologies. This includes the development of fabrication technology for bolometric detectors, as well as our work on phase switch devices, which constitutes a part of a receiver system. In this chapter, we also discuss astronomical observations performed by sub-millimeter instruments using bolometers and some resulting scientific achievements.

Among the important achievements in radio astronomy using modern technologies, the most fundamental is discovering the Cosmic Microwave Background (CMB) anisotropy and polarization. This is because at the moment the CMB is the best experimental supporting evidence of the Big Bang theory. The Cosmic Microwave Background is the relic of the radiation emitted by the Big Bang. The radiation that is measured today contains information regarding its interaction with matter about 13.7 billion years ago, when the recombination of the ionized matter started and atoms could remain stable. Thus, the CMB measurements allow understanding of the evolution and early history of the Universe.

Following the Big Bang, the universe expanded. When the Universe cooled down to around 3000 K, the ionized matter started to recombine and neutral matter was formed, consisting mainly of hydrogen atoms. This happened approximately 300 000 years after the Big Bang, at which point the Universe became transparent to electromagnetic radiation. Due to further expansion, the temperature has continued to decrease and nowadays the measured CMB temperature is around 2.73 K, while the radiation intensity of the black body peaks at a frequency of 160.2 GHz.

According to modern cosmological models, the Big Bang was followed by an Inflation period. The inflation theory suggests a very rapid expansion of the space approximately 10^{-35} s after the Big Bang. An assumption of such an expansion solves many cosmological problems that have risen after the CMB discovery and measured data analysis.

The Big Bang model supported by Inflation predicts the observable Universe to be flat and explains many other phenomena and cosmological problems that can not be explained otherwise, e.g. the Hubble expansion, the large-scale structure of the space (i.e. the distribution of matter across the space), as well as the temperature and density variations during the time of the evolution of the Universe.

Measurements of the CMB by various instruments (such as COBE [3], WMAP [4]) confirmed the black body nature of the radiation and were consistent with the anisotropy power spectrum models predicted by Inflation.

The expansion of the early Universe can be described by the Hubble law which can be written as

$$v = H_0 \cdot d$$

where v is the recession velocity and d is the distance of remote galaxies, and H_0 is Hubble parameter which determines the rate of the expansion.

Due to gravitational attraction, the rate of the expansion of the Universe is determined by the density of the matter in the Universe. The currently accepted value of the Hubble constant determined by WMAP data is $H_0 = 70.5 \pm 1.3$ km·s^{-1}·Mpc^{-1}, corresponding to an age of the Universe of 13.72 ± 0.12 Gyr.

CMB measurements have shown that the radiation temperature is very uniform across the sky, and only very small variations in its black body temperature were observed, at the level of 100 μK. This reflects very small fluctuations in density in the early universe [5]. A number of experiments [6-13] were conducted in order to measure the distribution of CMB temperature, and even the full-sky distribution has been mapped by satellite experiments (Fig.1.1), such as WMAP satellite [12], and Planck [13].

The measured temperature distribution of the CMB can be expressed by its angular power spectrum using a Fourier transform expansion:

$$\frac{\Delta T(\theta,\phi)}{T_0} = \sum_{lm} a_{lm} Y_{lm}(\theta,\phi)$$

where T_0 is the mean CMB temperature, $T_0 \equiv 2.73$ K; $Y_{lm}(\theta, \varphi)$ are the spherical Fourier harmonic components in the direction (θ, φ) on the sky, with l being the angular scale of the Fourier mode, and m gives the mode direction.

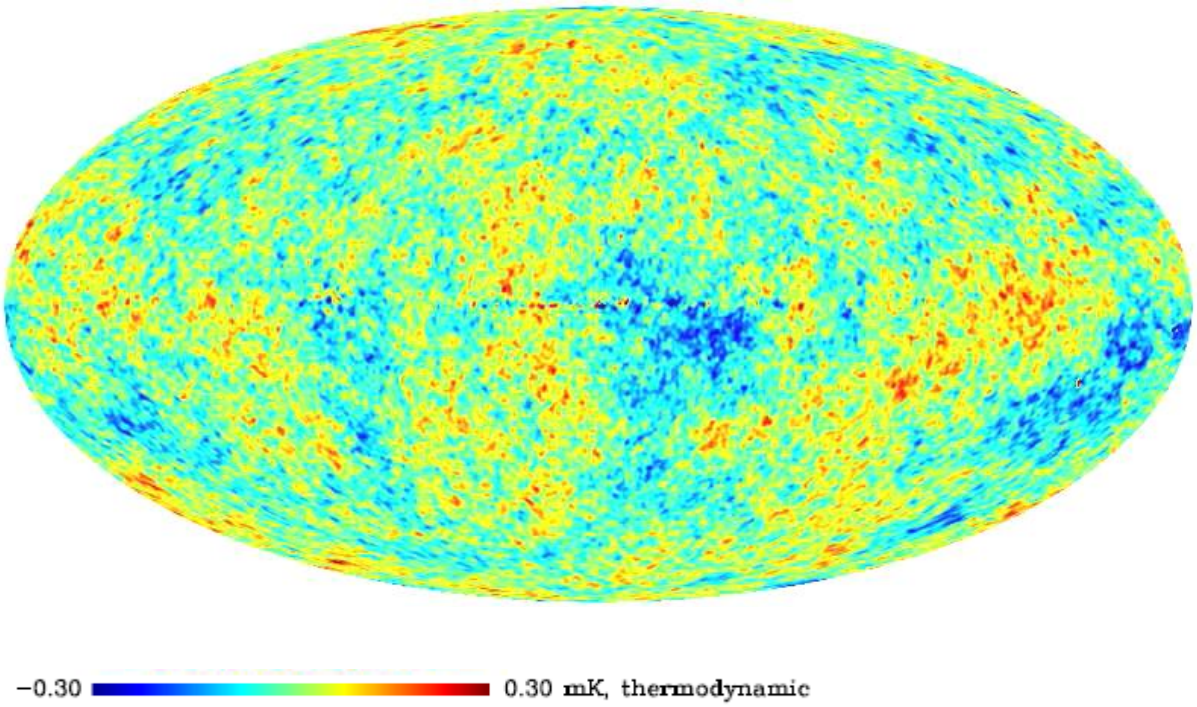

Figure 1.1: All-sky map of the CMB temperature [5, 12]. The full sky is projected onto a 2D image.

The angular power spectrum is then given by:

$$\left\langle a_{lm} a^{*}_{l'm'} \right\rangle = C_l \delta_{ll'} \delta_{mm'}, \text{ where}$$

$$C_l = \frac{1}{2l+1} \sum_m \left| a^2_{lm} \right|$$

The mean-square anisotropy is therefore expressed as:

$$\left\langle \Delta T^2 \right\rangle = T_0^2 \sum_l \frac{2l+1}{4\pi} C_l \approx T_0^2 \int \frac{l(l+1)}{2\pi} C_l d\ln l$$

The CMB angular power spectrum is shown in Fig. 1.2 as measured by several instruments and compared with a model that fits the data.

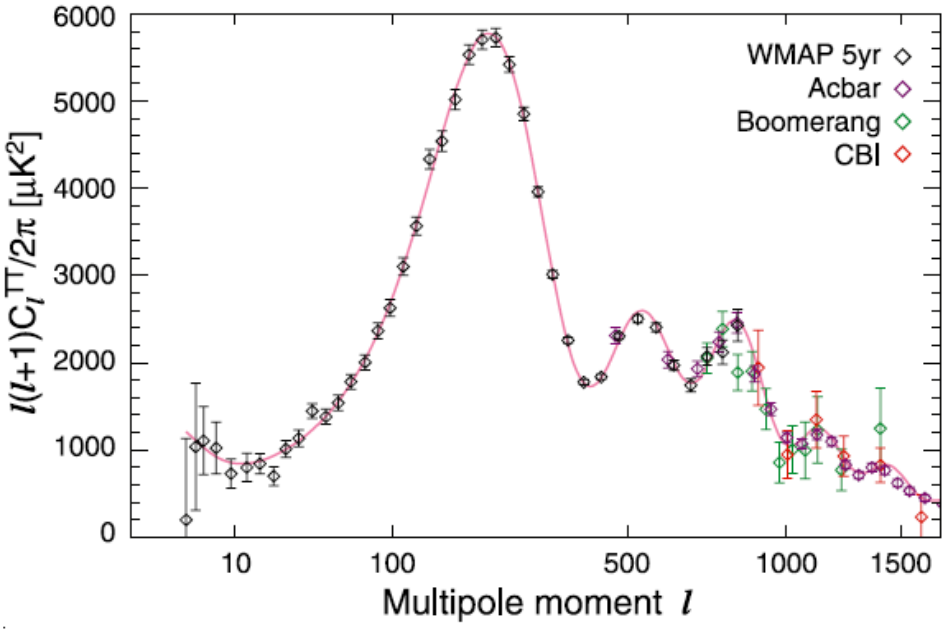

Figure 1.2. Angular power spectra of the CMB temperature [5, 6, 12]

1.2. CMB polarization

The cosmic microwave background (CMB) fluctuations are about 10% polarized. Polarization of the CMB radiation is produced by the Thomson scattering of photons by electrons near the last scattering surface [14, 5]. After scattering, the incoming photons with different energies are partially polarized, as explained by Fig. 1.3. It should be noted that anisotropy with regard to dipolar distributions does not polarize the light; only higher order distributions produce

polarization [5]. In the early Universe, perturbations after the Big Bang initiated density fluctuations that became amplified during Inflation. CMB radiation which is partially polarized due to scattering in anisotropic electromagnetic fields originates from temperature fluctuations caused by the density fluctuations after the Big Bang and Inflation.

An experimental confirmation of the Inflation theory could be obtained by the measurements of the CMB polarization as a sign of Inflation should be present in the CMB polarization. The CMB polarization measurement is the goal of most current CMB experiments, (e.g. BICEP [9], Planck [13], EBEX [15]).

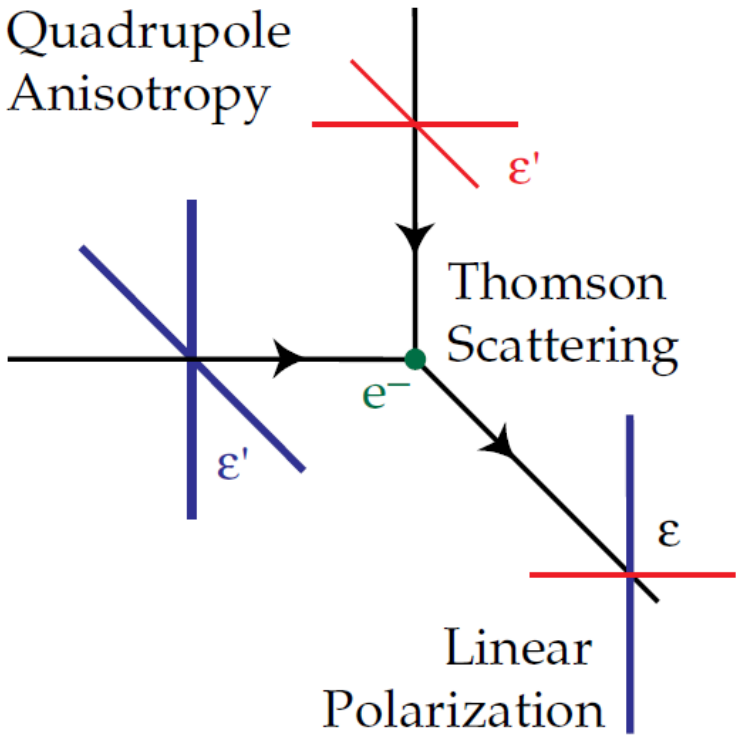

Figure 1.3. Thomson scattering of photons by electrons in a quadrupolar radiation field yields partially polarized radiation [5, 14].

The polarisation of the CMB can be decomposed into a curl (B-mode) and a curl-free component (E-mode) [16]. The E-mode component is generated by density perturbations, and has recently been detected [11, 17]. However, the B-mode signal which provides unique information about the universe [18] is estimated to be at least one order of magnitude smaller than the E-mode such that detection is still a challenge [16, 18]. Several ground based and balloon-borne cosmology instruments have been designed to detect the B-mode component, e.g. Clover comprises two independent telescopes operating at 97 / 150 and 225 GHz. Another experiment is BICEP (Background Imaging of Cosmic Extragalactic Polarization), a ground based instrument dedicated to high-precision CMB polarization measurements. The BICEP instrument with a flexible and upgradeable design of an array of 98 detectors operates at 100 GHz and 150 GHz, mapping an area on the sky around the South Celestial Pole [9].

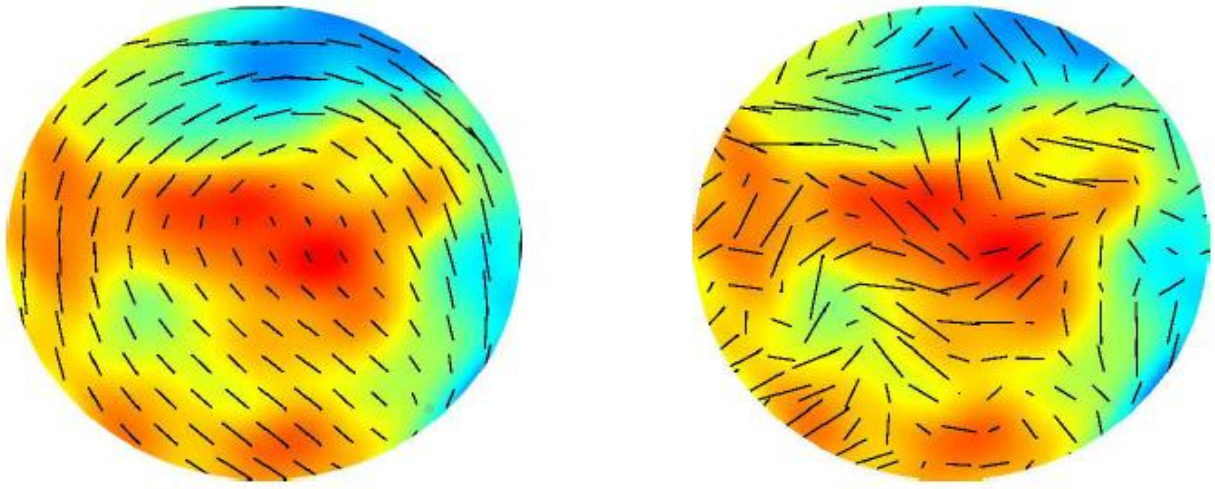

Figure 1.4: Simulations of: (Left) E-mode fields; (Right) B-mode fields. Amplitude of polarization shown by color, directions indicated with lines. The E-mode is correlated with the amplitude of the polarization, while the B-mode polarization angle is not correlated [5].

The angular spectra of the two components $C^{EE}{}_{\ell}$, $C^{BB}{}_{\ell}$ along with the temperature cross-correlation component $C^{TE}{}_{\ell}$, are calculated similarly to the temperature anisotropies [5]:

$$C_l^{EE} = \frac{1}{2l+1}\sum_{m=-l}^{l}\left|a_{lm}^{E\ 2}\right|$$

$$C_l^{BB} = \frac{1}{2l+1}\sum_{m=-l}^{l}\left|a_{lm}^{B\ 2}\right|$$

$$C_l^{TE} = \frac{1}{2l+1}\sum_{m=-l}^{l}\left|a_{lm}^{T} a_{lm}^{E*}\right|$$

This presentation of the polarization field determines the correlation between the polarization amplitude and direction: the E-mode polarization is directed perpendicular or parallel to the amplitude gradient; the B-mode is directed at 45 degree to the gradient [5], see Figure 1.4.

The theoretically predicted angular power spectra are shown in Fig. 1.5. The B-mode curve is shown in black, including a forecasted B-mode secondary signal caused by the gravitational lensing of partially polarized CMB radiation when travelling through large-scale structures. The predicted foreground signals power spectra based on polarization observations and unpolarized emission models [17, 19, 20, 21] are plotted for the C_{ℓ}over observation regions before cleaning. The polarized foreground signals are plotted for 225 and 97 GHz and represent thermal emission from dust grains and synchrotron emission respectively [22].

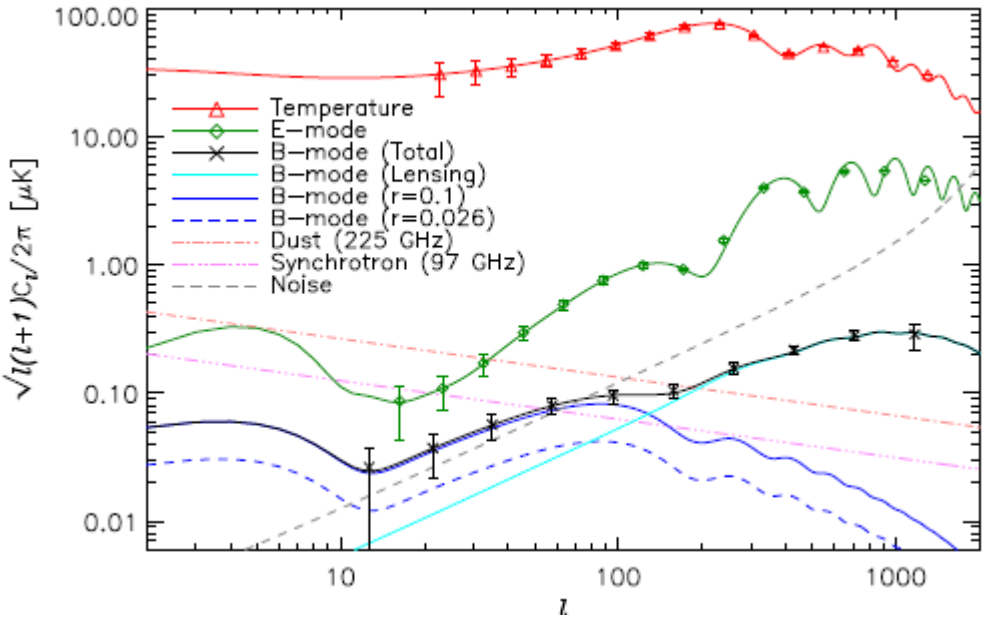

Figure 1.5: Theoretical angular power spectra for the temperature, E-mode and B-mode signals, and expected $C_\ell$over sensitivity [5, 21].

1.3. Measurements of CMB polarization

The electric field in a polarized electromagnetic signal can be represented by its orthogonal components, E_x and E_y. The Stokes parameters are then expressed by the average values of the amplitude of the electric field over many cycles of the electromagnetic wave, i.e. [5]:

$$I = \langle E_x^2 + E_y^2 \rangle$$

$$Q = \langle E_x^2 - E_y^2 \rangle$$

$$U = \langle 2E_xE_y \cdot \cos(\varphi) \rangle$$

$$V = \langle 2E_xE_y \cdot \sin(\varphi) \rangle$$

where ‹…› means time averaging over periods and φ is the phase difference between the fields in the x and y directions.

The polarization of an electromagnetic wave can therefore be determined by measuring the Stokes parameters I, Q, U, V where I is the total intensity, V measures the degree of circular polarization and Q and U measure the degree of linear polarization in two orthogonal directions [18]. In the pseudo-correlation polarimeter, shown in Fig. 1.6, the signal received by one of the focal plane horns is split into two linear polarizations using an orthomode transducer (OMT). The signals are then converted into circular polarization using a quadrature hybrid. One signal is then phase modulated relative to the other. Finally the two signals are converted back to linear polarization and measured by the detectors. It can be shown that the output signals D_1 and D_2 in Figure 1.6, measured by the detectors are [18]:

$$D_1 = I - Q\cdot\cos\varphi - U\cdot\sin\varphi \tag{1.1}$$

$$D_2 = I + Q\cdot\cos\varphi + U\cdot\sin\varphi \tag{1.2}$$

Since the CMB is linearly polarized, we will therefore focus on the measurements of U and Q.

According to the equations (1.1) and (1.2), the output is sensitive to I, U and Q Stokes parameters and it is therefore possible to determine the linear polarisation parameters by taking the difference of the detector outputs. By switching the phase difference between 0 and 180 degrees, the U term remains zero and Q is measured. By changing the phase difference between 0 and 90 degrees we switch the output between Q and U [18].

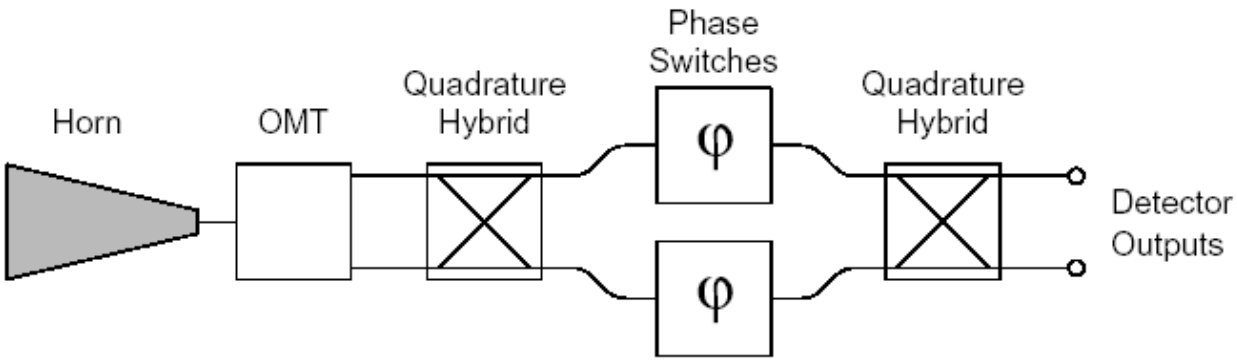

Figure 1.6: The layout of a pseudo-correlation polarimeter [18].

1.4. CMB polarization instruments

In recent years, experimental observations yielded accurate measurements of the CMB anisotropies. A number of cosmological instruments aiming to measure the CMB have been built. E.g., the space-borne telescope WMAP (Wilkinson Microwave Anisotropy Probe) mapped the CMB in detail across the whole sky [4, 17]. DASI is a 13-element interferometer designed to measure temperature and polarization anisotropy of the CMB radiation over a large range of scales with high sensitivity [23, 24].

WMAP and DASI were able to detect the TE and EE polarization, but the BB component is yet to be measured. This is because the B-mode signal is expected to be at least one order of magnitude weaker than the EE component. Consequently, B-mode instruments must use very sensitive detectors for these measurements. In order to achieve this, superconducting bolometric devices (or bolometers) are used by all the newly designed instruments.

A UK instrument $C_\ell$over was designed as a ground-based experiment for measuring the B-mode polarization of the CMB. Ground-based experiments have some advantages over space-borne and balloon experiments, due to easy access to the instrument. On the other hand, the atmosphere adds a background noise to the signal to be detected. In order to overcome this and achieve a reasonable sensitivity, a large number of very sensitive detectors must be used.

Transition edge sensor (TES) detectors were designed to have sensitivity which is limited by the photon noise. The design of the experiment included 576 superconducting TES detectors, cooled to 100 mK; to be multiplexed with a time-domain readout. Observations were planned in frequency bands centered at 97, 150 and 225 GHz using two instruments, one for 97 GHz and another one for 150 and 225 GHz. These frequency bands corresponded to atmospheric transmission windows at Llano de Chajnantor Observatory, while the CMB blackbody spectrum peaks at ~ 150 GHz.

Two receiver systems with the detectors were planned to be mounted at the focal planes of antennas with low cross-polarization. The schematic design of each instrument showing the receiver and optical setup is shown in Figure 1.7. Inside the receiver cryostat, each pixel includes a horn, an orthomode transducer (OMT) to decompose the incident electromagnetic wave into two orthogonal linear polarization components, and two TES detectors for the two orthogonal polarizations.

An example focal plane layout is shown in Fig. 1.8. The three-way symmetry of the focal planes gives symmetry in the position of different detectors and thus the polarization angles to be detected [5].

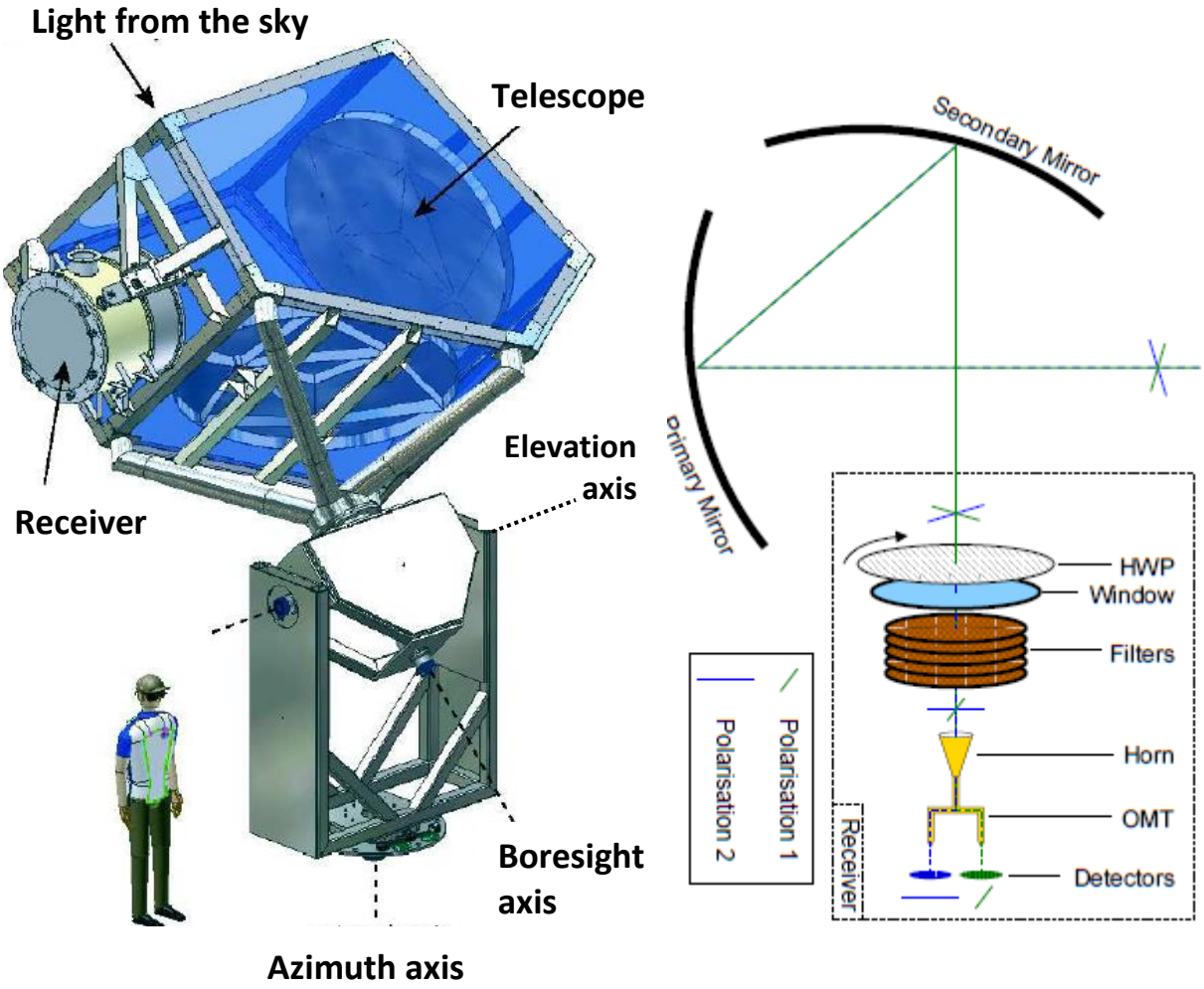

Figure 1.7. (Left) The design of a $C_\ell$over instrument, by the Oxford Physics Design Office, with the hardware made through the Oxford Physics Workshops [5, 21]. (Right) The optical path of each pixel through the 97 GHz instrument [5]. The incoming beam is focused onto the focal plane. The half-wave plate (HWP) rotates the polarizations of the incoming wave. After filtering, the signal is collected by the horn and decomposed by the OMT into two polarizations, detected then by TES detectors [5].

The instruments employ a compact range antenna (CRA) telescope [25], made of parabolic and hyperbolic concave mirrors. This approach ensures reasonably low level of cross-polarization across a large focal plane. For all focal plane elements the cross polarization was expected to be better than −38 dB [5].

Each horn in the focal plane has a somewhat different signal pathway, and the resulting projection of the focal plane on the sky is a regular array. Each horn irradiates some area of the secondary, so the beams structure becomes somewhat complex in the main beam and in the sidelobes; the sidelobes are at the same time as low as < -70 dB at $\sim 3^{o}$ from the main beam.

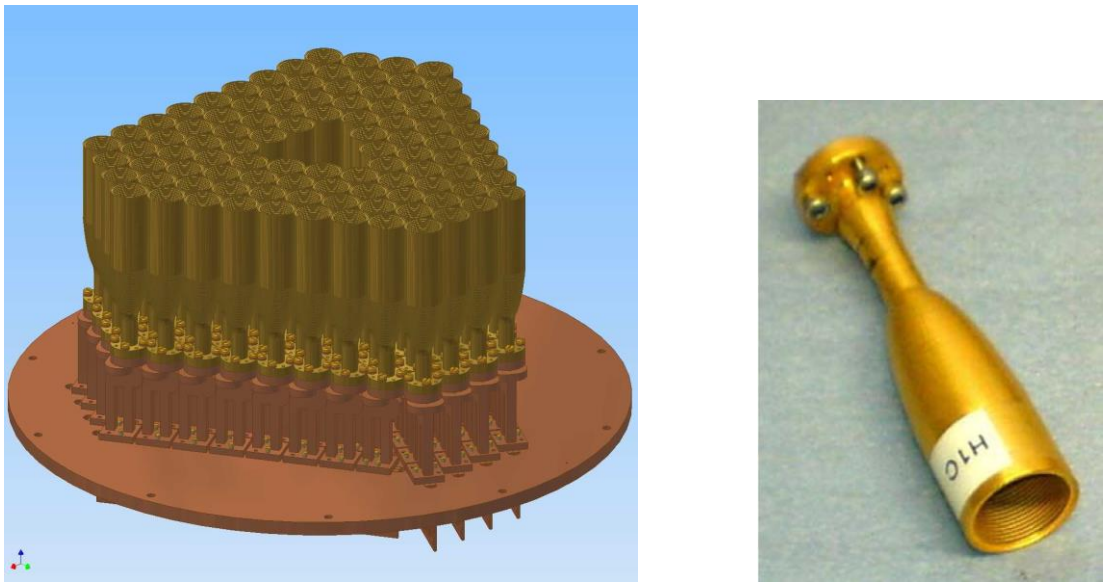

Figure 1.8. Layout of the detector block arrays within the focal plane array (left) and a 97 GHz prototype horn for Clover instruments (right), [5, 21, 34]

Horns that are used for high-precision CMB-related measurements were designed for preventing the propagation of higher-order modes and for minimizing the cross-polarization. An attractive option in this case is to use corrugated horns that have azimuthal corrugations on the inward surface creating isotropic boundary conditions at the surface for E- and H-field components [1], which prevents the propagation of higher-order modes and allows primarily propagation of the modes contributing to polarized signals at the output. The above features

result in the narrow radiation pattern with minimum sidelobes and low cross-polarization levels [1, 5].

Many pixels are desirable in such experiments in order to achieve a reasonable sensitivity and distinguish the signal from the atmospheric background noise. So, as many as 192 detectors were designed at each frequency [5], giving 96 pixels for each frequency, which is determined by the dimensions of the focal plane that is limited by the size of cryostat window. Two TES detectors in each single pixel are placed orthogonally to each other, which enables the detection of the electromagnetic waves with two polarizations.

1.5. Millimeter-wave direct detectors

Millimetre-wave detectors can be divided in two classes based on different ways of operation. The first are so-called direct detectors and the second are coherent detectors. Direct detectors measure the power of the incoming radiation with wide RF bandwidth [26], which enables the detection of very weak signals. Coherent detectors are employed in heterodyne receivers, where the incoming RF signal is first downconverted to a lower frequency, called Intermediate Frequency (IF), before it is amplified and read by a spectrometer. This preserves the phase information of the incoming signal and makes it possible to use low-frequency amplifiers, filters and other RF components which are difficult or impossible to use at hundreds of GHz and THz frequencies, because of high losses. As a result, the sensitivity of the receiver is somewhat reduced compared to direct detection, since it is limited by the IF bandwidth of the receiver (e.g., the cryogenic amplifier or the mixer).

Bolometers are used in millimetre and far-infrared instruments and they form a component of novel concepts such as bolometric interferometers [24] and pseudo-correlation polarimeters [18]. Many discoveries in astrophysics have been made by millimetre-wave and far-infrared bolometer instruments. For example, SCUBA has discovered a new class of dusty sub-mm luminous galaxies and observed the effects of formed planets on protoplanetary discs [27].

In recent years, both coherent detectors and bolometers were made of superconducting thin films. Two examples of superconducting direct detectors that are now thoroughly investigated are the Kinetic Inductance Detectors (KID) [28-30] and the Transition Edge Sensors (TES) [22, 26].

The recently developed microwave Kinetic Inductance Detectors (KID) are superconducting photon detectors relying on modulating the impedance of a superconductor by changing its kinetic inductance by incident electromagnetic signal, which modifies the density of Cooper pairs and quasi particles. The principle of operation of the KID detector is based on the fact that, apart from geometrical inductance, superconductors display kinetic inductance due to the energy that is stored in the supercurrent, which is effectively equivalent to an inductance. Incident photons change the impedance of a superconductor by modulating its kinetic inductance [31]. This effect occurs because the kinetic inductance increases upon photon absorption due to increased density of quasi particles.

A change in the kinetic inductance can be measured using a thin film resonant circuit and hence the incoming power can be estimated. Therefore, receiver systems based on KID detectors employ distributed resonant components comprising superconducting microwave

resonant circuits. Each single KID superconducting resonator with an antenna or absorber is capacitively coupled to a coplanar waveguide. The quality factor and the central frequency of the resonator are determined by the geometry of the integrated circuit (Fig. 1.9). Several resonators with different geometries and resonance frequencies can be coupled to one line and read out simultaneously. In that way, the frequency domain multiplexing at GHz frequencies is employed in KID detectors, which enables simultaneous reading of several detectors.

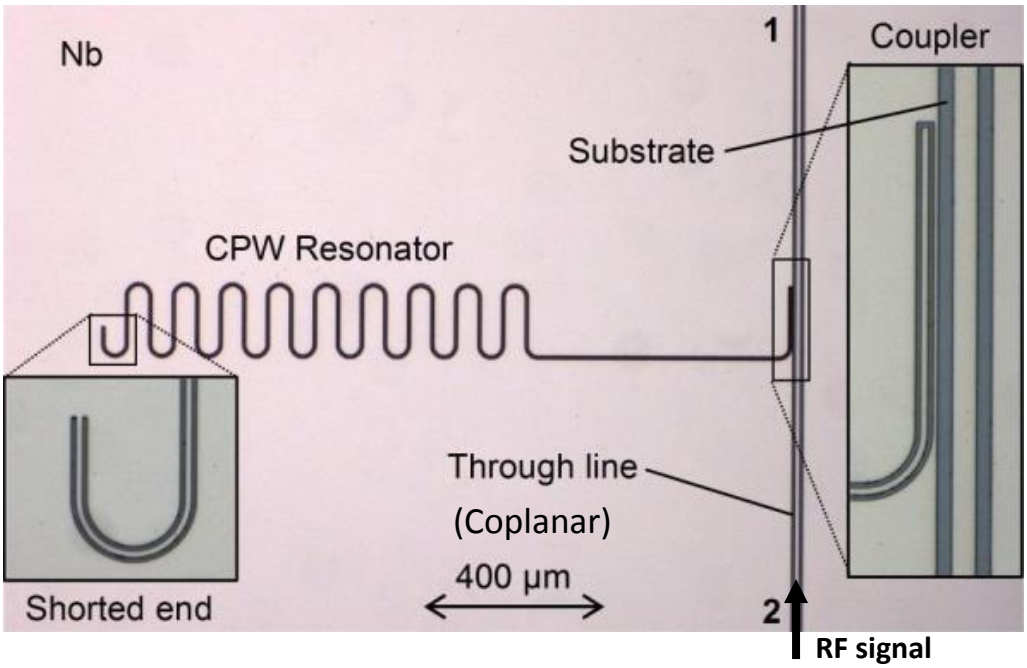

Figure 1.9. A typical KID microwave circuit: CPW resonator coupled to a through line [29, 30, 31].

Consider a superconducting film that absorbs an incident signal. At temperatures far below the transition temperature, most of the electrons in a superconductor are condensed into Cooper pairs with density n_c, while the density of the quasiparticles n_{qp} is much less than Cooper pair density n_c. [31]. An incident electromagnetic wave with a frequency $f > 2\Delta/h$, where Δ is the

gap of the superconductor, h Planck's constant, breaks Cooper pairs, resulting in increasing number of quasi-particles:

$$n_{qp}^{excess} = \frac{\eta P \tau_{qp}}{\Delta}$$

where P is the incident power, τ_{qp} the quasi-particle lifetime and η the efficiency of energy transfer [31]. The sensitivity of such a detector can be expressed by the NEP [29, 31]:

$$NEP = \frac{2\Delta}{\eta}\sqrt{n_{qp} V / \tau_{qp}}$$

where V is the detector volume.

An equivalent circuit of the KID superconducting resonator is shown in Fig. 1.10. By changing the complex impedance of the resonance circuit, one can change the resonance frequency. The measured transmission of a resonator (Figure 1.10, right) displays a minimum at resonance frequency that moves towards lower frequencies upon absorption of the incoming power [31].

KIDs arrays have not yet been deployed in real millimetre wave instruments but extensive research is now carried out in this area [29, 30].

The Transition-Edge Sensor (TES) comprises a ~50 μm superconducting film deposited on a thin membrane [32, 33]. Detection of incoming signals in TES is made by holding the superconductor at the transition between the superconducting and normal states [5]. An

example TES circuit schematic is shown in Figure 1.11. In this scheme, the incoming power heats the device, causing a strong increase in the device resistance as it makes the transition from the superconducting to the normal states [5]. This sharp increase in the resistance leads to a flux change, which is measured by a SQUID.

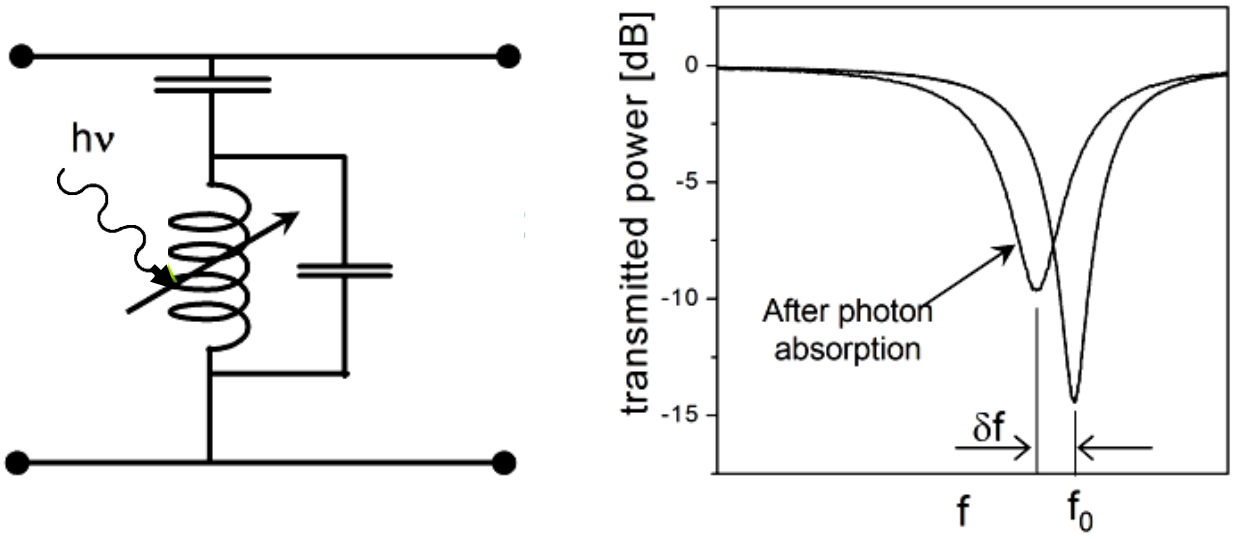

Figure 1.10. (Left) KID equivalent circuit with changing complex impedance of the KID resonator [29, 30, 31]. (Right) Transmission of a KID resonator, $\delta f \cdot h$ = incident photon energy [29, 30, 31].

In the TES circuit topology shown in Figure 1.11, the biasing is implemented using a voltage source V_{bias} and a load resistor R_{bias} [5]. The SQUID readout system is employed by coupling an inductance L to a SQUID flux meter that effectively measures the TES current by measuring the input flux to the SQUID.

Using the thermal conductivity G, the Noise Equivalent Power (NEP) of TES detectors derived from phonon fluctuations can be expressed as [33]:

$$NEP = \sqrt{4k_B T^2 G}$$

where k_B is the Boltzmann constant and T is the temperature of the detector. The reported values for NEP of TES detectors vary between ~10^{-18} and ~10^{-16} W/ $Hz^{1/2}$.

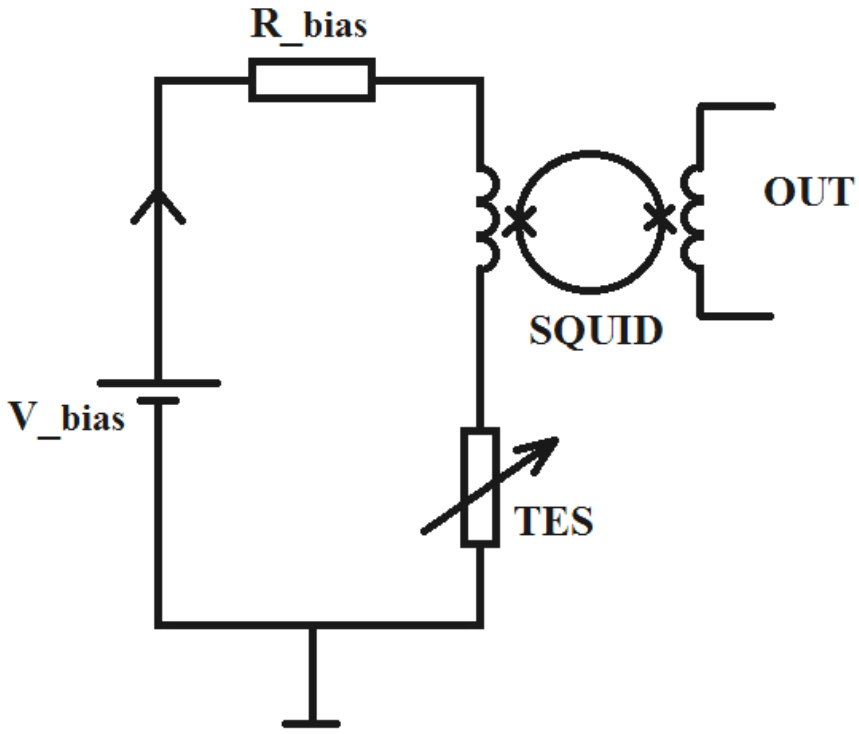

Figure 1.11. TES equivalent circuit schematic with SQUID readout [5]

TES bolometers are used in many CMB-related projects such as the above-mentioned ground-based telescope BICEP, operating at 100 and 150 GHz, and EBEX (the E- and B- Experiment) that is a balloon-borne instrument designed to measure the intensity and polarization of the CMB radiation [15] and hence probe the inflationary epoch that took place shortly after the

Big Bang. EBEX consists of a 1.5 m telescope with a resolution below 8 arcminutes over four focal planes, operating at frequencies of 150, 250, 350, and 450 GHz. The experiment was designed to employ 330 TES detectors per focal plane, that is 1320 TES detectors in total, with NEP reported around $1\text{-}2\cdot10^{-17}$ W/ $Hz^{1/2}$ [15].

Another example of telescope projects employing TES detectors was Cℓover that was designed as an instrument relying on TES-microstrip integrated circuits with high sensitivity and overall noise performance. The TES system design proposed for Cℓover [21] operates as follows (see Figure 1.12). The RF power is delivered to the bolometer through a microstrip terminated by a resistor. The power received by the TES is then dissipated in the terminating resistor which results in heating the TES resistor (absorber). This architecture was chosen due the strict requirements of Cℓover on sensitivity and on cross-polarization (< -35 dB). The microstrip-coupled TES architecture allows for coupling to the waveguides with high efficiency compared to free-space coupling of a detector chip. In addition, the microstrip coupling provides flexibility by separating the bolometer from the microstrip-waveguide interface [22]. This allows optimization of the TES independent of the absorber. As a result, similar TES detectors can be used with different RF system topologies [34].

An example prototype 97-GHz Cℓover detector chip is shown in Figure 1.12. The chips were fabricated on a 2" wafer using deep reactive ion etching (DRIE) used for patterning the chip outline and the silicon nitride membrane. The processing was performed by the Detector Physics Group at the Cavendish Laboratory in Cambridge [35].

The 97-GHz TES detectors use finline transition to couple the signal from the waveguide [22]. Power coupling from the waveguide to the detector chip is realized using a finline taper (Figure 1.13) made of superconducting Nb film with an insulating SiO_2 layer [5, 22]. The finline chip was designed by the millimeter-wave detector group at Oxford.

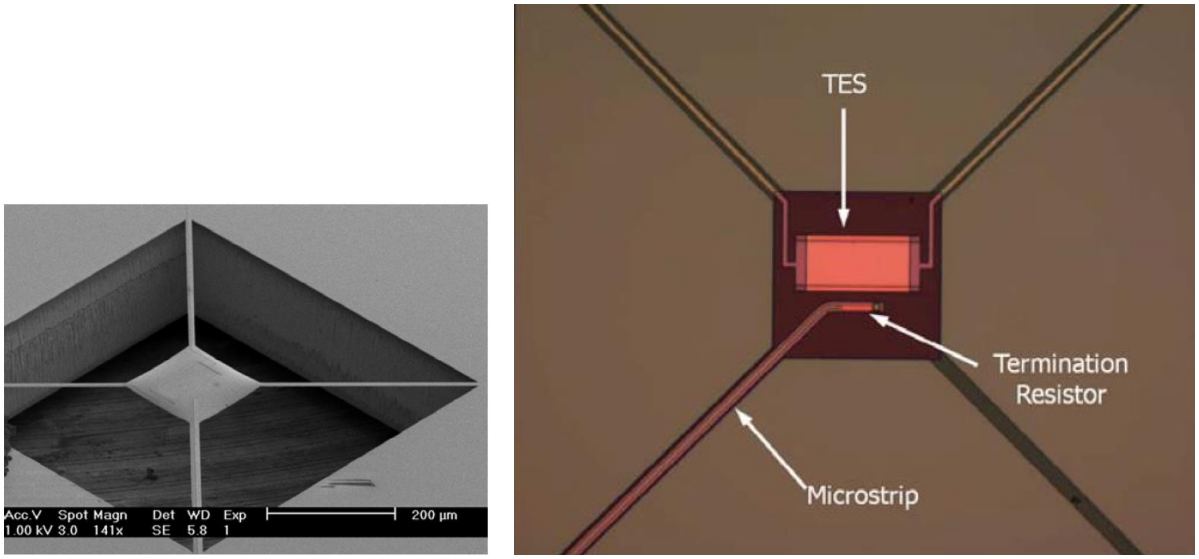

Figure 1.12. $C_t$over prototype bolometer on a silicon nitride membrane: TES and microstrip leading to termination resistor [22]; a scanning electron microscope image (Left) and an optical image (Right). The devices were fabricated at the Detector Physics Group (Cambridge).

For Clover, the required NEP level was $5 \cdot 10^{-17}$ W/ $Hz^{1/2}$ for 97 and 150 GHz channels and $9 \cdot 10^{-17}$ $W/Hz^{1/2}$ for the 225 GHz detectors [5]. The reported measured values for TES detectors are $1.7 \cdot 10^{-17}$ to $3 \cdot 10^{-17}$ W/ $Hz^{1/2}$ [22, 34]. The NEP values reported for other projects employing TES detectors, such as e.g. BICEP and EBEX, have the same order of magnitude, $\sim 10^{-17}$ $W/Hz^{1/2}$ [5, 15].

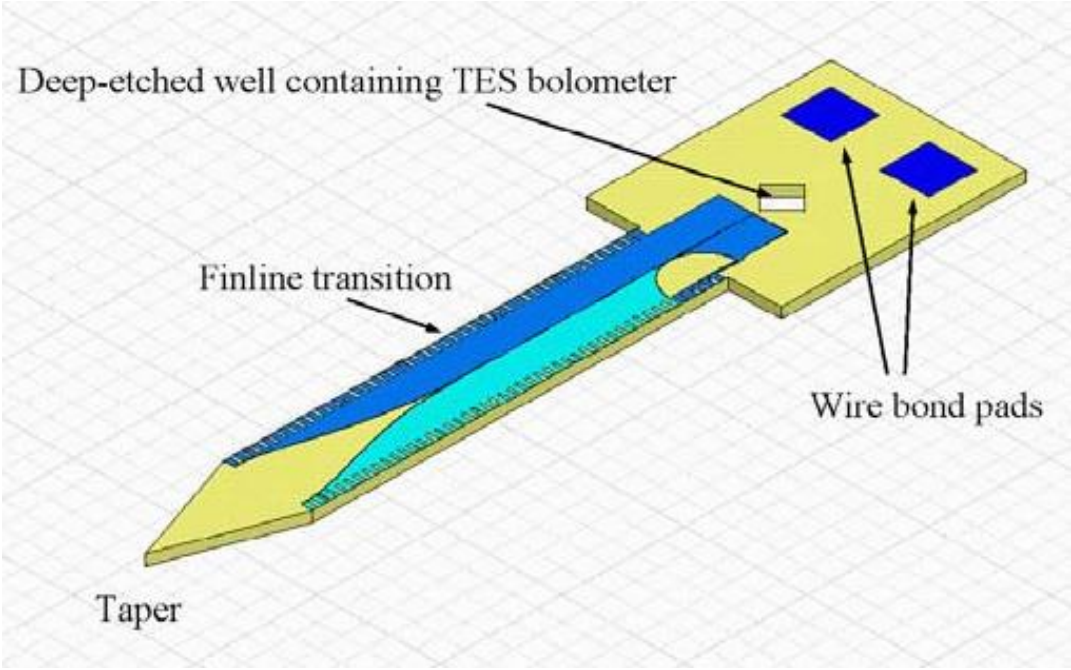

Figure 1.13. Layout of prototype 97-GHz C$_t$over detector chip [22], designed by the Detector group at Oxford

1.6. Cold-Electron Bolometer

The main drawback of TES is its very limited saturation power. This is a serious issue due to the stochastic nature of the signals coming from space. TES bolometers saturate when the incident signal is strong enough to turn the device fully normal. This is because DC bias heating is applied to enable normal operation of TES, which leads to excess noise of the TES-based receivers. Also, due to the very low impedance of the TES detector, they must be read out using SQUID readout amplifiers. Both SQUIDs and TESs are very susceptible to magnetic fields, requiring shielding of the instrument [5].

In order to overcome the above problems related to using TES detectors, a novel concept of the Cold-Electron Bolometer (CEB) [36-43] has been introduced by Leonid Kuzmin in 1998. Cold Electron Bolometer with SIN tunnel junctions is a millimeter-wave detector which employs a strip of a normal metal that changes in temperature as it absorbs the incoming radiation [44, 45].

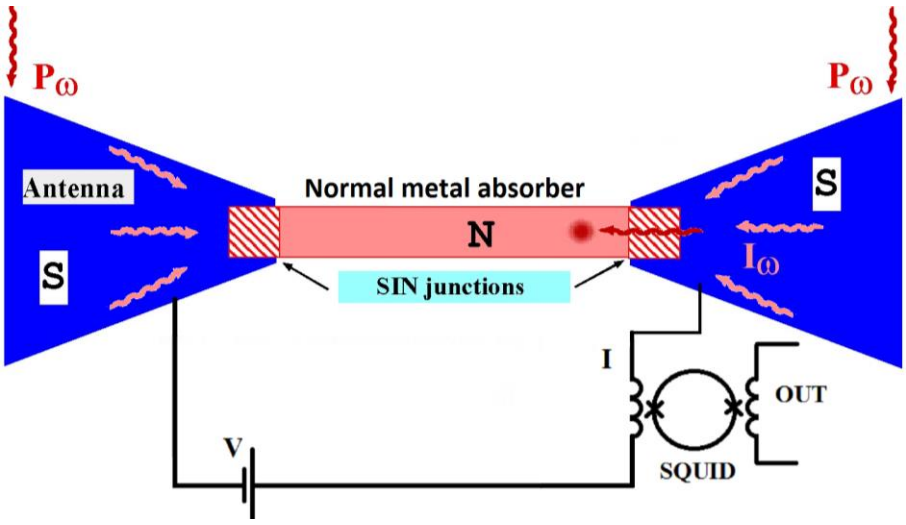

Figure 1.14. Cold-Electron Bolometer (CEB) with SIN tunnel junctions [46]. The signal power is supplied to the sensor through capacitances of tunnel junctions and dissipated in an absorber. The photon energy is absorbed by the electrons in the normal metal; thus, the electrons in the absorber are heated; this increase in temperature can be measured by the SIN junctions.

The CEB devices considered in this thesis consist of a normal metal absorber coupled to superconducting electrodes via SIN tunnel junctions at each end of the absorber (Figure 1.14). RF power from the antenna is thus capacitively coupled through the SIN tunnel junctions into the absorber. Incoming photons are absorbed by the normal metal causing hot electrons to be excited to a higher energy level (4 meV for 1 THz signal). The electrons are then relaxed due to electron-electron interactions and their energy is distributed between hot electrons at quantization level k_BT for normal metal, with the electron temperature over that of the

phonons, see Figure 1.15. The resulting change in the absorber electron temperature gives a substantial increase in the tunnelling current through the SIN junctions, due to exponential dependence of this current on the normal absorber temperature [47, 48]. The tunnelling current is then amplified and measured, which allows measuring the temperature of the absorber and thus the incoming RF power [44-49]. Thereby, SIN junctions are employed in this topology as CEB readout, as the change in the absorber electron temperature is measured with SIN junctions [48-51].

The key features of this type of detectors are: large dynamic range of the CEB that prevents the system from saturation when the incoming RF power is relatively high; hence the ability to operate in a wide range of background load; easy integration in arrays on planar substrates; and the possibility of polarization measurements [46, 52]. Yet another important advantage is a very simple and cheap readout system used for CEB detectors.

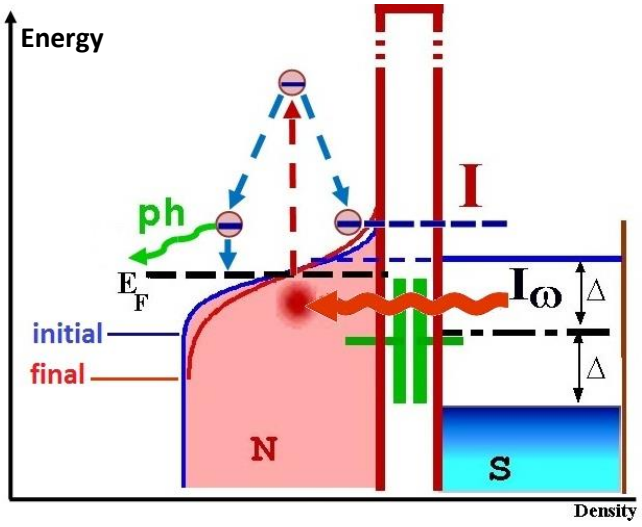

Figure 1.15. Energy diagram for SIN tunnel junctions in CEB [46]. As RF power is coupled to the absorber, the absorbed power excites electrons in the absorber; the electrons are then relaxed due to electron-electron interactions and their energy is distributed between hot electrons at quantization level k_BT for normal metal, thus increasing the electron temperature.

Since the electrons with the highest energy tunnel most rapidly through the oxide barrier of SIN junctions, the temperature of the absorber is reduced. This phenomenon is referred to as electron cooling. The electron cooling by SIN tunnel junction was reported in 1994 by Nahum et al., [53]. Later, effective cooling of normal-metal absorbers from 300 to 100 mK was successfully realized by several groups [54-56]. Electron cooling provides strong negative electrothermal feedback for the signal [42]. Unlike TES [48], the heating is replaced by electron cooling of the absorber using SIN tunnel junctions, down to an electron temperature that is below phonon temperature [46], [56]. This electro-thermal feedback makes the saturation power of a CEB well above that of other types of millimetre-wave direct detectors. Besides the high saturation power due to direct electron cooling by removing incoming power from the absorber, the noise of a device is reduced when decreasing the temperature.

The development of sensors based on SIN tunnel junctions started in the 1970s by Bakker et al [57]. Next, methods of measuring the temperature with SIN junctions were developed and experimentally verified by Pekkola [49] and Agulo [58], where SIN tunnel junctions and arrays were used for temperature sensing, which is also a part of CEB operation. Later, this approach was further developed by Ernst Otto, the author of this thesis, and the experimental results were published in the Journal SUST by Otto et al [36] in 2007. In that work, the total sensitivity of up to 100 SIN junctions was measured, and the approach was shown to be a feasible method of measuring the normal absorber temperature and, apparently, the incoming RF power, upon further technology development and the design improvements.

The CEB can be used with both JFET [59] and with SQUID readout [60-62]. For ground-based and balloon-based instruments, the JFET readout can be used, with NEP levels down to $5 \cdot 10^{-18}$ W/Hz$^{1/2}$ [60]. For space-borne telescopes, sensitivity better then NEP $\approx 10^{-18}$ W/Hz$^{1/2}$ can be achieved using the SQUID readout [61]. The goal is to achieve NEP approaching the level of the photon noise of the CMB radiation at given background power.

When used with JFET voltage readout and current-biasing scheme, CEBs could be integrated on planar substrates using parallel/series arrays, proposed by L. Kuzmin for efficient noise matching between the detector output and the JFET amplifier readout [46, 56]. In such an array, made of several CEBs, additional capacitors are employed for AC connecting adjacent absorbers to the antenna in the RF path, while disconnecting some absorbers from the antenna in the DC lead, see schematic in Figure 1.16.

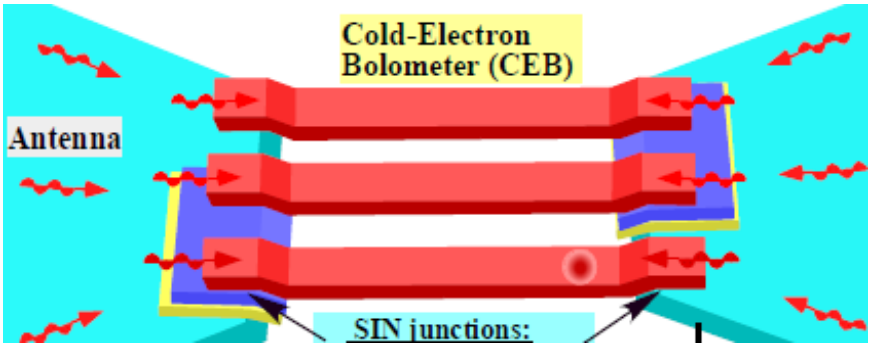

Figure 1.16. Schematic of three CEBs connected in a parallel/series array [56]. Additional capacitors (shown in blue) make AC connections between absorbers and the antenna, while DC disconnected.

The parallel/series array shown schematically in Figure 1.16 can be represented by two equivalent circuits for DC and RF signals shown in Figures 1.17 (top) and 1.17 (bottom), respectively. For a DC signal, tunnel junctions are connected in series with absorbers and are displayed in the equivalent circuit in Figure 1.17 as non-linear resistors. Capacitors are made

with a thick oxide layer so no tunneling can occur through the capacitors which are therefore to be considered as open circuits for DC signal. As a result, for the DC signal, the array shown in Figure 1.16 constitutes a series array of normal absorbers in series with tunnel junctions in between, see Figure 1.17, top.

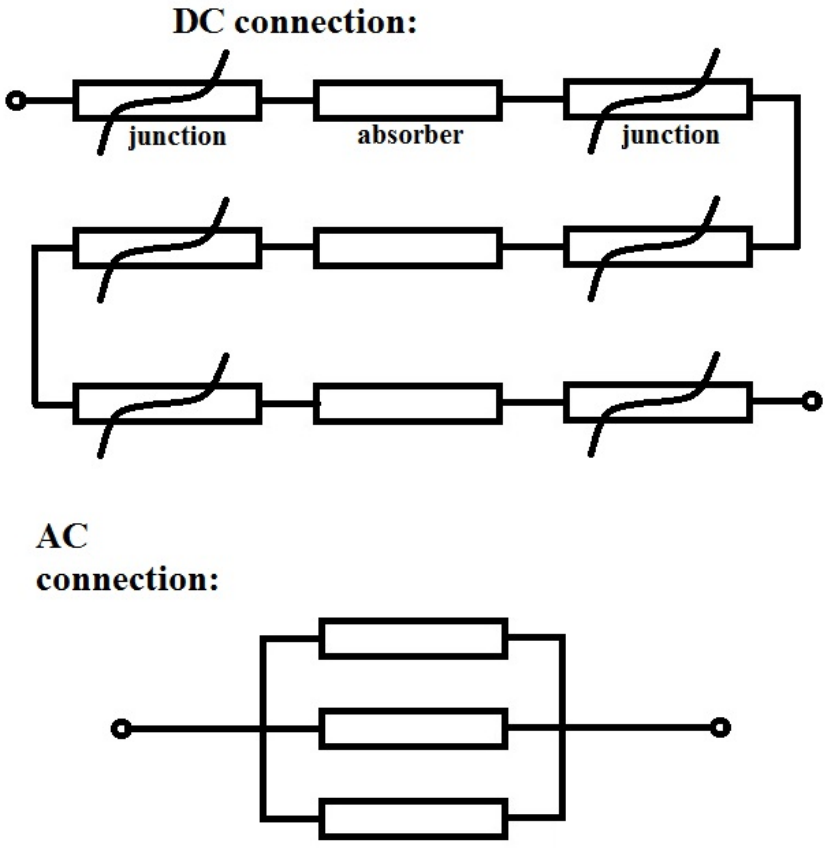

Figure 1.17. Equivalent circuit of a parallel/ series array for DC signal (top) and RF signal (bottom)

For an RF signal in GHz range, both the capacitors and tunnel junctions exhibit very low impedance at GHz frequency, to be regarded as zero impedance in this representation (compared to absorbers and tunnel junctions in kΩ range). Therefore, for the RF signal, the array is represented by a parallel array of normal absorbers shown in Figure 1.17, bottom.

Both the capacitors and the tunnel junctions are regarded as short circuits for GHz signals in this equivalent circuit. This simplified model is only valid when tunnel junctions are large enough for a given RF frequency. An implementation of this approach will be demonstrated in Chapter 4 for an array of CEB devices integrated in an antenna operating at 350 GHz.

For the production of CEB devices, various fabrication methods can be used. Traditionally, Cold-Electron Bolometers with SIN tunnel junctions were manufactured using shadow evaporation technique based on one-cycle deposition of both superconducting electrode and normal metal absorber [58, 63]. Another approach is a direct-write trilayer technology [64] for manufacturing Al-based SIN tunnel junctions operating at 100-300 mK, that is the temperature at which the bolometer operation is most efficient in terms of sensitivity and noise. This technology allows us to manufacture SIN tunnel junctions both in laboratory environment for the research on CEB applications and in the future in industry for mass production of millimetre-wave detectors. Devices fabricated using this method will be presented in this thesis. In addition, advanced techniques for fabricating Cold-Electron Bolometers are considered here. These are fabrication procedures based on depositing the normal absorber and oxidizing it prior to the superconducting electrodes. Different fabrication methods will be described in detail in Chapter 2.

In this thesis we will focus on antenna coupled CEB detectors deposited on planar substrates and fed by electromagnetic horns. RF power is coupled to the CEB through a waveguide using a unilateral finline or directly to planar antennas using quasi-optical coupling.

1.7. Thesis outline

Following this introduction, we will present the development of Cold-Electron Bolometers based on SIN tunnel junctions and integrated in various planar circuits. We shall also investigate the combination of a detector and a superconducting phase switch for modulating the polarization of electromagnetic radiation. The devices presented in this thesis were all fabricated by the author using microfabrication technologies developed during the PhD course at Oxford.

We will present the successful operation of CEB devices, focusing on the fabrication technology and different advanced implementations of CEB devices for efficient detection of electromagnetic signals at millimeter wavelengths. In Chapter II, the fabrication technologies developed for manufacturing CEB and Phase Switch devices are described. In Chapter III, we present the CEB detector integrated across a unilateral finline deposited on a planar substrate and report the results of the performance measurements.

In Chapter IV, we present CEB devices fabricated using advanced technologies, integrated in log-periodic, double-dipole and cross-slot antennas. The CEB performance was measured using hot-cold method and using a black-body source that is heated and controlled by the external current.

In the Chapter V, we investigate a planar NbN phase switch integrated in a back-to-back finline for modulating the polarization of weak electromagnetic signals. The investigated planar phase shift circuits operating at 230 GHz can be integrated in planar receiver circuits

and systems. We will examine the switching characteristics and demonstrate that the switching speed of the device is well above the speed required for phase modulation in astronomical instrument and is mainly limited by the time constant of the measurement system (~10 μs).

Chapter 2

Fabrication

In this work, we aim at fabricating very high performance detectors. Our goal is to detect very weak signals of power levels around the photon noise level and below it, in the presence of realistic background power load. The fabrication process therefore needs to fulfill certain requirements regarding layout geometry that depend on RF matching issues as well as thermal balance considerations. In order to achieve this, we have to use e-beam lithography for most critical parts of our design, where high-precision patterning is required. For less critical components we use photo lithography whenever possible as that process is simpler and less technologically demanding. Both processes will be discussed and compared in this chapter.

2.1. General fabrication principles

Lithography is the process of transferring mask patterns to a resist film on the surface of a substrate. Resist is a thin layer of a material sensitive to either UV radiation or electron beam (e-beam) and is normally spun on a wafer and baked at a certain temperature. A *positive* resist means that exposed areas are dissolved by the development process and removed. A *negative* resist works in the opposite way by removing unexposed portions of resist [65]. Negative

resists are useful for inverting patterns. They are mainly used for patterning by etching when the material deposited on the wafer is to be entirely removed later except for the exposed structures.

The patterns formed in such a way define certain regions in an on-chip structure, assigned for subsequent metal deposition, wet or plasma etching or other technological processes, e.g. oxidation of the deposited materials. The features of the design are first reflected in the resist pattern; then, these features are later reproduced in the real materials, to be used as the building elements of the final chip structure. This is normally performed by either depositing metals into open resist windows or an etching process which selectively removes uncovered parts of the materials previously deposited on the substrate. In this chapter we also describe in detail different lithography processes, as well as different deposition techniques and etching, including both wet etching and plasma chemical etching processes.

For the fabrication of high performance devices a clean processing room is required, because the air contains a lot of dust particles that can otherwise adhere to the surface of the substrate or on the top of the deposited materials and thus are likely to produce defects in the fabricated structures. E.g., particles remaining in a film of aluminium during its deposition or oxidation may cause inhomogeneity in the oxide film created by the oxidation of a thermally deposited aluminium film. A particle in the oxide layer can result in increased tunnelling current at the location around the particle and possibly even leakage DC currents through the oxide barrier. Dust particles settled on the surface of a photomask interfere with mask patterns, and the final distorted patterns may be represented in the device layout. Typically, dust particles on

photomasks may produce pinholes in insulating layers or short circuit different conducting parts; particles at the edges of a pattern may cause current disruptions [65].

The total number of dust particles per unit volume in a clean room, the temperature and humidity are very critical parameters that are crucial for the performance of the fabricated devices. For example, in a class 100 clean room there are 100 particles of certain size per cubic foot of air. There are many more dust particles of smaller size, so for the fabrication of especially small structures with very fine features a cleanroom with more stringent control of the environment is required, such as a class 10 clean room or even better [65].

2.1.1. Electron-beam and photo lithography

The steps that are used for pattern transfer from a mask to a device chip are shown in Figure 2.1. Usually, an insulating layer is formed on the surface of the Si wafer prior to any fabrication of detectors and related structures. In our case, a 400 nm thick SiO_2 layer is thermally grown on Si wafer by placing it in an oven filled with oxygen at a certain temperature (few hundreds Celsius). For my samples, this is done in Chalmers cleanroom, which is illuminated with yellow light, since neither photoresists nor e-beam resists are sensitive to wavelengths above 0.5 μm**.** In order to be covered with a resist layer, the wafer is placed onto a vacuum spindle, and liquid resist is pipetted onto the wafer. After that, the wafer is spun at a constant speed for at least 1 minute. As a result, a uniform thin film of a resist is formed on the surface of the wafer, and the thickness of the film depends only on the rotational speed for a given resist at a given solvent concentration (and is independent of the rotation time etc). Final thickness for a certain rotational speed is normally provided by the

manufacturer of each type of resist and each value of solvent concentration. E.g. spinning 10% copolymer resist dissolved in Ethyl Lactate at 3000 rpm results in c:a 350 nm thick copolymer resist film.

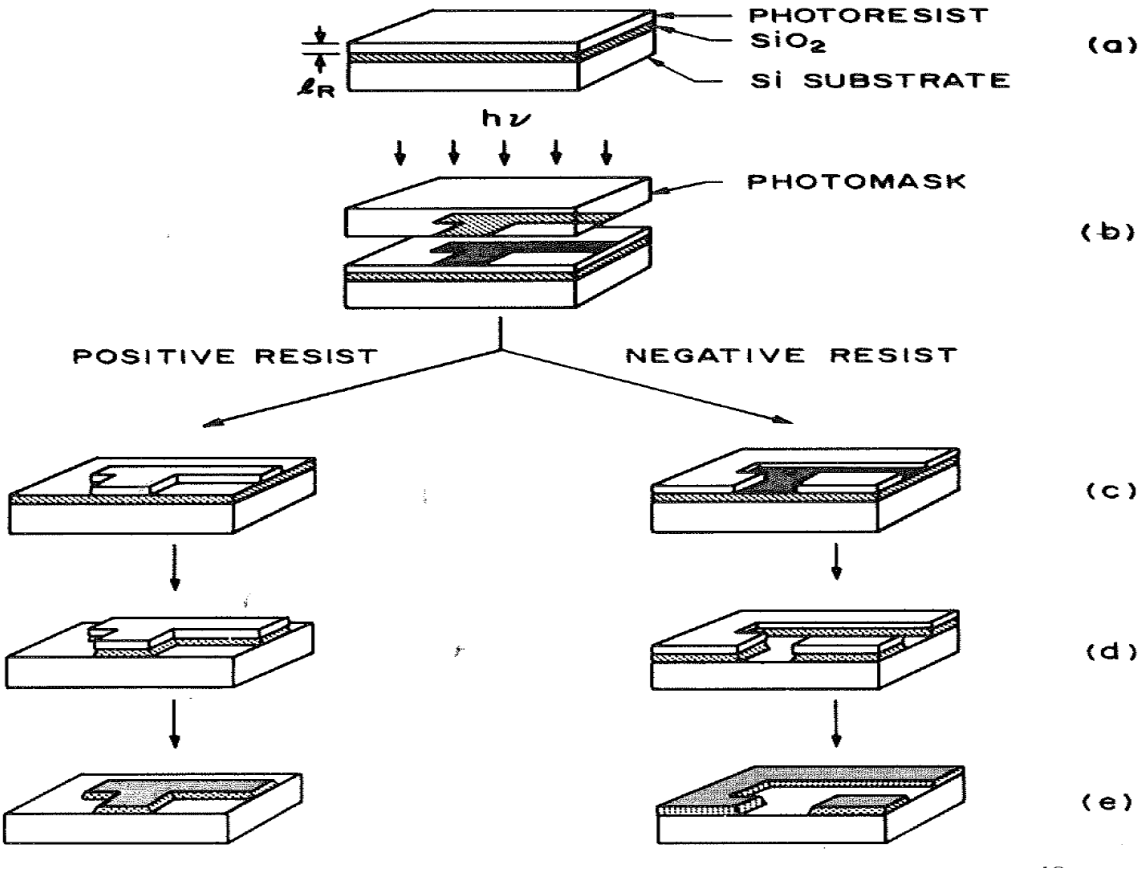

Figure 2.1. Details of an optical lithographic transfer process [65].

At Chalmers, we use a spin speed of 3000 to 6000 rpm to give a 100 – 900 nm thick resist film while using lower rotational speed might result in non-uniform films that are undesirable for both photo and e-beam lithography. After spinning the resist, it is normally baked either on hotplate or in oven at temperatures 90 – 195 ºC. When baked, the resist is ready for the UV or

e-beam exposure. The wafer with the resist is exposed to UV radiation or e-beam. After exposure, a post-exposure baking at 110 – 130 ºC may be required for certain resist types to accomplish the process. When using the positive resist, the resist in the exposed areas is to be dissolved in the developer, which is usually done by dipping the wafer with the exposed resist into the developer; after that the wafer can be rinsed and blow dried with nitrogen. A positive resist pattern is thus formed on the substrate (Figures 2.2a and 2.2b). The metal (e.g., aluminium) or another material is then deposited over the whole surface of the wafer, including the resist and the substrate (Figure 2.2c). In order to avoid any contact with the resist walls, the material that is deposited must be thinner than the resist film. As a rule, the thickness of the deposited material does not exceed a half of the total resist thickness. The parts of the material film that are deposited on the resist are then removed by dissolving the resist layer in a liquid solvent that selectively removes organic resists while keeps metals and other materials untouched. As a result, the material film on the top of the resist layer is lifted off and finally removed (Figure 2.2d). This method of patterning is called the ***lift-off*** technique and is extensively used for microwave and mm-wave detectors fabrication, as it provides very high resolution and other features required for high-performance device fabrication.

When using negative resists and etching process, the unexposed areas are removed, which results in a mirrored image in the resist pattern related to the pattern in the original layout drawing. The wafer is then subjected to a chemical plasma etching within the open areas or wet etching in a liquid that removes the materials within the open resist windows but does not

affect those covered by the resist mask (at Chalmers, we use H_3PO_4 for Al wet etching and CF_4 plasma for NbN patterning). Finally, the resist is removed using acetone or another solvent, such as Shipley remover, and a material image repeating the original layout is left on the surface.

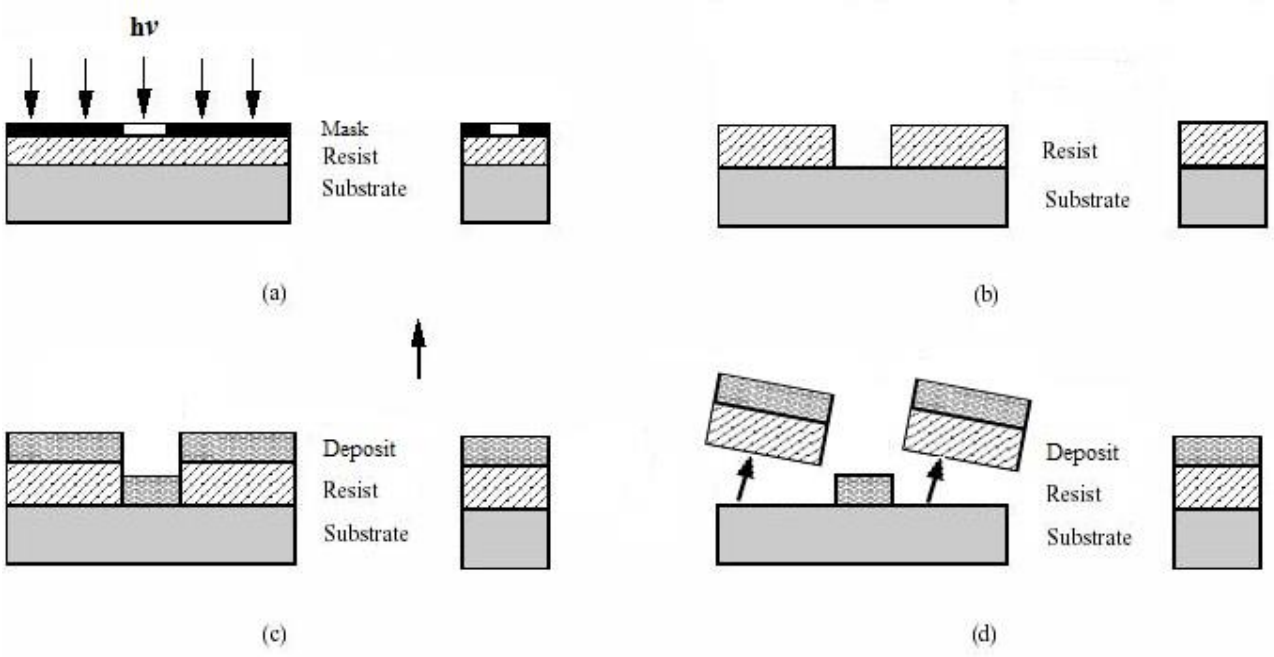

Figure 2.2. Lift-off process: a) Illuminating of positive photoresist through a photomask; b) development; c) deposition of the material; d) lift-off [65]

Most layers of my wafers in this thesis were patterned using electron-beam (e-beam) positive lithography and lift-off. Photo lithography was also used for some of the samples and negative e-beam lithography with etching was only used for few devices. Exposure, development and deposition with lift off are performed in the same way when using either e-beam or photo lithography.

When using e-beam lithography, exposed areas are defined by an electron beam focused on the surface of the wafer and controlled by e-beam machine. The JEOL JBX-5DII machine employed at Chalmers for fabrication of my devices uses 50 kV accelerating voltage and two magnetic lenses for focusing: a lens for rough exposures and another one for exposing fine patterns. The JBX-5DII consists of the main console (Figure 2.3) and the computer system. The main console includes the optics system and the mechanical system.

2.1.2. Electron optics system

A schematic of an e-beam lithography system is shown in Figure 2.4. The electron gun generates a beam of electrons; the JEOL JBX-5DII system available at Chalmers employs an electron gun using LaB_6 single crystal cathode and an in-lens deflector [66]. The deflector focuses the electron beam to a nanometer-scale spot, thus enabling nanometer writing. The lens system consists of two intermediate lenses (second and third lenses) and one objective lens (fourth or fifth lens) (Figure 2.4.). Condenser lenses focus the electron beam to a spot on the wafer surface. Beam-blanking plates are used to turn the electron beam on and off. The beam deflection coils (referred as "Final Lens" in Figure 2.4) are employed to direct the focused electron beam to a location on the substrate. A mechanical stage moves the substrate from one position to another during the exposure; this is necessary because the scan field size is 800×800 μm for the 4^{th} lens and about 80×80 μm for the 5^{th} one, which is much less than the area to be exposed. All the coils, lenses and the mechanical stage are controlled by a computer according to the pattern to be written.

Figure 2.3. JEOL JBX-5DII e-beam machine, photo of the Main Console [66].

The image of the crossover generated by the electron gun is reduced by the second and third lenses. Either the fourth lens or the fifth lens is used as the objective lens depending on the application: the fourth lens is used for larger patterns (down to submicron sizes) and the fifth lens for smaller patterns (down to nanometer sizes). Beam size can be changed for large and small patterns by changing the exciting currents of the second and third lenses. In order to enable proper circular spot shape and direction of the electron beam, the electron optics system incorporates a stigmator coil and alignment coils. The stigmator coil corrects the oval beam into a round beam. The electron beam emitted from the electron gun has a tilt component and a horizontal component. To compensate for these components, the alignment coil is composed of two deflection coils. These deflection coils operate in the X- and Y-directions to correct the deviation of the electron beam relative to the lens axis [66].

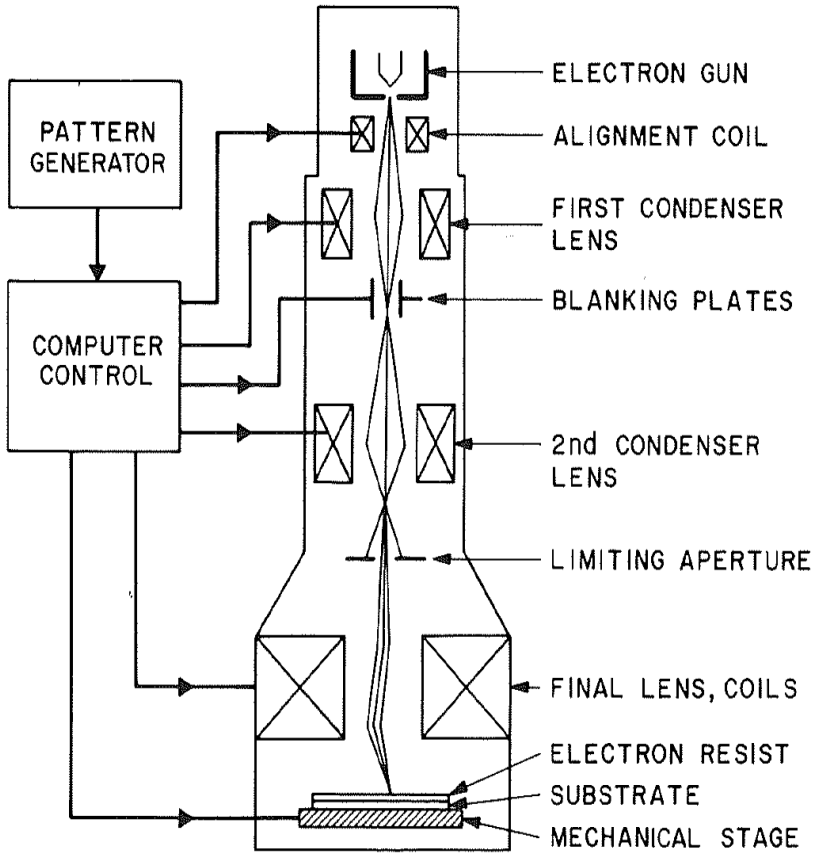

Figure 2.4. Electron optics system of JEOL JBX-5DII [66]

The advantages of using e-beam machines in our work are nanometer-scale writing, automated operation with full control, better focus compared to optical lithography, and direct writing on a wafer without using a chromium photo mask. A disadvantage of e-beam machines is the speed of processing: e.g. exposing contact pads for a CEB wafer takes 4 to 5 hours compared to 17 s when using optical lithography. A similar exposure with submicron resolution would require 12 to 15 hours. Such a speed might be acceptable for making photomasks or for writing small on-chip areas with delicate design features. In my design, CEB absorbers and tunnel junctions areas were most often exposed using e-beam machines,

especially when a very narrow absorber was required by the design considerations. For maskless direct writing, the highest speed of operation of the e-beam machine corresponds to the largest beam diameter that is acceptable for the given minimum feature size of the device considered.

2.1.3. Development

Developing the resist is the last lithography step which contributes to patterning the resist film across the surface of the wafer. In essence, this is a chemical wet etching process. For e-beam exposure, resists are developed just before evaporation, while for photo resists the development follows directly after exposure. This is true for all photo resists including UV5, which happens to also be used for some e-beam exposures. Some resists must also be baked immediately following exposure to ensure proper development.

2.1.4. Photoresist and e-beam resist

The photoresists are compound materials sensitive to the UV light. Most photoresists, including the ones used in this thesis, can be classified as positive, due to the type of their response to the exposing UV signal. As has been mentioned before, the exposed regions become soluble and therefore removed during the development. As a result, the patterns or images formed in the positive resist are the same as in the original layout drawing. For negative resists, the unexposed areas are removed during the development, and the images formed in the negative resist are the reverse of the original layout drawings.

In [65] three components of positive photoresists are selected: a photosensitive compound, a base resin, and an organic solvent [65]. The solvent is mainly used to make the resist liquid (less viscous) in the very beginning to help spinning the resist and then part of it evaporates during the baking after spinning. The unexposed photosensitive compound is insoluble in the developer solution, while the UV radiation received in the exposed areas changes the chemical structure of the compound, and the latter becomes soluble and can easily be removed during the development.

In negative photoresists that are polymers combined with a photosensitive compound, the latter receives the electromagnetic energy during exposure and converts it into chemical energy [65]. This initiates a polymer linking reaction, thus causing cross linking of the polymer molecules. Finally, the polymer becomes insoluble due to a higher molecular weight and remains on the surface of the wafer, while the unexposed areas are removed during the development. During the development process the resists mass absorbs the developer solvent and becomes somewhat bigger, which limits the resolution of negative photoresist, being the major drawback of a negative photoresist [65].

Electron resists or e-beam resists are in essence polymers, in which a chemical or physical change is induced by the electron beam, which is used for patterning. During the e-beam exposure, the polymer-electron interaction causes chemical bonds to be broken by the electrons with high kinetic energy of 50 keV and form shorter molecular fragments, Fig. 2.5a. In the exposed area, the molecular weight of the polymer is reduced, and the irradiated resist is dissolved in a developer. One of the most common positive electron resists that allows for

60 nm resolution is poly methyl methacrylate, or PMMA, and it is extensively used in this thesis for most exposures.

In negative e-beam resists, the electron beam provokes polymer linking as shown in Fig. 2.5b. The polymer crosslinking creates three-dimensional structures [65] that are not affected by the developer solution, while the rest of the resist is dissolved during the development.

The Proximity Effect

The resolution of photo lithography is determined by the UV wavelength as the image transferring is limited by diffraction of UV radiation, while for the e-beam exposures the electron scattering determines possible distortions of the image and quality of the resulting resist pattern. The accelerating voltage in our e-beam system is 50 kV, and the corresponding Lois de Broglie wavelengths of the electrons are in the nanometre range. After penetrating the resist film electrons hit the surface of the wafer. Collisions of the electrons with atomic lattice of the substrate or the deposited material lead to energy loss and backscattering.

Due to backscattering, electrons can expose the resist far away from the electron beam centre (Fig. 2.6). The beam at each given point affects the exposure in neighbouring areas and the total effect can be expressed by the total dose or charge that is given by the sum charge of the re-scattered electrons from the neighbouring areas; this is known as the ***proximity effect*.** Due to this effect, large areas are overexposed and are therefore swelled in the resist patterns, while very narrow lines are underexposed and are therefore not developed properly. Besides, minimum spacing between different exposed parts of the pattern is somewhat limited as they

can merge when overexposed due to the backscattering. For the *proximity correction*, different parts of the pattern are exposed by different doses; the total exposure dose is thus made of the sum charge of the incident electrons in different segments of the pattern [65].

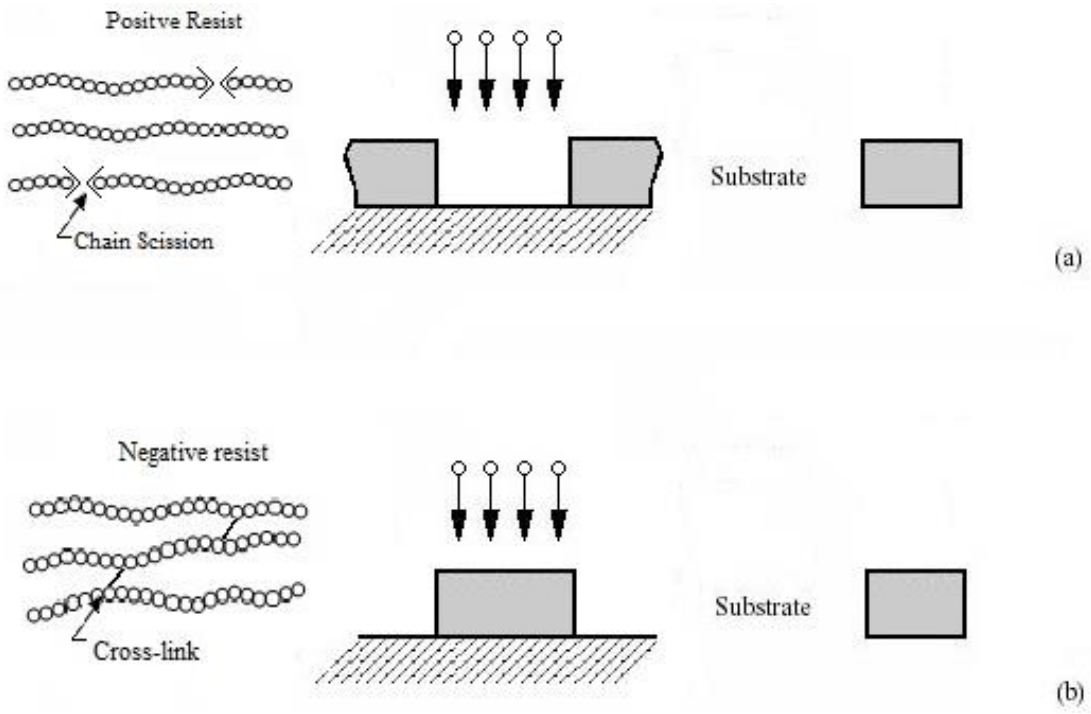

Figure 2.5. Cross-liking, positive (a) and negative (b) e-beam resists [65].

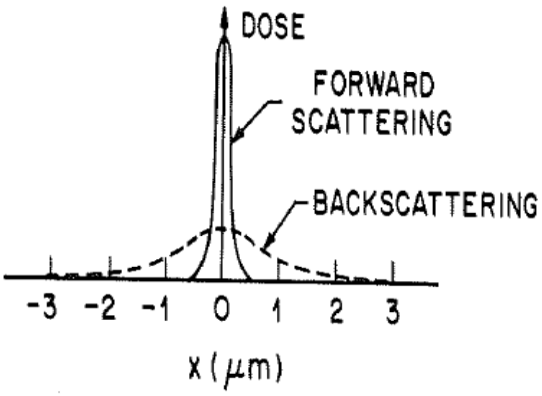

Figure 2.6. Dose distribution at the interface between the resist and the substrate surface [65].

2.1.5. Thermal evaporation and lift-off

Most materials in my structures were deposited using thermal evaporation, including the aluminium layer for tunnel junctions in trilayer structures. In order to do this, a source filled with source material is placed at the bottom of a vacuum chamber and the wafer is placed, face down, at the top of the chamber. The boat is then heated by an electric current melting the material and causing it to evaporate. When the evaporated material reaches the wafer, it condenses on its surface and crystallizes.

a) 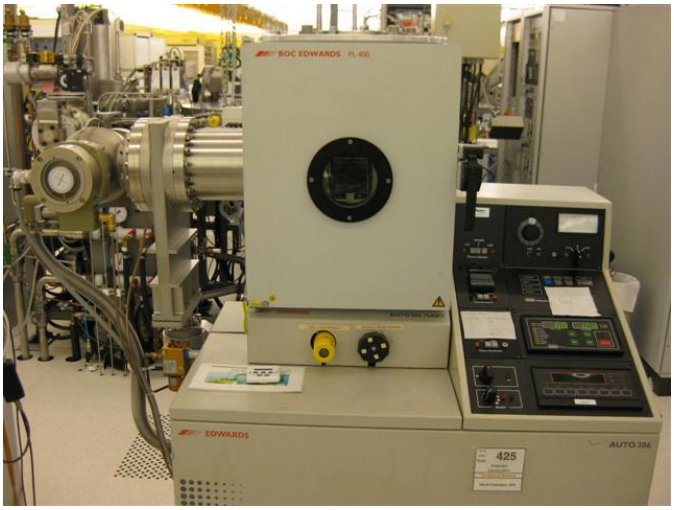

b) 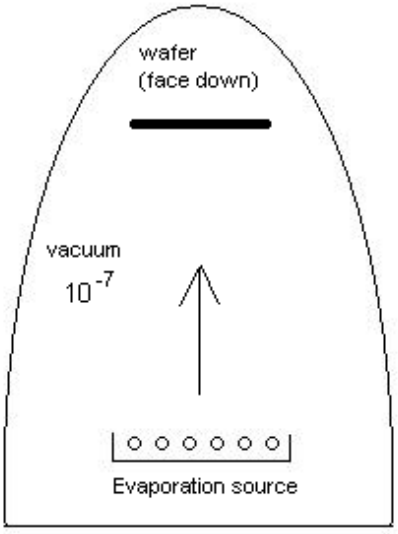

Figure 2.7. a) BOC Edwards HPTS Evaporation system, equipped with a 4-position evaporation source; the turbo pumping system gives a base pressure of $5 \cdot 10^{-7}$ mbar. – Chalmers MC2. b) schematic view of the evaporator.

We are interested in depositing amorphous or polycrystalline films for most materials, so we have to keep proper evaporation rate to enable correct crystallisation. For aluminium, a rate of 1 – 8 Å/s may be used; however experience shows that optimum rate is between 4 and 7 Å/s

for best Al film property and subsequently Al oxide quality. A photo of the thermal evaporation system is shown in Fig. 2.7a and a schematic view in Fig. 2.7b.

After the evaporation, the resist with redundant material on the top is removed by dissolving it in acetone, for e-beam resists, or other solvent, e.g. Shipley 1165 remover for photo resist. To help the lift-off, a lift-off layer is normally used for lift-off lithography prior to the top resist layer. The lift-off layer is developed either by the same developer in case of photo lithography or by different one in the e-beam case. The lift-off layer is normally not sensitive to UV exposure in the photo case, so it is just etched under the open windows by the developer. In the e-beam case, lift-off resist must be exposed at higher dose to obtain an appropriate undercut that is slightly larger area of the developed lift-off layer compared to the resist layer. As a result, the deposited material does not touch the walls of the developed resist, which makes the lift-off process easy and straightforward.

2.1.6. Thermal evaporation of SiO / SiO_2 dielectric layer

In order to make on-chip capacitors, we need to deposit an oxide layer, e.g. SiO or SiO_2. Both materials are widely used as insulating layers for planar on-chip capacitors. We have designed, fabricated and tested a new source for thermal evaporation of SiO. The schematic view is shown in Fig. 2.8b, the photo is shown in Fig. 2.8a. The design is based on another thermal source evaporator which has been scaled down in order to fulfill the requirement of lower currents in the Edwards BOC evaporation system.

The boat is made of 1 mm thick Mo plate and consists of three parts, namely a container for SiO, a lock with small holes and another top lock with a large hole in the middle. The main container is 11 mm wide, 21 mm long and has 11.5 mm long extensions on both sides for bolted contacts. The intermediate lock has 5 holes on each side, 1.7 mm diameter each. The top lock has a 5 mm diameter hole in the middle. The latter is required for prevention from the re-sputtered material during the thermal SiO evaporation. When the top lock is used, the material remains on the surface of the intermediate lock in the form of large grains, and only the gaseous form of SiO leaves the boat and expands towards the wafer where it is deposited. 45 to 100 nm of SiO were successfully deposited at a rate of 0.3 - 0.5 nm/s and a pressure of 10^{-6} mbar.

Another option for making an insulating layer is to deposit SiO_2 in an electron gun (e-gun) evaporation system (Fig. 2.9). In that case, the material is heated by electron beam and deposited in the same way as for thermal evaporation. Hence, the e-gun evaporation is a similar process to thermal evaporation. We use e-gun evaporation system for the deposition of materials with rather high melting temperature, 2500 ºC and above, e.g. Ti and some other metals. Thermal evaporation by heating the material in a boat in not efficient for such materials and is therefore not an option for the deposition of those. SiO_2 is yet another example of materials to be deposited in e-gun evaporation system.

Because of poor adhesion of both SiO and SiO_2 to the surface of SiO_2 substrate or gold pads, we proposed to use adhesive layer to overcome this problem. In the following experiments, I have deposited 10 nm of Al_2O_3 prior to SiO or SiO_2 on the SiO_2/gold surface.

a)

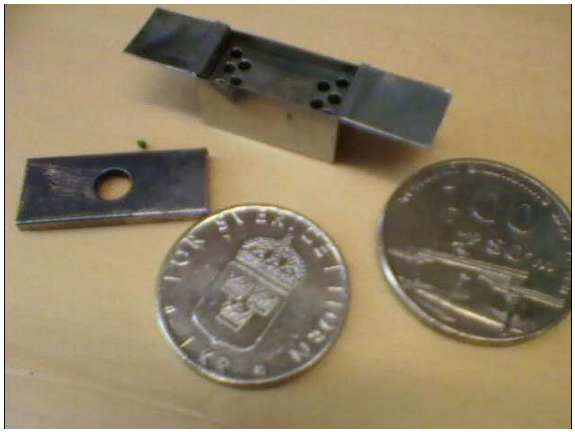

b)

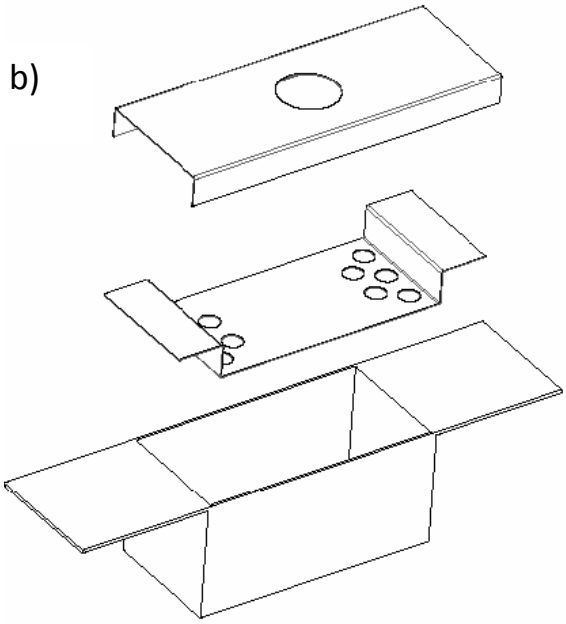

Figure 2.8. Mo boat for SiO evaporation, fabricated at Chalmers, a photo and a schematic view

Figure 2.9. AVAC HVC600 e-gun evaporation system - Chalmers MC2.

2.2. Fabrication of CEB devices

The CEB is a device made of a normal metal absorber with two or more tunnel junctions between a superconductor and normal metal or Superconductor-Insulator-Normal metal (SIN) junctions for temperature measurements and detection of millimetre-wave radiation. Both applications are based on the dependence of current-voltage characteristics of SIN junction on the temperature [48-51]. Thus the design and performance of CEB devices are determined to a large extent by the details of the SIN junctions fabrication procedure as the performance of the devices depends strongly on properties of available SIN tunnel junctions.

For example, the dynamic resistance at the bias point affects noise matching with the readout amplifier. At the same time, the specific normal resistance should be high enough to enable a reasonably good ratio of the normal to subgap dynamic resistance as the sharpness of IV curve depends on the oxidation time and thus normal resistance. Experience shows that a longer oxidation time and a thicker oxide barrier provide a robust oxide barrier, therefore reducing leakage currents, which yields higher ratio between the normal and subgap resistance and consequently a sharper IV-curve. The superconducting gap should be large enough at operating temperature to enable strong voltage to the temperature response as gap suppression reduces the voltage response.

Assuming JFET readout amplifiers are to be used at room temperature, an optimum choice of the technology and geometry requires typically 1 to 10 kΩ normal resistances, while

employment of CMOS electronics makes it possible to use tunnel junctions of tens to hundreds of kΩ normal resistance. The simulations described later in Chapter 4 show that tunnel junctions of areas of 1.5 to 4 μm^2 should be fabricated using trilayer direct-write technology with 12 Å thick Al_2O_3 as insulator and junctions of area of 3 to 20 μm^2 are to be fabricated with TiO_2 as an insulating barrier. This allows maximum voltage response at a reasonable normal to dynamic resistance ratio. Therefore, e-beam lithography must be used for trilayer fabrication with Al_2O_3, while it is possible to use photo lithography to fabricate devices with TiO_x as insulating barrier.

CEB devices with SIN tunnel junctions have traditionally been manufactured using the so-called shadow evaporation technique based on one-cycle deposition of both superconducting electrode and normal metal absorber. First, the superconducting electrode is deposited at a certain angle and oxidized, and after that the table with the substrate is rotated so the absorber is deposited at another angle, resulting in a small overlap area that constitutes the tunnel junctions. This technique has certain advantages, such as its simplicity and possibility to make narrow absorbers and small tunnel junctions, and has therefore been used for years for SIN tunnel junction fabrication, especially in laboratory and academic environment as it does not involve too advanced equipment. However, it is not the most appropriate technique for CEB application and it has many drawbacks and limitations.

First of all, the main limitation is related to the size of tunnel junctions which cannot be made as large as required due to the principle of shadow evaporation. It makes the shadow

evaporation technique very useful for single-electronics where small area of tunnel junctions is advantageous. But for bolometer fabrication this approach can only be used within certain frequency ranges, down to 300 GHz, due to the small area of tunnel junctions fabricated in such a way and therefore small capacitance value for RF signals. Second, geometry considerations impose severe limitations on the layout and orientation of the structures on chip. And, finally, this technique does not allow for use of magnetron sputtering which is commonly used for manufacturing of high-quality tunnel junctions.

The CEB devices described in this thesis were fabricated using cleanroom facilities at the department of Microtechnology and Nanoscience at Chalmers University in Sweden.

2.2.1. Fabrication of CEB with SIN tunnel junctions in trilayer technology

Fabrication of high quality CEB devices requires the development of new technologies, such as a direct-write trilayer technology [64] for manufacturing Al-based SIN tunnel junctions operating at 100-300 mK, which is the temperature range in which the bolometer operation is most efficient in terms of responsivity (dV/dP) and sensitivity (low noise). Direct writing means that the pattern in the drawing is directly transferred to a pattern in the resist layer and thus in the deposited material, unlike techniques employing photomasks or shadow evaporation when the pattern is distorted during the process, due to different evaporation angles.

The trilayer technology allows us to manufacture SIN tunnel junctions of high quality, suitable for millimetre-wave detectors and cryogenic thermometers. In this technology, the deposition procedure and direct writing of both superconductive layer and absorber do not impose any requirements on deposition of both layers in one vacuum cycle of evaporation. That simplicity of the technology gives us additional freedom in realizing any possible layouts in any geometry.

The procedure of fabricating CEB devices, similar to the one shown in Fig. 2.10, using trilayer technology, is as follows. A silicon wafer, oxidized thermally to obtain 400 nm oxide thickness, is covered by a lift-off resist LOR3A and positive photo resist S1813 and baked. Contact pads are then patterned by a standard process of photo lithography involving exposure in UV mask aligner and development by MF-319. The wafer is then cleaned using a standard reactive ion etching process in oxygen plasma for 30 seconds. A gold layer is next deposited after the lithography for better alignment with the following layers.

SIN tunnel junctions are patterned as an overlap between a normal absorber and an Aluminum electrode. For patterning the superconducting electrode, a lift-off resist and e-beam resist are spun over the wafer (Fig. 2.10a), exposed in the e-beam lithography system, and developed (Fig. 2.10b). Then, an aluminium layer is deposited at a pressure of $\sim 10^{-7}$ mbar and oxidized during 30 minutes in oxygen ambient at $5 \cdot 10^{-2}$ mbar [36]. Then copper is evaporated as a normal metal electrode of a tunnel junction and covered by gold for passivation (Fig. 2.10c). Next, the normal metal copper/chromium absorber is patterned by e-beam lithography

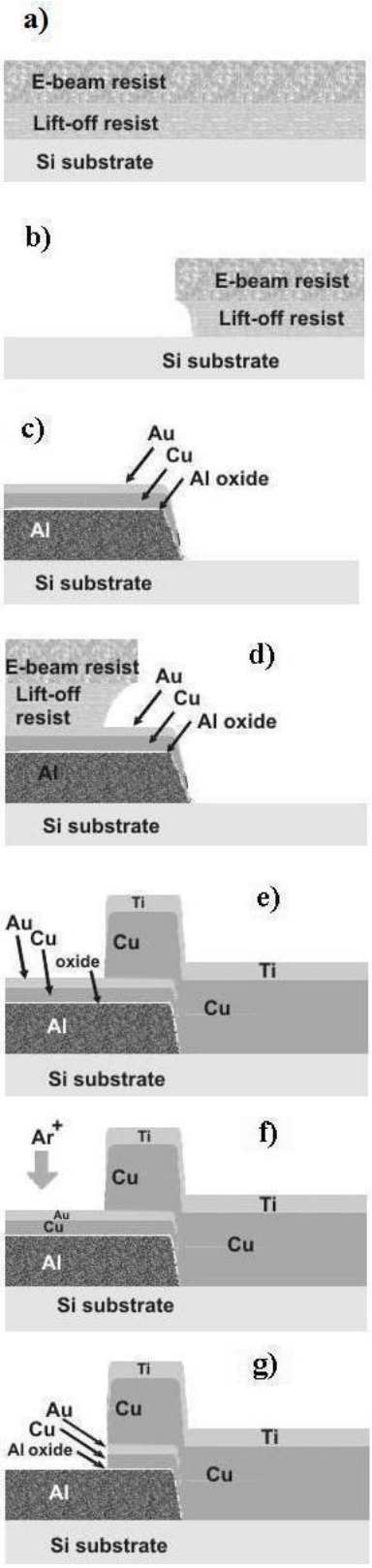

=> Si wafer with 400 nm thick thermally grown SiO_2 layer covered with a lift-off resist and an e-beam resist or a photo resist, with both layers spun and baked.

=> The resists exposed and developed. The bottom resist layer is slightly overexposed and /or overdeveloped.

=> The materials are deposited and lifted off: about 40 nm Al deposited as a first layer, then oxidized in oxygen; 8 nm Cu deposited as second layer and then 8 nm Au deposited for passivation. The tunnel junctions are created between Al and Cu with Al_2O_3 as tunnel barrier.

=> Next lithography layer: two resist layers are placed on the top of the deposited Al-Cu-Au structure.

=> The absorber is deposited and lifted off. Absorbers are made of Cu or Cu/Cr sandwich, 55-80 nm in total, covered as a rule by a hard material such as Ti with natural TiO_x layer that is very resistant to Ar ion beam etching.

=> In order to shape tunnel junctions, self-alignment is used: Au and Cu are removed from areas, not covered by Ti and TiO_x , using Ar ion beam etching (ion milling)

=> The profile of the final structure. Tunnel junctions areas are shaped; shown in the picture between Al and Cu, to the right from the arrows.

Figure 2.10. CEB fabrication procedure, trilayer technology [36]

and thermal evaporation (Fig. 2.10 d,e). Finally, argon ion beam etching performed in Oxford CAIBE system is used to remove copper and gold from the top of the trilayer structure, (see Fig. 2.10 f,g). An AFM image of an example CEB device fabricated in this way [45] is shown in Fig. 2.11.

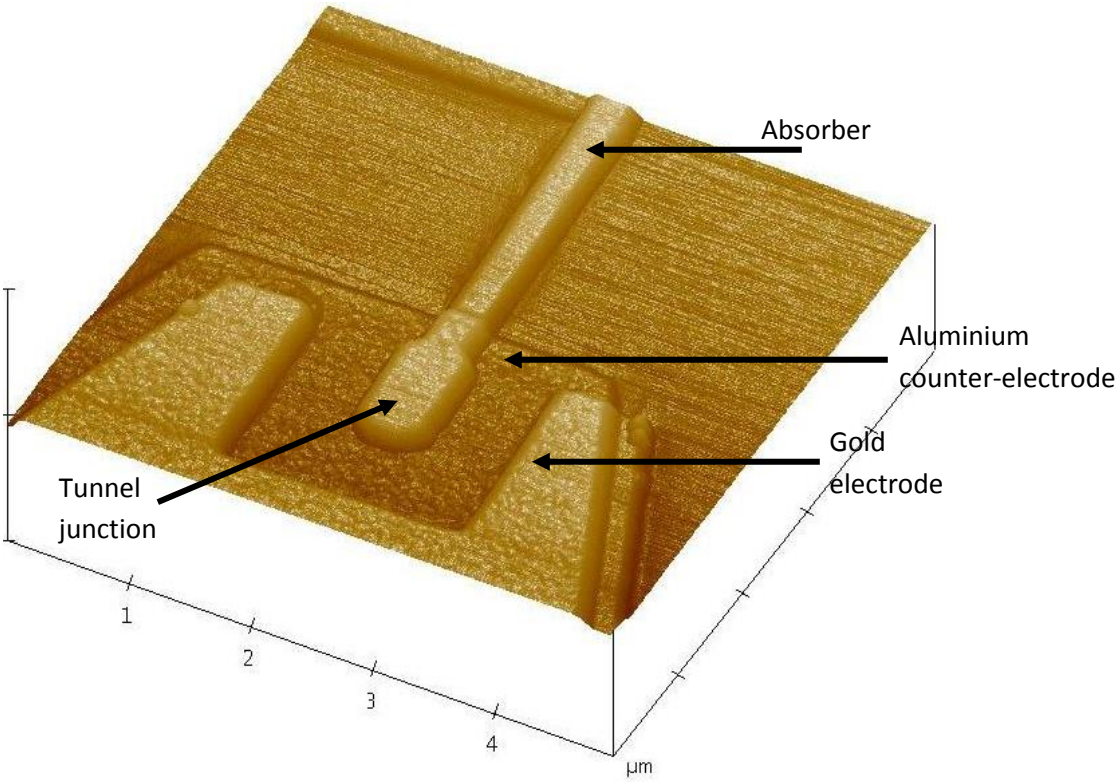

Figure 2.11. An AFM image of a CEB device manufactured with trilayer technology [45, 64].

The fabrication method described here is suitable for fabricating devices with large area tunnel junctions and big absorbers. The major drawback of this method is that the absorber is deposited on the top of the superconducting Al layer, which results in a bigger absorber than in the case when the absorber is deposited first. This is due to the fabrication golden rule

which states that every consequent layer must be 10-15% thicker than the previous one to enable a secure contact between successive layers. As a result, very thin and narrow absorbers cannot be fabricated using this method. In addition, the absorbers fabricated using this method are not flat and contain bending parts on the top of the tunnel junctions. Another disadvantage of this method is that it limits the temperature at which the resist for absorber patterning should be baked. When the resist is baked after creating the tunnel junctions, the temperature should not exceed 140 ºC, in order not to endanger the junctions. This reduces the resolution of the lithography and therefore limits the minimum size of the absorber fabricated using this method. In the next section we shall describe a novel approach that does not have these limitations.

2.2.2. Titanium-based fabrication technology

This is a novel direct-write technology for fabricating Ti-TiO_2-Al tunnel junctions for bolometer devices and thermometry applications [38]. The goal of this method is to develop simple and efficient technology for the fabrication of SIN tunnel junctions between Ti and Al with TiO_2 as insulating barrier. The key point of this technology is the deposition of a normal Ti film as a bottom electrode and the superconducting Al film as the top layer after oxidation of Titanium.

It has already been shown in the previous section that the CEB performance is largely determined by the SIN junctions properties. Another important aspect is the CEB layout and

geometric considerations. One of the key parameters of a CEB is the volume of the absorber since it determines the bolometer's sensitivity due to the principle of operation of a CEB. As we have indicated earlier, an absorber with large volume limits the performance and the cooling feedback of the CEB. It turns out that it is extremely important to make the absorber as thin as possible. This is because a thinner absorber increases the sensitivity and ensures efficient electron cooling.

The Titanium-based approach allows one to realize thicknesses of the absorber down to 5 nm as the absorber is deposited prior to the other electrode and the tunnel junctions are created after deposition of the absorber. Another advantage is the ability to realize a fully flat absorber with no bending parts, which are inevitable in other processes and create leakage currents that degrade the high-frequency properties of the RF detector.

Since the absorber is patterned before creating tunnel junctions, we have no limitation on the width of the absorber related to lithography resolution due to limited resist baking temperature.

The process includes two steps of lithography and deposition: first the Ti film is deposited, patterned and oxidized and then the Al counter-electrode is deposited and formed. It uses ex-situ Ti oxidation for creation of TiO_2 insulating barrier. The details of the fabrication process are shown in Fig. 2.12.

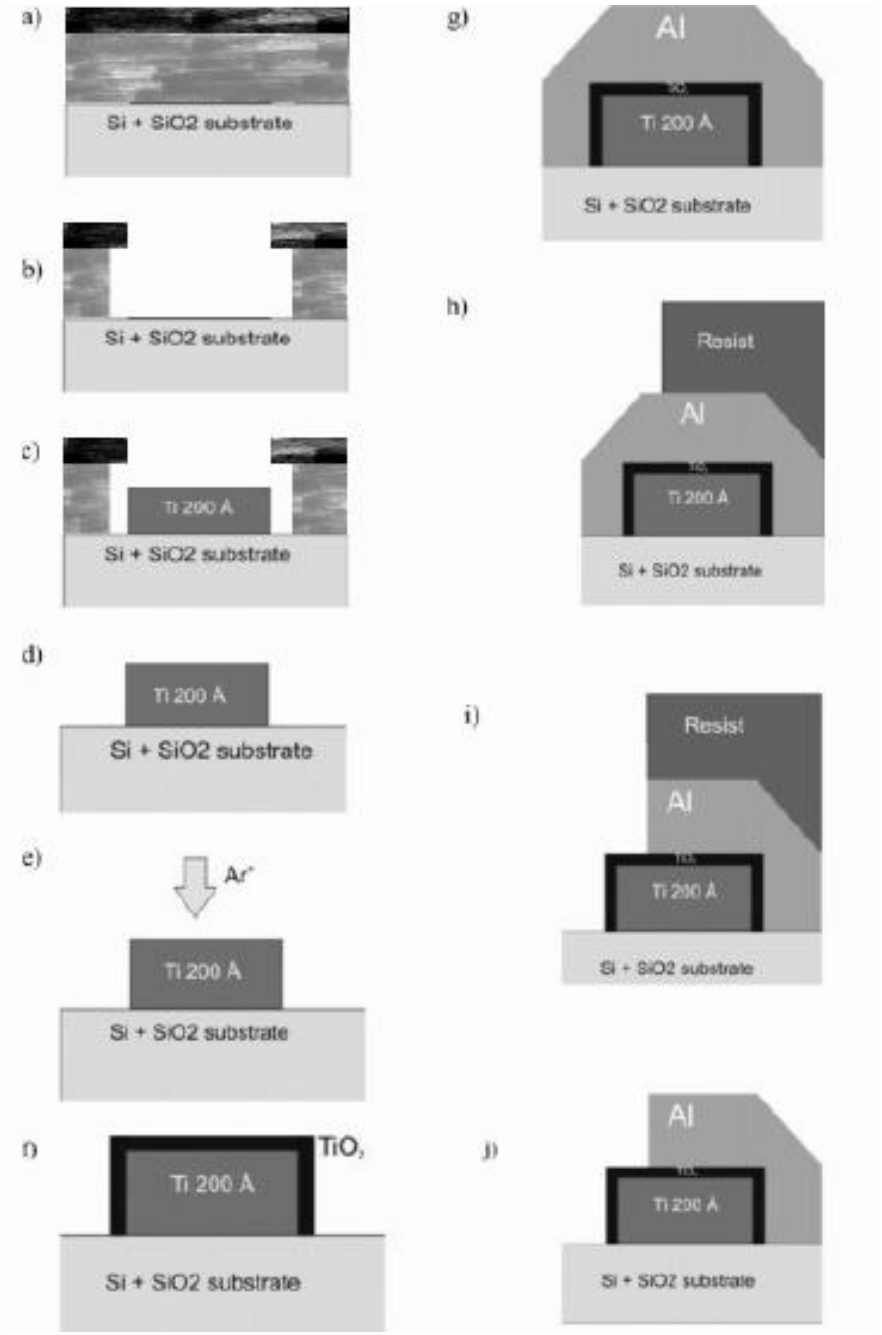

Figure 2.12. Fabrication procedure for Ti-based technology [38]. A lift-off layer and photo resist are spun and baked on a thermally oxidized silicon substrate for the following optical lithography (a). After exposure and development (b), a Ti film is deposited by magnetron sputtering (c). After lift-off (d), the surface of Ti is cleaned using ion milling in Ar ion beam (e) and oxidized in atmosphere during ~3 hours at 150°C (f). Then an Al film is deposited (g) and patterned by lithography (h) and chemical wet etching (i). Final structure after resist removal (j). [38, 84]

In the first step, a photo resist is spun and baked on a thermally oxidized silicon substrate for the following optical lithography. After exposure and development, a Ti film is deposited by magnetron sputtering. After lift-off and oxygen plasma etching, the surface of Ti is cleaned using ion milling in Ar ion beam and oxidized in oven in air ambient. Then an Al film is deposited and patterned by lithography and chemical wet etching. The final structure after resist stripping is shown schematically (Fig. 2.12,j) and in an optical image (Fig. 2.13).

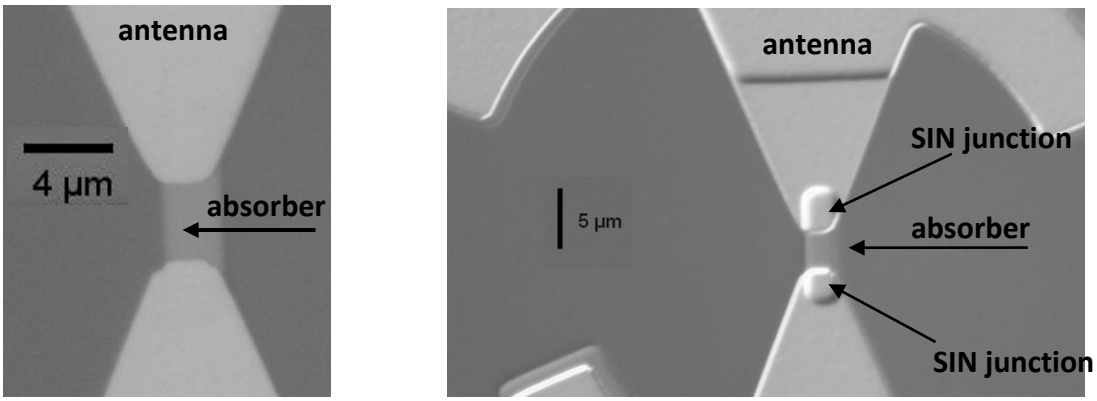

Figure 2.13. Optical image of a CEB fabricated in the Ti technology:
a plain photo (Left) and a quasi-3D picture (Right) of the central part. [84]

2.2.3. The fabrication of CEB-finline Integrated Circuits

In what follows we describe the fabrication of CEB devices integrated into unilateral finlines, as shown in Fig. 2.14. The finline taper was designed and optimized using our own software package [5, 26, 80]. We have already shown that a finline-CEB integrated structure is an attractive realization of a CEB concept so the task now is to fabricate a SIN bolometer across the slot of a unilateral finline.

The finline considered here is a tapered unilateral finline 1270 μm wide and 3 mm long with a slot width of 5 μm, deposited on a 200 μm thick silicon substrate, which yields a characteristic (wave) impedance of ~42 Ω. The CEB device deposited across the slot consists of a 4 μm long absorber with two 2×2 μm^2 SIN tunnel junctions.

The CEB samples have been fabricated using e-beam lithography in direct-write mode according to the trilayer technology principle of fabricating tunnel junctions as described in section 2.2.1. Firstly, gold contact pads and wires were patterned using e-beam exposure and thermal evaporation. Then, Al finlines were patterned in the same way and finally the Cold-Electron Bolometer structures have been fabricated in the middle of the finline slot using trilayer process described above and presented in [36, 64]. As the last step, the Cu-Au layer on the top of the trilayer structure was removed by Ion-Beam Etching. The photo of the fabricated CEB on finline is shown in Figure 2.14.

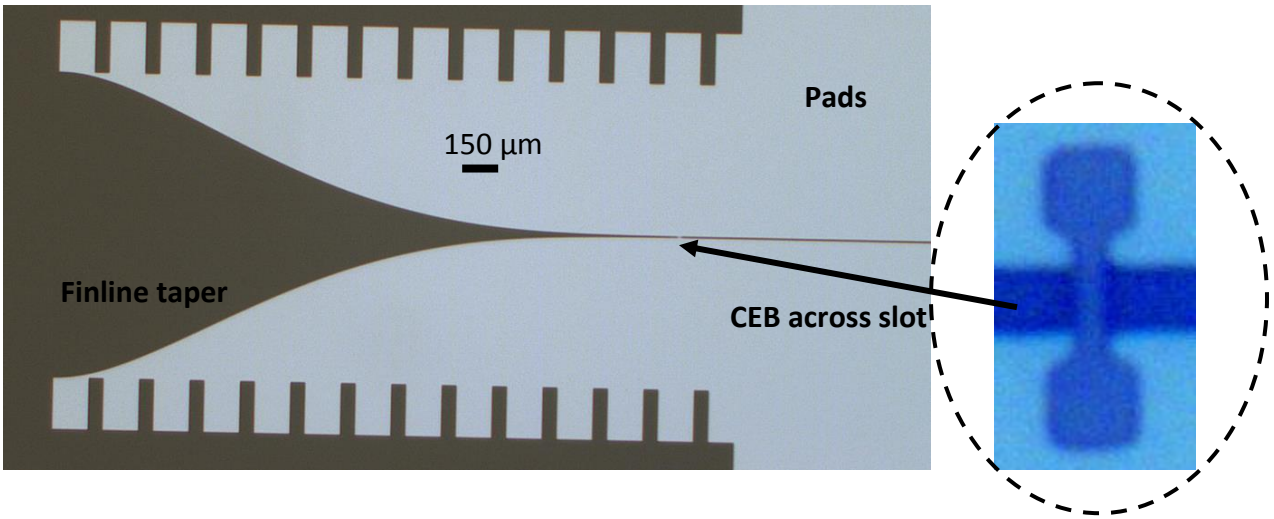

Figure 2.14. A fabricated 97-GHz finline with the CEB structure in the slot.

2.3. Fabrication of nanoswitches

The devices described here are nanoswitch devices fabricated across back-to back finline slots. The nanoswitches are made of NbN as it has a high specific resistance in the normal state – a property which is important for this application, since it increases the switch resistance in Open state. The series resistance of a 0.5 μm wide nanobridge is about few hundred Ohms which is essential for a reasonable dynamic range. On the other hand, NbN is a superconductor with the critical temperature of 10-14 K; we therefore expect low impedance value in Closed state. The finlines were fabricated of NbN and partly covered by 100 nm gold for easier bonding. The wires and contact pads were also made of NbN-gold layer.

The finline tapers were 950 μm wide and 2 mm long with a slot width 5 μm, fabricated on a fused quartz substrate (fused silica). Using crystalline quartz turned out to be not a good option as a substrate material due to mechanical tension arising during the deposition of the NbN film which resulted in cracks in the NbN film and on the substrate surface.

For patterning the phase switch devices, a method employing negative or image-reversal resist was used combined with plasma etching. As we have described in Section 2.1, in this process the unexposed areas are removed, which results in the image reverse of the pattern in the mask layout. The NbN film was then subjected to CF_4 plasma etching that removed NbN within the open resist windows. After that, the resist was removed using Shipley 1165 remover, and finally we have a NbN image reproducing the original layout.

The phase switch devices were fabricated at Chalmers by depositing the nanostrip across the terminals of a back-to-back unilateral finline on a 200 μm thick quartz substrate. The fabrication process of the finline coupled nanostrip devices includes two lithography steps, namely photo lithography for fabricating the contact pads and e-beam lithography for patterning the NbN nanostructures. The whole fabrication procedure is shown in fig. 2.15.

First, a NbN film was deposited on a ~1 nm titanium buffer layer sputtered on a quartz substrate by magnetron sputtering. The deposition of NbN was performed using a niobium cathode in argon-nitrogen mixture plasma (Fig. 2.15a). This was done at room temperature in a magnetron sputter (the heating of the substrate is optional and was not used for this thesis). The thickness of the deposited NbN layer varies between 20 and 150 nm.

Two layers of resist were then spun on the wafer: a lift-off resist LOR3A and a photoresist Shipley S-1813. After baking both of the resist layers, the wafer was exposed to UV radiation at wavelength of 400 nm through a photo mask to pattern the gold pads and finlines. During the development of the photoresist, an undercut was formed in the lift-off layer (Fig. 2.15b). The wafer was then cleaned in the etching process by soft oxygen plasma and a thin layer of chromium and 100 nm of gold were evaporated through the resist mask and lifted off (Fig. 2.15c).

The next process step was the e-beam lithography for the patterning of the NbN nanostructures. First, the negative e-beam resist SAL-601 was spun on the wafer and baked (Fig. 2.15d). Then, the NbN structures were patterned by an e-beam exposure. After the development of the e-beam resist, the NbN structures were formed by the reactive ion etching

in CF_4 plasma (Fig. 2.15e). This was performed in Oxford RIE/CVD system. The rest of the resist was then removed in the Shipley 1165 remover (Fig. 2.15f) and finally the wafer was diced using a diamond saw. A typical device with a 5 μm long nanostrip fabricated in this way is shown in Figure 2.16.

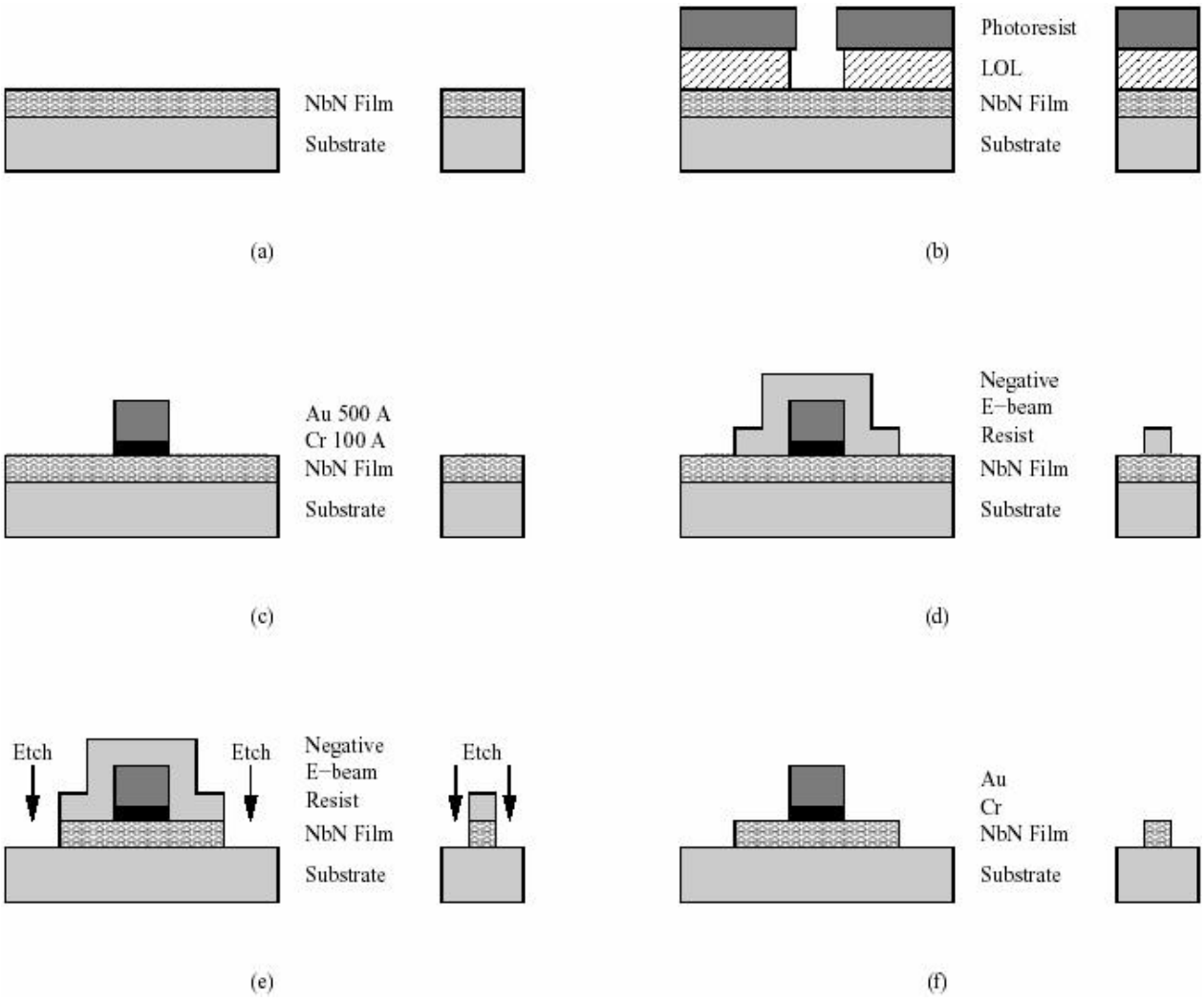

Figure 2.15: Fabrication of the nanostrip across a unilateral finline [18]. On each picture: (Left) Finline, (Right): nanobridge.

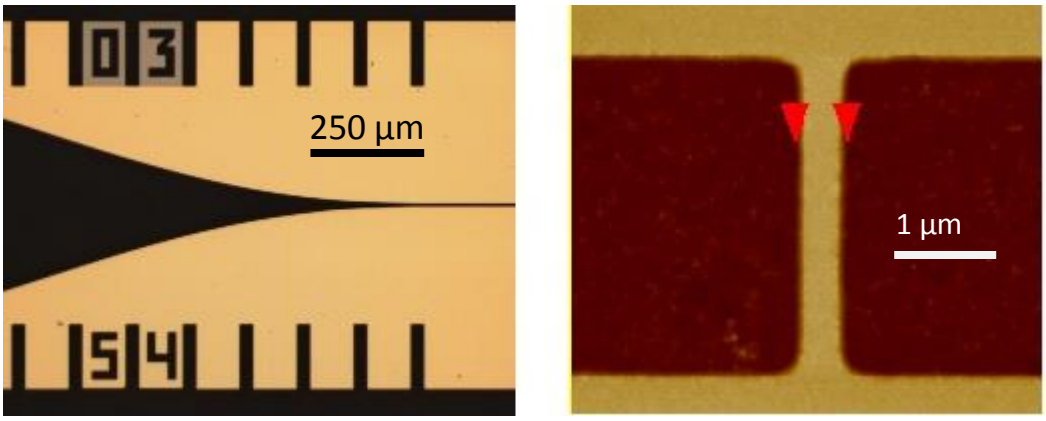

Figure 2.16: An image of the NbN nanostrip switch showing the finline phase switch device [18].

The Phase Switch devices are designed for phase modulation in cosmology instruments. The principle of operation of Phase Switch devices will be described later in Chapter 5, and the experimental details and results will be presented, while this chapter (Chapter 2) is dedicated to the detailed description of the fabrication procedures. In the next Chapter 3 we will present the CEB operation principle in detail, and the experimental details and results on CEB devices will be presented in Chapters 3 and 4.

Chapter 3

Finline-Integrated CEB Devices

In this chapter, we will first describe the general theory of SIN (Superconductor-Insulator-Normal metal) tunnel junctions and then analyze the CEB detector performance.

We will then describe the experimental investigation on testing CEB-finline devices, including DC tests and RF experiments performed with an external RF source at Chalmers, followed by calibrated RF testing using a thermal power load inside the cryostat, performed at Oxford University.

3.1. SIN tunnel junction theory

In a normal metal CEB bolometer a normal metal strip, thermally isolated from the environment, is heated by incoming radiation. The change in temperature is then measured with SIN junctions [48-49]. Two different types of tunnel junctions are discussed in this thesis: SIN and SIS, either as a device developed and tested in this work, or a detector used for testing other devices. For that reason, we shall first examine the properties of tunnel junctions, focusing on SIN junctions that are used with CEB devices and their current-voltage characteristics.

A tunnel junction is basically a structure of two metal layers separated by a thin insulating material layer (~10-20 Å). Even for a particle with a kinetic energy lower than the potential energy across the insulating barrier, there is a non-zero probability to "tunnel" across the barrier. This can be explained by the Schrödinger equation [48, 67], and the tunneling probability depends exponentially on the barrier thickness at a fixed energy height of the barrier. Quantum tunnelling in a tunnel junction therefore becomes significant if the insulating barrier is sufficiently thin [48]. The total tunnelling current through the junction is given by the integration of single tunnelling charges over the energy band of interest. The current in an SIN tunnel junction displays non-linear dependence on the applied voltage [68], and the current-voltage characteristic of the junction is given by the expression [48, 68-69]:

$$I_{SIN} = \frac{1}{eR_N}\int_{-\infty}^{\infty}\frac{E}{\sqrt{(E^2-\Delta^2)}}\left[f(E-eV)-f(E)\right]dE \tag{3.1}$$

Here, R_N is the normal resistance of the SIN junction, Δ is the energy gap of the superconductor, $f(E)$ is the Fermi-Dirac distribution function, and E is the energy of the quasi-particles [69].

We have assumed that the normal metal strip and the superconductor are in equilibrium and their distribution functions are given by [69]

$$f_{N,S}(E) = \frac{1}{e^{\frac{E}{K_B T_{N,S}}}+1} \tag{3.2}$$

A theoretical IV curve at the temperature of 0 K is shown in Fig. 3.1 for a voltage range around the superconductive gap Δ. In this limit, there is no current flow at voltages below the

gap Δ. When the voltage approaches Δ, the energy levels in the normal metal are moved up by the applied voltage V, and electrons at the Fermi level in the normal metal can tunnel to empty states above the superconducting gap Δ (Fig. 3.2). Therefore, the current starts to increase and then increases rapidly at bias voltages just exceeding Δ.

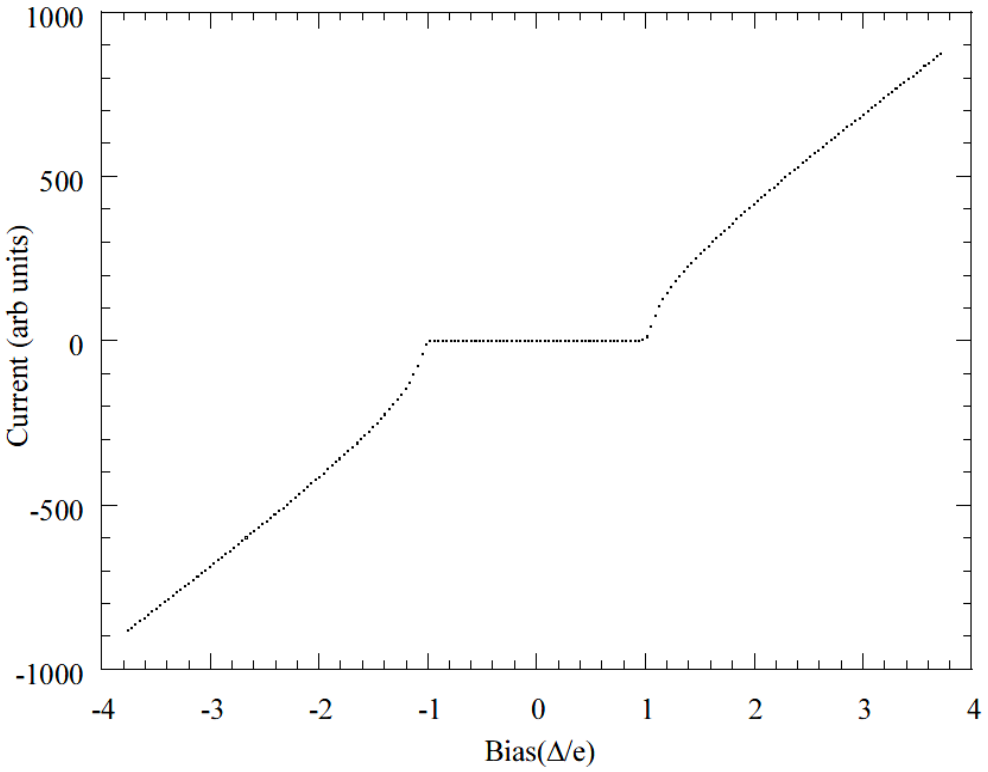

Figure 3.1. Current-voltage characteristic of an SIN tunnel junction [48].

For sufficiently high voltages above Δ, the density of states approaches that in the normal state, and the IV curve according to Eq. 3.1 can be approximated by a linear asymptote, described by the normal resistance R_N:

$$I_{SIN}(eV >> \Delta) \approx \frac{V}{R_N} \tag{3.3}$$

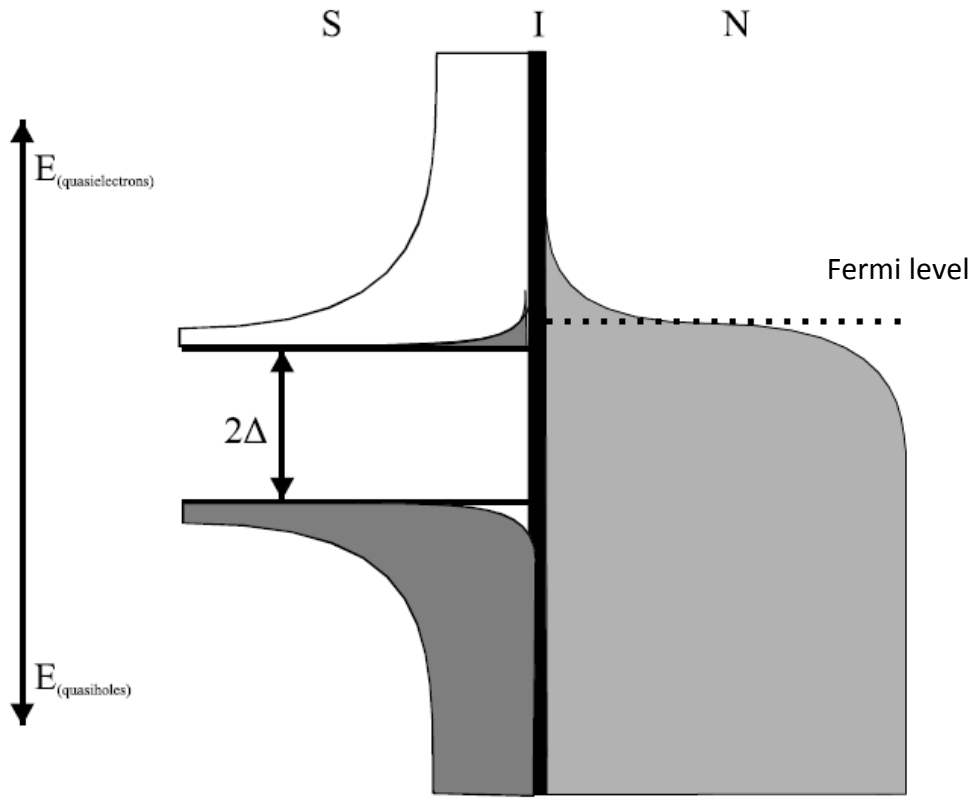

Figure 3.2. Energy diagram of an SIN junction showing the density of states distribution [48].

Considering the temperature dependence of the current-voltage characteristic, at high enough bias voltages ($V >> \Delta$), the current-voltage characteristic does not depend substantially on the temperature as it approaches the linear asymptote. For bias voltages below Δ, the IV curve varies strongly with the temperature, according to the Eq. 3.1. The tunneling current versus temperature in the normal metal is shown in Fig. 3.3. The current depends mainly on the temperature of the normal metal, because the temperature dependence is different for the number of electrons in the normal metal that are able to tunnel and the quasiparticle population in the superconductor [70].

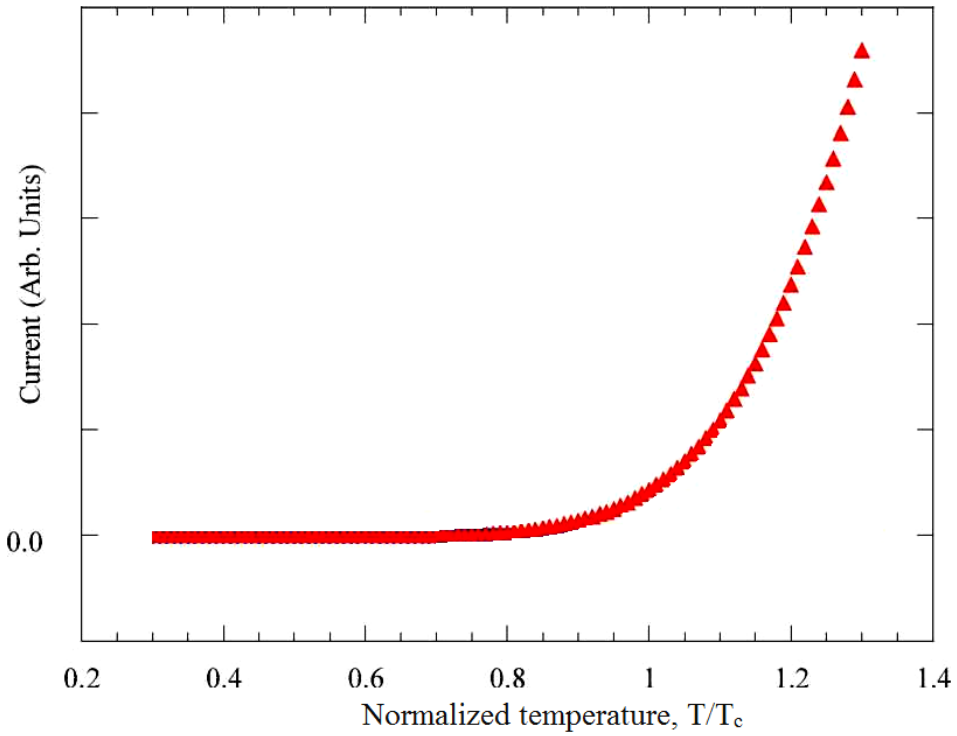

Figure 3.3 Current versus normal metal temperature in an SIN junction at fixed voltage around Δ [48]

Consider a CEB device with normal metal absorber, illuminated by an RF signal δP. The temperature of the metal absorber is determined by the heat balance between the electron subsystem and the phonons. The heat balance equation for a CEB can be written as [61]:

$$P_C(V,T_e,T_{ph}) + \Sigma\Lambda(T_e^5 - T_{ph}^5) + C_\Lambda \frac{dT}{dt} = P_0 + \delta P(t) \qquad (3.4)$$

where Σ is a material constant, Λ - absorber volume, T_e and T_{ph} are, respectively, electron and phonon temperatures of the absorber, P_C is the cooling power of the SIN tunnel junction, and C_Λ is the specific heat capacity of the normal metal. The right-hand part of the equation represents the incident RF background power P_0 and the time-dependent $\delta P(t)$ is the incoming RF power to be detected.

Power flowing in and out of the CEB may be separated into two parts: a time independent term,

$$\Sigma\Lambda(T_{e0}^5 - T_{ph}^5) + P_C(V,T_{e0},T_{ph}) = P_0 \ , \tag{3.5}$$

where T_{e0} is the electron temperature in the presence of power load, and a time dependent term,

$$(\partial P_C/\partial T + 5\Sigma\Lambda T_e^4 + i\omega C_\Lambda)\ \delta T = \delta P, \tag{3.6}$$

which is obtained by differentiating the Eq. 3.4 and considering a small change in temperature δT and in power δP, respectively, assuming that the incident signal is an electromagnetic wave at an angular frequency of ω.

The term $G_{SIN} = \partial P_C/\partial T$ is the effective cooling thermal conductance of the SIN junction that gives rise to the negative electrothermal feedback (ETF). It reduces the temperature response δT because the cooling power P_C compensates for the change of signal power in the bolometer. The next term is the electron-phonon thermal conductance of the absorber:

$$G_{e\text{-}ph} = 5\Sigma\Lambda T_e^4 \tag{3.7}$$

that represents the heat flow between electron and phonon sub-systems that can be expressed as

$$P_{e\text{-}ph} = \Sigma\Lambda(T_e^5 - T_{ph}^5), \tag{3.8}$$

where Λ is the volume of the absorber and Σ is almost constant for a given material.

From Eq. (3.6) we define an effective complex thermal conductance which controls the temperature response of the CEB to the incident signal power [61]

$$G_{eff} = G_{SIN} + G_{e\text{-}ph} + i\omega C_{\Lambda} \tag{3.9}$$

The effective thermal conductance of the CEB is increased by the effect of electron cooling, thus producing negative Electro-Thermal Feedback.

The value of thermal conductance is crucial for the noise performance of a CEB device since at equilibrium the phonon noise is given by $4k_BGT^2$, where G is the thermal conductance [71]. Lower heat conductance corresponds to higher sensitivity because of phonon noise that increases linearly with thermal conductance. When the system is left to itself for energy relaxation through electron-phonon interaction, the system displays strong nonlinear dependence of electron-phonon thermal conductance on temperature [56]. Hence, the term representing thermal conductance due to electron-phonon interaction is very critical parameter for the CEB performance. Indeed, the knowledge of G_{e_ph} allows us to estimate the optical performance of CEB as millimetre-wave detector, assuming the DC voltage to temperature response at a fixed current has been measured.

3.2. Noise performance of the CEB device

The sensitivity of a CEB device is expressed by the noise equivalent power (NEP). The NEP is defined as the low frequency spectral density of RF-power fluctuations (input noise), which would generate the same output voltage noise in an ideal noiseless device [62, 69, 71].

Alternatively, the NEP can be defined as the signal power that gives a signal-to-noise ratio of one in a one hertz output bandwidth [72]. The NEP is equal to the current or voltage noise spectral density divided, respectively, by the current or the voltage responsivity. The voltage responsivity dV/dP is defined as a measure of change in voltage to the incoming RF power at a fixed bias current, and current responsivity dI/dP denotes the current response to the RF power at a fixed voltage.

Depending on the techniques that are used for the device characterization, one can distinguish between electrical and optical NEP. Electrical NEP results from the direct thermal energy change of the detector, while optical NEP characterizes the ability of the system to detect the incoming RF signal and includes the coupling efficiency of the whole RF system.

Since our goal of developing sensitive detectors is to measure extremely weak signals from deep space, we have to optimise the noise performance of the system. The total measured noise in the system includes the noise of the device and the noise of the readout amplifiers. In this work we focus on the noise of the bolometer, which consists of the SIN junction noise, noise due to electron-phonon interaction and amplifier noise.

3.2.1. CEB noise in the voltage-biased mode

Considering a circuit biased at fixed voltage (voltage biasing), we can first study the current responsivity $S_I = dI/dP$ at fixed voltage. There are three independent contributions to the noise equivalent power:

$$NEP_{total}^2 = NEP_{e-ph}^2 + NEP_{SIN}^2 + \frac{\delta I^2}{S_I^2}. \quad (3.10)$$

Here NEP_{SIN} represents the noise of the tunnel junctions, $\delta I^2/S_I^2$ the noise introduced by the amplifier due to its limited sensitivity δI, expressed in A/Hz$^{1/2}$, and $NEP_{e\text{-}ph}$ the noise due to electron-phonon interaction:

$$NEP^2_{e\text{-}ph} = 10 k_B \Sigma \Lambda (T_e^5 + T_{ph}^5) \quad (3.11)$$

The noise of the tunnel junction consists of shot noise $2eI$, the fluctuations of the heat flow and the correlation between these two processes [69]:

$$NEP_{SIN}^2 = \frac{\delta I_\omega^2}{S_I^2} - 2\frac{< \delta P_\omega \delta I_\omega >}{S_I} + \delta P_\omega^2 \quad (3.12)$$

The above-mentioned correlation represented by the second term in the above equation, reduces the shot noise by 30-70%, [56].

Analysis of the influence of the background power load on noise [46] shows that the optimal bolometer configuration is the CEB with voltage-biased SIN tunnel junctions and current readout by a SQUID. This is because the SQUID operates at low temperature and is a much more sensitive device than any room-temperature amplifier. SQUID detectors measure current effectively by measuring the magnetic flux, hence the voltage-biased operation of CEB is required when using SQUID-readout. For an absorber of volume of 0.01 μm^3, SQUID current noise of 5 fA/Hz$^{1/2}$ and 1 kΩ junction resistance, a total NEP = 1.2×10^{-19} W/ Hz$^{1/2}$ can be achieved for a microwave background power P_0 = 0.01 pW [46]. This value is mainly

determined by shot noise of the SIN tunnel junctions due to incoming power load. Electron-phonon and amplifier noise are, in that case, lower than noise of the SIN. A responsivity value $S = dI/dP$ of 150 nA/pW can be achieved, which is determined mainly by electron temperature of the absorber and by quantum efficiency of the CEB [46].

For 300 mK operation in the presence of the final background power load (P_0 = 0.1 pW) and current noise of the SQUID-amplifier of 10 fA/Hz$^{1/2}$, the analysis performed in [46] predicts NEP level of 10^{-18} W/Hz$^{1/2}$.

Quantum efficiency is defined as the number of excited electrons produced by one incident photon [56]. An incoming photon is absorbed and an electron is excited to an energy level of 4 meV for a 1 THz signal. The electron then relaxes due to electron-electron interactions and the energy is distributed between hot electrons at a quantisation level k_BT for a normal metal and between quasiparticle at quantization level Δ for a superconductor. This results in a lower quantum efficiency of ~20 for a superconductor compared to hundreds for a normal metal. Hence, using SIN junction bolometers with normal metal is advantageous in terms of quantum efficiency, compared to the superconducting absorber, and a higher responsivity is thus expected when using normal metal as the absorber material.

Low NEP and high responsivity to the incoming power are crucial parameters of a millimetre-wave detector, in particular in combination with fast response of the device.

The analysis mentioned above shows that the concept of a cold-electron bolometer can give the excellent noise performance in the presence of a realistic background power load. Since incoming power is removed from the absorber by cooling, the dynamic range of the system is substantially increased. The CEB concept could therefore be very promising for future space telescopes operating in the millimeter and sub-millimeter regions [56].

3.2.2. CEB noise in the current-biased mode

In this section we analyse the current-biased mode of operation of CEB with SIN junctions. This part of the CEB theory is most relevant to the material of my thesis as the current-bias mode is the scheme realized for testing of the devices presented here. JFET or MOSFET amplifiers were used for readout electronics so current-bias mode was the only option in this framework.

As has already been mentioned in the previous section, a bolometer is characterized by its responsivity, noise equivalent power and the time constant. The responsivity of a current-biased CEB, S_V, is expressed by the voltage response to the incoming power $\delta V_\omega/\delta P_\omega$ that is given by the following expression [56, 71]:

$$S_V = \frac{dV}{dP} = \frac{dV/dT}{G_{e-ph} + 2G_{SIN} + i\omega C_\Lambda} \tag{3.13}$$

where G_{SIN} is the thermal conductivity of SIN tunnel junction. The noise expressed by the noise equivalent power (*NEP*) can therefore be represented by three contributions. For a series array of N CEB devices, the NEP is defined as follows [56]:

$$NEP^2_{TOT} = N \times NEP^2_{e\text{-}ph} + N \times NEP^2_{SIN} + NEP^2_{JFET}, \quad (3.14)$$

Here, $NEP_{e\text{-}ph}$ represents the noise associated with electron-phonon interaction [56], NEP_{SIN} the noise of the SIN tunnel junctions, and NEP_{JFET} represents the amplifier noise. The SIN noise has three components: the shot noise and NEP associated with it $2eI/S_I$, the fluctuations of the heat flow through the SIN tunnel junctions and the correlation between these two processes [71, 73]:

$$NEP^2_{SIN} = \frac{\delta I^2}{(\frac{dI}{dV} S_V)^2} + 2 \cdot \frac{\langle \delta P \delta I \rangle}{\frac{dI}{dV} S_V} + \delta P^2 \quad (3.15)$$

This correlation is a form of the electrothermal feedback discussed earlier by Mather [74]. Due to this correlation the shot noise is increased by 30-50% in contrast to the CEB in voltage-biased mode where anti-correlation reduces the total noise [62]. The last term in the previous expression is due to the voltage δV and current δI noise of the JFET amplifier that are expressed in nV/Hz$^{1/2}$ and pA/Hz$^{1/2}$.

The availability of JFET readout electronics allows straightforward testing of our devices, whilst the employment of SQUID electronics mentioned in the previous section requires very involved laboratory equipment and advanced cryogenic electronics that might be a subject of a

separate research, not covered by this PhD project. In the future, it will be possible to realize a voltage-bias scheme with SQUID readout that is the best implementation of CEB detection for ultimate noise performance. In this thesis, however, current biasing is used in order to demonstrate the feasibility of CEB devices as a concept.

The analysis of a single current-biased CEB with JFET readout has shown [75-77] limitations of noise performance due to decreased voltage responsivity and degradation JFET voltage noise under high optical power load due to overheating of the absorber. It was therefore proposed to use a series of bolometers combined with additional capacitances for the HF coupling, in order to improve the noise performance and reduce NEP down to the photon noise level and below. This is because, in this case, the input power is divided between several absorbers in the array, thus limiting the electron temperature of the absorbers, which results in enhanced responsivity of the CEB array, as the voltage across all absorbers is summed and measured as total voltage collected from all the devices. At the same time, the noise is only proportional to the square root of the number of the devices, as the noise components coming from different devices are not correlated. This approach is partly realized in the current work and is presented in the chapter which discusses CEB arrays for Boomerang.

To estimate the required number of devices in an array, we recall that, for background power load of P_0 = 5 pW per polarization, the photon noise at 300 GHz could be estimated as

$$NEP_{phot} = \sqrt{2P_0 E_{quant}} = \sqrt{2P_0 \times hf} = 4.3 \cdot 10^{-17} \text{ W/Hz}^{1/2}.$$

For a given absorber material, the optimal number of the devices in an array is determined by the background power P_0 and the absorber volume Λ. By increasing the number of the devices N we can split the power load P_0 between the N bolometers until the point when the power load per device becomes equal to the phonon noise: $P_0/N = P_{ph}$, where the phonon power $P_{ph} = T^5_{ph} \cdot \Sigma \cdot \Lambda$ is determined by the volume of the absorber only. Increasing the number of the CEB devices in the array further does not bring any improvement as the power load per device becomes less than the phonon power, which saturates the sensitivity. In most practical cases, the amplifier noise dominates the junction noise, so the amplifier noise contribution is effectively reduced by increasing the number of CEBs up to the point when the amplifier noise per device becomes less than that of junction noise, thus resulting in the total noise below the photon noise level.

Bolometer arrays will be discussed later in the Chapter 4 of this thesis, where we will present our work on parallel/series arrays of several Cold-Electron Bolometers and analyze the measurements data obtained. In this chapter, however, we focus on single CEB devices with JFET readout in the current-biased mode, integrated in 97 GHz finlines. Although this approach does not yield maximum responsivity compared to CEB arrays, it will allow us to investigate the performance of a CEB as a millimeter-wave detector and the CEB-finline integrated circuit as a design to be used in microwave system comprising a waveguide in conjunction with horns and other microwave components.

3.3. CEB integrated in a 97-GHz finline

An attractive implementation of a millimeter-wave detector is to deposit the CEB directly across a unilateral finline on a planar substrate [46]. The advantage of this method is that the finline feeding the device, the required planar circuit and the CEB device can be fabricated on the same substrate and in the same fabrication run [78, 79].

A finline taper is in essence a slotline located in the E-plane of a waveguide, with gradually changing slot width. It is used as an impedance matching between the chip and the waveguide. Example layouts of a finline taper and two different finlines are shown in Figure 3.4.

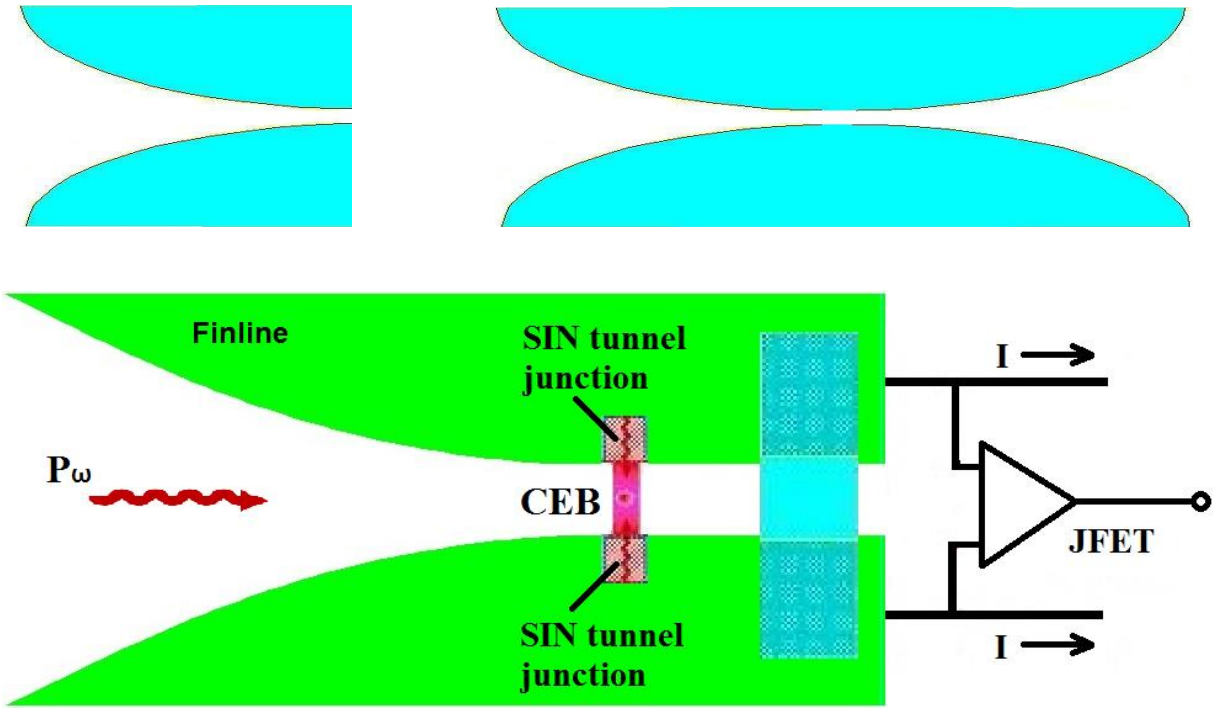

Figure 3.4. Top: (Left) A finline taper; (Right) A back-to back finline taper; Bottom: Cold-Electron Bolometer (CEB) coupled to a finline with JFET readout [56, 78, 79].

Among different types of finlines, unilateral and antipodal ones have been used in conjunction with bolometric detectors. For a unilateral finline, both electrodes of the slotline (called here *fins*) are located in the same plane, and, following the taper, the finline continues as a slotline with constant width. The fins of an antipodal finline are deposited in different planes and overlap at some point, with a thin insulating layer between them. The termination of antipodal finlines is a microstrip. The fabrication involves several steps of lithography and deposition of different materials, including an insulating oxide layer to form a planar 3-layer structure. On the contrary, the unilateral finline is a simpler configuration as both fins are made of the same material and can be deposited as one layer and patterned in one step of lithography.

In what follows we shall describe the design of a CEB with SIN tunnel junctions to couple the incoming radiation propagated through a 97–GHz waveguide into a finline (Figure 3.4, bottom). The profile of the finline taper was designed using an optimum taper technique, implemented in *Finsynth* which is a software package developed by our Oxford group, described in [5, 80]. The devices are fabricated using the trilayer direct-write technology described earlier in Chapter 2 of this thesis [36, 64]. This approach is especially suitable for low-frequency applications as it allows for large size tunnel junctions, which otherwise are difficult to fabricate using traditional shadow evaporation techniques. The latter is more suitable for higher frequencies (350 GHz and above) due to smaller size of tunnel junctions one can fabricate in that technology. Alternatively, the normal-metal absorber could be created prior to tunnel junctions and superconducting electrode, which is feasible using advanced technologies presented later in Chapter 4 in this thesis.

In a CEB-finline integrated circuit shown in Figure 3.4 (bottom), a CEB device consisting of two SIN junctions and a normal metal absorber is deposited across a finline and coupled to the finline through the SIN junctions. For the integrated circuit in Figure 3.4, a JFET amplifier is used as readout that can operate at room temperature. A current is applied using an external source and then the voltage across the CEB device is measured, using room-temperature electronics.

3.3.1. Analysis of CEB-finline integrated circuits

We have analysed the electromagnetic behaviour of the CEB-finline integrated circuit using Ansoft Designer and HFSS software. An equivalent circuit for the CEB-finline was simulated with an ideal transmission line in Ansoft Designer software (Figure 3.5). In this model, the incoming signal propagates through a transmission line of electrical length of 360º and the power is fed into the CEB represented here by an RLC tank circuit assuming matched terminals. The end of the transmission line is shorted at a distance called here "back short distance". This value was set initially to $\lambda/4$ and then optimised in order to achieve the best matching between the characteristic impedance of the transmission line and the input impedance of the RLC circuit over the band of interest.

Next we used HFSS to simulate a finline CEB with finline slot widths between 2 and 10 microns, deposited on silicon or quartz. The CEB itself was represented by an equivalent RLC circuit. Simulations performed in Ansoft Designer and HFSS showed that best RF matching between the finline and the CEB circuit can be achieved using tunnel junctions with the area

of 1.5×1.5 to 2×2 microns, which corresponds to capacitance values of 100-200 fF. For Si substrates, the optimum values were obtained for an inductance and a resistance of 2.4 pH and 45 Ω respectively. For a quartz substrate, the corresponding values were 2.6 pH and 70 Ω. Simulations also showed that the use of a back short distance of 225-250 µm with 5 µm slot width gives a reflection coefficient down to -20 dB for Si, while the result is insensitive to small variations in absorber resistance and inductance values. The return losses (S_{11}) for Si and quartz are shown in Figure 3.6, (left) and (right), respectively. Similar values (-18 dB) were obtained for a quartz substrate at a backshort distance of 500 µm (Figure 3.6, right).

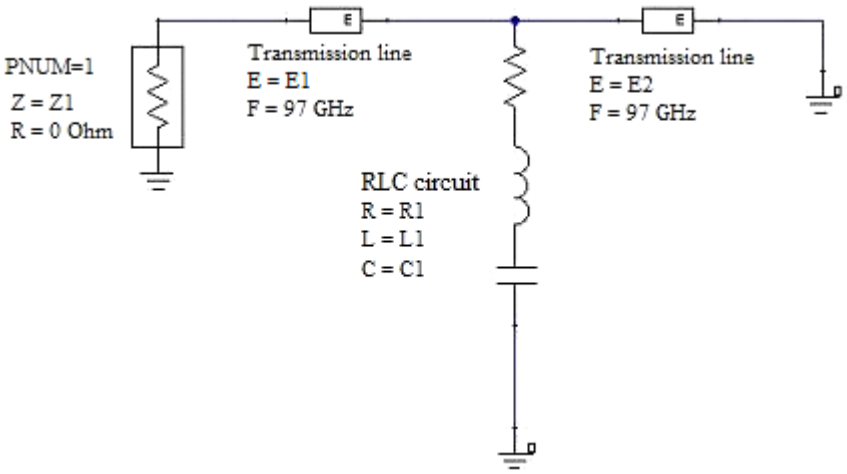

Figure 3.5. Equivalent circuit of the finline-CEB used for simulations in Ansoft Designer [78, 79]

Based on these simulations, we decided to fabricate a CEB-finline structure at the width of 5 µm on silicon substrate, although a quartz substrate remains an option. For a 5 µm long absorber with 0.5 µm width and thickness of 50 nm, the inductance was estimated as 2.5 pH.

The resistance value of 45 Ω can be obtained for a strip of the above size by making it of Cr/Cu bilayer. Thus, a 50 nm thick absorber made of Cr/Cu that is 5 μm × 0.5 μm large in combination with two 4 μm^2 tunnel junctions is a good choice for RF matching.

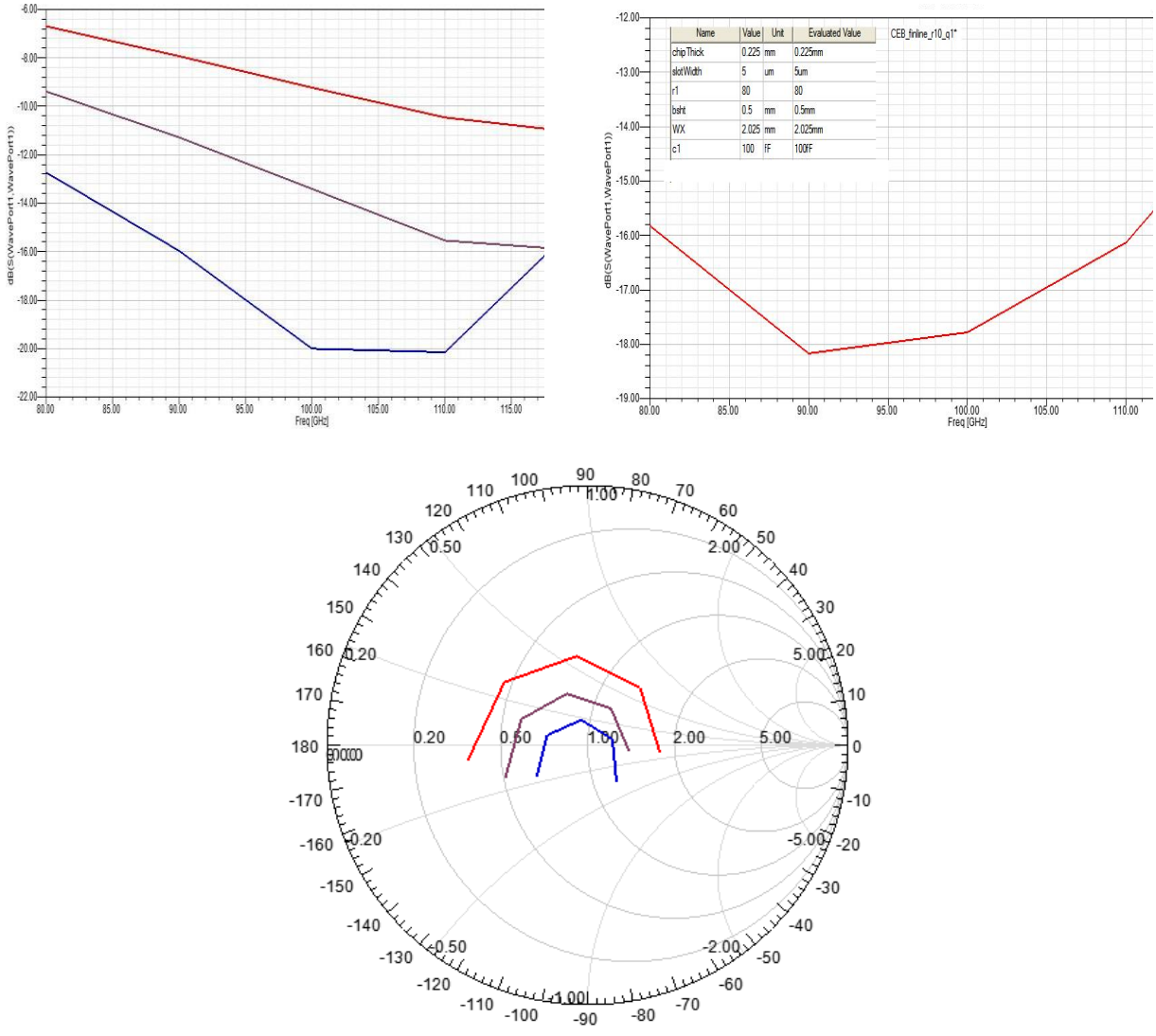

Figure 3.6. Reflection coefficient at the input of the CEB device for Si substrate (left) and quartz (right). Simulation performed using HFSS for a finline with 5 μm slot width. Different colours in these plots represent the back short distance, varying between 200 and 250 μm for Si and 350 to 500 μm for quartz. (Bottom) RF matching for Si substrate in Smith Chart [78, 79].

3.3.2. Fabrication of finline-CEB integrated circuits

The CEB-finline samples were fabricated using e-beam lithography in direct-write mode, using the trilayer technology principle of fabricating tunnel junctions developed by the author of this thesis and described in detail in Chapter 2 [36, 64, 79].

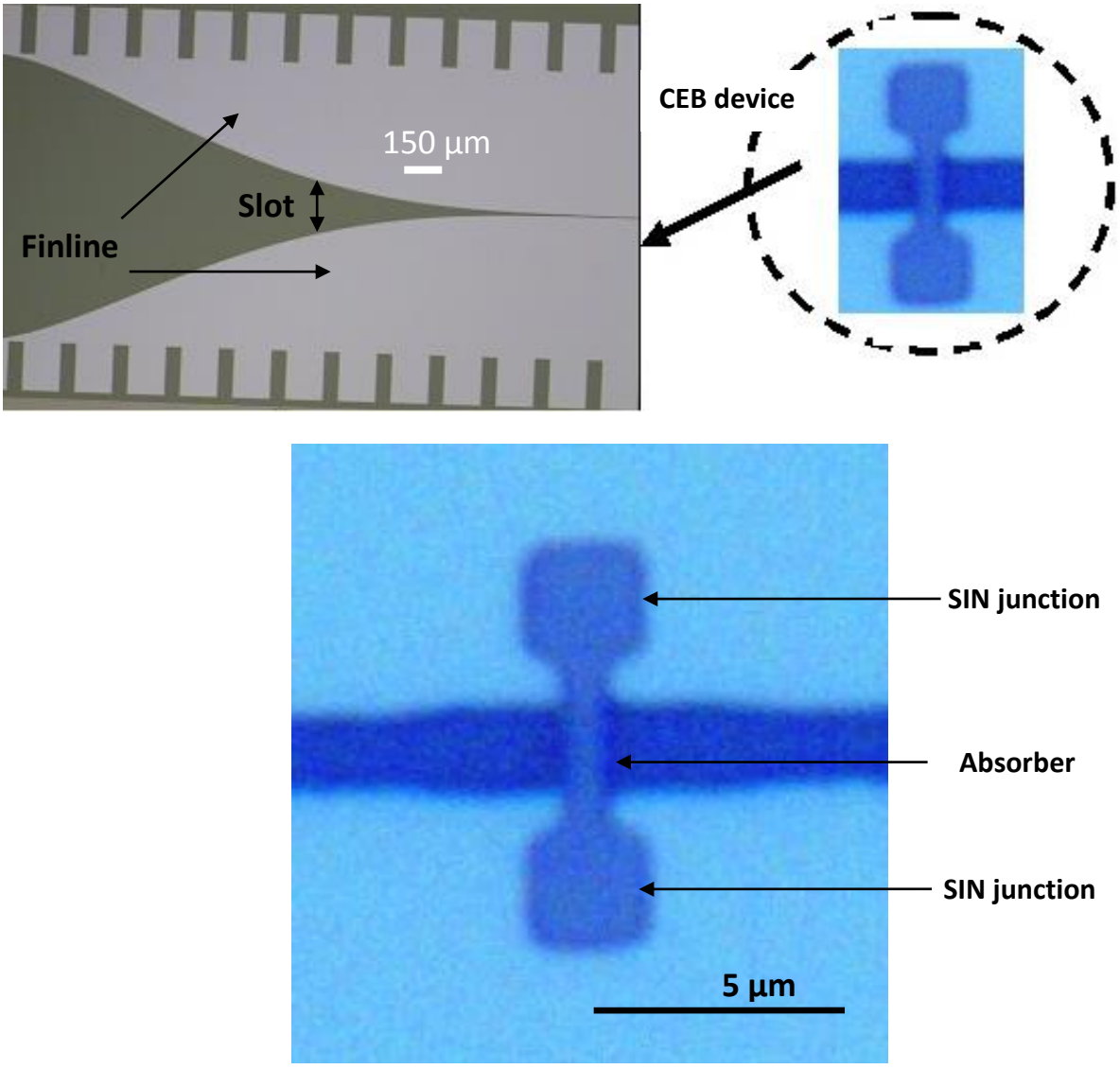

Figure 3.7 [78, 79] (Top) Photo of a finline with a CEB device across the slot (inset); (Bottom) Enlarged central part of the finline slot with a CEB device deposited across it.

First, 100 nm thick gold contact pads were created using e-beam exposure and thermal evaporation. Then, ~45 nm thick finlines made of Al and covered by gold and the Cold-Electron Bolometer structures were fabricated in the middle of the finline using the trilayer process described in Chapter 2 [36]. This is done by depositing Al as the bottom layer with subsequent oxidation in chamber for creating tunnel junctions, followed by depositing a layer of Cu and then gold on the top of it for passivation. As the last step, the Cu-Au layer was removed by ion-beam etching on the top of the trilayer structure. A photo of the fabricated CEB integrated in a finline is shown in Figure 3.7 [78, 79].

3.3.3. The experiment setup and readout

To test the performance of our samples at low temperatures, we used a Heliox AC-V cryostat, which is a "cryogen-liquid-free" system developed and fabricated by Oxford Instruments (Figure 3.8). This is a pulsed tube cooler, able to cool down to 270 mK without consuming any cryogen liquid. Its cooling power is above 100 μW at 350 mK and the hold time is about 4-5 hours. After recycling of ^{3}He which takes about 1 hour, the system can be cooled again down to 280 mK.

The DC current-voltage characteristics of the CEB devices presented here were measured using current biasing scheme, i.e. a current through a device is controlled using a current source, and voltage across the device is sampled and amplified using room temperature amplifiers. So, in current biased mode, the voltage over the bolometer is considered as a function of applied current through the bolometer. In our experiments, current biasing of CEB devices with SIN junctions is realized by a voltage source combined with a bias resistance

R_{bias} in series with the CEB device under test. The voltage across the device is then amplified and measured (Figure 3.9).

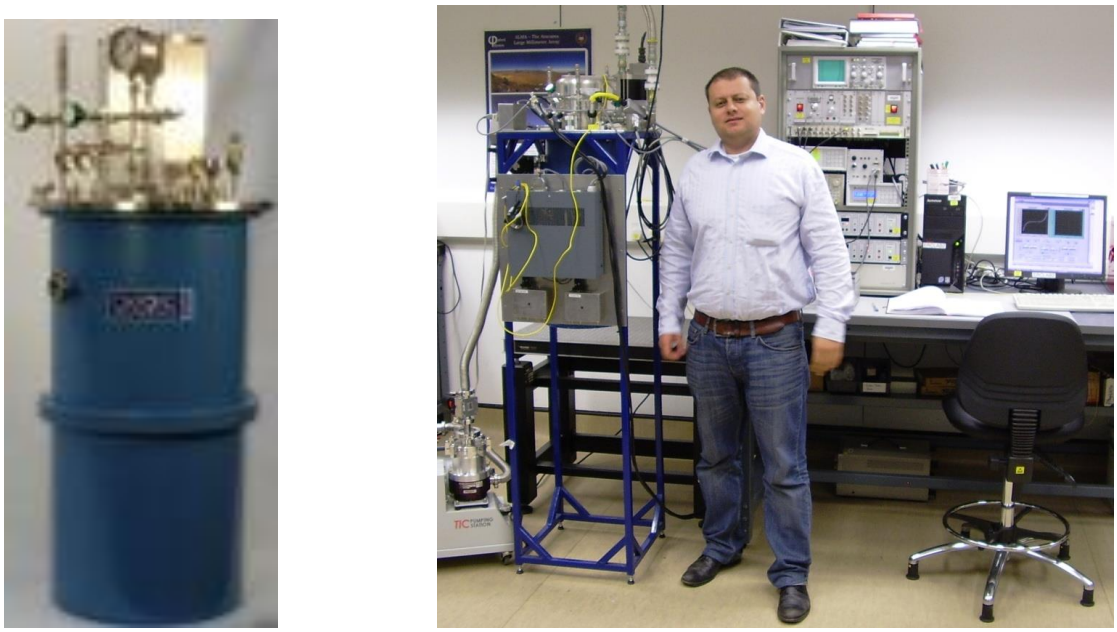

Figure 3.8. HELIOX "Cryogen-free" pulsed tube cryostat operating at ~300 mK

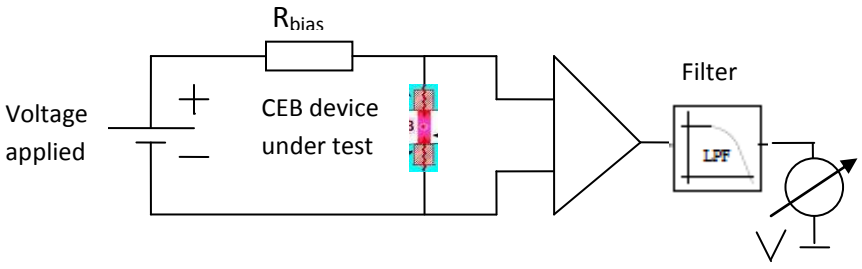

Figure 3.9. Current biasing circuit topology [45]

The detailed schematic of the room-temperature readout amplifier used for testing CEB devices in this work is shown in Fig. 3.10. It operates in the fixed current bias mode, using a differential bias circuit with room temperature amplifiers and bias resistors. This circuit uses a

driver circuit with bias resistance switchable in a range from 100 kΩ to 10 GΩ, and AD743 BiFET based first stage amplifiers with input voltage noise of around 4nV/√Hz. Current-voltage curves were measured for several bath temperatures between 286 mK and 356 mK.

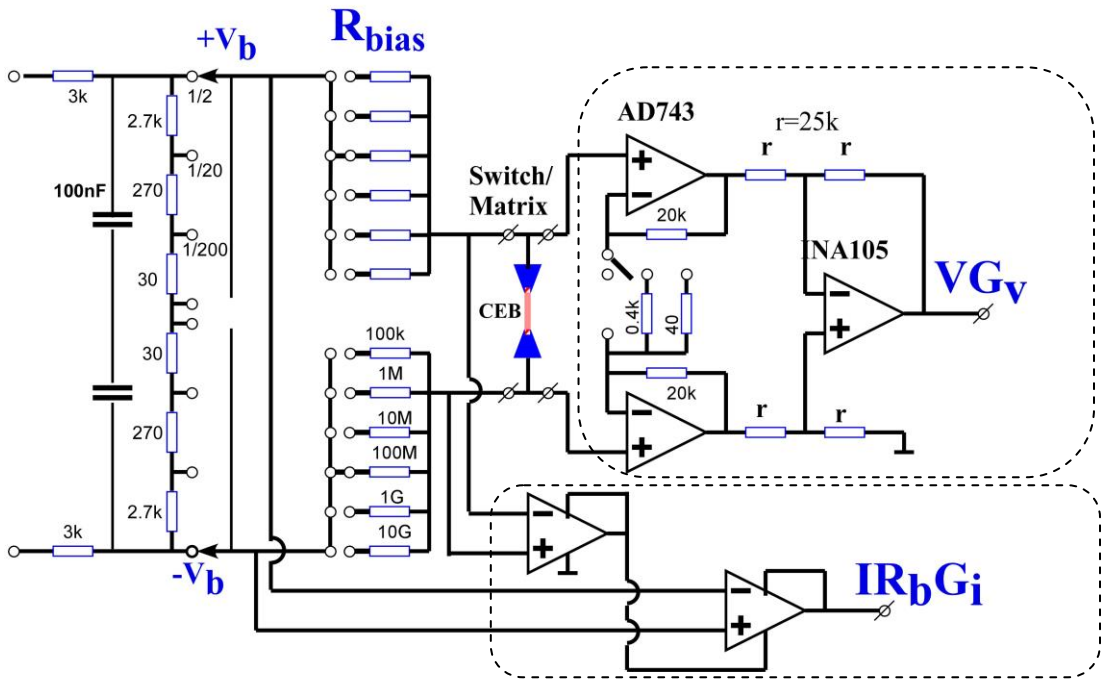

Figure 3.10. Circuit schematic of the room-temperature amplifier used for IV-curves measurements in current-biased mode [43]. The bias resistance is selected in a range between 100 kΩ and 10 GΩ.

Measurements of IV characteristics are performed as follows, see Figure 3.10. The bias voltage V_b is applied to the amplifier box, connected to the CEB device. The amplifier box contains two amplifier channels and has thus two outputs representing the current through the device and voltage across it. In Figure 3.10, the voltage and current outputs are labeled VG_V and IR_bG_i respectively, and the two channels are encircled by dashed lines.

In fact, both amplifier channels operate as voltage amplifiers. The voltage channel samples the voltage across the CEB device directly, amplifies it and reads out. The current channel samples the bias voltage across the bias resistors connected in series with the CEB device. This voltage is then amplified and measured as a voltage at the amplifier output. Both outputs are then connected to a computer and read out by LabView. The output voltage at the current channel output is proportional to the current through the bolometer I_{bolo} and the bias resistance R_{bias} , typically 20 or 200 MΩ. In order to obtain the actual current, the voltage sampled by LabView at the current channel output, is divided by R_{bias} and the channel gain. The voltage across the bolometer is obtained by sampling the voltage at the output of the voltage channel and dividing this value by 1000, which is typical value for the voltage gain of the channel. In current biased mode, the current through the bolometer is considered as the argument of the resulting IV curve, while voltage across the bolometer is regarded as the output function.

The operation of the cryostat is controlled by electronic equipment placed on a measurements rack along with temperature readout electronics, room temperature amplifiers, external sweep generators and other readout electronics. The current is determined by either the external sweep generator or digitally using LabView application. The IV curves can be observed on the screen of an oscilloscope or displayed in a LabView window (See Figure 3.11). The bias current is swept in a certain current range, and then both current and voltage values are logged by LabView as a datastream, at a certain step size. An example IV curve obtained in this way is shown in Figure 3.11, right.

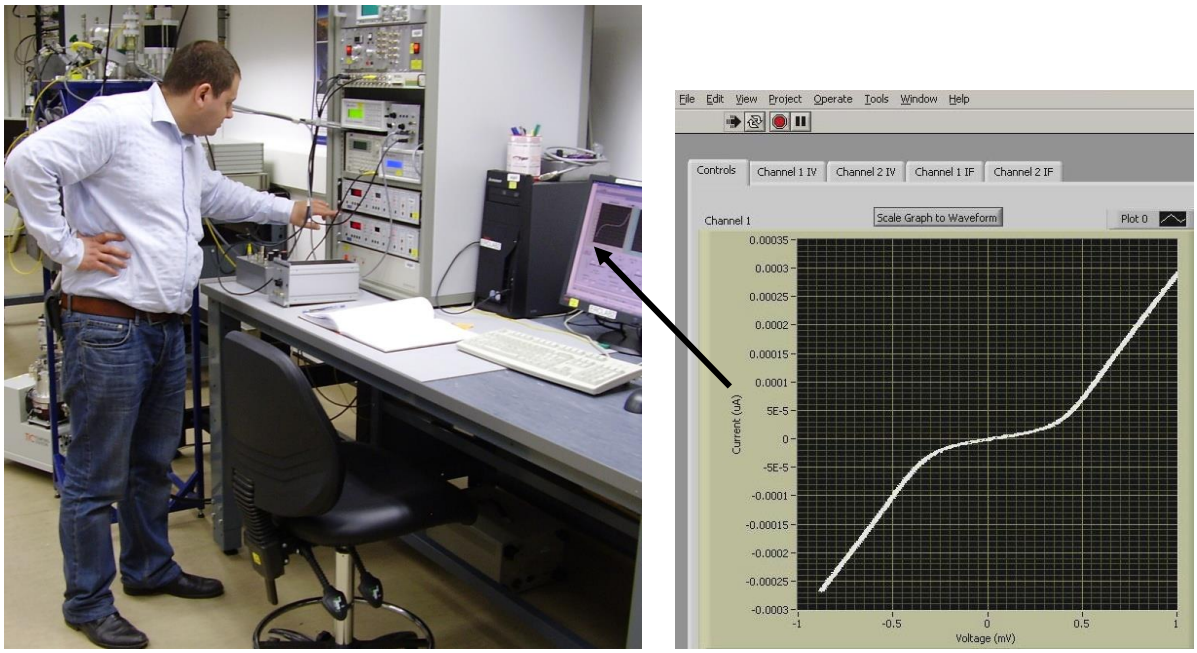

Figure 3.11. (Left) Measurement setup with LabView, readout electronics, control blocks etc. (Right) An example IV curve of SIN junctions in LabView representation.

3.3.4. DC and RF testing using an external power source

Preliminary testing of the CEB-devices was carried out at Chalmers University of Technology using an Oxford Instruments HELIOX-AC-V ^{3}He sorption cryostat, which can reach a base temperature of 280 mK. In order to keep the optical power load on the detectors to acceptable levels, two low-pass filters with cut-off frequencies of 1 THz and 3 THz and two neutral density filters with 10 dB attenuation each were mounted over the windows in the radiation shields inside the cryostat.

The voltage to temperature response, $S_{V/T} = dV/dT$, of the CEB was calculated by comparing the I-V curves at different bath temperatures at fixed bias current. An IV curve of the fabricated device and the voltage response to the temperature as a function of bias voltage are shown in Figures 3.12 and 3.13, respectively.

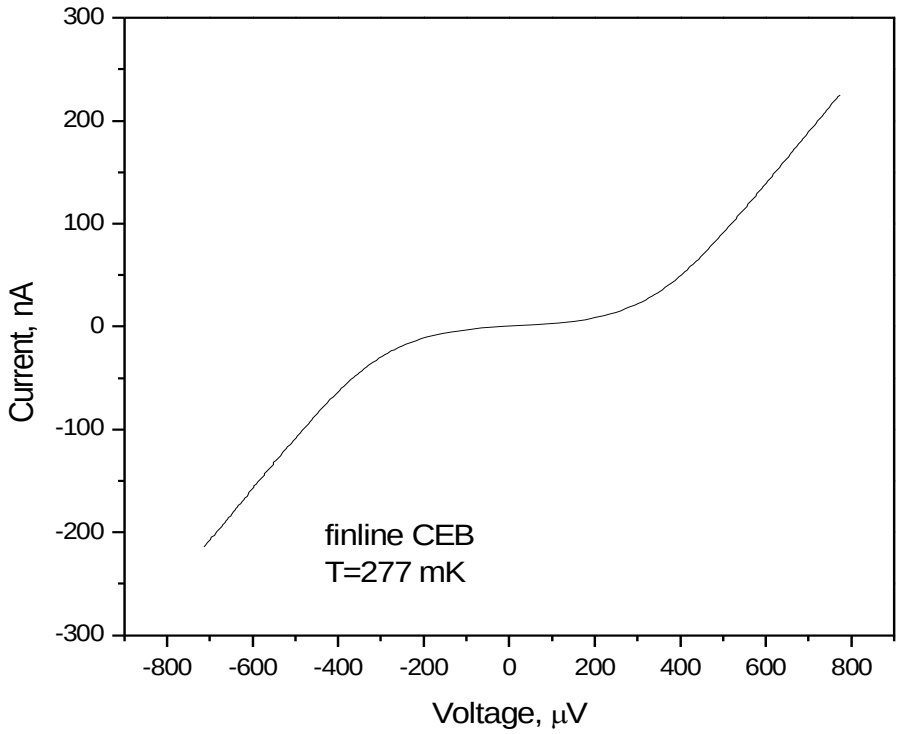

Figure 3.12. The IV curve of a CEB at temperature of 277 mK [78, 79].

Preliminary optical tests of the bolometers were performed at 110 GHz with IMPATT diode as a signal source. The optical response was measured using the experimental setup shown in Figure 3.14.

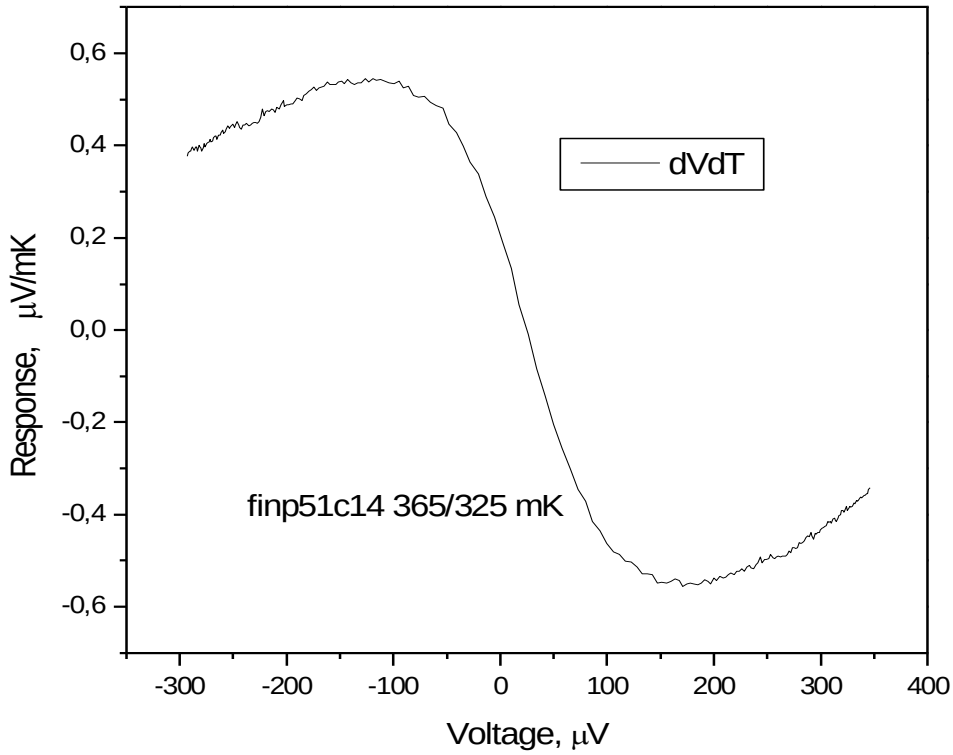

Figure 3.13. Voltage to temperature responsivity (dV/dT) of the CEB versus bias voltage [78, 79].

Measurements were performed by mounting the CEB-finline chip on a sample holder near to the cryostat window and illuminating it from the outside (Figure 3.15). In this experiment, a small amount of optical power from a 110 GHz IMPATT diode with a horn was coupled into the finline, which, when mounted in free space, behaves like a Vivaldi antenna, loaded on one side by the dielectric substrate. The output of the IMPATT diode was modulated at 127 Hz, and the bolometer response detected at three levels of signal power. The measured total voltage noise is shown as a function of bias voltage in Figure 3.16, and the optical response versus bias voltage is shown in Figure 3.17 [78, 79].

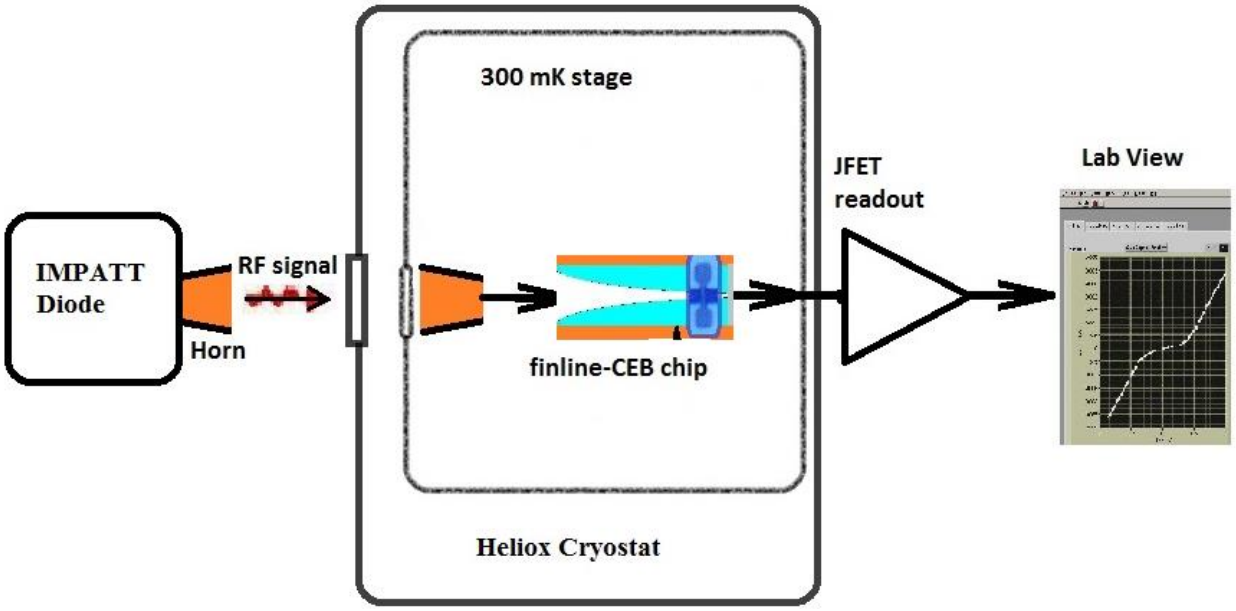

Figure 3.14. The experimental setup schematic. RF signal from IMPATT diode illuminates the finline-CEB chip through the cryostat window; the response is then measured by JFET readout.

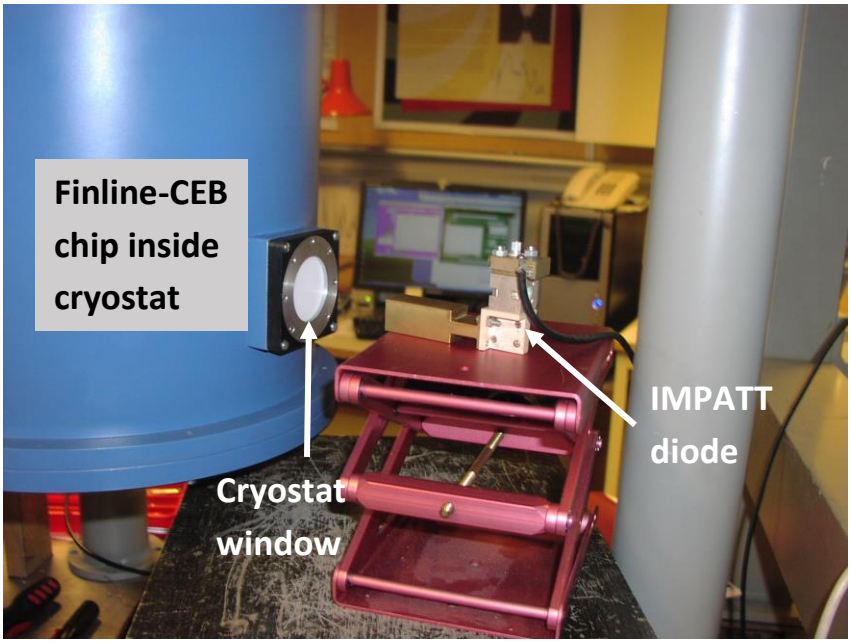

Figure 3.15. IMPATT diode source irradiating sample at 110 GHz through optical window [78, 79]

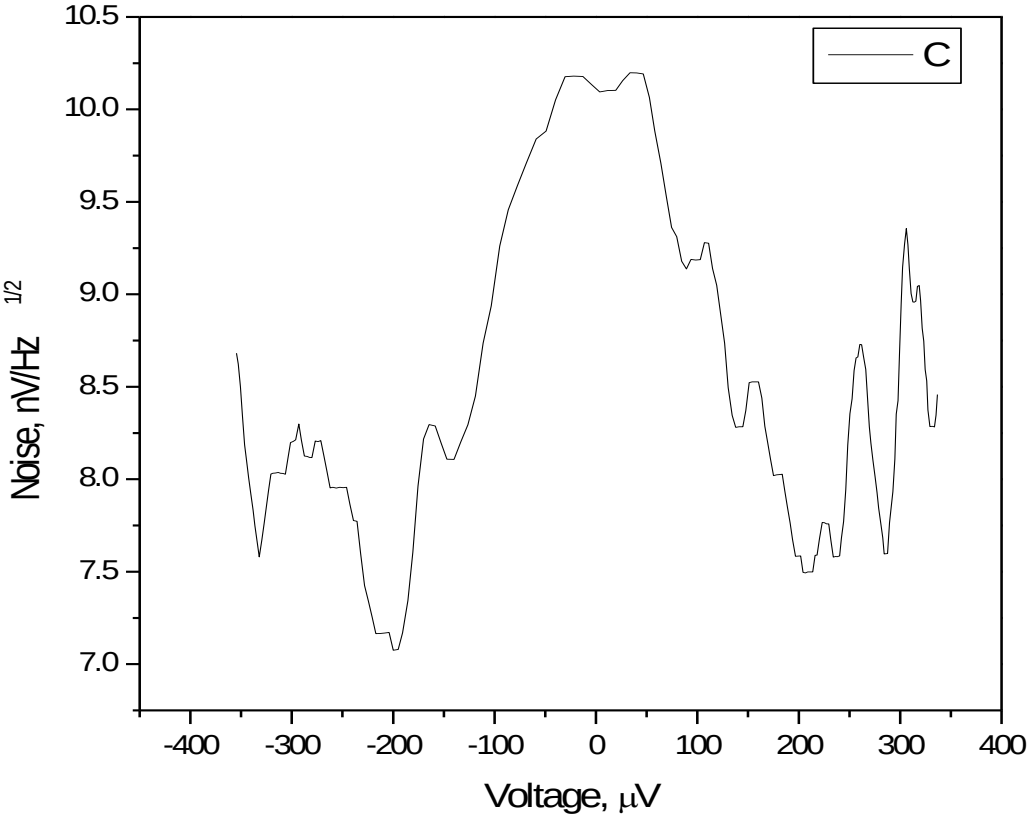

Figure 3.16. Noise of CEB at 127 Hz, measured with a room-temperature amplifier box [78, 79].

Taking into account the above experimental data we will first estimate the dark NEP. The voltage response is

$$S_V = \frac{dV}{dP} = \frac{dV}{dT}/G \tag{3.16}$$

where G is the total thermal conductivity. The thermal conductivity due to electron-phonon interaction is given by $G_{e\text{-}ph}=5\sum\Lambda T^4$. Another component of thermal conductivity is due to thermal flow by electrons:

$$G_i = \frac{dP}{dT} = \frac{d}{dT}\left(k_B T \frac{I}{e}\right) = \frac{k_B I}{e} \tag{3.17}$$

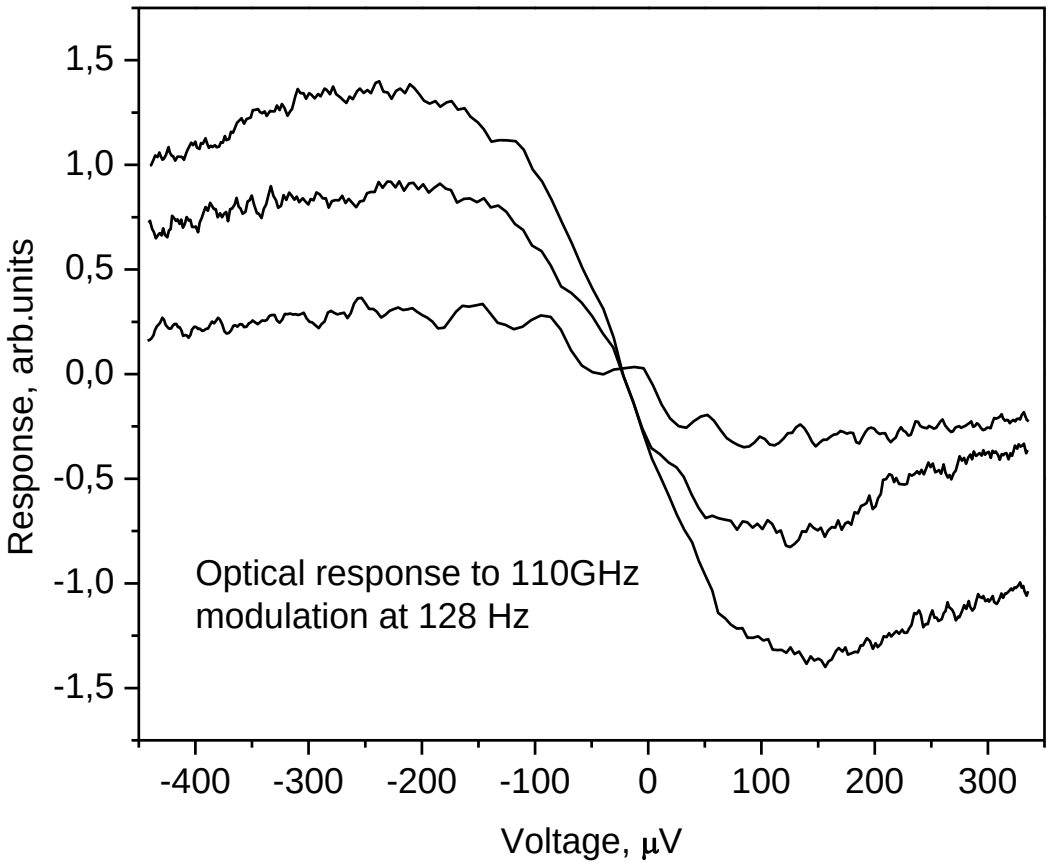

Figure 3.17. Voltage response of the bolometer to the incoming signal at 110 GHz at three levels of the signal power. After attenuation, the incident RF signal power is estimated to be around ~20 pW, with additional attenuation of 0 dB, 3 dB and 6 dB, displayed in the three different curves in the figure. The actual RF power was not measured exactly in this experiment.

For the sample with two SIN tunnel junctions of 1.5×1.5 μm^2, absorber thickness of 50 nm, volume of absorber is $\Lambda = 2 \cdot 10^{-19}$ m^3, material parameter $\sum = 3 \cdot 10^9$ Wm^{-3}K^{-5} for copper, at a bath temperature of 280 mK the thermal conductivity due to electron-phonon interaction can be estimated as $G_{e\text{-}ph} = 1.84 \cdot 10^{-11}$ W/K. At bias current of 20 nA the thermal conductivity due to the thermal flow by electrons will be $G_i = 1.6 \cdot 10^{-12}$ W/K, which yields a total thermal

conductivity of $2 \cdot 10^{-11}$ W/K. Using Eq. (3.16), for the experimental value of dV/dT = 0.5 μV/mK we obtain $dV/dP = 2.5 \cdot 10^{7}$ V/W. The NEP of our device can then be estimated using this value and the voltage noise v_n:

$$NEP = \frac{v_n}{dV/dP} \tag{3.18}$$

Taking the maximum experimental value for bolometer output noise of 10 nV/Hz$^{1/2}$ (including the amplifier noise) and temperature response 0.5 mV/K we can get an estimate

$$NEP_{ibias} \approx 5 \cdot 10^{-16} \text{ W/Hz}^{1/2}.$$

This is an encouraging value, considering the readout system used in this experiment. It demonstrates for the first time that the finline CEB operates as a sensitive bolometer. For a reduced absorber volume and in the voltage bias mode with SQUID readout the dark NEP of CEB should have much lower levels.

3.3.5. Calibrated measurements of RF response with power load

In this section, we describe our experiments with the CEB-finline integrated circuit (IC) mounted in a copper block with 97 GHz waveguide and connected to the external wires using bondwires. A black body radiation source was used inside the cryostat as an internal RF source for this experiment.

a. RF block with 97 GHz waveguide

The RF block for the CEB devices tested at Oxford was fabricated in the Oxford Physics workshop. The block was made of oxygen-free copper, with a waveguide groove for mounting a finline chip. A photograph of the RF block is shown in Fig. 3.19, and the layout with the

dimensions in Fig. 3.18. The rectangular waveguide has a cross-section of 1.27 × 2.54 mm and the chip groove is 1.87 mm wide, to fit the finline chip.

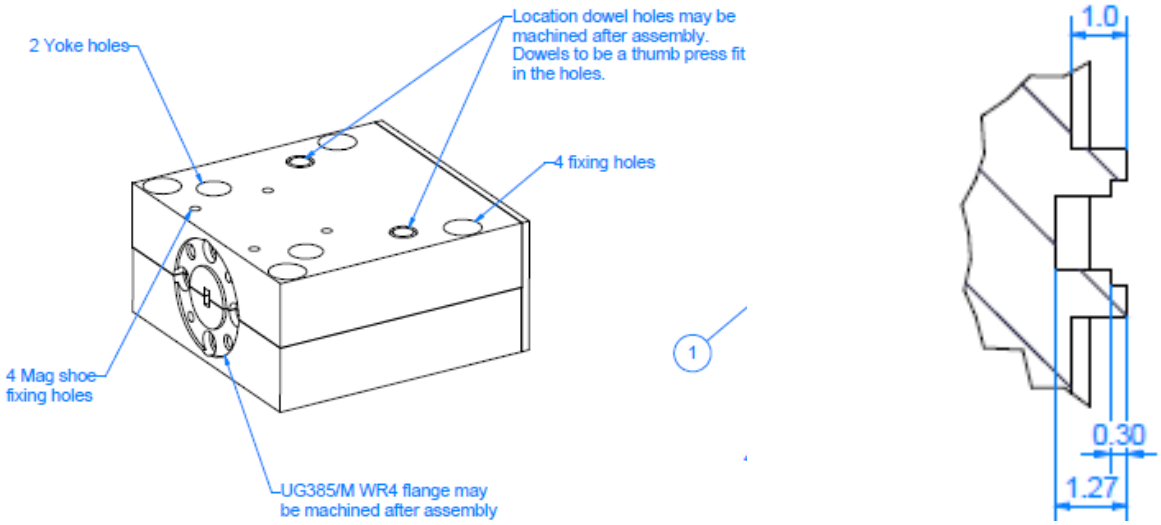

Figure 3.18. The layout of the RF block with the waveguide

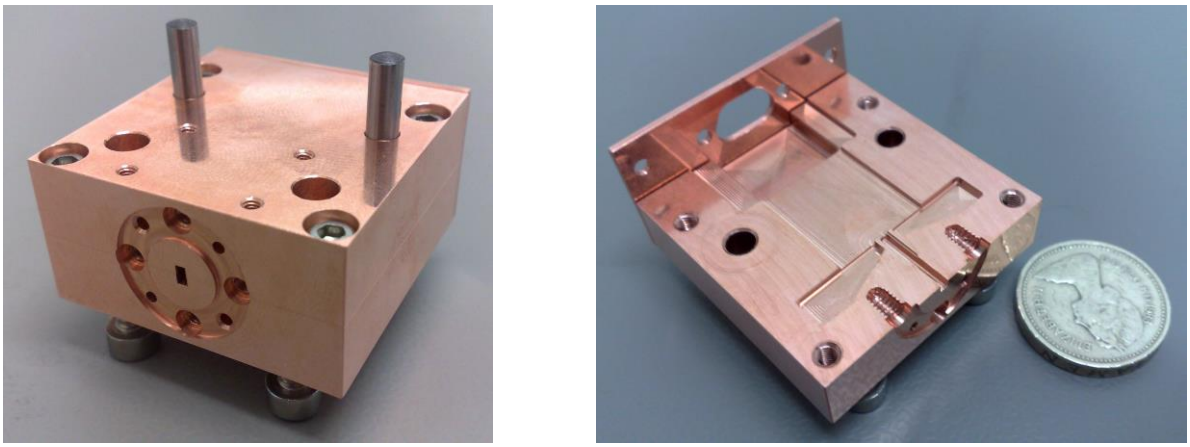

Figure 3.19. (Left) A photo of the 97 GHz waveguide block [78], (Right) Lower half of the block [79].

The chip with a CEB-finline integrated circuit was then mounted in the waveguide and attached using a wax called crystal bond. Bondwires were then attached to the finlines using a bonding machine, in order to connect the finlines to the DC readout electronics, as shown in Figure 3.20. A horn was then connected to the waveguide input window, for focusing the incoming RF signal onto the waveguide input.

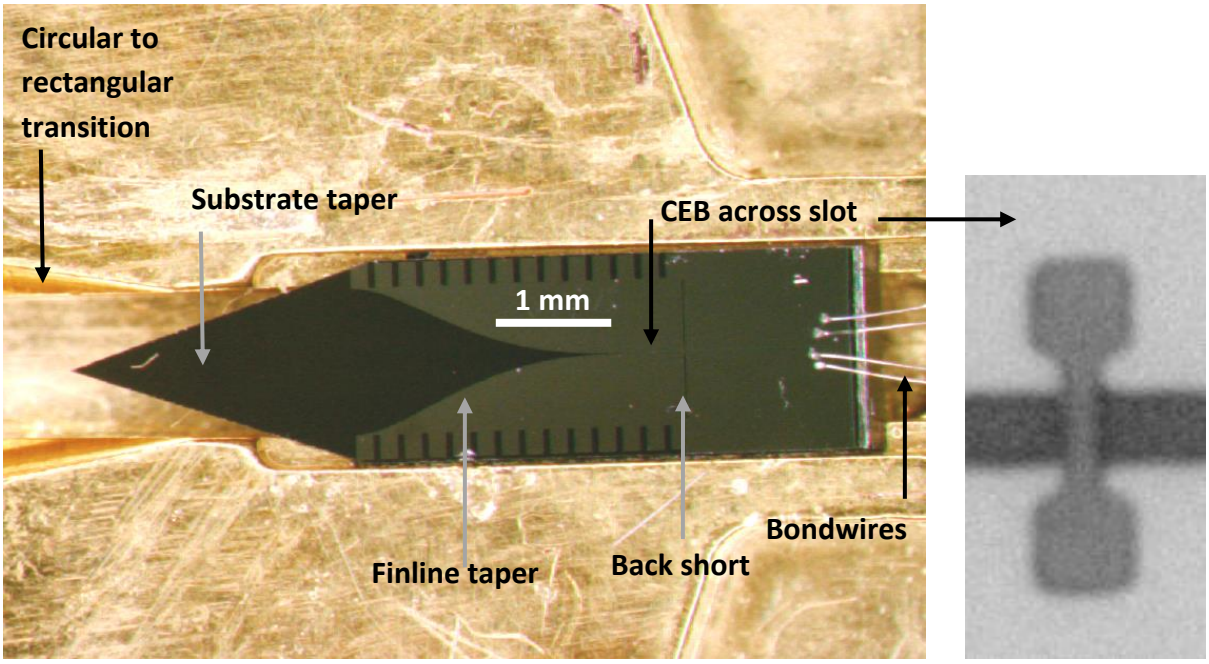

Figure 3.20. Photo of a 97 GHz finline-CEB IC mounted in the waveguide and bonded; (inset): enlarged CEB device across the slot.

b. The black body source

In this experiment, a variable temperature black body source (called here "Power load") was fabricated in the form of a cone to focus the radiated signal onto the RF horn input. The concave surface is about 30 mm in diameter and was covered by a black material with 99%

emissivity. The source was equipped with a heater made of a copper coil that heats the concave object when a current flows through it. The heating power could easily be controlled by adjusting the applied voltage and thus the power dissipated in the copper coil.

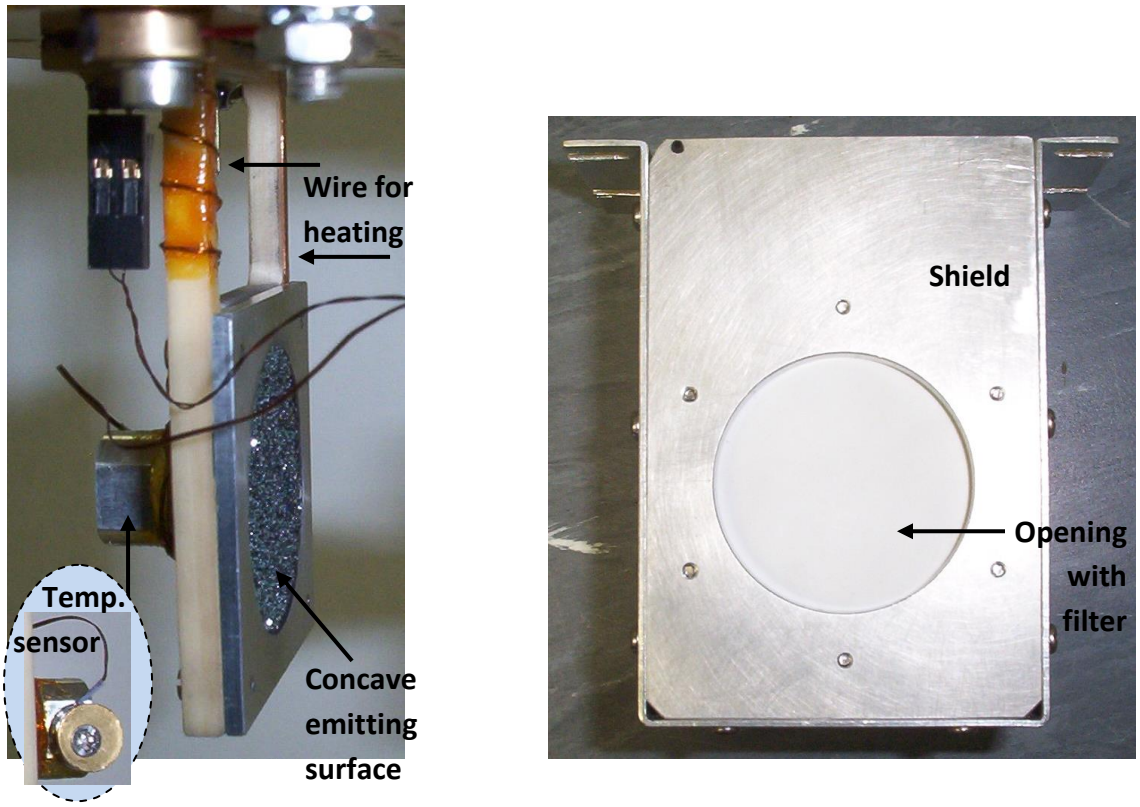

Figure 3.21. Black body RF power source (Left) with a cover (Right). A temperature sensor is mounted on the back side (inset), coupled to electronics through wires. The black connector on the top feeds the heating current into the power source.

The power load was also equipped with a temperature sensor connected to the readout electronics with feedback loop. This allowed setting a required temperature in a range between 3 K and 25 K and controlling it by measuring the actual temperature and adjusting the applied voltage correspondingly to the required temperature. The photo of the power load

is shown in Fig. 3.21, with a shield that was used for protection from excessive irradiation. The shield was made of Al and it has a window that is facing the waveguide horn.

c. Description of the experiment and results

In this experiment which was carried out at the Oxford University, we employed calibrated measurements of RF response of a finline-CEB device irradiated by a blackbody source at variable temperature, mounted inside the cryostat (described in the previous section). The CEB performance was tested in a ^{3}He sorption cryostat, at a bath temperature of 310 mK.

DC IV curves were measured in the current bias mode, and optical response was measured by irradiating samples with a microwave signal from the black body source mounted inside the cryostat. The finline chip with the CEB device was mounted in a waveguide block and connected to the readout system by bond wires. The RF signal from the power load was focused onto the waveguide input via a horn (see Fig. 3.22 and Fig. 3.23). The horn input was placed at a distance of 2 cm from the 30-mm RF source.

The signal response was measured by comparing different IV curves in current-biased mode at different RF source temperatures (Figure 3.24). A response of up to 155 μV was obtained as voltage difference at the same bias current from the IV curves for 5 and 20 K black body source temperatures (Figure 3.25). The corresponding value for 7 K and 10 K respectively was 40 μV. Based on this, the voltage to power response could be estimated using the Planck formula for given source temperatures (Eq. 3.19, later in this chapter).

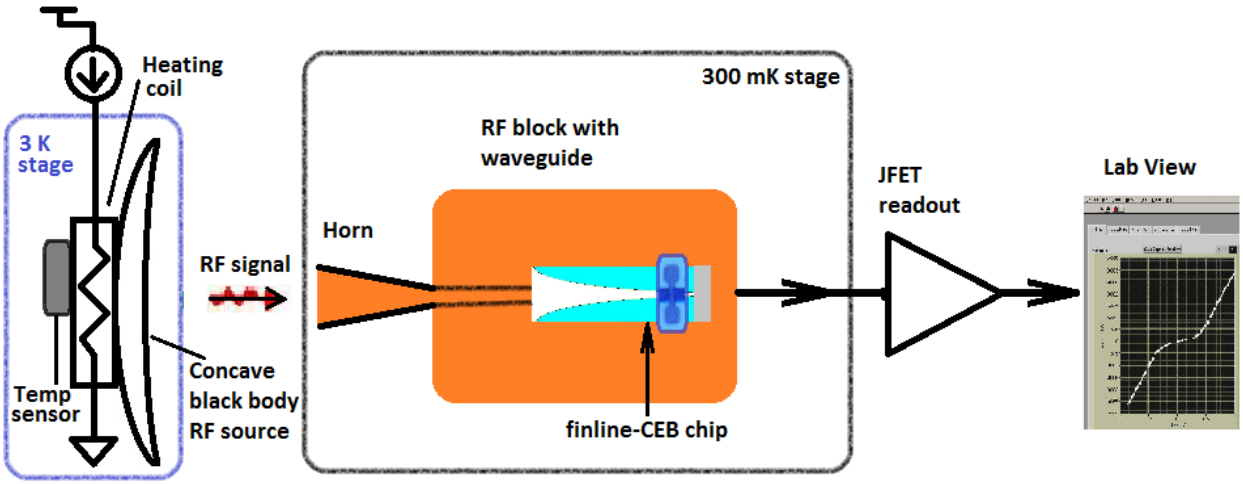

Figure 3.22. Schematic of the experiment. The RF signal is emitted by a controllable RF source and focused onto the waveguide input and detected by the CEB device mounted in the waveguide.

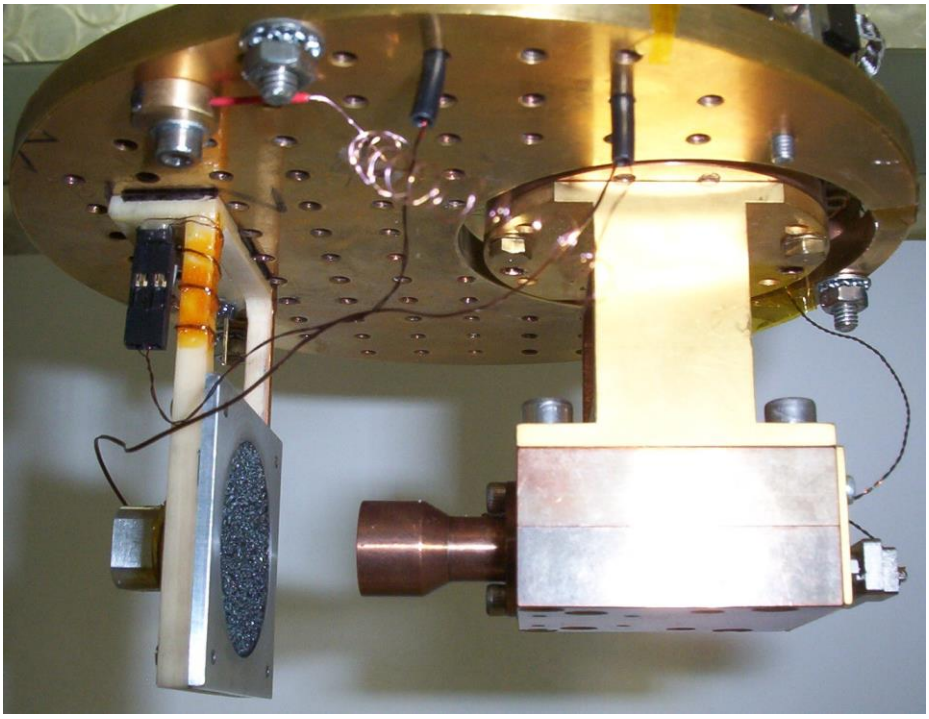

Figure 3.23. Photo of the setup: detector block with CEB device on the cold stage (300 mK), and power load on the 3K stage inside the cryostat.

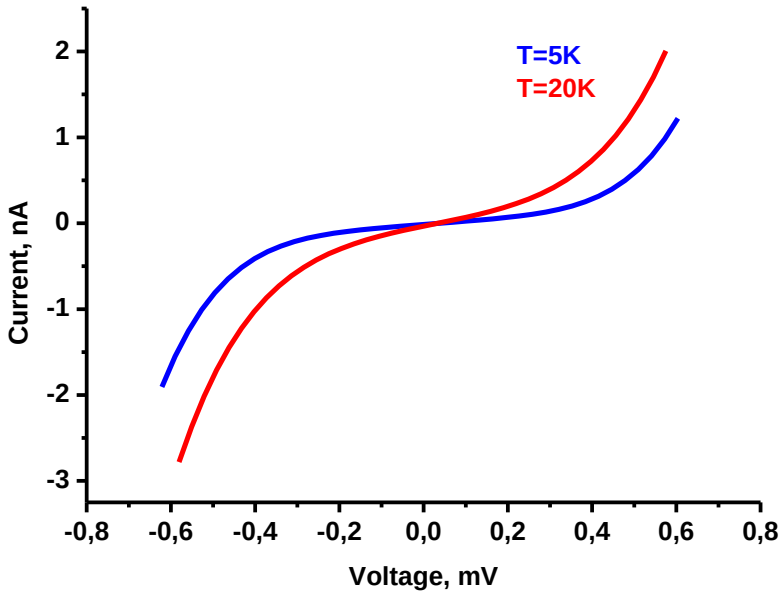

Figure 3.24. IV curves of the CEB in the waveguide at power load temperatures of 5 and 20 K

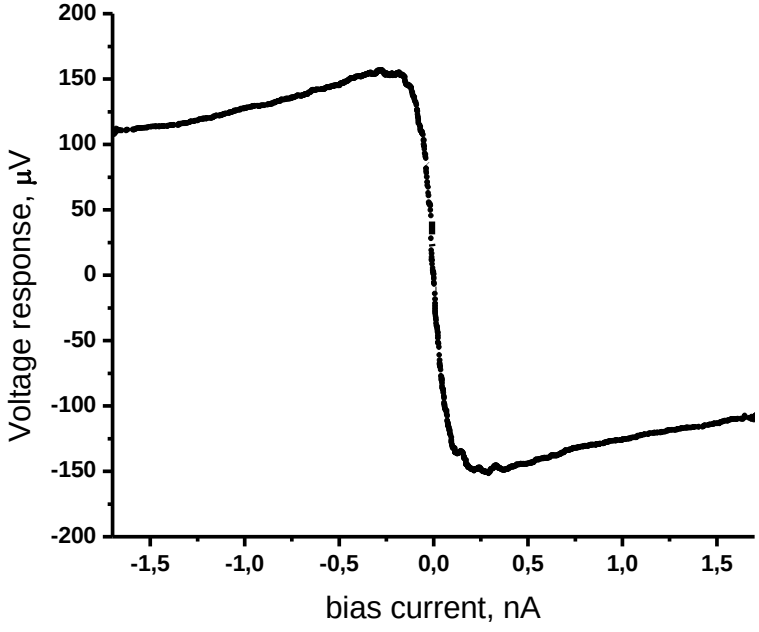

Figure 3.25. Voltage to RF signal response versus biasing current, for 5 to 20 K RF source temperature difference.

3.3.6. Analysis of the measured results.

The voltage to power response obtained by subtracting IV curves at the temperatures of 7 K and 10 K versus bias current is shown in Fig. 3.26. A maximum voltage response of 40 μV can be observed in this curve.

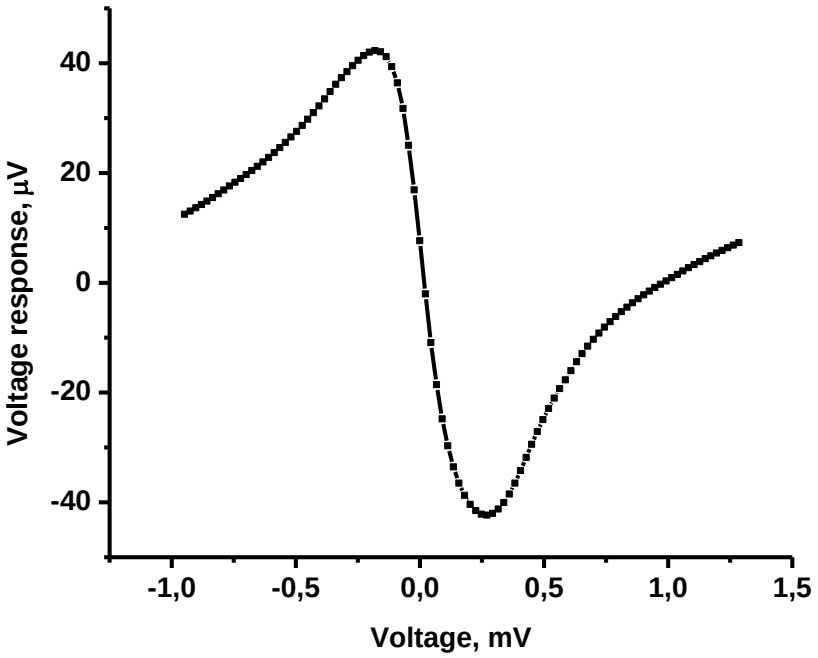

Figure 3.26. Voltage response to the incoming power versus bias voltage, 7 K and 10 K temperature

Simulations performed using HFSS software showed the effective bandwidth of the finline chip in the waveguide to be around 34 GHz (Courtesy Dr. Boon Kok Tan). The HFSS setup used for these simulations and the normalized transmission are shown in Fig. 3.27. The result

obtained is consistent with the fact that the waveguide operates as a band-pass filter that does not accept lower frequencies, determined by the waveguide dimensions, while high-frequency components are not matched with the finline impedance at the interface between the waveguide and the finline. In addition, high-frequency modes are filtered out by finline notches, see Figure 3.7 (top).

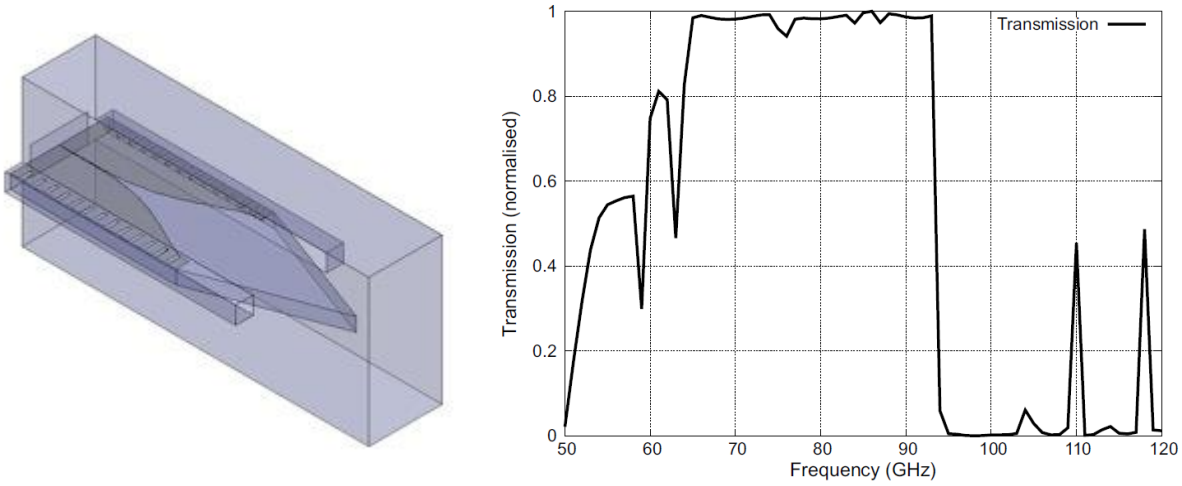

Figure 3.27. HFSS setup used for bandwidth estimation and the normalized transmission (Courtesy Dr. Boon Tan)

For a frequency range around the frequency of f = 78 GHz with a bandwidth of δf = 34 GHz, the power emitted by a black body at a temperature of T = 10 K is given by:

$$\delta P = \frac{\kappa \cdot hf \cdot \delta f}{\exp(hf / k_B T) - 1} = 3.87 \times 10^{-12} \text{ W}, \tag{3.19}$$

assuming the emissivity of the black body source κ = 1, where h is Planck's constant and k_B is the Boltzmann constant.

The corresponding power for 7 K is 2.5×10^{-12} W. Subtracting the calculated power values at source temperatures of 10 K and 7 K yields $\Delta P = 1.37\times10^{-12}$ W. Taking a voltage change of 40 μV for this power difference, we obtain:

$$S = dV/dP = \Delta V/\Delta P = 2.92\times10^{7}\ \text{V/W}\ , \tag{3.20}$$

The total voltage noise measured in this experiment was v_n = 11 nV/Hz$^{1/2}$ so we can obtain the optical NEP by dividing this noise value by the voltage to power response:

$$NEP = \frac{v_n}{dV/dP} = v_n/S = 3.76\times10^{-16}\ \text{W/Hz}^{1/2},$$

which is an excellent result for the first CEB in a waveguide.

We would like to emphasize that that the above quoted value is only a good estimate. While the connection from the RF source to the finline-CEB chip contains several interfaces, the coupling all the way from the source to the chip was still assumed to be ideal.

Regarding fabrication, a straightforward and robust technology was chosen for the production of these devices. This was a reasonable choice for developing this experiment, in that it allowed us to demonstrate the full functionality of the CEB device. It also allowed us to demonstrate the CEB-finline integrated circuit, complete with waveguide and horn, as a feasible design, for the first time.

However, our fabrication methods were not optimized in terms of device performance. The trilayer fabrication technology used for manufacturing these devices, did not allow for a thin and narrow absorber. Thus, the volume of the absorber was not chosen for best responsivity.

Therefore, the performance of our devices could be improved by using advanced technologies that currently are being developed. Future improvements will also come from advanced read-out schemes, including low-temperature readout amplifiers combined with measurements in voltage-biased mode, which are also currently under development.

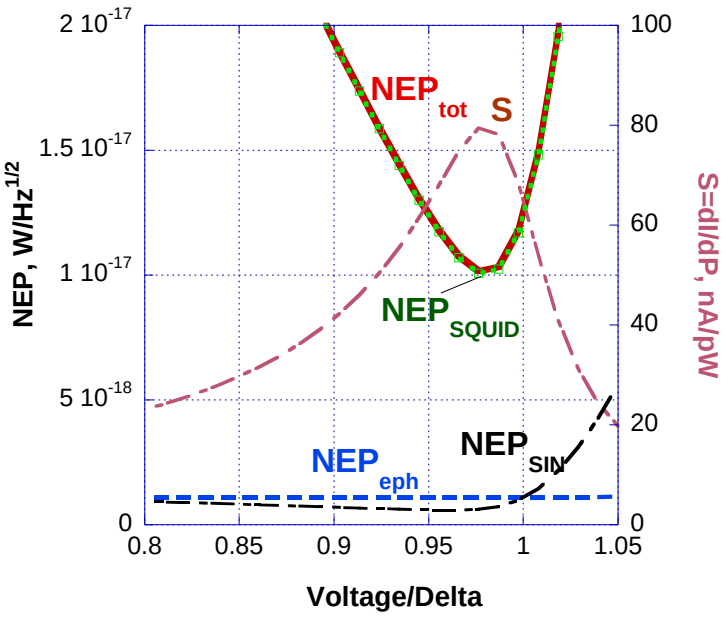

Figure 3.28. Simulated NEP components and responsivity S for improved parameters of the CEB, power load of 20 fW, and SQUID noise current of 0.8 pA/Hz$^{1/2}$ [46, 78, 79].

For a bolometer with reduced volume of absorber and in the voltage bias mode with SQUID readout the dark NEP of CEB should achieve rather promising levels, down to ~10^{-18} [46, 56]. In Fig. 3.28, the calculated NEP and current responsivity are shown, which are anticipated for a device which happens to have responsivity a few times better than the estimated value for our measured device. These results were obtained by simulation using CEB models, assuming a certain noise when using SQUID readout [46]. For most of the practical cases the NEP will

be determined by a background power load, about P_{bg} = 5 pW, and for a frequency of 100 GHz it corresponds to

$$NEP_{phot} = \sqrt{2P_{bg}E_{quant}} = \sqrt{2P_{bg}hf} = 2.4\cdot10^{-17}\ \mathrm{W/Hz^{1/2}}.$$

Therefore, our goal is to be able to detect signals of the above order of magnitude. Our measurement results demonstrated that we approach the required level in our development.

3.4. Conclusions

In this chapter, we presented the general theory of SIN tunnel junctions and CEB devices, focusing on the analysis of a Cold-Electron Bolometer, deposited across a unilateral finline on a planar substrate. This detector is a potential candidate for upcoming space cosmology missions and is also of interest to ground-based experiments. This is due to its simplicity of integration in planar circuits, as well as its high saturation power and fast response, combined with low NEP values.

We have fabricated a finline-coupled CEB device using direct-writing of the detector structures. We have demonstrated a successful operation of a CEB device by measuring its DC and RF characteristics. Furthermore, we have estimated the dark noise equivalent power for the devices in the current biased mode operating at 300 mK and read out by room-temperature op-amps as NEP = $5\cdot10^{-16}$ W/Hz$^{1/2}$.

We have also measured the detector's optical response by focusing an RF signal onto the waveguide input using a horn. The voltage to RF power response was obtained, and the

analysis of the results was performed. The preliminary estimated optical NEP ~4×10^{-16} $W/Hz^{1/2}$ is approaching the requirements of CMB polarisation measurements. This value can be improved by improving the optical coupling and readout electronics. Another improvement by a factor of 10 should be possible by the employment of smaller volume absorber and further modification in the fabrication technology. To the best of our knowledge, this is the first finline-integrated CEB device in a waveguide ever reported. Further development of the design using advanced technologies and readout schemes should yield future improvements in the device performance.

Chapter 4

Advanced technologies for CEB integrated in planar antennas

The devices and receiver systems considered so far employ on-chip finlines coupled into waveguide systems with horns which is a standard solution for millimetre-wave receivers. The advantages of corrugated and dual-mode horns are characterised by high coupling efficiency, low losses and low cross-polarisation levels with both types being used extensively at frequencies up to 300 and 500 GHz respectively [81]. This is still a rather expensive solution, mainly due to difficulties in fabrication. At the same time, the bolometric devices presented in this thesis are fabricated on-chip using electron-beam and photo lithography, so it seems attractive to integrate antennas and devices onto the same chip and if possible fabricate them in one fabrication run. Planar antennas in combination with quasi-optical coupling schemes [81, 82] have been used since the mid-70s when the first experiments took place [82, 83] and have become increasingly widespread for high-frequency applications during the last decades.

This approach has certain advantages compared to coupling using waveguide systems, such as simpler and cheaper fabrication procedures, better accuracy and control over dimensions, as well as the option of integrating with large arrays on the same chip [81, 82].

In this chapter we will discuss SIN tunnel junctions and CEB devices integrated in planar antennas that were fabricated using methods different to the trilayer technology considered in the previous chapters. We will also analyze CEB performance, including experimental results. First, we consider the design of the CEB detectors and then present experimental results on the testing of CEBs comprising a thin Ti film absorber and two SIN junctions integrated in planar antennas, such as log-periodic antenna and double dipole antenna. We will describe the experiments for testing these CEB devices, including DC tests and RF experiments performed using a thermal power load inside the cryostat. The CEB performance was tested in a ^{3}He sorption cryostat HELIOX-AC-V at bath temperatures of 280 to 305 mK. The optical response was measured using the hot/cold load method by flipping a Cu reflector opposite a blackbody surface inside a 3 K shield and using a thermal source with variable temperature.

Next, we will describe the CEB array concept and the CEB devices that we fabricated for the Boomerang project using an advanced shadow mask technique and the experiments we ran for testing these CEB devices. This includes: (i) DC tests including IV curves and voltage response to the DC power dissipated in the absorber; (ii) RF experiments performed with an external RF source, and (iii) calibrated RF testing using a thermal power load inside the cryostat and a rotating holder with different source temperatures.

4.1. Titanium-based CEB device

It has already been shown in the previous sections that the CEB performance is strongly determined by the properties of the SIN junctions as well as the CEB layout. The volume of the absorber determines the CEB's sensitivity due to the principle of operation of bolometric detectors. An absorber with a large volume limits the sensitivity and the overall performance of the CEB. It is therefore very desirable to make the absorber as thin as possible, which is not quite feasible with the technologies described in the previous sections, such as the trilayer direct-write technology. This is because in that process, the absorber is deposited on the top of the superconducting Al layer, which results in a bigger absorber compared to the case when the absorber is deposited prior to the superconducting electrode. Therefore, very thin and narrow absorbers cannot be fabricated using the trilayer technique. For instance, depositing a copper absorber with subsequent oxidation prior to the superconducting electrodes is not feasible in this process because natural copper oxide is not robust enough for making tunnel junctions. In addition, after creating the tunnel junctions, the temperature at which the resist for absorber patterning should be baked is limited; this temperature should not exceed 140 ºC, which reduces the resolution of the lithography and therefore limits the minimum size of the absorber fabricated using this method. Now, we shall describe a novel approach that allows us to overcome these limitations.

4.1.1. The concept of the Ti-based CEB

To optimize the CEB performance, new technologies have been explored [36, 38], including the employment of titanium-based CEB devices as an alternative to Al-based structures [38].

This is a novel direct-write technology for fabricating Ti-TiO_2-Al tunnel junctions for bolometer devices and thermometry applications [38, 45]. The goal of this method was to develop a simple and efficient technology for fabrication of SIN tunnel junctions between Ti and Al with TiO_x as an insulating barrier. The key advantage of this technology is the deposition of a normal Ti film as a bottom electrode and the superconducting Al film on the top of it after creating a TiO_x insulating barrier by *ex-situ* oxidation of Ti. The process consists of two steps: first the Ti film is formed and oxidized and then the Al counter-electrode is deposited and patterned. The fabrication procedure was described in detail in Chapter II and shown in Fig. 2.12.

The approach described here allows for an absorber thickness down to 5 nm since the absorber is deposited prior to the superconducting counter-electrode and the tunnel junction is created after the absorber has been deposited. This is possible due to the use of TiO_x as an insulator for the tunnel barrier that is created by natural oxidation of Ti that is deposited as the first layer. Another advantage of this method is the ability to realize a fully flat absorber with no bending parts, which are inevitable in other processes and create leakage currents that degrade the high-frequency properties of the RF detector. Since the absorber is patterned before creating tunnel junctions, we have no limitation on the width of the absorber related to lithography resolution due to limited resist baking temperature.

4.1.2. Fabrication and chip layout

The devices described here were fabricated by the author of this thesis using photo-lithography and the technology for fabricating tunnel junctions proposed by L. Kuzmin [38].

The procedure uses *ex-situ* Ti oxidation for the creation of the TiO_2 insulating barrier, and the fabrication process is described in detail in Chapter II. Some example devices and structures with SIN junctions fabricated in this way are shown in Fig. 4.1 [84].

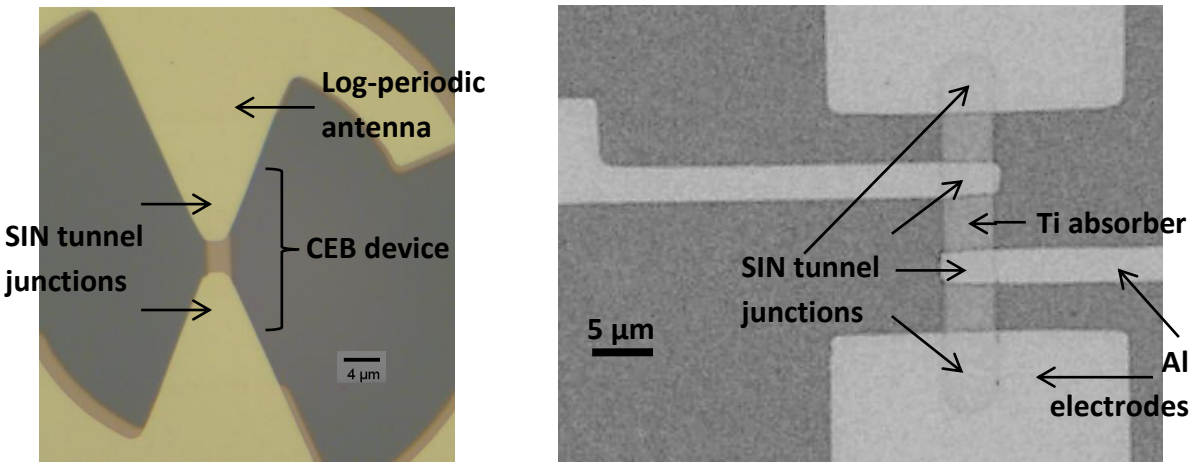

Figure 4.1. Optical images of a CEB fed by a log-periodic antenna (left) and a 4-junction bolometer structure (right) fabricated in the Ti technology [84].

Due to the oxidation temperature of 130 to 150 ˚C one can expect better quality of the junctions than the ones created at room temperature when the molecules of water and/or hydrogen atoms take part in creating the tunnel barrier. One of the key points of *in situ* evaporation is the deposition at a very low pressure and oxidation at the same low base pressure. This results in the influence of water and hydrogen being mostly eliminated, apart from contaminations and other issues, which deserve a separate discussion. In our process, the temperature exceeds the water evaporation temperature, which ensures absence of hydrogen in the vicinity of the tunnel barrier. As for other sources of contamination such as residues of organic materials which can degrade the quality of the tunnel barrier, these can be eliminated

by oxygen plasma etching followed by subsequent ion milling. This completely removes any compounds of Ti and other elements, built on the surface. Measurements have shown that this step is very critical in the whole fabrication procedure as the quality of the tunnel junction strongly depends on the process time of ion milling. If this time is not long enough, say below 4 minutes at ion gun voltage of 500 V, the quality of the tunnel barrier is very poor. Increasing this time up to 5.5 minutes or longer at the same ion gun voltage assures a complete removal of any substances from the surface which would degrade the quality of the tunnel barrier.

The chip layout of the devices presented here includes CEB devices integrated in a double dipole antenna (Fig. 4.5) and is optimized for measurements in the 100 GHz frequency band around the central frequency of 300 GHz while CEB devices integrated with a log-periodic antenna (Fig. 4.1, left) are for measurements at frequencies between 30-150 GHz. Both dipole and log-periodic antennas were fabricated on a Si wafer oxidized thermally to form a 400 nm thick SiO_2 layer.

Double dipole antenna design and characteristics are considered in detail in [48], and a general layout is shown in Figure 4.2 [48]. A double dipole antenna is a simple and widely used class of planar antenna [82], consisting of two bilaterally symmetrical conductive elements (Figure 4.2) that in our case are made from thin metal films deposited on a Si substrate. The signal incident on the receiver is taken as a differential signal between the two halves of the antenna [48], unlike monopole antennas which receive single-ended signals between a conductor and a ground. Double dipole antennas are resonant elements, with standing waves between the two halves of each element. The length of the elements in the antennas is determined by the

wavelength to be received: in a half-wave dipole, each half of the two elements is about 1/4 wavelength long, so the whole antenna is a half-wavelength long [48].

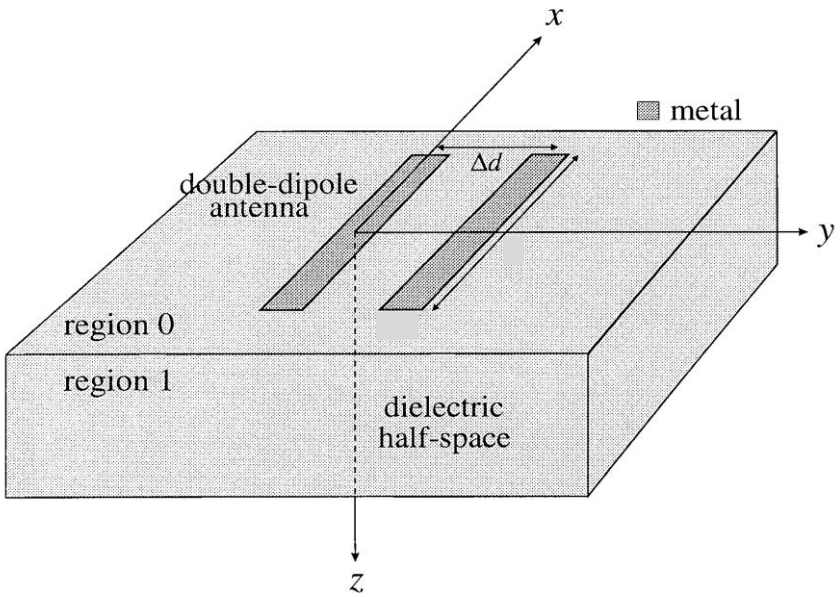

Figure 4.2. A general layout of a double dipole antenna made of 2 thin metal film elements deposited on a dielectric substrate [48].

Log-periodic antennas are broadband narrow-beam antennas with regularly repeating characteristics as a logarithmic function of the radio frequency received. This is achieved by designing the layout of the elements of a log-periodic antenna in such a way that their lengths and the spacing between them increase logarithmically from the interior part to the exterior one (see e.g. the antenna in Figure 4.3). As a result, the input impedance depends as a function of logarithm on the incident signal frequency. This approach is used for high-frequency applications when a wide frequency range is desirable and at the same time narrow beam is of interest. The log-periodic antennas used in our design are dipole elements driven by a balanced (differential) signal between the two halves of the antenna, see Figure 4.3.

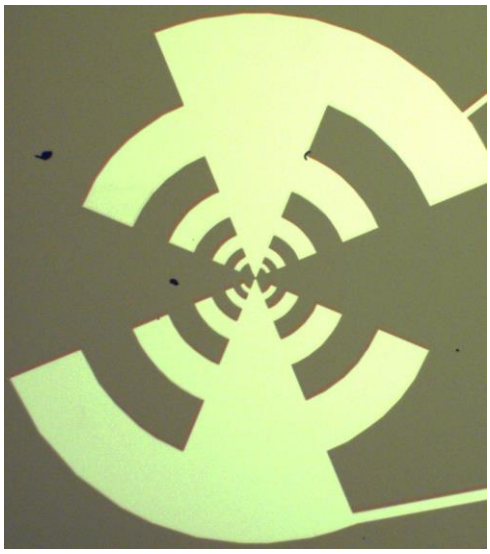

Figure 4.3. An optical image of a log-periodic antenna, fabricated for feeding a CEB device.

A photograph of a test CEB device comprising a bolometer integrated into a 4-probe structure is shown in Fig. 4.1, right. The device consists of an absorber and 4 tunnel junctions connected to 4 wires for measurements by 4 points. Our mask design allowed the fabrication of 24 chips, 7×7 mm each, on a single 2-inch Si wafer.

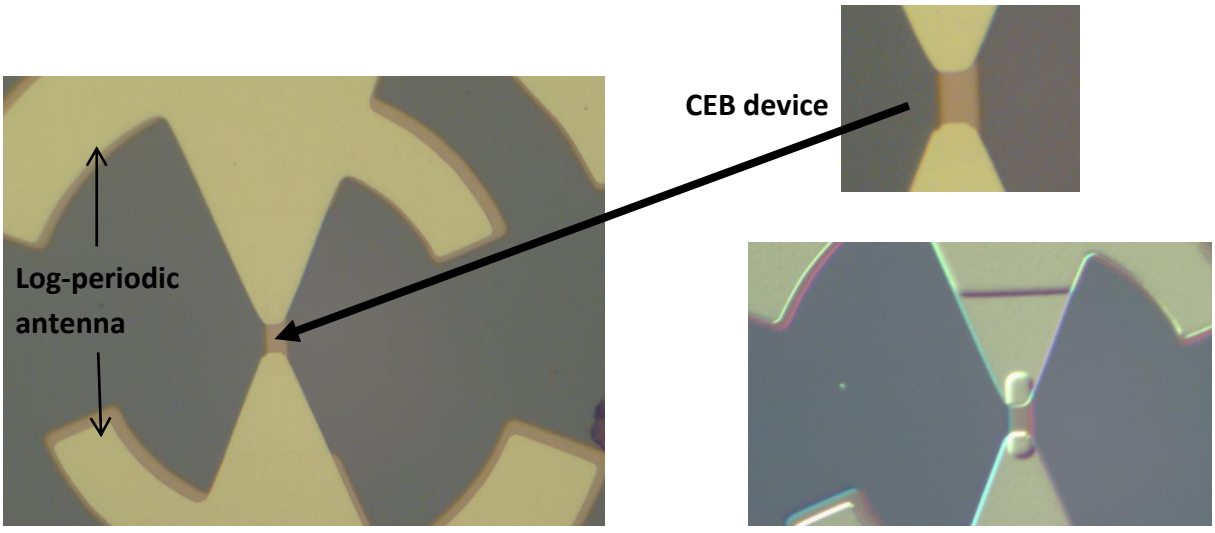

Figure 4.4. Optical image of a CEB detector with log-periodic antenna:
a plain photo (Left) and a quasi-3D picture (Right) [84].

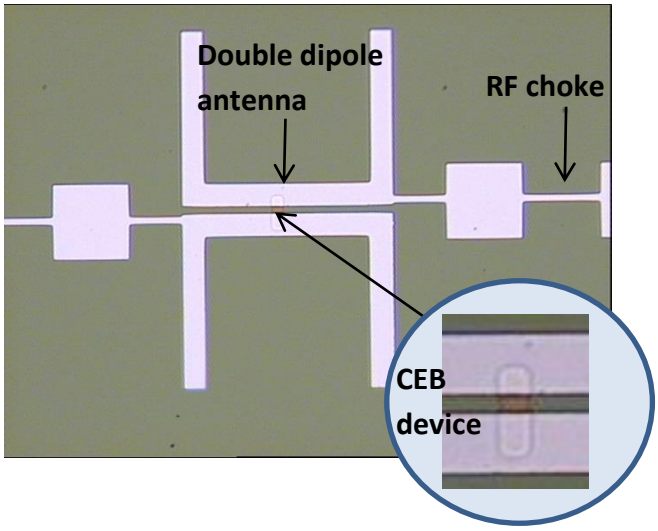

Figure 4.5. Photo of a CEB detector fed by double-dipole antenna designed for 280-350 GHz, connected through an RF choke for filtering out high frequency components from the DC path [84].

4.1.3. Experimental results and analysis

CEB devices fabricated with Ti-TiO_2-Al tunnel junctions and integrated in log-periodic antennas or double dipole antennas were measured at temperatures of 280-310 mK using the HELIOX AC-V cryostat manufactured by Oxford Instruments. DC testing was performed in current bias mode using a bias resistance of 20 MΩ to 2 GΩ (see Figure 3.10). Ti was not superconducting in this temperature range, and the tunnel junctions showed typical behavior of SIN junctions. An example IV curve of a single SIN tunnel junction is shown in Fig. 4.6. Both the dynamic resistance at zero voltage R_d and the normal resistance R_n were measured, and ratio R_d/R_n was estimated, as a measure of quality of the tunnel junctions. Measurements have shown high quality of fabricated tunnel junctions along with low leakage currents, as ratios R_d/R_n of up to 1000 were achieved at 280-300 mK. This value is comparable to

previously reported results for Al-based tunnel junctions fabricated using the shadow-evaporation technique [54, 63].

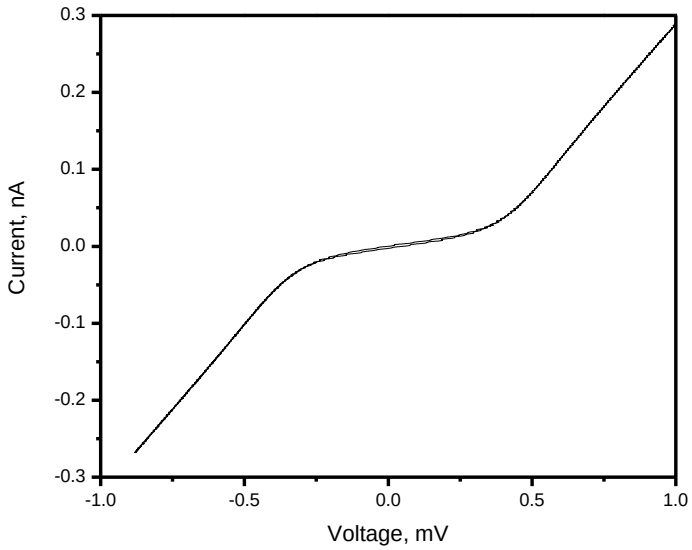

Figure 4.6. IV curve of a single SIN tunnel junction fabricated with Ti-based technology.

The temperature response of the device was obtained by measuring the voltage response to the bath temperature in the cryostat at temperatures of 300 to 800 mK. A dV/dT value of 1 mV/K was achieved for two junctions in series, which corresponds to 0.5 mV/K for each junction. Increasing number of junctions in series yields higher sensitivity [36, 58], which enhances the potential of using of SIN tunnel junctions fabricated in this technology for measuring the on-chip temperature and the RF power.

It has already been shown [36, 58] that a total voltage response of a series array of SIN tunnel junctions at fixed biasing current is proportional to the number of junctions, whereas the noise

of the junctions should be proportional to the square root of that number. Therefore, by increasing the number of junctions in the array, one can increase temperature sensitivity of the whole array. This was fully confirmed for an array of 100 Al-based tunnel junctions in our work [36], where a dV/dT of 52 mV/K has been achieved for 100 junctions in series, which in turn corresponds to 0.52 mV/K for each single junction.

Noise voltage spectra were also measured using a room temperature MOSFET readout amplifier together with a lock-in detector to observe a voltage noise down to v_n ~10 nV/Hz$^{1/2}$. Based on DC testing, a dark Noise Equivalent Power (NEP) can be estimated by measuring the output noise and dividing by a voltage to power response *dV/dP* estimated from *dV/dT* measurements:

$$NEP = \frac{v_n}{dV/dP}$$

Taking dV/dT of 1 mV/K for two junctions in series and a voltage noise of 10 nV/Hz$^{1/2}$ one can estimate dV/dP as ~10^8 V/W, which yields NEP ~ 10^{-17} W/Hz$^{1/2}$. This however is a very rough preliminary estimation based on DC results. More accurate results that were obtained with RF measurements will be presented later in this chapter.

The next step in the testing of the performance of the CEB devices was to measure the optical response using the hot/cold load method. For this, a rotating table carrying a Cu reflector and a blackbody surface inside the 3 K shield of the cryostat was used. Magnets placed on the table allow an external magnet placed outside the cryostat to position either the absorber or reflecting surface in front of the bolometer (Fig. 4.7). The detector chip was mounted across a

waveguide fed by a horn to couple the beam emitted by the black body or reflected by the reflector to the detector antenna. By switching between the reflector and the blackbody source we could change the incident radiation temperature seen by the detector from 3 K to 270 mK and measure the changes in the bias voltage at fixed tunnel current (Fig. 4.8). This is because the reflecting surface reflected radiation emitted by the 280 mK stage when it faced the horn. The measured response for the detector integrated with a double-dipole antenna is

ΔV_{out} = 120 μV.

Temperature responsivity expressed in μV/K is the measure of how much a detector's output changes given a certain RF source temperature change. When a signal is converted to an image representing temperatures, the noise can be measured in terms of the source temperature [83, 85]. This measurement is expressed by Noise Equivalent Temperature Difference (NETD), which is a measure of noise in an image or the equivalent temperature difference of the noise, related directly to the overall quality of an image. The voltage at the output of the detector represents the amount of signal, or temperature, the detector perceives. Higher responsivity results in higher output signal so the signal to noise ratio increases which, by definition, decreases NEDT.

One can calculate the NETD as follows [85, 86]: $NETD = \frac{T - T_B}{S/N}$,

where T is the target temperature, T_B is the target background temperature, and S/N is the signal to noise ratio. In our case, taking 11 nV/ $Hz^{1/2}$ noise and a signal of 120 μV for a temperature difference of ~2.5 K, we obtain NETD = 0.23 mK/ $Hz^{1/2}$.

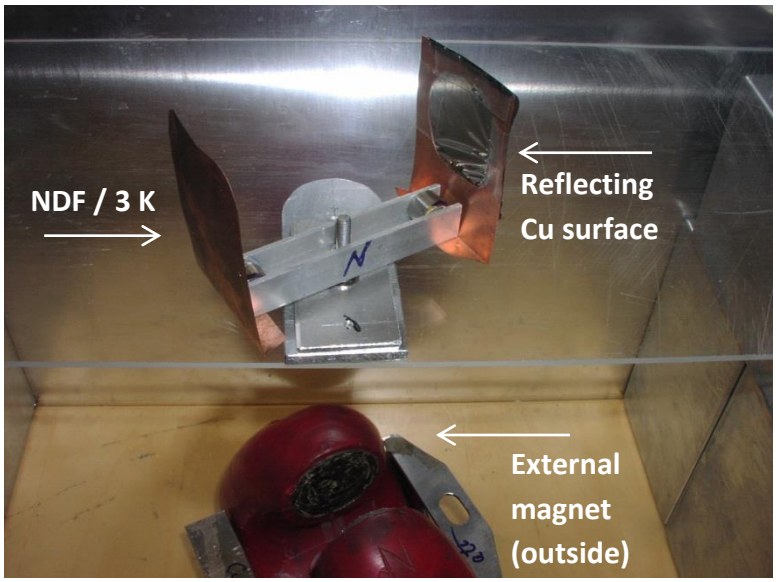

Figure 4.7. Photo of cold rotatable surfaces which were later mounted inside the cryostat at 2.7 K. Below there is a magnet which was used to switch between the Cu shield and NDF in front of the window [55].

The optical properties of a double dipole antenna were studied earlier [87] and verified by our Swedish collaborators using the Hilbert-spectroscopy technique [88]. Based on published data from experimental results, we estimate the bandwidth of our CEB-antenna integrated circuit to be around 100 GHz.

Considering the CEB-antenna integrated circuit as a single mode detector, we can easily calculate the radiation power δP incident on the detector [89]: the power received by 300 GHz antenna with a bandwidth δf =100 GHz, assuming a radiation source temperature of 3 K, gives a radiated power:

$$\delta P = \frac{\kappa \cdot hf \cdot \delta f}{\exp(hf / k_B T) - 1} = 3.8\times10^{-13}\ \text{W},$$

where h is Planck's constant, k_B is the Boltzmann constant, and $\kappa = 1$ is the emissivity of the black body source. Combining this with the maximum measured voltage response of $\Delta V = 120$ μV yields an estimate of the voltage to power response of

$$dV/dP = 3.18 \cdot 10^{8} \text{ V/W}.$$

In this calculation, we neglected the RF power irradiated at 270 mK which is orders of magnitude lower than that at 3 K due to an exponential dependence of the power on the temperature in Planck formula. For the measured dark noise of $v_n = 10 \cdot 10^{-9}$ V/Hz$^{1/2}$ the optical noise equivalent power is therefore:

$$NEP = v_n/(dV/dP) = 3.5 \cdot 10^{-17} \text{ W/Hz}^{1/2}.$$

In the next experiment [84], we employed calibrated measurements of the RF response of CEB device with a log-periodic antenna to RF radiation when illuminated by a variable temperature blackbody source, mounted inside the cryostat. The CEB was tested in a ^{3}He sorption cryostat with a base temperature of 280 mK.

In order to select a frequency band of interest, a bandpass filter [84] was placed between the RF source and the sample. This is a mesh filter with a central frequency of ~300 GHz, fabricated by the author of this thesis at Chalmers University using optical lithography and wet etching of a copper film on a 2-inch in diameter quartz substrate. The photo of the filter is shown in Fig. 4.9.

For measuring the transmission of the filters, a backwards-wave oscillator was used as an RF source, and a pyroelectric detector measured the propagating power.

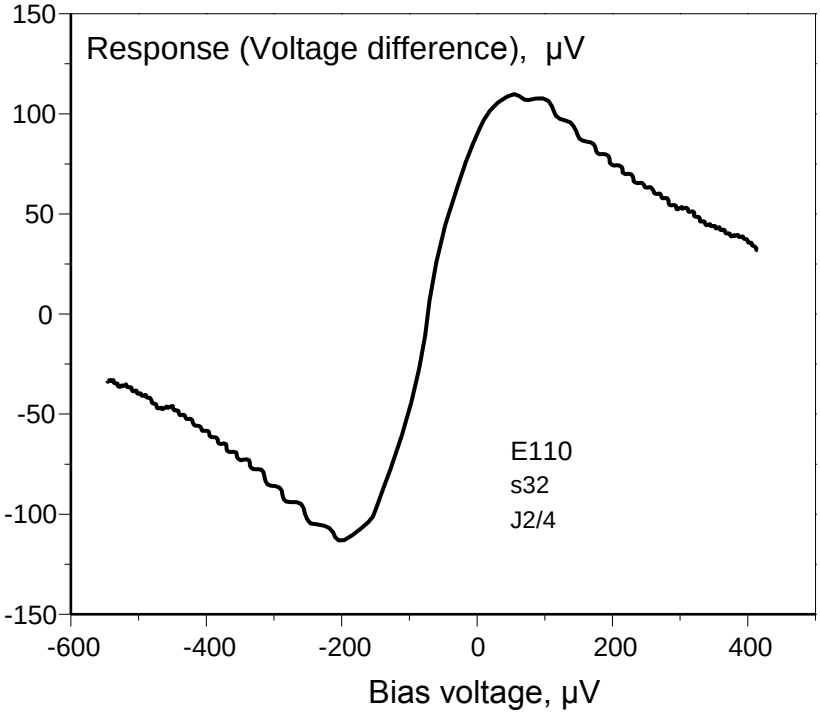

Figure 4.8. Optical response to hot/cold load, source temperature of 3 K and 270 mK [84]

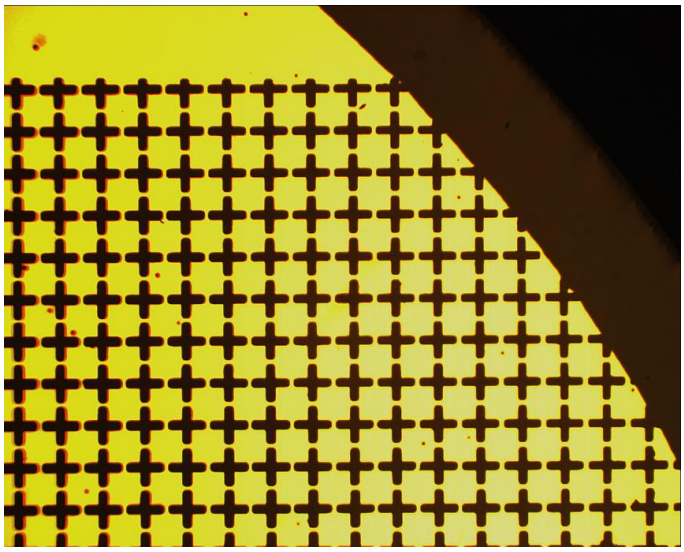

Figure 4.9. Photograph of the mesh filter made of copper on 2-inch quartz substrate.

The design and operation of the filter used in this experiment is similar to the one described in our work on mesh filters for several different frequencies [90]. This is a resonant bandpass filter consisting of meshes that are flat periodic structures called frequency-selective surfaces (FSS), made of metal on a dielectric substrate. Filters made of arrays with slots of different shapes in metal films deposited on dielectric substrates are well described in literature [91]. Reports on resonant meshes were first published by Ulrich [92], Davis [93] and Tomaselli et al [94]. Mesh filters initially manufactured using optomechanical equipment and vacuum electronics were later replaced by meshes created by means of microfabrication, which became more accessible [91]. In our experiments, resonant metal-mesh bandpass filters made of copper films perforated with arrays of cross-shaped apertures were used. These filters are compact, easy to fabricate, can be cooled to millikelvin temperatures, and exhibit high center-band transmission, narrow pass-band, and significant stop-band rejection [91].

When designing our filters, we used easy-to-manufacture *thin* meshes, the thickness of which is much smaller than the resonance wavelength λ_0. This is a scalable design, i.e. the central wavelength is scaled proportionally to the mesh period, while the spectral characteristic remains the same under such variations. According to the terminology of Ulrich [92], meshes with openings that are connected by conductive links, are inductive [90]. In our case, inductive meshes with holes in the form of crosses were selected for the band-pass filters (Fig. 4.10). The proper selection of dimensions L and W (see Fig. 4.10) allows one to obtain a filter with a reasonable quality factor and a passband without an absorption line at the wavelength equal to the period ($\lambda=P$). This is one of the advantages of using cross openings compared to square or circular ones for example, which were used in former technologies [90].

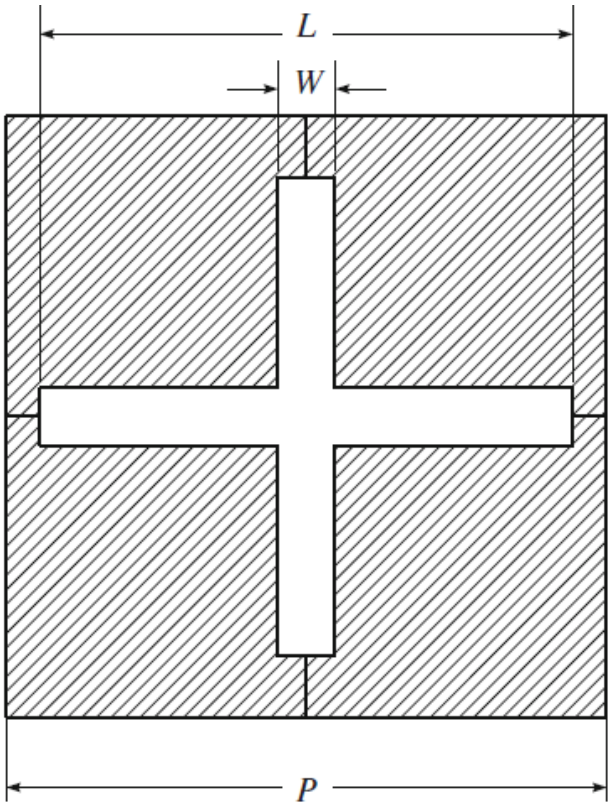

Figure 4.10. Layout of a unit cell of a band-pass mesh filter [90].

DC IV curves of the CEB devices with log-periodic antennas were measured in a current bias mode. The optical response was measured by illuminating the devices with a black body source mounted inside the cryostat, at a 3 K stage. A 20 dB attenuator with reflectivity of about 1% made of NiCr film on a KAPTON carrier was used as the black body source. It was glued onto a Cu plate equipped with a heater and a temperature sensor. The source temperature was changed by Joule heating due to the current flowing though the power load. The signal response was measured by comparing the IV curves at different RF source temperatures (Fig. 4.11). The voltage response to the incoming radiation at different emitter temperatures and bias currents is shown in Fig. 4.12; the temperature dependence is shown in

Figure 4.13. The response up to 45 μV was obtained for the voltage difference at the same bias current for 3 and 8 K black body source temperatures. Based on this value, the voltage to power response can be estimated using the Planck formula for given source temperatures.

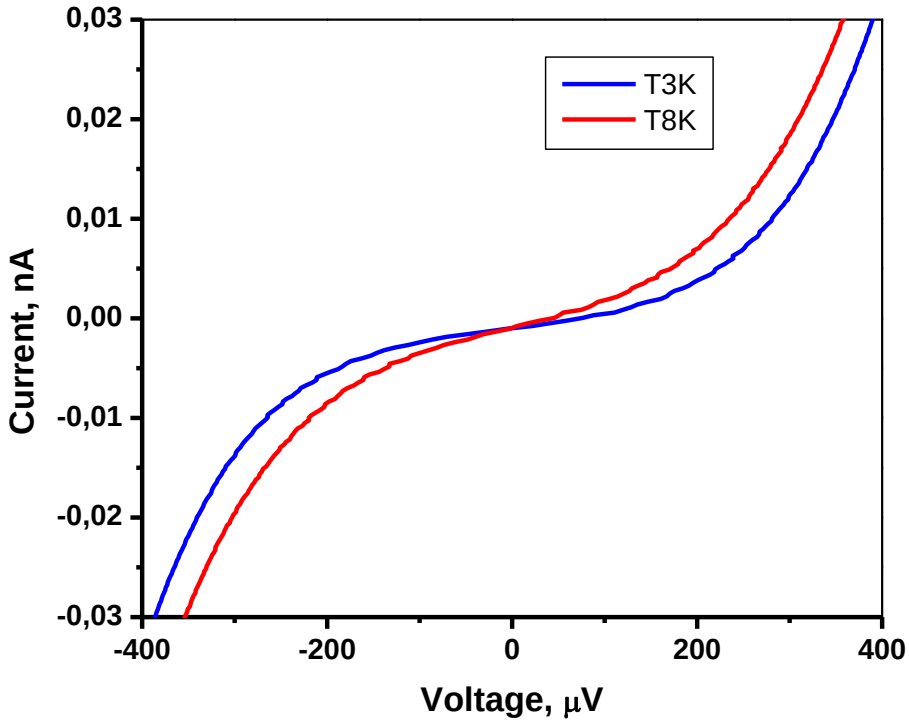

Figure 4.11. IV curves of CEB at 310 mK for 3 and 8 K black body source temperatures.

For a center frequency of f = 300 GHz and a bandwidth of 10 GHz, calculating the radiation power δP incident on the detector, with the CEB-antenna integrated circuit as a single mode detector [89], yields the power emitted by a black body at a temperature of T = 8 K given by

$$\delta P = \frac{\kappa \cdot hf \cdot \delta f}{\exp(hf / k_B T) - 1} = 4.3\times10^{-13}\ \text{W},$$

where h is Planck's constant, k_B the Boltzmann constant, δf = 10 GHz the bandwidth, and κ=1 is the emissivity of the black body source. The corresponding power for 3 K is ~3×10^{-14} W.

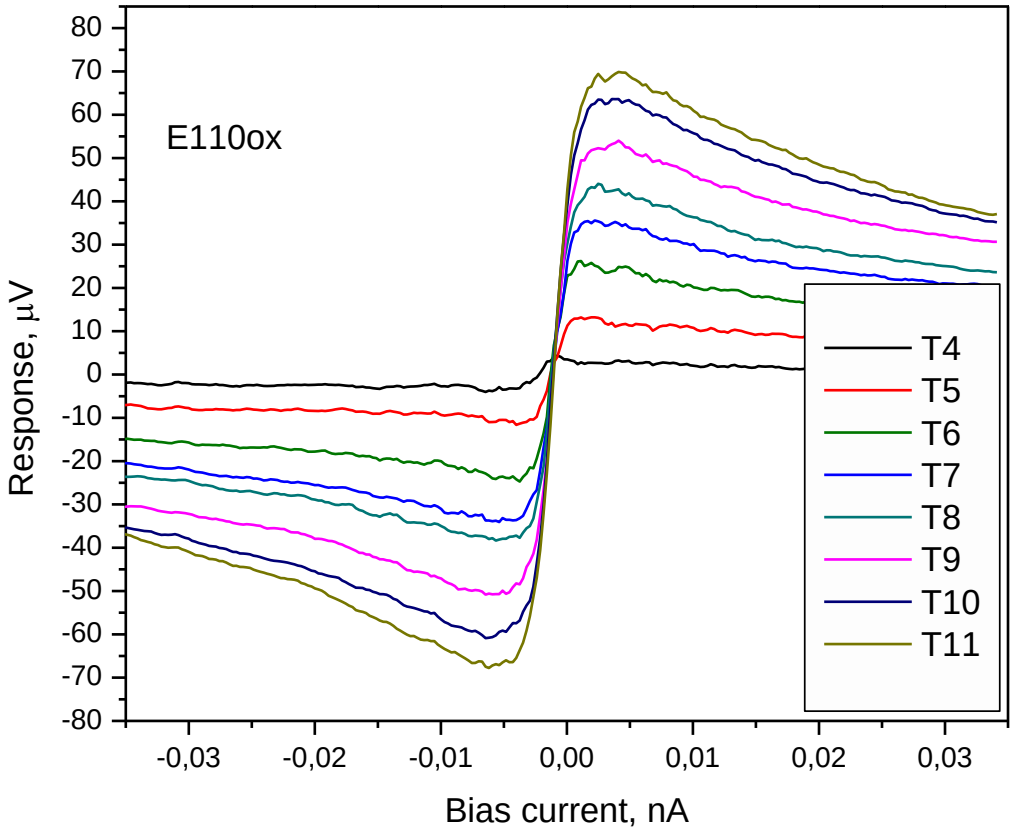

Figure 4.12. Optical response of a CEB versus bias current at different RF source temperatures; measured with 300 GHz bandpass filter. The blackbody temperatures used in this experiment were: T = 4, 5, 6, 7, 8, 9, 10 and 11 K [84].

Subtracting the calculated power values at source temperatures of 3 K and 8 K yields the difference in the incident power at these temperatures: $\Delta P = 4\times10^{-13}$ W. Taking a voltage change of 45 μV for this power difference, we obtain the responsivity:

$$S = dV/dP \approx \Delta V/\Delta P = 1.125\times10^{8} \text{ V/W}$$

The optical NEP is obtained by dividing the total voltage noise of v_n = 10 nV/Hz$^{1/2}$ by the voltage to power response:

$NEP = v_n/S = 8.88 \cdot 10^{-17}$ W/Hz$^{1/2}$

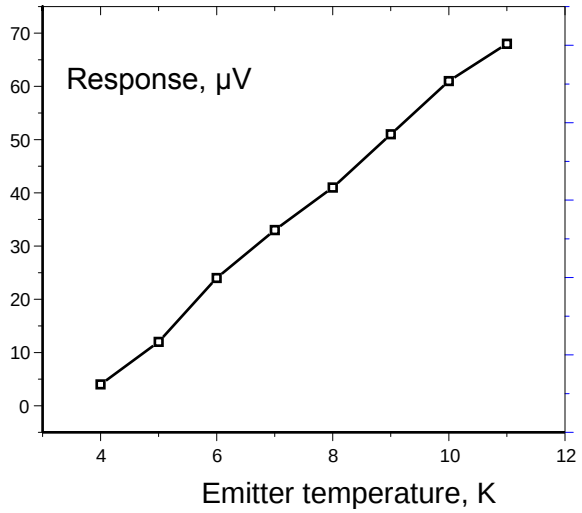

Figure 4.13. Voltage response versus emitter temperature [84].

4.1.4. Discussion

The optical NEP values derived above are only estimates. The connection from the RF source to the CEB detector contained several interfaces, and the losses due to the mismatches at different interfaces from the source to the detector in the present configuration were only estimated. In addition, the optical losses at temperatures below that of the load will reduce the power received from the load by the detector, meaning that our value of S is underestimated. This implies that our optical NEP is an overestimate of the intrinsic optical NEP of the device.

The voltage noise of ~10 nV/Hz$^{1/2}$ was measured using the room-temperature amplifier box. As a result, the noise coming from the amplifier dominates the total noise measured. So, we expect much better noise performance when using cold amplifiers for noise measurements.

Regarding fabrication, a straightforward and robust technology was chosen for the production of these devices. This was a reasonable choice for developing this experiment, in that it allowed us to demonstrate the full functionality of the CEB device as a state-of-the-art bolometer. It also allowed us to demonstrate the CEB-antenna integrated circuit as a feasible design. This is an important conclusion for the employment of the CEB in large format focal plane arrays.

However, our fabrication methods were not optimized for best device performance. The volume of the absorber was not chosen for best responsivity, due to lower yield and poor reproducibility observed for devices with reduced volume of absorber, when fabricated using this technology. Therefore, we expect improvements in the fabrication and design of the next generation of devices and readout electronics to yield improved responsivity and overall performance.

Although photo lithography has been used to manufacture the given samples, the e-beam lithography and negative e-beam resist can be used in order to achieve better resolution and therefore smaller volume of absorber which is critical for the performance of the CEB [46, 56]. New devices with a reduced absorber volume and in voltage bias mode with a SQUID readout or another high performance amplifier should achieve much better NEP levels [46].

For most of practical cases the NEP will be determined by a background power load that is about P_{bg} = 5 pW (the CMB level) for ground based observations at a signal frequency of ~100 GHz, which corresponds to a photon NEP of

$$NEP_{phot} = \sqrt{2P_{bg}E_{quant}} = \sqrt{2P_{bg}hf} \quad = 2.4 \cdot 10^{-17} \text{ W/Hz}^{1/2}.$$

Our preliminary measurements have already demonstrated that such NEP values can easily be achieved with standard SIN CEB devices.

4.1.5. Conclusions

We developed a novel technology for the fabrication of tunnel junctions between Ti and Al using titanium as a base electrode and titanium oxide as an insulating barrier. The devices have been fabricated with the absorber deposited prior to the superconducting counter-electrodes. We have fabricated CEB devices with Ti-TiO_2-Al SIN tunnel junctions and measured their performance at 300 mK. The results of DC and RF measurements on a Cold-Electron Bolometer deposited across a double dipole antenna and another one fed by a log-periodic antenna on a planar Si substrate have been presented. The fabricated junctions are rather high-ohmic due to a very long oxidation time used for creating the tunnel barriers. Shortening oxidation time combined with proper choice of temperature should allow us to create more low-ohmic tunnel junctions. Thus, more development work is needed to realize low-ohmic junctions that are more suitable for CEB applications. Because of medium on-chip and chip-to-chip reproducibility, some optimization work is required in order to achieve optimal oxidation conditions during the creation of the tunnel barrier.

Our preliminary measurements have yielded NEP ~3×10^{-17} W/Hz$^{1/2}$ which is close to the CMB power level. Improving the design, using series arrays of SIN junctions and improving the readout should yield an NEP level below 1×10^{-17} W/Hz$^{1/2}$.

Therefore, the detector can be a potential candidate for the next generation of space cosmology missions and is also of interest to ground-based astronomical experiments as a result of the simplicity of its integration to planar circuit technology, high saturation power and fast response.

4.2. CEB Array for Boomerang

In this section, we present experimental results on the testing of Cold-Electron Bolometer (CEB) detectors comprising a non-superconducting thin absorber made of a CrO_x/Cr/Al trilayer film and an array of Superconductor-Insulator-Normal (SIN) tunnel junctions integrated in a planar cross-slot antenna. Each antenna contains two series/parallel arrays of 10 Cold-Electron Bolometers with SIN tunnel junctions integrated in orthogonal ports of the antenna. Several wafers with CEB devices were fabricated using Advanced Shadow Evaporation technology with minor modifications. The CEB performance was tested in a ^{3}He sorption cryostat HELIOX-AC-V at bath temperatures of 280 to 350 mK and in a dilution refrigerator TRITON down to 50 mK. We will first demonstrate that this technology is suitable for detector fabrication by producing high performance IV curves and then describe our experiments on the measurements of the voltage response to the incoming RF power [55]. The optical response will be measured in two different ways: using the hot/cold load method by flipping a Cu reflector opposite a blackbody surface inside a 3 K shield and then using a

black-body source placed in front of the detector chip mounted in a quasioptical sample-holder inside a 3 K shield. Later in this chapter, we will demonstrate electron cooling that increases the dynamic range of the device.

4.2.1. Balloon-borne telescope Boomerang

Among the projects dedicated to the CMB-related measurements, the BOOMERANG should be mentioned here as a project employing bolometric detectors for mapping the CMB radiation. The BOOMERANG experiment, which stands for Balloon Observations of Millimetric Extragalactic Radiation and Geophysics, is a sub-orbital (high altitude) balloon-borne telescope project that is dedicated to the measurements of cosmic microwave background radiation of a part of the sky [6, 95, 96, 97]. The balloon and the instruments before the launch are shown in Figure 4.14.

This experiment made it possible to obtain reliable images of the CMB temperature anisotropies. The atmospheric absorption of the millimeter-wave signals was minimized by measuring with a telescope at the altitude of 42000 meters. This was a considerably less expensive solution compared to a satellite or a space-borne telescope; although just a small part of the sky was scanned.

For detecting the electromagnetic signals, bolometric detectors operating at 270 mK are used. At this temperature the heat capacity of materials is very low, and the absorbed electromagnetic wave power makes a significant change in temperature, which is then measured.

Figure 4.14. Boomerang experiment: The balloon and the instruments before the launch [95, 97].

After a test flight over North America in 1997, first flights of BOOMERANG around Antarctica started in 1998 in order to map the Cosmic Microwave Background (CMB). One of the first missions of the BOOMERANG, the Long Duration, was completed in January 1999 after making a circle around the South Pole during approximately ten days. The instruments following with the balloon made about 1 billion measurements of variations in the temperature of the CMB across the sky, thereby mapping the CMB temperature anisotropies. The second flight in 2003 was dedicated to measuring both temperature and polarization anisotropies [95, 98]. In both cases, the balloon was carried by the Polar vortex winds in a circle and returned to the same place after two weeks like a boomerang, hence the name. Using the CMB

measurements data obtained by Boomerang that convey the information about the conditions in the early universe, one can prove and correct cosmological models, derive fundamental parameters etc., e.g. the overall density and density of various components [95, 98]. This was the largest and most precise set of CMB data collected at that time, according to BOOMERANG team member Julian Borrill, Computing Center NERSC, Berkeley [96]. From that dataset, the BOOMERANG team produced the most detailed map of the CMB's temperature fluctuations.

The principle of operation is similar to other CMB-related projects. A mirror focuses the incident signal onto the focal plane consisting of 16 horns, operating at 145 GHz, 245 GHz and 345 GHz. The horns are arranged into 8 pixels; hence, only a fraction of the sky can be seen simultaneously, and the telescope needs to be rotated in order to scan the whole area [6, 98].

From the map of temperature fluctuations, an angular power spectrum was derived, similar to the ones in other CMB-related experiments such as WMAP or Planck. The angular spectrum presents the strength of the temperature fluctuations on different angular scales, which thus provides information about the early universe, such as its geometry and the amount of matter and energy in it [95, 98].

To derive the spectrum, the processing power of NERSC's 696-node Cray T3E supercomputer was used, as well as a software package MADCAP, developed for this purpose (Microwave Anisotropy Dataset Computational Analysis Package). The processing time on the Cray T3E for the project amounted to about 3 weeks. The angular power spectrum from the data

obtained during the BOOMERANG Antarctic flight allows for the determination of fundamental cosmic parameters at an accuracy of a few percent [96].

4.2.2. The concept of parallel/series CEB arrays

For applications in radio astronomy and in particular balloon-borne and space experiments, such as the balloon-borne BOOMERANG telescope project [95], the power of the microwave background radiation determines the requirements for the detector performance. It is desirable that the NEP of the potential detector is below the photon noise of an optical power load of 5 pW; in general, for observations of foregrounds and CMB polarization the cross-polar response should be at least 25 dB below the co-polar one, including balloon experiments. In this chapter, we will consider detectors that can be used for the 345 GHz channel of BOOMERANG [95].

In order to satisfy power load requirements of 5 pW with JFET readout for CEB, a novel concept of a series/parallel array of Cold Electron Bolometers (CEBs) in current-biased mode has been proposed for efficient noise matching between the detector output and the JFET amplifier readout [46, 56].

The main innovation of the CEB array, in comparison to a single CEB [37], is the distribution of power between several bolometers, and hence the increased dynamic range. An effective distribution of power is achieved by a parallel RF connection of CEBs, which couple to the RF signal through additional capacitances (Fig. 4.15, 1.17). For an individual CEB in an array of N devices, the total absorbed power is reduced by the factor of N. This has several

advantages: (1) it reduces the power absorbed by each device and limits the overheating and saturation of the absorber, which substantially increases the dynamic range; (2) Since the background power is divided among single absorbers, this prevents overheating and increases the sensitivity of the array. Indeed, the amplifier noise becomes less important, since the voltage response of the array is multiplied by *N* whereas the noise is only proportional to the square root of this number; (3) Combining several devices in series for DC connection (see Figure 1.17) enables proper matching of the output impedance to the JFET amplifier.

The efficiency of this approach has already been demonstrated in our previous work [36] where a series array of 100 SIN junctions was investigated. On the other hand, increasing the number of CEB devices in an array leads to an increase of the total absorber volume and corresponding electron-phonon noise. In our design an optimal number of 10 CEB devices was found, where the total noise of the detector becomes less than the photon noise of the incoming signal [55, 56].

To optimize the performance, new technologies were explored [36-41], such as the Advanced Shadow Evaporation technique proposed by L. Kuzmin [41]. As mentioned in the previous section, by using a parallel-series array a noise level below the photon noise level can be achieved [46]. In this work, an array of Cold-Electron Bolometers with a series connection for DC bias and a parallel connection for the RF signal was optimized for better yield and high response. Two arrays with several of CEBs integrated in orthogonal ports of a cross-slot antenna demonstrate identical characteristics. The figure of merit for each array is the ratio of resistance at zero bias to asymptotic resistance. The achieved figure of merit of over 3000 at

100 mK provides clear proof of a good quality of tunnel barrier and proper measurement conditions with low levels of interference. Additional test structure with two pairs of SIN tunnel junctions connected to an absorber strip was used for DC characterization of a single bolometer. In what follows, we will demonstrate that this design is suitable for detector fabrication by producing high performance IV curves and observing a voltage response to the incoming RF power [55]. Later in this chapter we will also present the optical testing and noise measurements results for detectors fabricated using this technique, with minor modifications in the patterning procedure and tunnel barrier thickness.

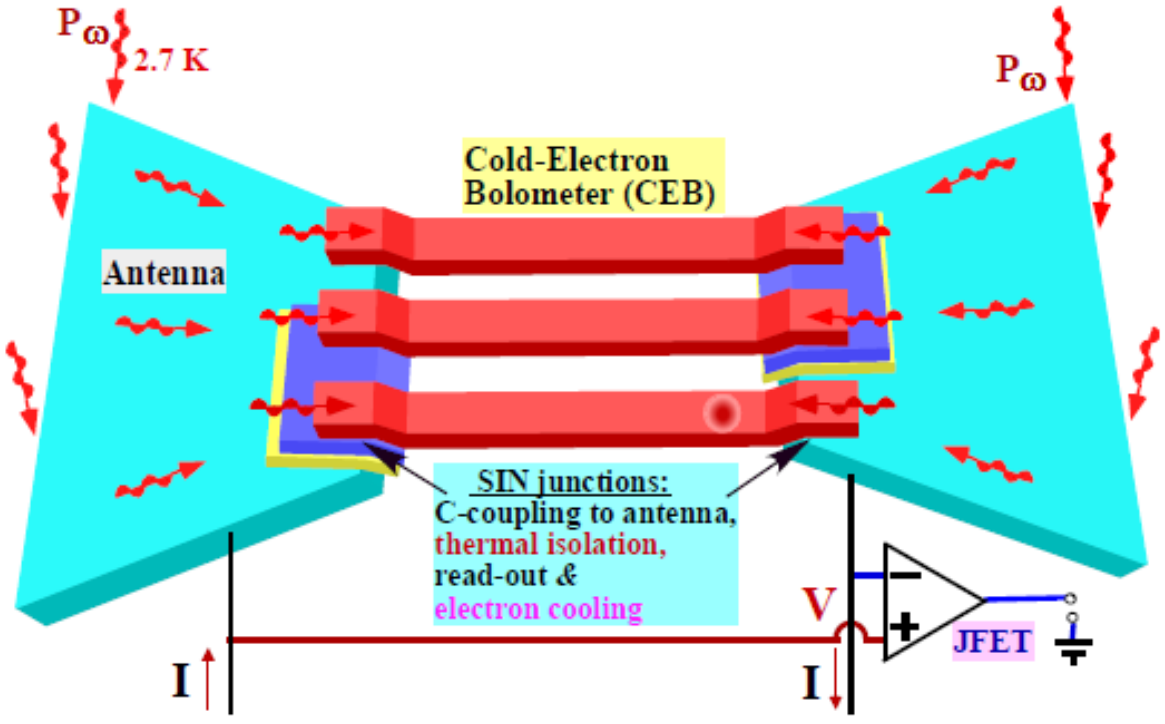

Figure 4.15. Schematic of an array of three CEBs. Series DC connection and parallel RF connection through the additional capacitors between the superconducting islands and the antenna; shown in blue [55, 56].

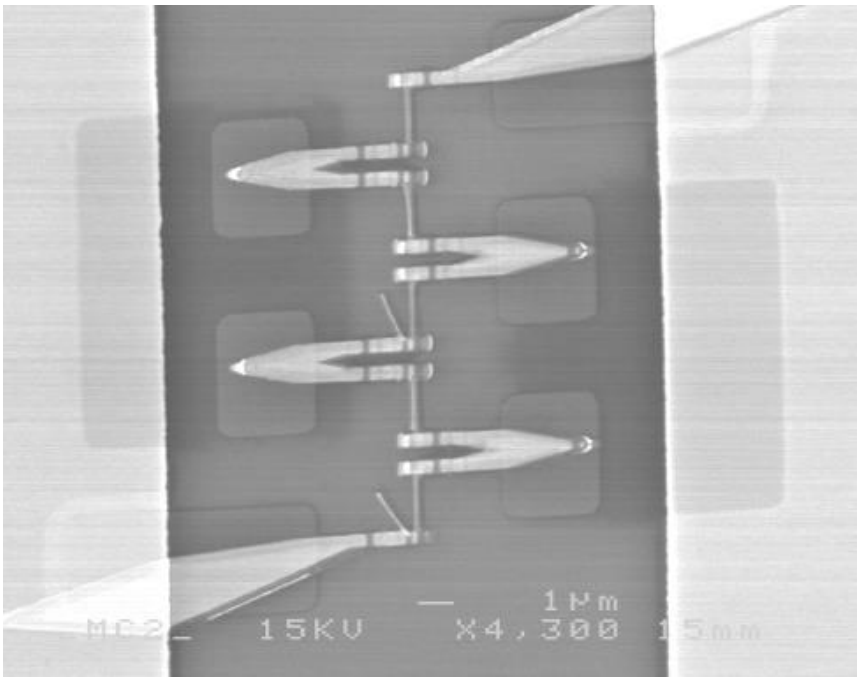

Figure 4.16. SEM image of a half of array consisting of 5 absorbers and 10 SIN tunnel junctions [55]

4.2.3. Chip design and fabrication

The samples have been fabricated using electron-beam lithography using Advances Shadow Evaporation technology for fabricating tunnel junctions proposed by L. Kuzmin [41]. As we have already stated, this procedure employs *in-situ* Al oxidation for the creation of the Al_2O_3 insulating barrier. The process involves two steps of deposition in one vacuum cycle: first the normal Al absorber is deposited and oxidized and then the Al counter-electrode is deposited.

The layout design of CEB arrays was optimized for CMB and foregrounds polarization measurements with the balloon-borne telescope BOOMERANG in a frequency band around 345 GHz. The bolometers were integrated in a cross-slot antenna that was placed at the center of a 7×7 mm chip on a thermally oxidized Si substrate with a 400 nm thick SiO_2 layer. There

are 32 chips on a single 2-inch Si wafer, and several wafers were produced using nearly the same fabrication procedure. The layout of the antenna is based on a well-known cross-slot antenna design that was studied before and described in e.g. [99]. This is in essence a slot antenna consisting of 4 slots for 4 structures in total, 2 pairs of slots for each polarization component. Based on published data and our previous experimental results, the bandwidth of our CEB-antenna integrated circuit is estimated to be around 100 GHz.

Each orthogonal array consists of 10 CEB devices connected in series for DC bias and DC readout. An optical image of the antenna is shown in Fig. 4.17. The dark narrow slots in Fig. 4.17 are covered with an AlO_x/Al capacitive layer, thus making capacitive coupling between the two CEB arrays. Each port of the antenna contains 5 CEBs that are connected in series with each other and fed by the same polarization, making an array of 10 CEBs for vertical polarization and 10 CEBs for horizontal polarization components. The SIN tunnel junctions for the CEB devices were made of CrAl/AlO_x/Al trilayer, in which the first layer is made of non-superconducting Al and then oxidized to form a thin oxide barrier. This trilayer structure was deposited using an advanced shadow-evaporation technique for CEB fabrication [41]. A detailed SEM view of a half of an array with 5 absorbers and 10 tunnel junctions is presented in Fig. 4.16. In this view, two CEB devices on the left and two devices on the right of the absorber are coupled capacitively, similarly to the capacitors shown in Fig. 4.15.

This chip comprising the two CEB arrays integrated in the cross-slot antenna can be fed by an extended hyper-hemispherical Si lens with an antireflection coating, or by a horn for simple measurements with a cold radiation source. The lens or the horn faces the optical window

through low-pass filters on two temperature stages, as shown in Fig. 4.18. To suppress overheating by IR radiation, the optical window was protected by low-pass filters (LPF) and bandpass filters (BPF). Commercial low-pass multi-mesh filters from QMC Instruments™ provided attenuation of more than 10 dB above the cut-off frequency of 3 THz for LPF W97s and above 1 THz for LPE B694. The filters were placed in front of the Si lens.

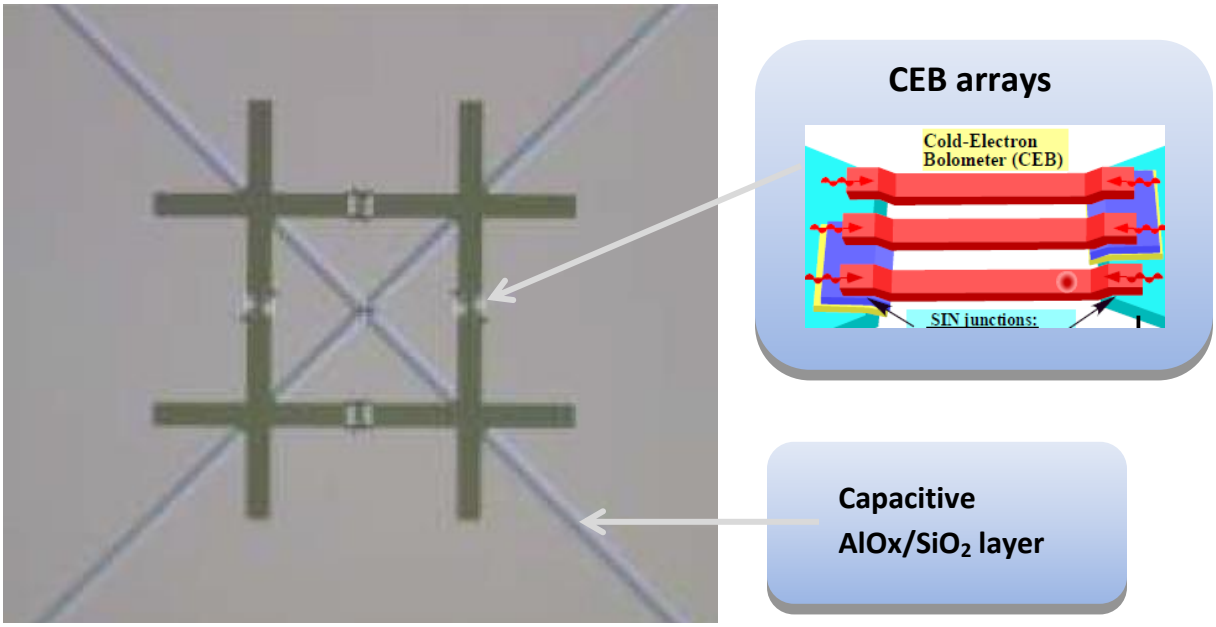

Figure 4.17. Optical image of a cross-slot antenna with CEB arrays (inset). [55]

The use of commercial filters in optical windows, however, resulted in significant overheating of the cold stage and reduced the holding time of the ^{3}He sorption cooler. This is because the filters were made of arrays of metal film squares on a thin dielectric carrier. The metal squares are radiation heated from the warmer side of the cryostat and as a result their equilibrium

temperature is an average between the hot and the cold sides. This means that such a filter acts as a source of thermal radiation above the cut-off frequency. In our case we improved the thermal performance by placing neutral density filters (NDF) with attenuation of about 6 dB in front of each LPF. As a result, the IR radiation was suppressed; the temperature of self-irradiation became the same as that of the radiation shield and no visible overheating of the cold stage or reduction of the holding time was observed. A band-pass filter consisting of cross-shaped holes in a metal film can be better from the overheating point of view, because it can be well thermally anchored to the radiation shield, and its equilibrium temperature is the same as that of the shield.

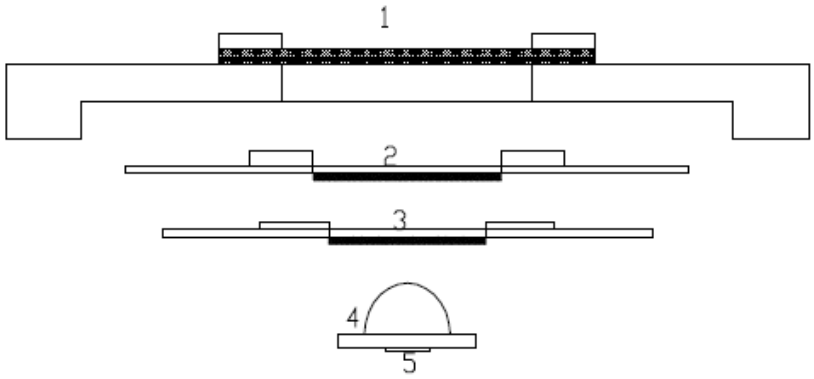

Figure 4.18. Schematics of quasioptical beam path in the cryostat [55]: (1) - Teflon window, (2) - first low-pass filter, (3) - second low-pass filter, (4) – Si extended hyper-hemisphere lens, (5) –detector chip

4.2.4. Results of experimental measurements on CEB arrays

First, we measured the DC characteristics of the fabricated CEB devices by applying a bias current and measuring the voltage across each array. We have demonstrated high performance IV curves, which is an indication that this technology is suitable for detector fabrication. The

topology of the readout system used in this experiment was described earlier in the Chapter 3 and the circuit schematic is shown in Fig. 3.10. The IV characteristics of an array of 10 cold-electron bolometers and the voltage response to temperature differences [55] are shown in Fig. 4.19. The dynamic to normal resistance ratio of the fabricated devices was measured to be 500 to 1000 at 300 mK.

The voltage shown here is the total voltage across the whole array so the superconducting gap that is observed in this graph represents the sum gap voltage of the SIN junctions in the array. The voltage across an array at a bias current of 0.1 nA as well as the dynamic resistance at zero bias are both plotted as a function of temperature in Fig. 4.20. The maximum voltage response to the temperature obtained in this experiment was 8.8 μV/mK [55].

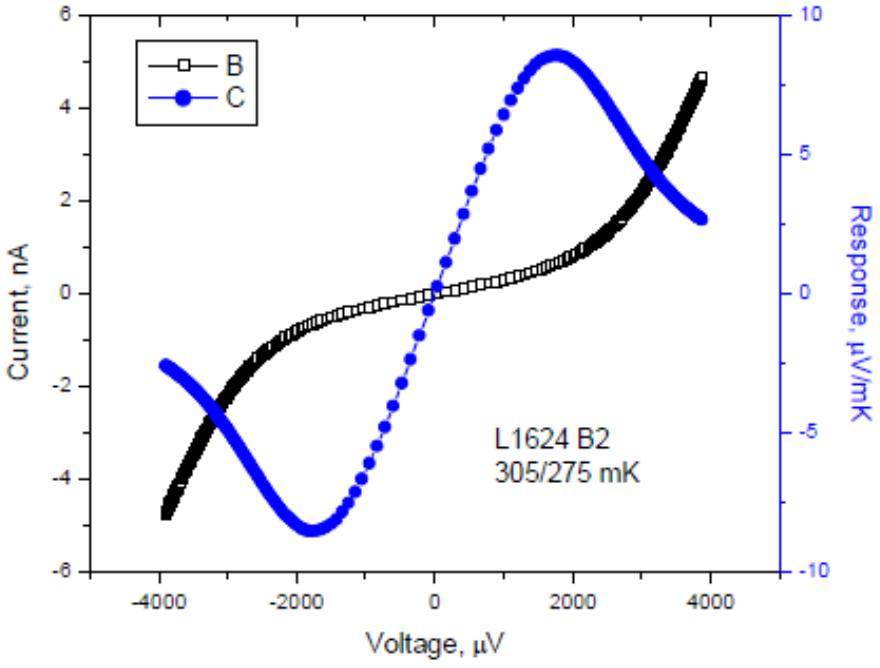

Figure 4.19. IV curve and voltage response for temperature difference of 305-275 mK, r_d/R_n ~500 [55]

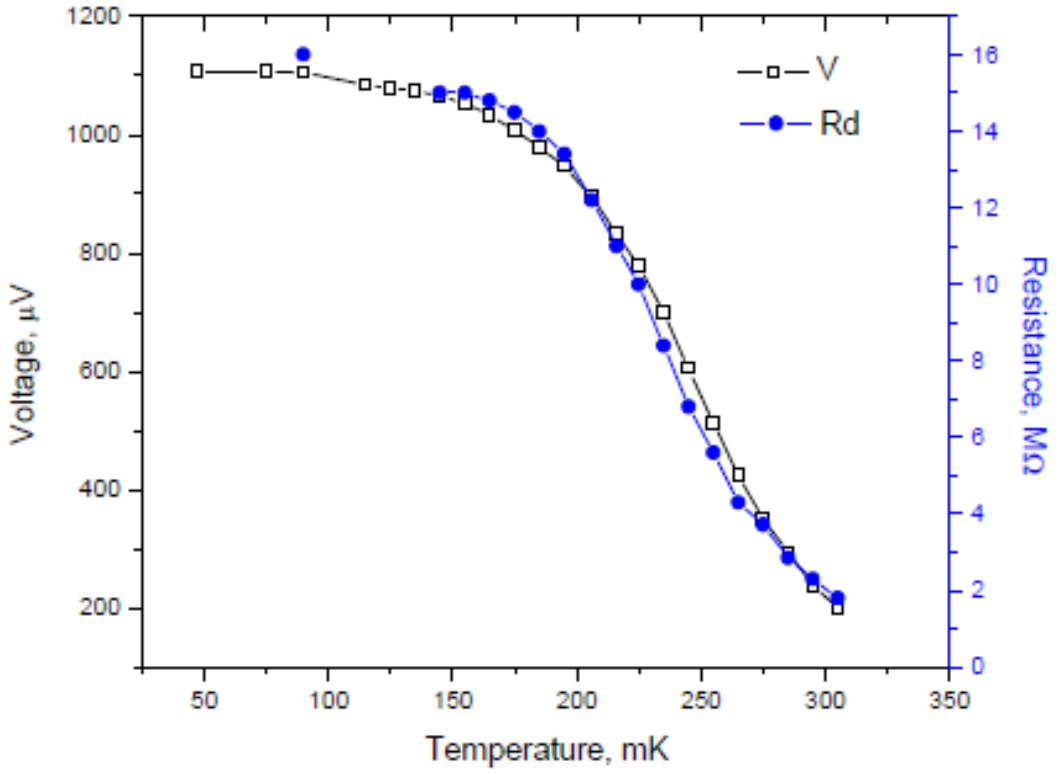

Figure 4.20. Voltage across an array of 10 bolometers for a bias current 0.1 nA and the dynamic resistance at zero bias versus temperature of the array [55]. The maximum responsivity is 8.8 μV/mK.

In the next experiment, in order to get an additional calibration of the bolometer input, we installed a rotatable holder inside the cryostat with a reflecting Cu foil screen and a 10 dB NDF attenuator at 3 K. This was similar to the experiment described in the first section of this chapter. An external magnet could be used to rotate the holder while the device was cold. In this way the CEB detector could be situated to face a blackbody load at 3 K or 300 mK. A photo of this setup being tested at room temperature is presented in Fig. 4.7; the measured voltage response signal versus bias voltage is shown in Fig. 4.21.

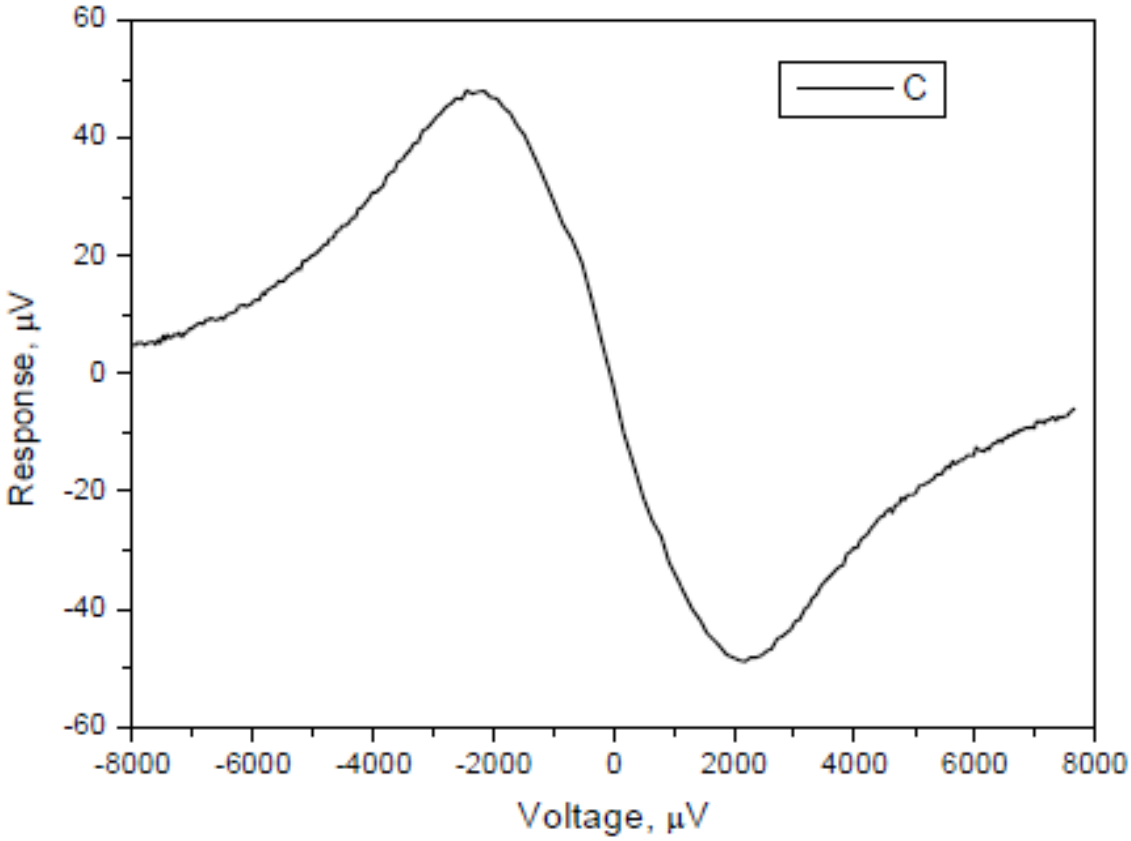

Figure 4.21. Voltage response to switching the load illuminating the detector from Cu foil (T = 300 mK) to an attenuator at 3 K. [55]

The measured radiation temperature sensitivity is 17 μV/K and the optical noise equivalent temperature difference is NETD = 0.65 mK/Hz$^{1/2}$, as already defined above:

$$NETD = \frac{T - T_B}{S/N},$$

where T is the target temperature, T_B is the target background temperature, and S/N is the signal to noise ratio.

To estimate the dark NEP, we measured the output noise of the array using a MOSFET OPA111 instrumentation amplifier as the input integrated circuit. For theoretical estimations of the CEB array noise performance we assume that it is mainly determined by the power flow due to electron-phonon interaction $P = \Sigma\Lambda(T^5-T_0^5)$ so that the thermal conductivity will be

$$G=dP/dT=5\Sigma\Lambda T^4,$$

where Σ is the absorber material parameter and Λ is the volume of the absorber. Consequently, the responsivity can be expressed as

$$S = \frac{dV}{dP} = \frac{dV}{dT} \times \frac{dT}{dP} = \frac{dV}{dT} / G$$

The volume of the absorber for an array of 10 bolometers is Λ=10^{-19} m^3 and for aluminium the parameter Σ = $1.2 \cdot 10^9$ $Wm^{-3}K^{-5}$, so the thermal conductivity is G = $3.6 \cdot 10^{-12}$ W/K at 280 mK phonon temperature. Taking the measured bolometer output voltage noise of v_n = 11 $nV/Hz^{1/2}$ in the white noise region, and a temperature response of dV/dT = $8.8 \cdot 10^{-3}$ V/K (see Fig. 4.20), we can estimate the minimum phonon-limited dark noise equivalent power as

$$NEP = \frac{v_n}{dV/dP} = 6 \cdot 10^{-18}\ \mathrm{W/Hz^{1/2}}.$$

For a power load of 5 pW at 345 GHz (e. g. the CMB noise), the photon contribution to the NEP can be estimated as $NEP_{phot}=(2 \cdot P_0 \cdot h \cdot f)^{1/2}$=$5 \cdot 10^{-17}$ $W/Hz^{1/2}$. Taking into account experimental values of noise and response, we can plot the dark NEP of our bolometer array as a function of bias voltage and frequency. This is shown in Figures 4.22, 4.23, respectively.

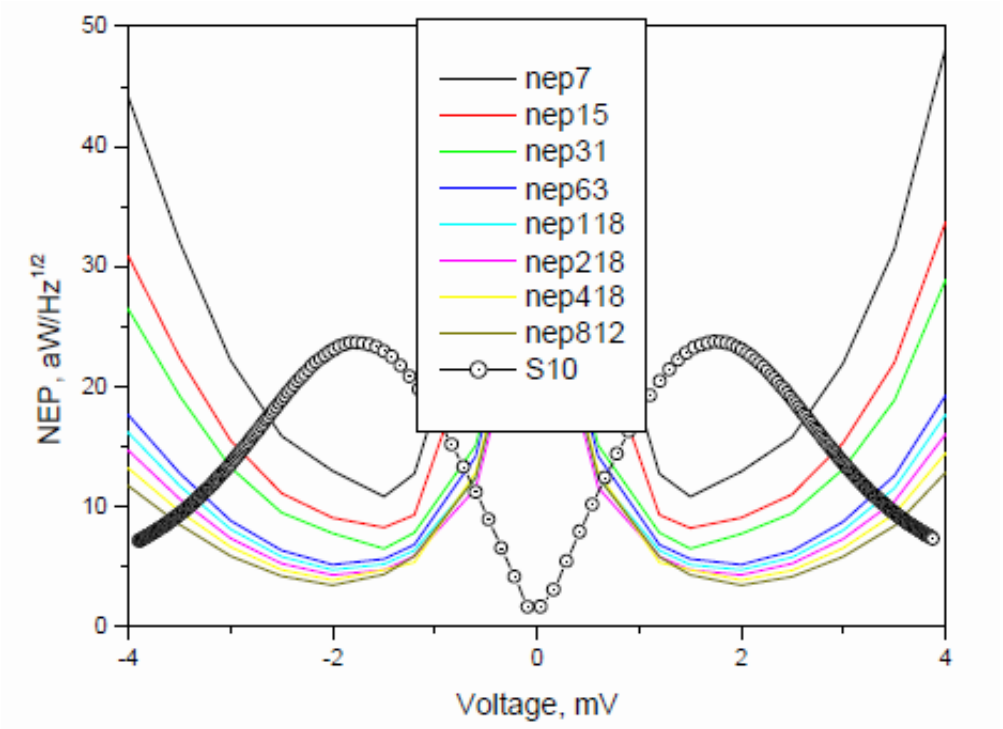

Figure 4.22. Noise Equivalent Power and absolute value of voltage response for array of 10 CEBs [55]

We can also estimate the optical NEP, relying on the data presented in Fig. 4.21. Considering the CEB-antenna integrated circuit, we can calculate the incident radiation power δP with the Planck formula for a single mode detector [89]. For a frequency range around the frequency of f = 350 GHz within a bandwidth of a cross-slot antenna of δf = 100 GHz, the power emitted by a black body at a temperature of T = 3 K is given by [89]:

$$\delta P = \frac{\kappa \cdot hf \cdot \delta f}{e^{hf/k_B T} - 1} = 1.1\times10^{-13}\ \text{W},$$

where h is Planck's constant, k_B is the Boltzmann constant, κ=1 is the emissivity of the black body source, assuming that the effective RF bandwidth is 100 GHz. A neutral density filter placed on 3 K stage was used as the black body source in this experiment. The corresponding

power for 280 mK is far below 10^{-15} W and can be neglected. So the difference in power values for source temperatures of 3 K and 280 mK yields $\Delta P = 1.1\times10^{-13}$ W. Taking a voltage change of 50 μV for this power difference, we obtain the voltage responsivity:

$$S = dV/dP \approx \Delta V/\Delta P = 5\times10^{8}\ \text{V/W}\ .$$

The optical NEP is obtained by dividing the total voltage noise of v_n = 11 nV/Hz$^{1/2}$ by the voltage to power response:

$$NEP = \frac{v_n}{dV/dP} = 2.2\cdot10^{-17}\ \text{W/Hz}^{1/2}\ .$$

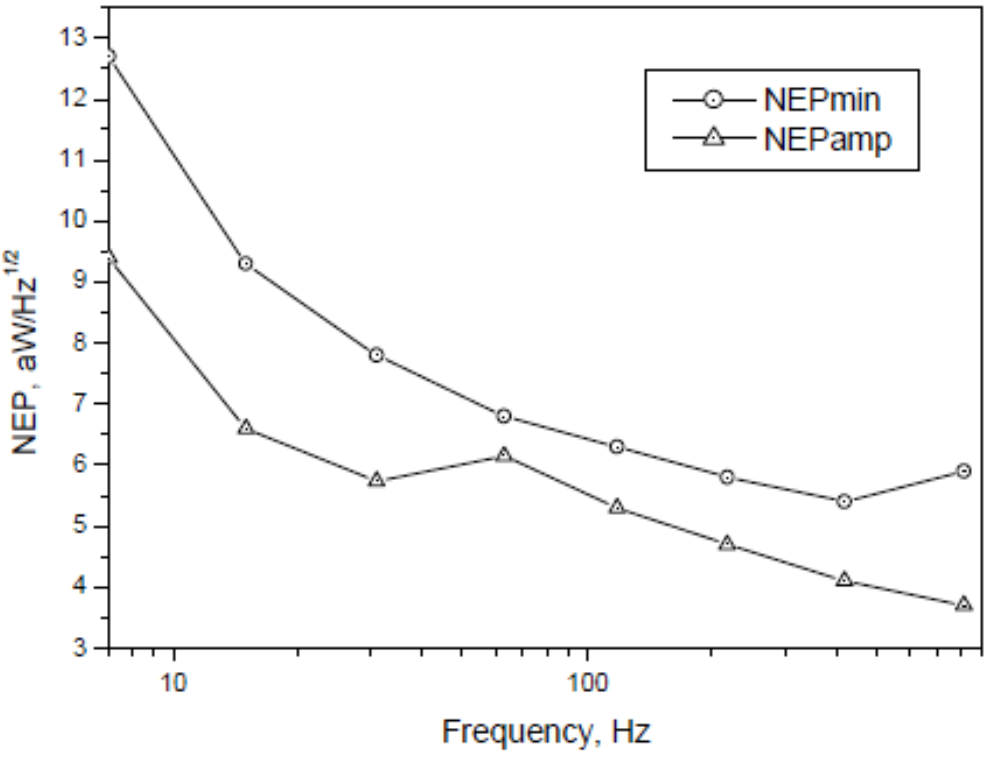

Figure 4.23. Minimum Noise Equivalent Power (NEP) and the contribution due to the amplifier [55].

The effectiveness of connecting bolometers in an array and electron cooling can be illustrated by direct optical measurements of the dynamic range. For such an experiment we used a Backward Wave Oscillator (BWO) that operates in a frequency range of 250 - 380 GHz for anode voltages in the range 1100 - 3800 V. A calibrated polarisation grid attenuator was used for accurate control of the incident power. Inside the cryostat besides the 20 dB NDF cold attenuator at the optical window we also used our cold rotatable stage with the reflective Cu surface, a 10 dB NDF, and an open aperture. A photo of the setup is presented in Fig.4.24. The measured output voltage dependence on the signal attenuation is presented in Fig. 4.25.

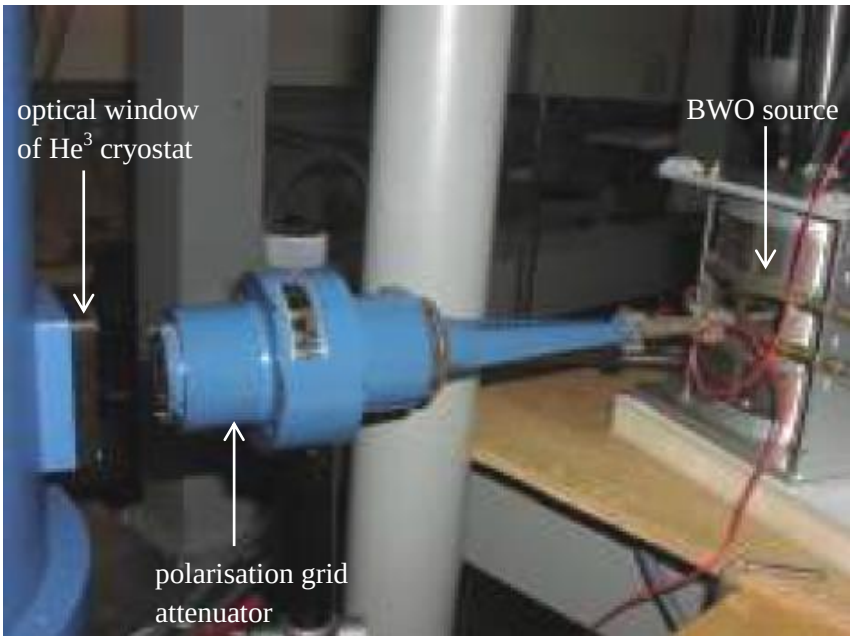

Figure 4.24. Measurements of the CEB array dynamic range: Backward wave oscillator (to the right), polarisation grid attenuator (in the center), and the optical window of the ^{3}He cryostat (to the left) [55].

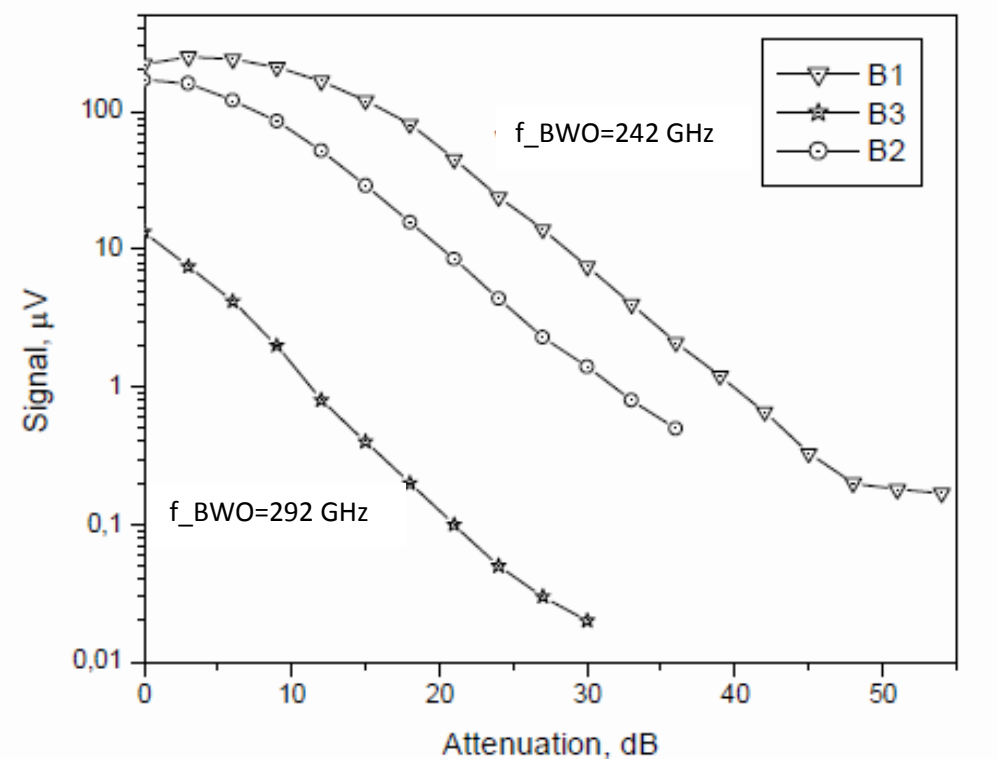

Figure 4.25. The output voltage versus the incoming signal attenuation for a signal of ~300 GHz from the backward wave oscillator. B1, B2 – arrays for the vertical and horizontal polarization components respectively, B3 – bolometer integrated with 4-probe test structure [55].

The accuracy of such measurements was limited by mechanical instabilities and leakage of power through the NDF. Nevertheless even in this experiment a dynamic range over 40 dB was demonstrated. Considering the lower signal level equal to an amplifier noise of 11 nV/Hz$^{1/2}$ and the saturation level of 200 µV as presented in Fig. 4.25, both measured with an integration time of 1 s, this results in a full dynamic range of the bolometer array of about 43 dB. This can also be observed in Figure 4.25 (see the curve for B1 array in the range between 0.2 µV and 200 µV for the voltage response). This is a remarkably high dynamic range, in particular if compared with that of the TES which is a few dB.

4.2.5. Experiments on DC response and electron cooling using bolometer integrated in 4-junction test structure

In what follows next, we describe experiments on a set of bolometric devices fabricated in a similar way using the same technology with minor modification; the chip layout (Figure 4.26) includes bolometers integrated in 4-probe test structures consisting of 4 SIN junctions and an absorber, similar to the one described in the first part of this chapter. This is a bolometric device with two additional electrodes connected to the absorber though SIN tunnel junctions, which enables for proper 4-point measurements.

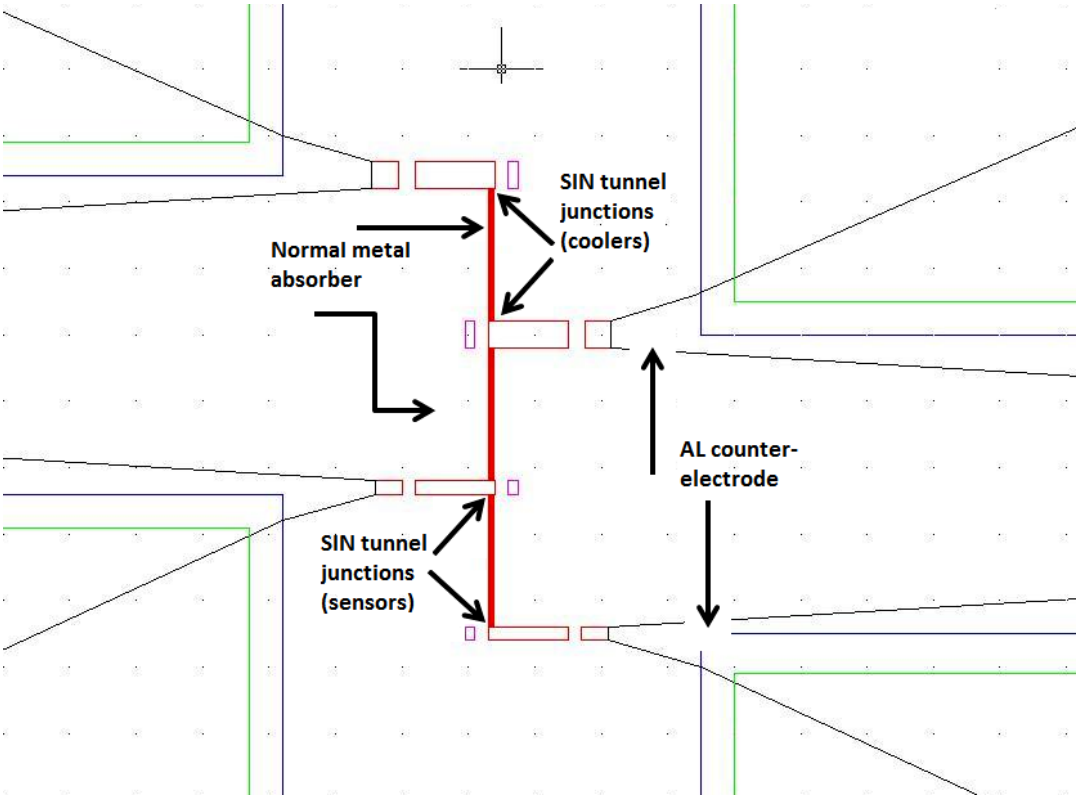

Figure 4.26. AutoCAD drawing of 4-probe bolometer made of a normal absorber and 4 SIN junctions

I-V curves were taken at several bath temperatures between 286 mK and 356 mK, and a voltage to temperature response, $S_{V/T} = dV/dT$ was obtained for our 4-junction structures by comparing the I-V curves at different bath temperatures. For a 4-junction structure shown in Figure 4.26, we measured the voltage at 0.12 and 0.25 nA bias current as a function of temperature. Voltage across two junctions in series versus temperature at fixed current for a 4-junction bolometer structure is shown in Fig. 4.27.

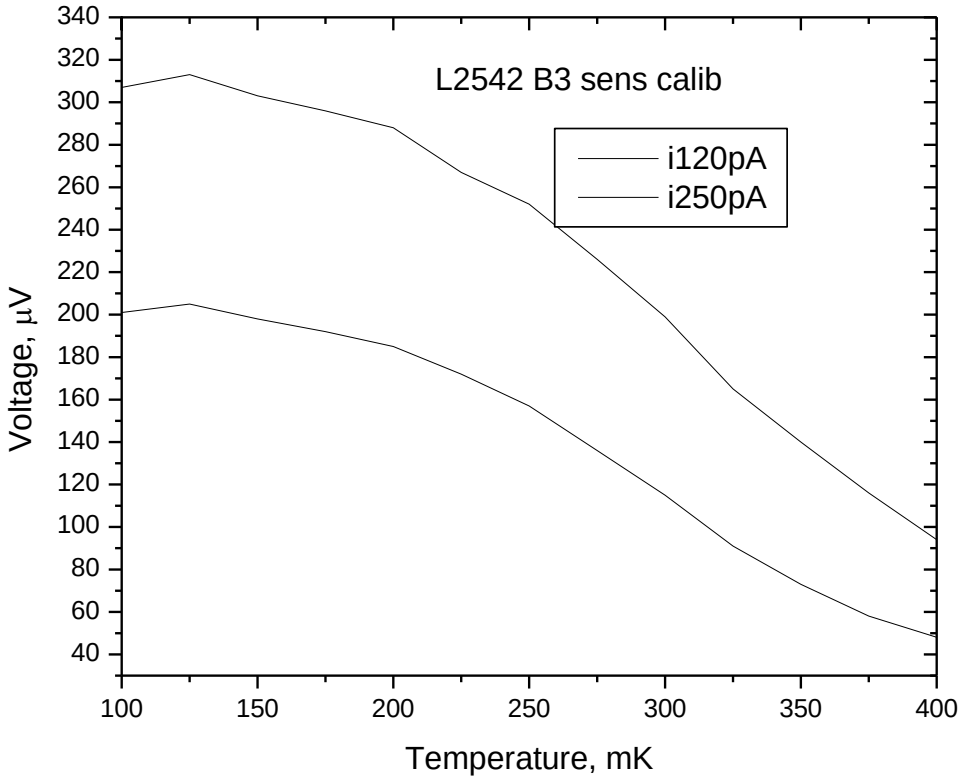

Figure 4.27. Voltage across sensor junctions at bias currents of 0.12 nA and 0.25 nA versus bath temperature

Next, a DC response as an indication of how the bolometric device reacts on heating was measured on our 4-junction structure fabricated on the same chip as the CEB arrays. We have measured the response to DC heating by applying a DC current to two tunnel junctions in a 4-junction test structure (Figure 4.26) and measuring the DC voltage across the other two junctions. The result of this measurement is shown in Figure 4.28.

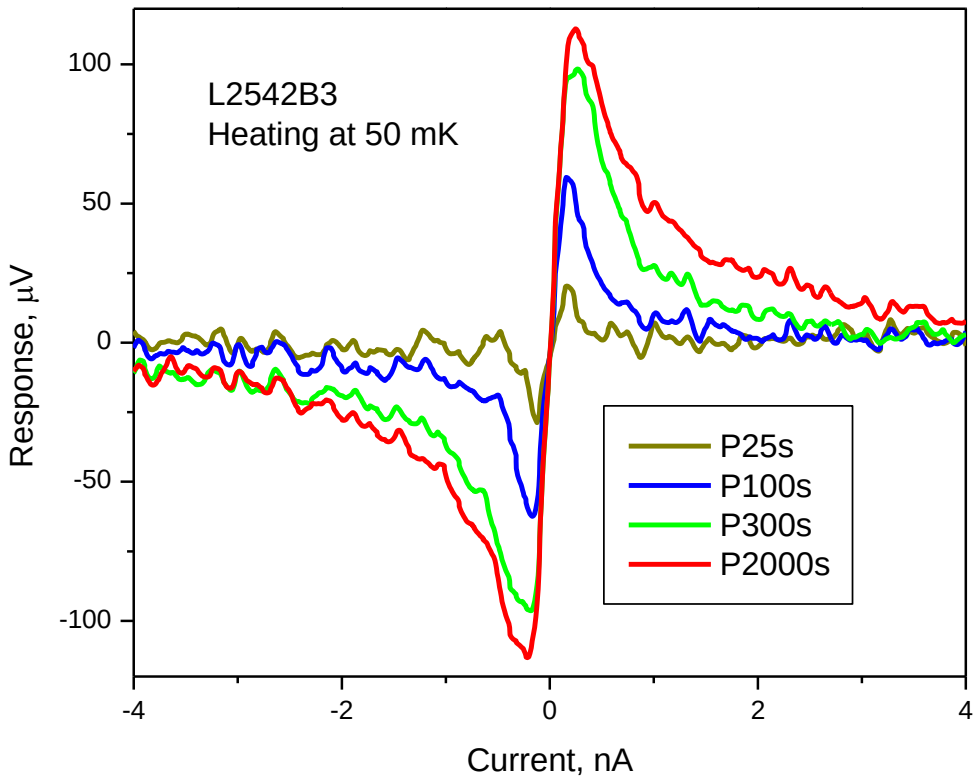

Figure 4.28. The voltage response of an absorber in a test structure to DC power dissipated in the absorber by applying DC current. The different curves represent response to 4 different values of DC power dissipated in the absorber: 25 fW, 100 fW (blue), 300 fW (green) and 2000 fW (red).

We shall now use our 4-junction test structure for an experiment on the measurement of the electron temperature that allows us to observe the electron cooling and measure the electron temperature independently, by using SIN junctions of different areas. Two of the SIN junctions in our structure (called here coolers) operate in electron cooling mode, while the other two junctions of smaller area (called sensors) were used for the temperature sensing as thermometers. The voltage across sensing junctions is then amplified and measured, Figure 4.29.

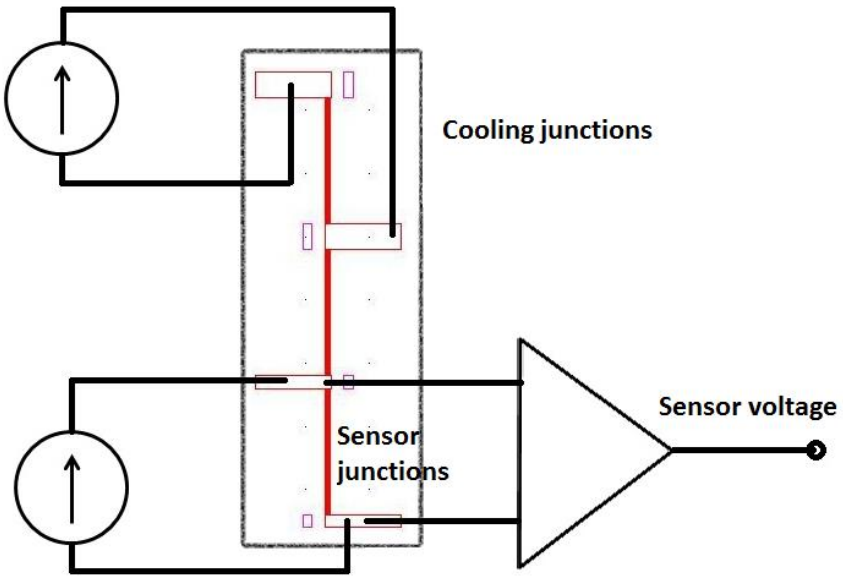

Figure 4.29. The schematic diagram of the cooling experiment. The top 2 junctions are cooling the absorber when a bias current is applied; the voltage across 2 sensor junctions (bottom) is read out.

The area of the cooling junctions was 0.48 μm^2, while the sensor SIN junctions used as thermometers had an area of 0.24 μm^2 each. A photo of such a structure is shown in Figure 4.30.

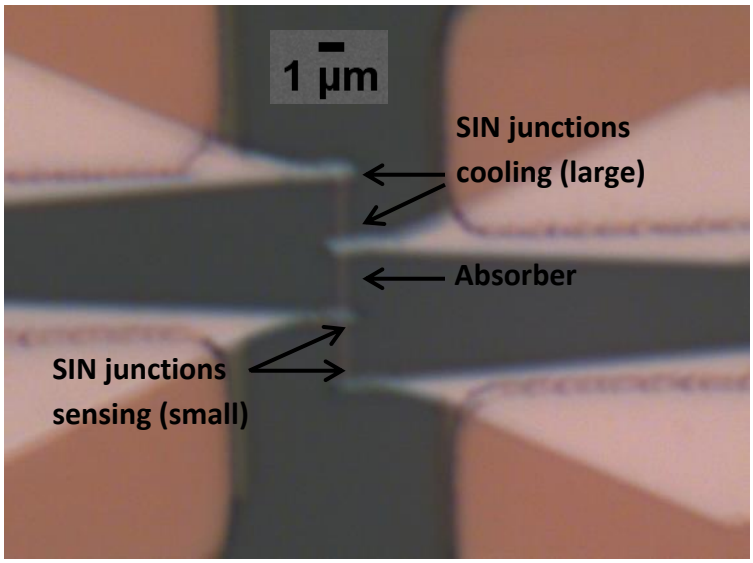

Figure 4.30. An optical image of a bolometer integrated in 4-probe structure.

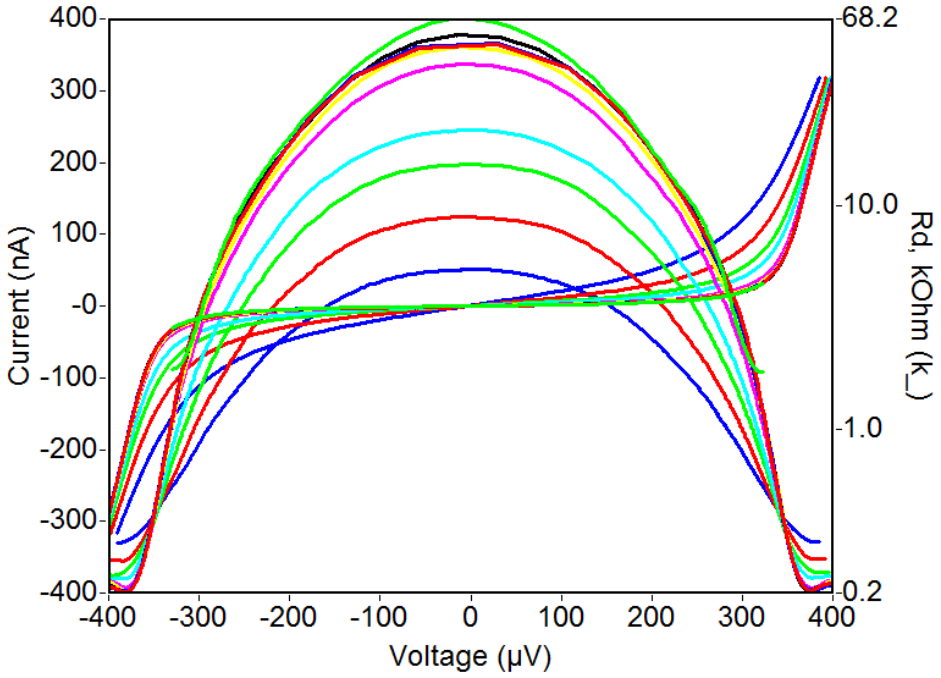

Figure 4.31. A family of IV curves of cooling SIN junctions at temperatures of 120 to 550 mK and the dynamic resistance versus bias voltage; curves at different temperatures are shown in different colours.

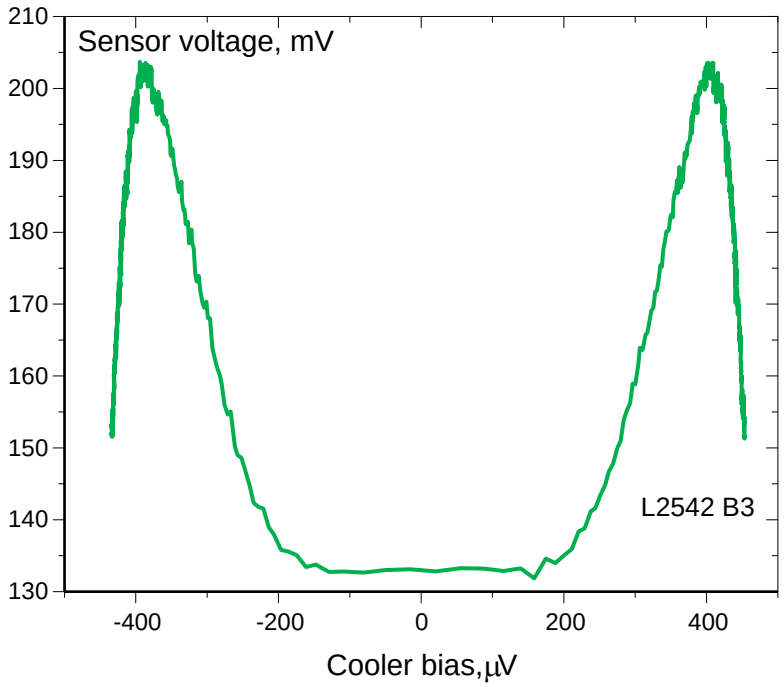

Figure 4.32. Sensor voltage versus the bias voltage across cooling junctions. At low bias voltages the temperature is close to the bath temperature of 280 mK, while at maximum cooling it corresponds to 125 mK according to the calibration by the curve in Fig. 4.27.

IV curves of the cooling SIN junctions measured at different temperatures are shown in Figure 4.31, the sensor voltage versus the phonon temperature at fixed bias current in Figure 4.27, and the voltage across the SIN thermometer on the SIN cooler voltage is shown in Figure 4.32 and Figure 4.33.

The electron cooling shown in Fig 4.32 can be considered as an underestimate as there is some electron heating in the SIN thermometer at low bias voltages, which can be seen in Fig 4.32. Apart from this, the coolers and the sensors are located at different ends of a 7 μm long absorber that results in a temperature gradient between them so the absorber temperature near the cooling junctions will be below that near the sensor that in addition heats a part of the

absorber artificially. Therefore, it seems interesting to estimate the electron cooling relying on the IV curves of the cooling junctions.

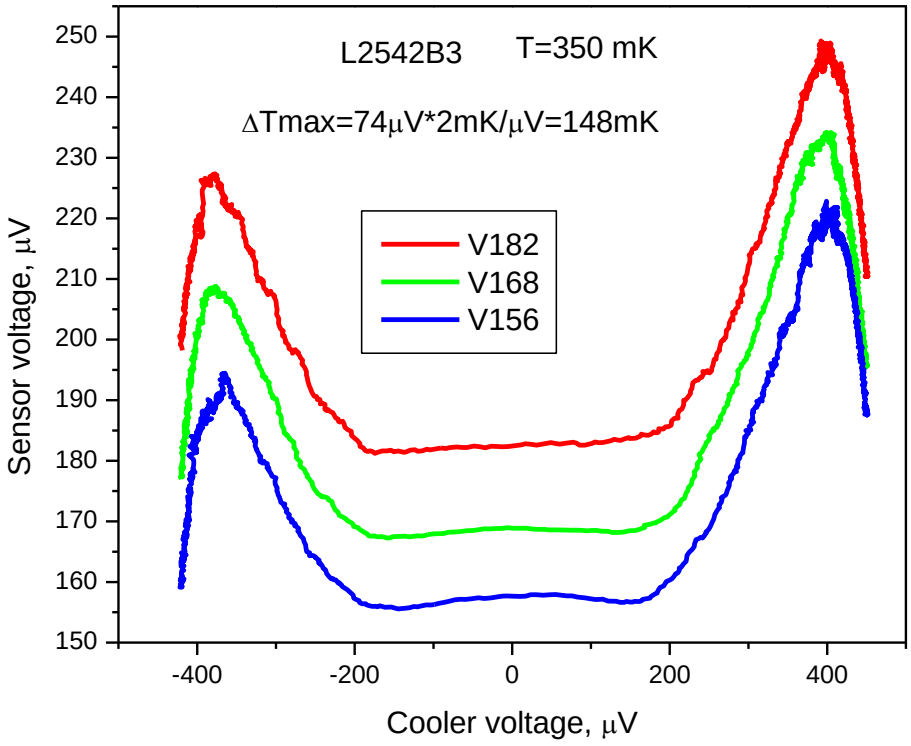

Figure 4.33. Example of electron cooling at 320 mK.

As can be seen in Fig 4.31, the electron cooling effect modifies the shape of the IV curve, as near the gap the electron temperature is significantly decreased. In reality, the structure is also affected by the external radiation and electromagnetic interferences that may cause the heating of the electron system and, as a result, regions with an electron temperature both below and above the phonon temperature can be presented in the IV curve.

These processes could be described by the thermal balance equation:

$$\Sigma\lambda\left(T_e^5 - T_{ph}^5\right) + P_{SIN}(V, T_e, T_S) + C_\lambda \frac{dT}{dt} = \frac{P_0}{N} + \frac{V^2}{R_S}$$

where $\Sigma\lambda(T_e^5 - T_{ph}^5)$ is the heat flow from the electron system of the normal metal to the phonon system, Σ is the material parameter of the absorber, λ is the volume of the absorber, T_e and T_{ph} are the electron and phonon temperatures of the normal metal; $P_{SIN}(V, T_e, T_S)$ cooling power by SIN junctions; C_λ is the heat capacity of the normal metal; P_0 is the background power load, and V^2/R_S is the heat load due to the leak resistance R_S. The accuracy of such modeling is rather low, as several parameters are included that are not possible to determine independently and exactly, such as the material parameter, effectiveness of electron cooling, heat capacity of the normal metal, background power load, effectiveness of the heat sink in the superconductor etc. In addition, the definition itself of the electron temperature becomes incorrect, because the energy distribution of the electron becomes different to the Fermi distribution. The number of electrons with energy above the Fermi level in the case of electron cooling turns out to be substantially less than that for the equilibrium state, while when heated by the incoming photons with energy higher than the superconducting gap, this number is considerably more than in the equilibrium. Hence, an equivalent electron temperature could be considered that can be defined as the temperature of the SIN junction in the equilibrium at which the same differential resistance is observed at the same bias voltage or current. Estimating an equivalent electron temperature for many different bias points allows plotting it versus the bias voltage. The same can be done for other IV

curves at different temperatures. As an example, three curves representing the equivalent electron temperatures versus bias voltage are shown in Figure 4.34 for the phonon temperatures of 540, 380, and 260 mK.

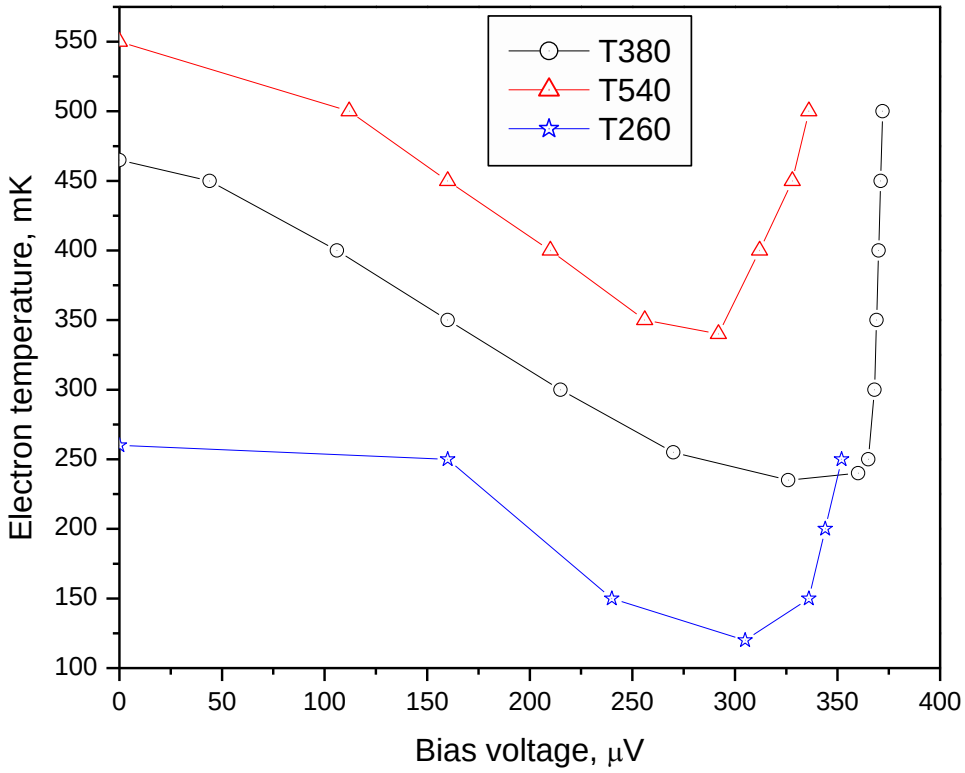

Figure 4.34. Equivalent electron temperatures versus bias voltage at phonon temperatures of 540, 380, and 260 mK.

As can be seen in Figure 4.34, at base temperatures of 540 mK and 260 mK at zero bias the electron temperature is close to the phonon one, while at 380 mK and zero bias some overheating up to 460 mK is observed. This overheating corresponds to an absorbed power of 0.24 pW. When shifting the bias point towards the gap, some cooling is observed down to 350 mK which corresponds to the cooling power of 0.4 pW. At the base temperature of 540 mK

the maximum cooling power amounts 0.9 pW, while at 260 mK it is reduced to 20 fW. In general, the cooling power can be expressed by the formula [100]:

$$P_c = \frac{\sqrt{2\pi\Delta kT}}{2eR}\left(\frac{\Delta}{e} - V\right)\exp\left[-\frac{\Delta - eV}{kT}\right]$$

The exponential decrease of the cooling power with the decreasing base temperature results in the fact that it is difficult to obtain electron temperatures below 100 mK using Al-based SIN junctions with a gap of around 200 μV. Even small overheating by interference currents or background radiation will not allow for cooling down to 100 mK. In order to increase the cooling power, a superconductor with a gap of 60 – 80 μV must be used.

The increased electron temperature at zero bias can be explained by a process of tunneling of hot quasi particles from the superconductor to the normal metal because the density of quasiparticles above the gap exceeds the density of electrons in the normal metal. As a result, hot quasiparticles leave the superconductor and tunnel to the normal metal, which results in the electron temperature of the normal absorber becoming higher than the phonon temperature

4.2.6. Conclusions

In this chapter part, the measurement results of a Cold-Electron Bolometer array deposited across a cross-slot antenna on a planar substrate have been presented. The devices have been fabricated using the Advanced Shadow Evaporation technique, with the absorber deposited prior to the superconducting counter-electrodes. The detector is a potential candidate for the next space cosmology missions and is also of interest to ground-based experiments as a result

of the simplicity of its integration to planar circuit technology, high saturation power and fast response.

Cold-Electron Bolometer array integrated in a cross-slot antenna was measured in a ^{3}He sorption pump refrigerator within a temperature range around 0.3 K. The optical response with a NETD of 650 μK/Hz$^{1/2}$ was measured using a cryogenic black body radiation source; the estimated noise equivalent power in the current biased mode as read by room temperature op-amp electronics amounts $NEP = 2.2 \cdot 10^{-17}$ W/Hz$^{1/2}$. Voltage to temperature response dV/dT = 8.8 μV/mK, voltage to RF power response $dV/dP = 1 \cdot 10^{8}$ V/W, dark $NEP = 6 \cdot 10^{-18}$ W/Hz$^{1/2}$, and a dynamic range over 40 dB were measured at T = 280 mK for an array of Cold-Electron Bolometers integrated in a cross-slot antenna. Electron cooling of 70 to 125 mK at different bias points improves the NEP of such a detector and increases the dynamic range. The measured characteristics approach the requirements for the balloon-borne experiment BOOMERANG and CEBs could be considered for future balloon and ground-based radio telescope experiments.

Chapter 5

Integrated superconductive phase switch for cosmology instruments

In this chapter, we will discuss planar NbN phase switch circuits that were designed, fabricated, and tested in collaboration between Chalmers and Oxford University, in order to replace mechanical switches for modulating microwave signals in waveguides. The investigated planar phase shift circuits integrated with back-to-back finlines were fabricated by the author of this thesis; some devices were tested by him both at Oxford and at Chalmers.

We will examine the switching characteristics that were measured at a switching rate of up to 100 kHz. We will demonstrate that the switching speed of the device is well above the speed required for phase modulation of astronomical instrument and was mainly limited by the time constant of the measurement system (~10 μs). Real switching time of a nanobridge should be much shorter, about 30 picoseconds, when not limited by thermal effects.

The polarization of an electromagnetic wave can be determined by measuring the Stokes parameters I, Q, U, V, defined in Chapter 1, where I is the total intensity, V measures the degree of circular polarization and Q and U measure the degree of linear polarization in two orthogonal directions [18]. In the pseudo-correlation polarimeter, discussed in Chapter 1, the signal received by each of the focal plane horns is split into two linear polarizations using an orthomode transducer (OMT). The signals are then converted into circular polarization using a quadrature hybrid, one of those is phase modulated and then the two signals are converted to linear polarization and measured by the detectors (see Figure 1.6 in Chapter 1). The output signals D_1 and D_2 measured by the detectors are [18]:

$$D_1 = I - Q\cdot\cos\psi - U\cdot\sin\psi \tag{5.1}$$

$$D_2 = I + Q\cdot\cos\psi + U\cdot\sin\psi \tag{5.2}$$

According to the equations (5.1) and (5.2), the output is sensitive to I, U and Q Stokes parameters, defined in Chapter 1, and it is therefore possible to determine the linear polarisation parameters by taking the difference of the detector outputs. By switching the phase difference between 0 and 180 degrees, the U term remains zero and Q is measured, while by changing the phase difference between 0 and 90 degrees we switch the output between Q and U [18].

The methods proposed for phase modulation in cosmology instruments, such as a rotating half-wave plates [15], Faraday rotators [101], and rotated waveguide sections, suffer from significant RF losses [101], use rotating mechanical parts, are difficult to fabricate and do not provide the required accuracy. There is therefore an urgent need for developing phase

modulation using planar circuits [16] for cosmology instruments. Planar high-frequency circuits are easy to fabricate and they do not use rotating components. It will allow for fabrication of the whole polarimeter in planar circuit technology with the horn and OMT only implemented in waveguide while the rest of the array will be integrated in the detector block. This will solve the problem of phase modulation at high frequencies and will allow for fabricating huge arrays reliably and cheaply [18].

5.1. Properties of the RF circuit

An electromagnetic wave propagating along a lossless and matched planar transmission line [18] is transmitted in the Open mode and reflected in the Closed mode, when shunted by a switch. A low loss transmission and high reflection can be achieved by proper choice of the impedance Z across the terminals of the transmission line and the characteristic impedance Z_0. If the impedance of the load changes between $Z_{off} << Z_0$, and $Z_{on} >> Z_0$, the device switches from the Closed to the Open state respectively.

The On/Off switch is formed by fabricating a directly or capacitively coupled superconducting nanostrip across the electrodes of the transmission line (see Figures 5.1 (a) and 5.1 (b)). By applying a bias current signal through the superconducting nanostrip, it can be switched from the superconducting state with impedance given by

$$Z_{off} = i\omega(L_g + L_k) + 2/i\omega C = (2 - \omega^2 LC)/i\omega C \quad (5.3)$$

to the normal state with an impedance

$$Z_{on} = R_N + i\omega L_g + 2/i\omega C = R_N + (2 - \omega^2 L_g C)/i\omega C, \quad (5.4)$$

where R_N is the normal resistance and L_g, L_k and L are respectively the geometrical, kinetic and total inductances of the strip [18]. At resonance ($\omega^2 LC = 2$), the impedance in the superconducting state becomes small, resulting in high reflection, which means that the switch is closed. If $\omega L << R_N$, then the impedance in the normal state is mainly determined by the normal resistance of the nanostrip. The material and geometry of the nanostrip are therefore chosen to make R_N as high as possible to ensure that its normal resistance $R_N >> Z_0$, making the switch open in the normal state, where Z_0 is the characteristic impedance of the slotline.

Niobium Nitride is the material that meets this requirement. NbN is a superconductor with a relatively high critical temperature (up to 14 K) that in the normal state becomes a conductor with relatively high specific resistance. In our preliminary measurements, a 22 nm thick NbN film displayed about 70 Ω per square sheet resistance, which is consistent with the table value of 200 μΩ·cm for the specific resistance of NbN. On the other hand, its characteristic temperature (7 to 14 K for our films) allows testing our devices at liquid He temperature, i.e. around 4 K.

In our work, most of the devices used were DC coupled to the finlines. This is due to the simplicity of fabricating NbN nanobridges in one layer with the finlines that can easily be patterned in one e-beam exposure. While this approach does not yield best performance as it does not provide strongest mismatch between the nanobridge and the finline in Open state due to kinetic inductance of the nanobridge, it still allows us to verify the concept of switching the RF signal between Open and Closed states using planar phase switch (PS) devices.

For example, a 20 nm thick and 1 μm wide niobium nitride film nanostrip of length l = 5μm has a normal resistance of ≈ 500 Ω (assuming the specific resistance of NbN of 200 μΩ·cm), a geometrical inductance of ≈ 3 pH and the kinetic one of ≈ 12.6 pH [18]. The DC coupled nanobridge with such dimensions will thus display a considerable total inductance, yielding relatively high impedance in the Closed state, comparable to the characteristic impedance of the finline (~70 Ω). This could deteriorate the performance of our devices to some extent compared to the case with capacitive coupling; but making and testing DC coupled devices will allow us to verify the concept of switching the RF signal in the waveguide by shorting the transmission line with a NbN nanostrip, using a simple and straightforward approach for fabricating DC coupled phase switch devices. Fabricating capacitively coupled devices is a bit more challenging task and will be considered later in this chapter.

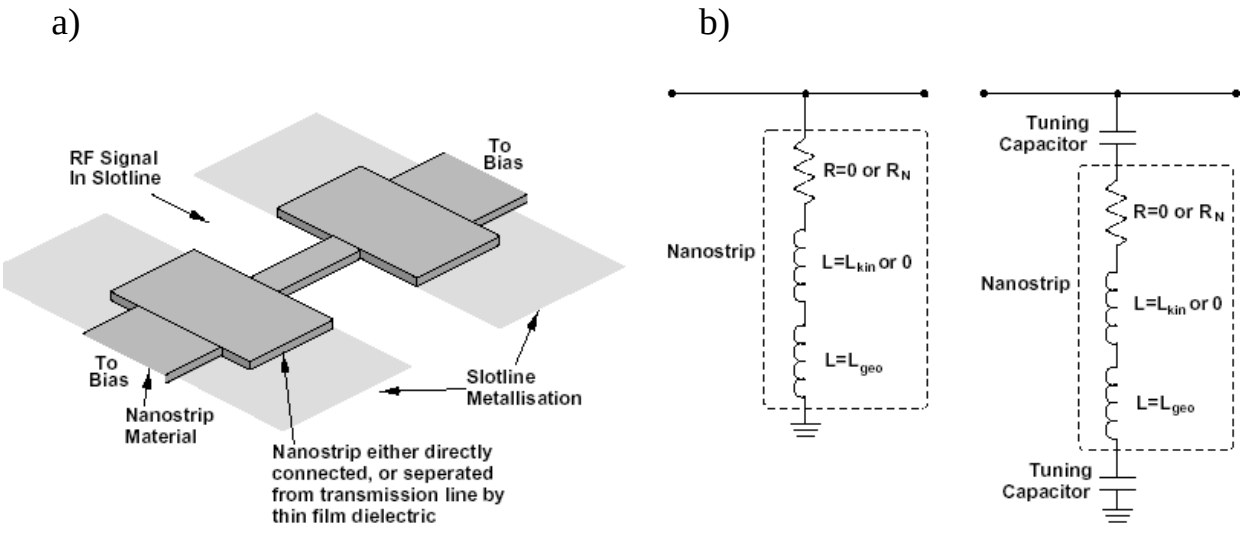

Figure 5.1: (a) Geometry of a nanostrip switch in slotline transmission line. (b) Equivalent circuits for the directly and capacitively coupled nanostrip switches. [18]

5.2. Chip layout and fabrication

The chip layout is shown in Figure 5.2. Phase switch devices were fabricated on quartz wafers ("Fused Silica"). Quartz was chosen as the material for the substrate due to a lower dielectric constant of quartz compared to Silicon. Crystalline quartz was used for the fabrication of a few samples, and was later replaced by fused quartz (fused silica).

There were 24 chips on a 2-inch wafer, 7×7 mm each, and the layout of a single chip included 5 finline-integrated phase switch devices with different nanobridge widths, varying between 0.3 μm and 2 μm. Later, the layout was modified so that the nanostrip width varied between 0.3 μm and 1 μm. Most of the devices were used for testing but the devices with widths of 0.5 to 0.8 μm were tested most as they showed the best RF switching.

The devices were fabricated at Chalmers by depositing the nanostrip across the terminals of a back-to-back unilateral finline on a 200 μm thick quartz substrate. The fabrication process of the finline coupled nanostrip devices included two lithography steps, namely a photo lithography for fabricating the contact pads and e-beam lithography for patterning the structures made of NbN. The whole fabrication procedure is described in detail in Chapter 2 and is shown here in Fig. 5.3.

First, a thin Ti film was deposited on a quartz substrate using magnetron sputtering of Ti. This is a buffer layer deposited prior to NbN for better adhesion and in order to improve the superconductive properties of the final structure. This allows to achieve much higher critical

temperatures compared to our previously published data [45, 102]. Next, a NbN film was deposited by magnetron sputtering of a niobium cathode in an argon-nitrogen plasma mixture (Fig. 5.3(a)). In our previous work [18, 102], the NbN molecules were deposited on a hot

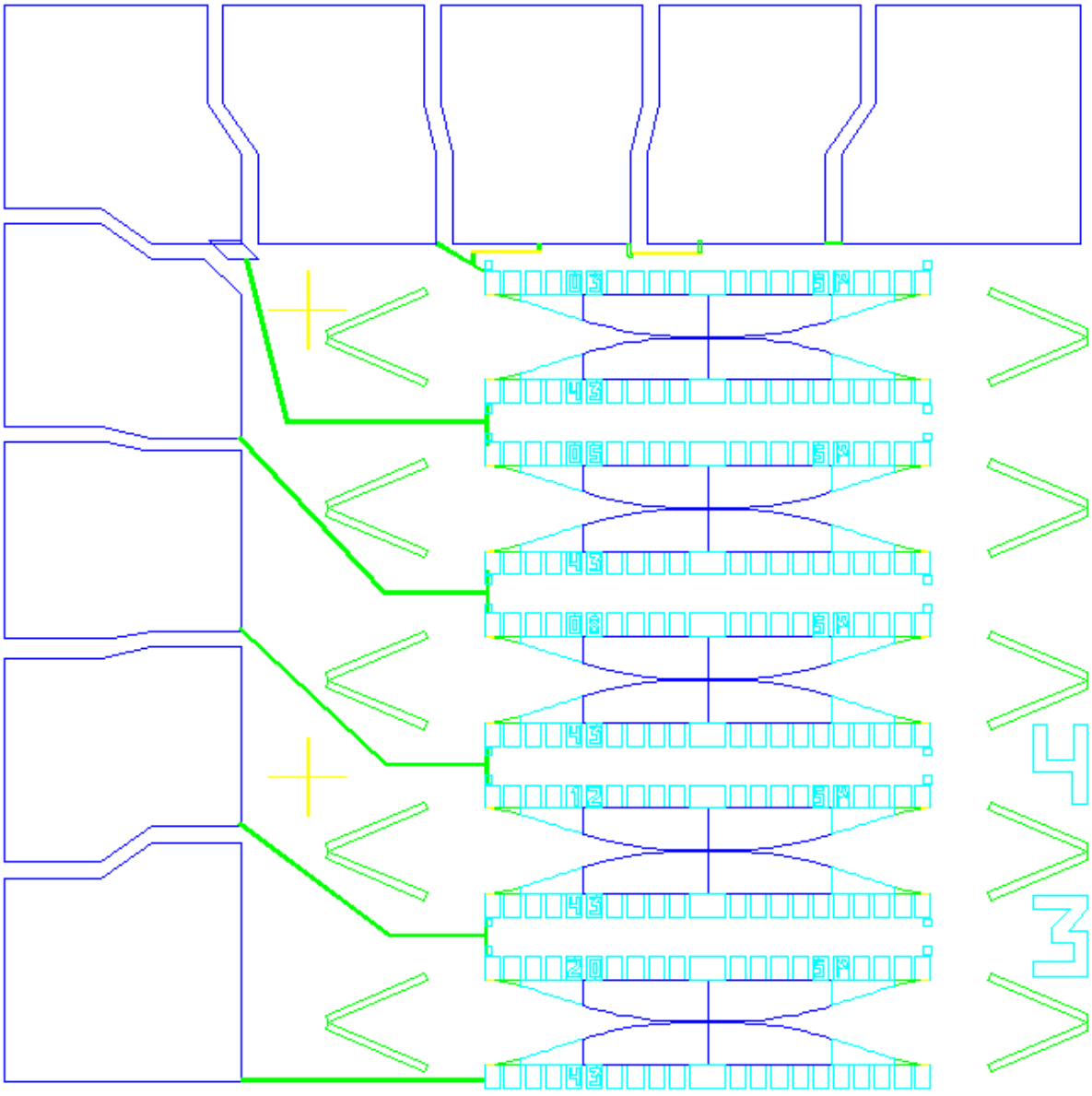

Figure 5.2. Chip layout with 5 phase switch devices integrated with back-to back finlines (AutoCAD)

substrate which was heated by a lamp before and during the deposition process. Now, we used room-temperature processes for the fabrication of devices presented in this thesis. The resulting critical temperature (11-12 K) is somewhat lower compared to films produced with heating (14 K) but sufficient for the purposes in this thesis.

Two layers of resist are then spun on the wafer: a lift-off resist LOR3A and a photoresist Shipley S-1813. After baking both of the resist layers, the wafer was exposed to UV radiation at a wavelength of 400 nm through a chromium mask to pattern the gold pads and the finlines. After the development of the photoresist, an undercut was formed in the lift-off resist (Fig. 5.3b). The wafer was then cleaned in the etching process by soft oxygen plasma and a 10 nm layer of chromium and 100 nm of gold were evaporated through the resist mask and lifted off (Fig. 5.3c). The finlines are thus made of NbN covered with ~100 nm of gold.

The pads and the finlines formed at this stage are shown in Figure 5.4. The next step of the process was the e-beam lithography for the patterning of the NbN nanostructures. First, the negative e-beam resist SAL-601 was spun on the wafer and baked (Fig. 5.3d). Then the NbN structures were patterned by an e-beam exposure. After the development of the e-beam resist, the NbN structures were created by the reactive ion etching in CF_4 plasma (Fig. 5.3e). The rest of the resist was then removed in the Shipley 1165 remover (Fig. 5.3f) and finally the wafer was diced using a diamond saw. An example device with a 5 μm long nanostrip integrated in a finline is shown in Fig. 5.5.

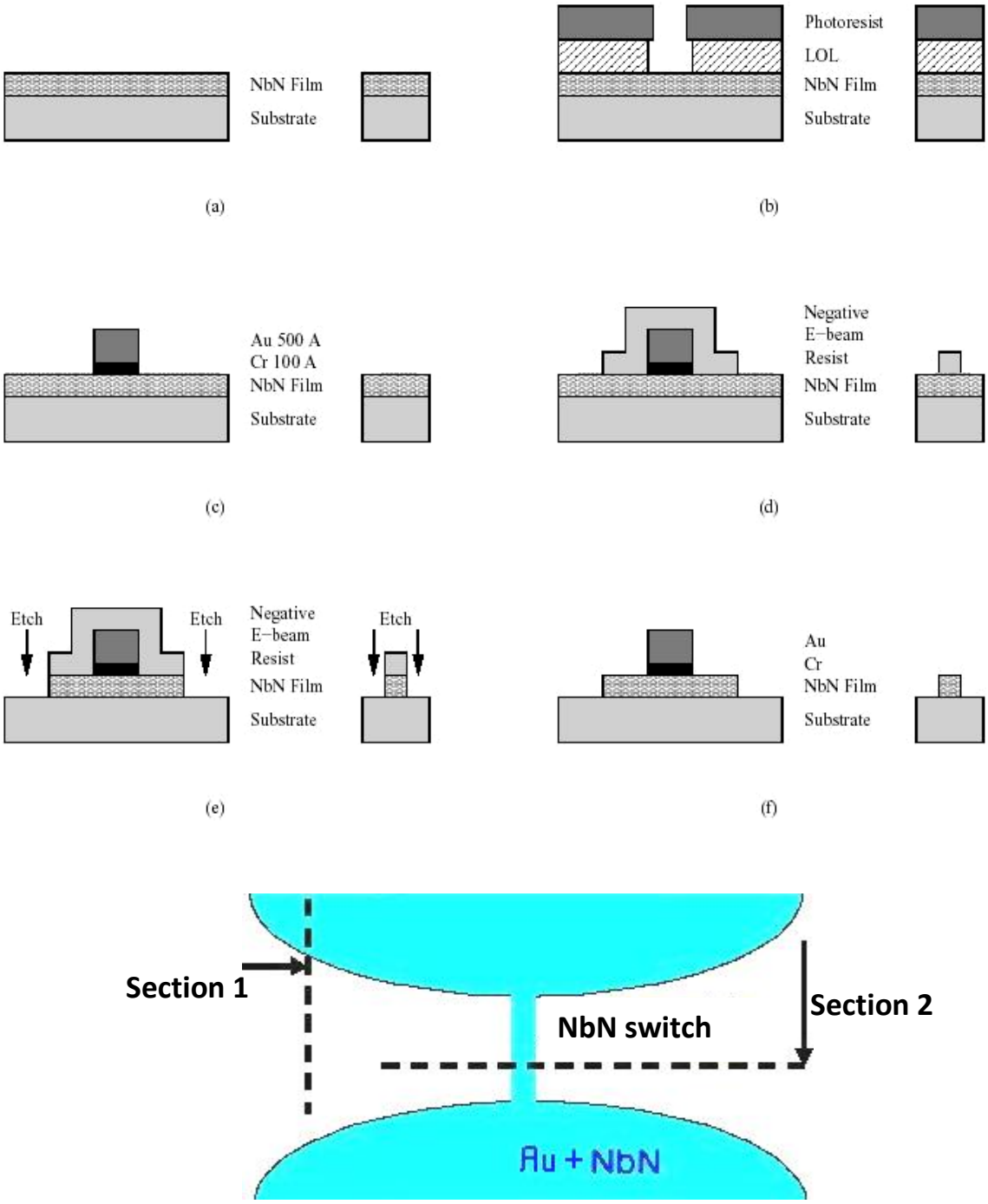

Figure 5.3: (Top) Fabrication of the nanostrip across a unilateral finline [18, 102]. In each picture, the fabrication steps are shown on the left-hand side for the Section 1, the finlines, and on the right-hand side for the Section 2, the nanobridge. The Sections 1 and 2 are shown in the schematic (bottom).

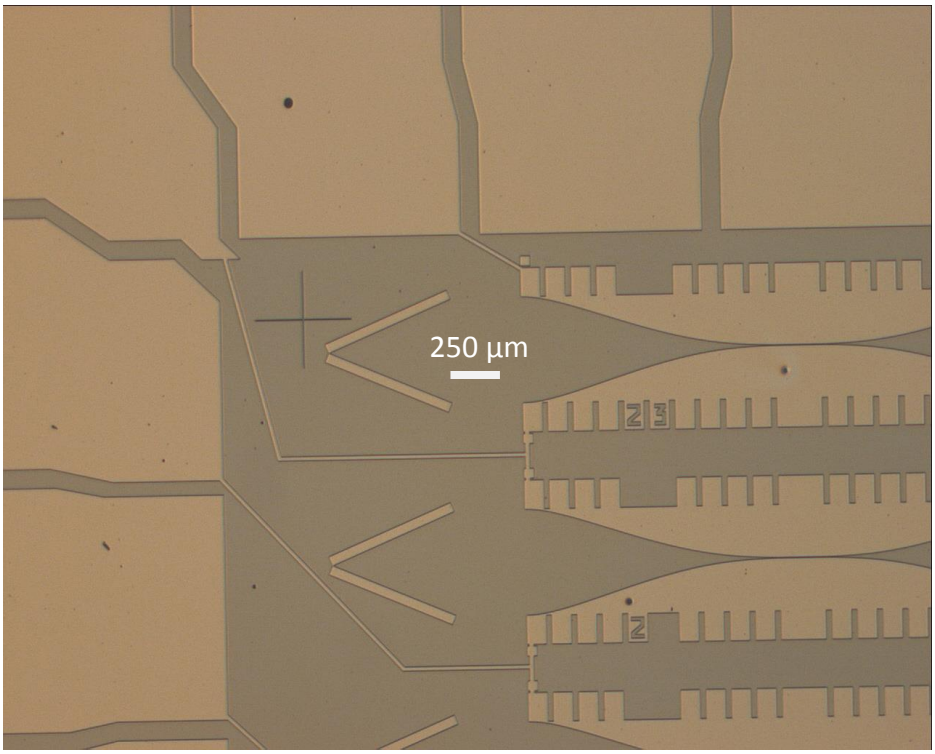

Figure 5.4. Gold pads and finlines formed by photo lithography and thermal evaporation

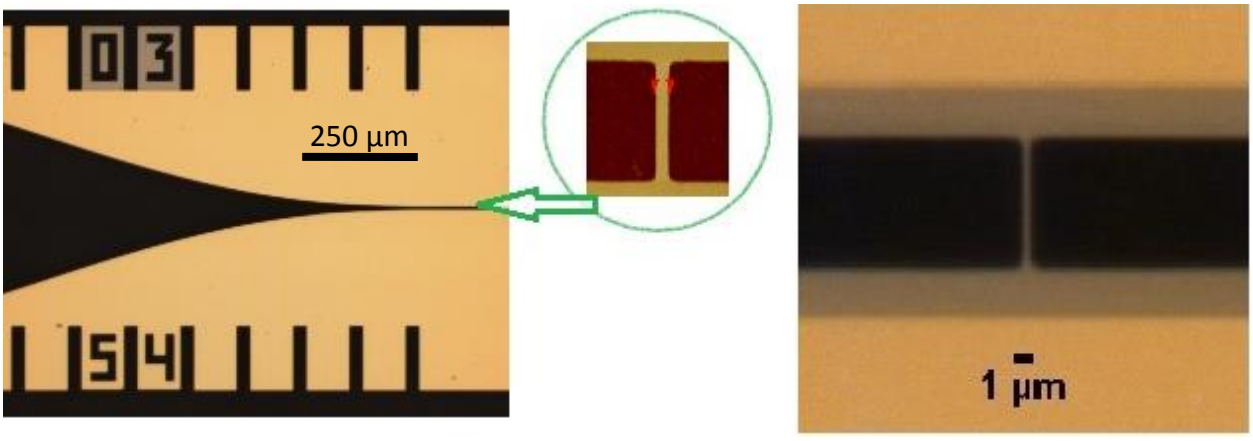

Figure 5.5. An image of a NbN nanostrip switch showing the back-to back finline device [16, 18].

5.3. Preliminary DC tests

Several samples with the finline gap of 5 μm and a characteristic impedance of 70 Ω were DC tested at 4.2 K. The thickness of NbN film was 22 nm and width ranged from 0.2 to 0.8 μm. The critical temperature of the NbN film was about 12 K, and the critical currents for different nanostrip widths varied from 1 to 2 mA.

The IV curves and DC switching of the fabricated PS devices were tested at Oxford by dipping them into liquid He using a dipstick. An IV curve obtained in current-biased mode is shown in Figure 5.6. In this figure, a jump from the superconducting state to the normal one can be observed when applied current exceeds the critical value. After decreasing the current, the device remains in the normal state at currents down to a lower value than the critical one (Figure 5.6). When decreasing the current even further, the device becomes superconducting again and so on.

Time domain DC switching was observed by applying a square-wave current to the PS device. In Figure 5.7 one can observe the current changing rapidly from non-zero value to a higher value, while voltage changes from zero to a finite value at the same time. This is an indication that the device toggled between the normal and the superconductive states.

The time scale seen on the screen is 250 μs per division so the delay time was no more than 30 μs. Since long coax cables were used, with stray capacitance and some series resistance in wires, one can assume that the relaxation time is determined mainly by the above factors.

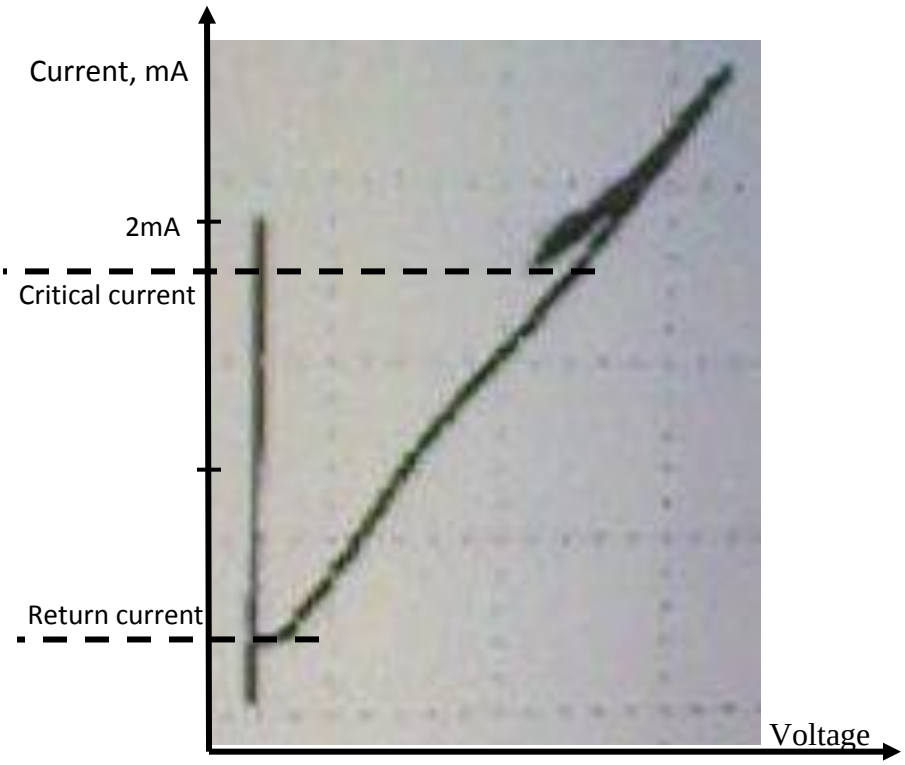

Figure 5.6. The IV curve of a PS device, measured in liquid He using a dip-stick.

The above time-domain measurements of the switching were performed at frequencies from 100 Hz to 100 kHz. A time delay of few microseconds was observed at the edges of the modulation signal, which is negligible compared to switching period (Figure 5.7). The delay is caused by the RC chains in the measurement setup, which was confirmed by measuring the RC-delay of the experimental setup without the nanoswitch device.

This result is consistent with published data on this subject, e. g. [103] where the delay in switching of a NbN strip was less than 36 ps or switching rate up to 16 GHz. The required switching speed for large format interferometers is about 100 Hz.

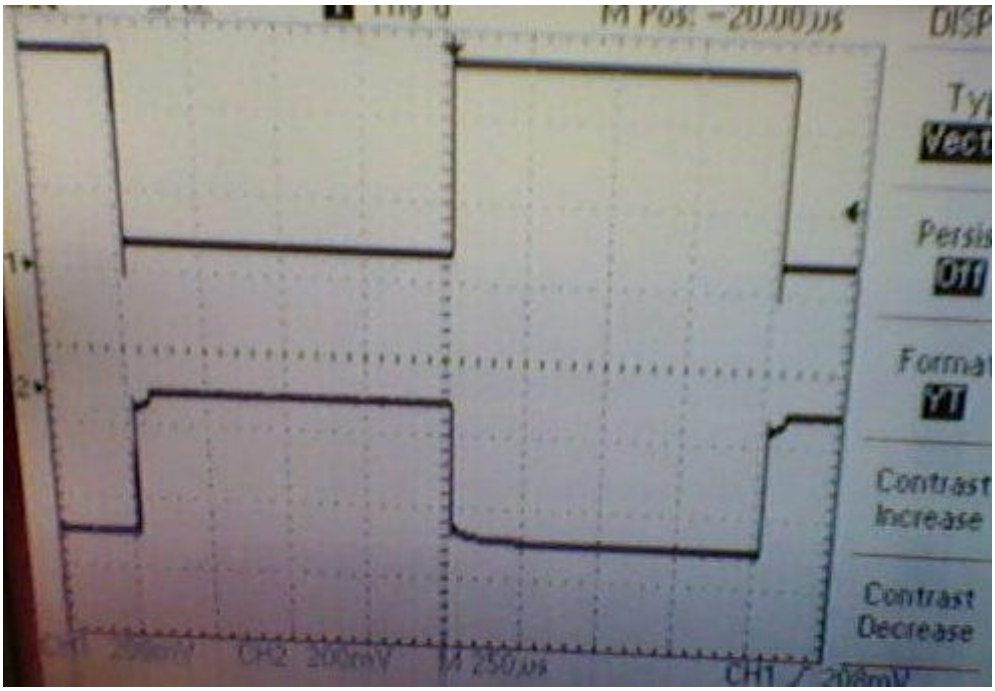

Figure 5.7. DC test of the finline nanostrip in time domain, performed in Experimental Radio Cosmology Lab at Oxford. The upper trace is the bias current and the lower one is the output voltage across the strip.

5.4. RF testing of the phase switch

After DC testing, the wafers were diced by a diamond saw to the width corresponding to the groove size in the waveguide of 0.55 × 1.1 mm in cross section. The phase switch finline chip mounted in the waveguide is shown in Figure 5.8.

A detector based on an SIS junction was used for measurements of the signal transmitted by the finline at 230 GHz. The measurement of the current–voltage characteristics of the SIS junction allows determining the signal level at the output of the phase switch. In this

experiment, the phase switch device and the SIS device were mounted in the same RF block and operating at the same temperature (around 4K), as shown in Figure 5.9.

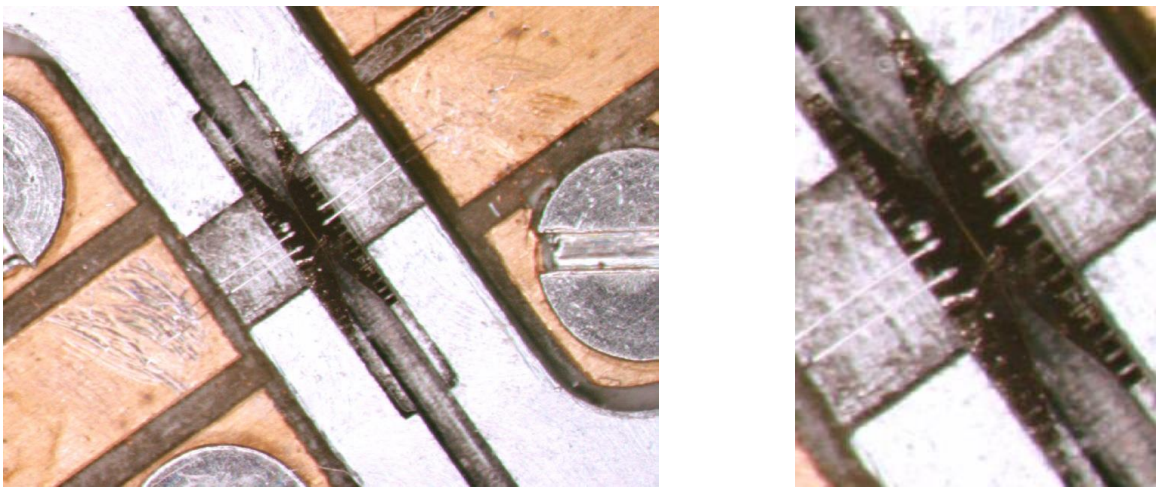

Figure 5.8. Phase Switch device mounted in a waveguide, different zoom

The SIS device (Figure 5.10) is placed across a unilateral finline deposited on a quartz substrate and consists of a Nb/Al_2O_3/Nb trilayer structure fabricated using Nb technology. In the system used for RF testing at Oxford University, the local oscillator consisting of Anritsu MG3692B signal generator and Radiometer Physics 2008004b frequency multiplier chain created a signal at 198-252 GHz by generating a signal at 11-14 GHz and then multiplying the frequency by the factor of 18. The RF signal was fed through a horn into the input of the waveguide with the finline chip and the detector. The RF block fabricated in Oxford workshop (shown in Figure 5.9) with the 0.55 × 1.1 mm waveguides contains both the phase switch device and a the SIS detector (Figure 5.10) with an option to suppress Josephson current by magnetic field produced by a Nb coil around the finline chip with the SIS device (Figure 5.9,

left). The block with the phase switch device and the SIS detector was cooled down to 3.8 K using a HELIOX Pulsed Tube Cooler.

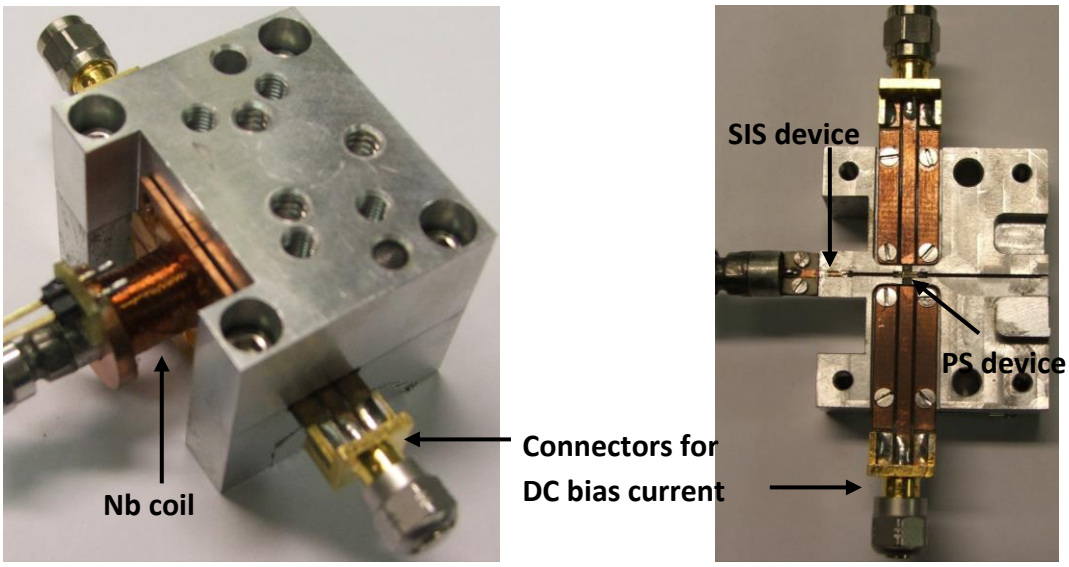

Figure 5.9 (Left) RF block fabricated in Oxford, with a coil for suppressing Josephson current with magnetic field; (right) the top view of the RF block, with Phase Switch and SIS device mounted.

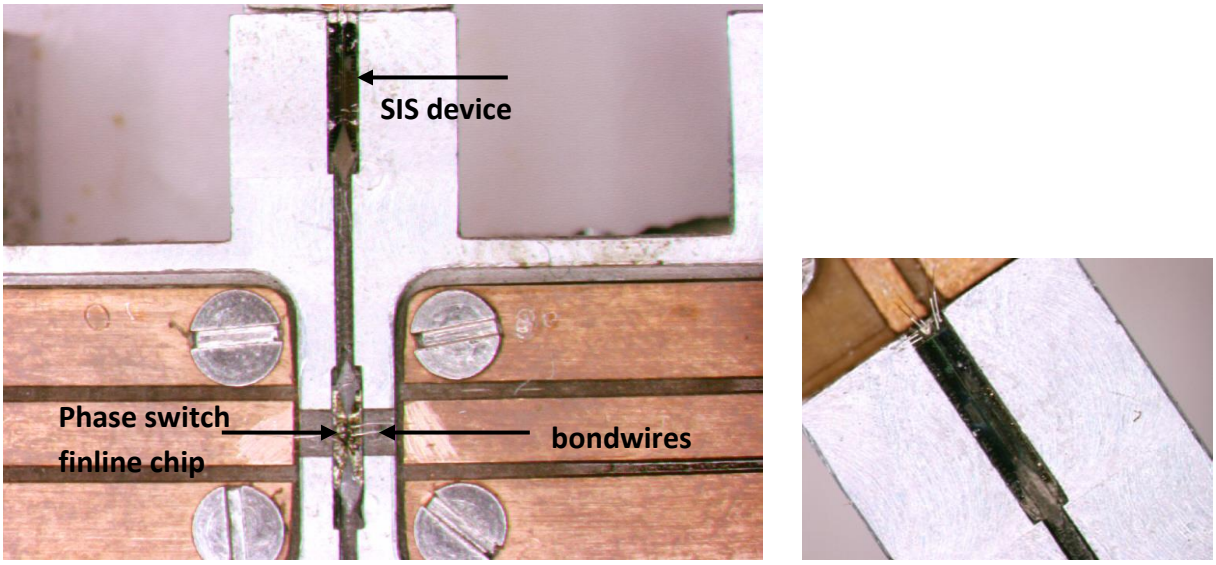

Figure 5.10. (Left) Phase Switch and SIS devices mounted in the waveguide.
(Right) Enlarged SIS device

The experiments with PS and SIS devices mounted in the same split-block were conducted in collaboration with Dr. Christopher North [5], being a DPhil student at Oxford Astrophysics.

The IV curve of the SIS detector (Figure 5.11) is pumped by incoming RF signal which results in photon steps on IV curve, as a result of photon-assisted tunnelling. The steps on IV curves of SIS detector for phase switch device in Open and Closed state and RF signal at 243 GHz are shown in Figure 5.11, right. Multiple IV curves correspond to several cycles of bias voltage sweeping in both directions (Figure 5.11).

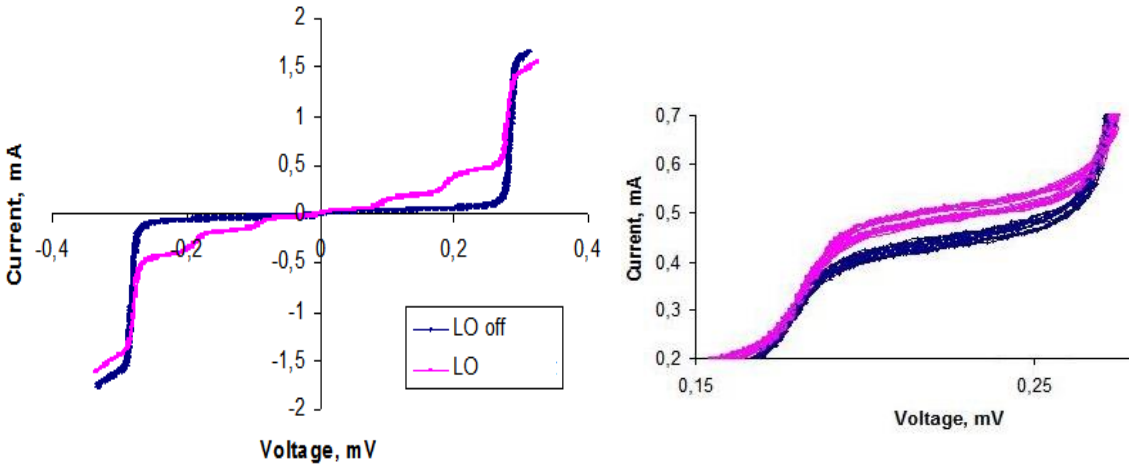

Figure 5.11. (Left) IV curves of SIS detector with and without RF signal; (Right) Steps on IV-curve corresponding to open and closed state of the switch.

In the next experiment, the RF signal was modulated by a chopper at 115 Hz and the phase switch was switched on and off 8 times per second by modulating the bias current between zero and 1-2 mA. An SR830 DSP lock-in amplifier made by the company Stanford Research System was then used for demodulating the RF signal in order to distinguish the signals in On and Off positions and to reduce the noise coming from the SIS detector. The voltage across

the phase switch device in time-domain and the demodulated signal after the lock-in amplifier are shown in Figure 5.12. The reference signal for the chopper and the current of SIS detector modulated by chopper at 115 Hz and by phase switch at 8.13 Hz are shown in Figure 5.13.

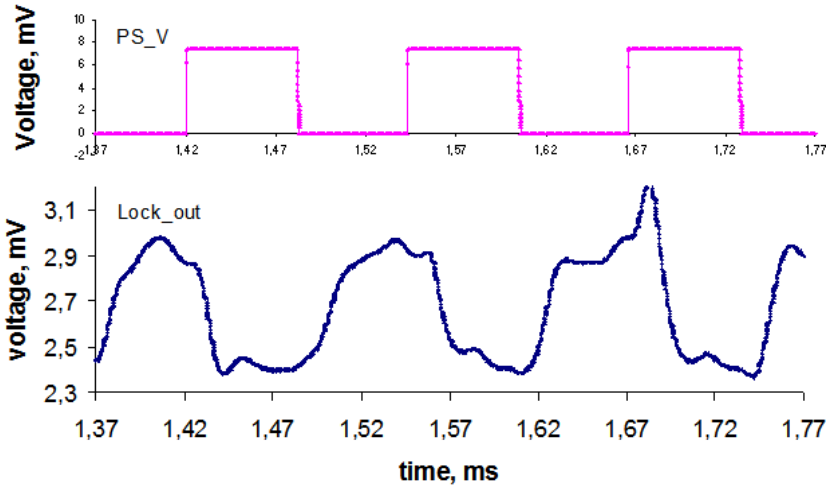

Figure 5.12. (Top) the on/off voltage across the phase switch device. (Bottom) The demodulated signal after the lock-in amplifier.

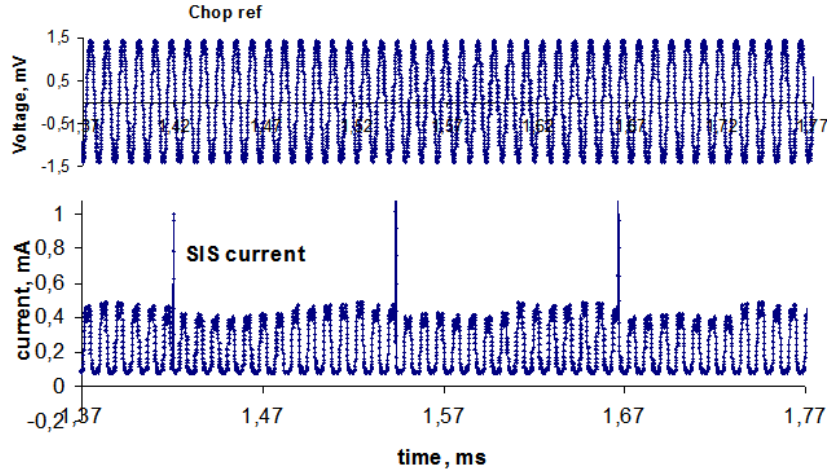

Figure 5.13. (Top) Chopper reference signal; (Bottom) The current of SIS detector modulated by chopper at 115 Hz and by phase switch at low frequency (8.13 Hz)

The experiments above confirm that switching the nanostrip between the superconducting and normal states changes the finline transmission. The modulation was relatively low, about 5 dB. At some frequencies, even the inverted switching was observed, i.e. the transmission was lower in the normal state than in the superconducting state. Most tested devices display such a behavior around 235 – 245 GHz, and the proper switching of right polarity at ~200 - 205 GHz. This is a clear indication that the kinetic inductance limits the switching ability, which effect becomes less significant at lower frequencies around 200 GHz and degrades switching at higher frequency ~225 GHz and then leads to the inverted switching at even higher frequencies, 235 - 245 GHz.

5.5. Further development of the switches

It has already been shown that using capacitive coupling to the finline (as shown in Figure 5.1) one can achieve far better performance of phase switch devices than with DC coupling between the nanobridge and the finline [18]. Therefore, a new technology for fabricating capacitively coupled phase switch devices with improved performance became necessary. The devices with capacitive coupling to the finlines were fabricated according to the following procedure. First, a NbN layer was deposited on a quartz substrate using an adhesive Ti layer. Then, gold pads were patterned and deposited using e-beam lithography and thermal evaporation (Fig. 5.14a). As the next step, the NbN finlines were patterned using e-beam exposure and reactive ion etching (Fig. 5.14b). Next, a capacitive layer was deposited on the top of the NbN finlines as a bottom layer for the capacitors (Fig. 5.14 c, d). Two flat

capacitors of 2×2 μm^2 in series should yield a total capacitance of 50 fF. Later, an insulating layer of SiO_2 of ~100 nm thickness was formed as shown in Figure 5.15 and, finally, DC coupling to the nanobridge was realised by DC leads from bondpads to the nanobridge over the insulating layer on the top of the finline, as shown in Figure 5.15. This allows for DC biasing of the nanobridge without DC connection to the finlines.

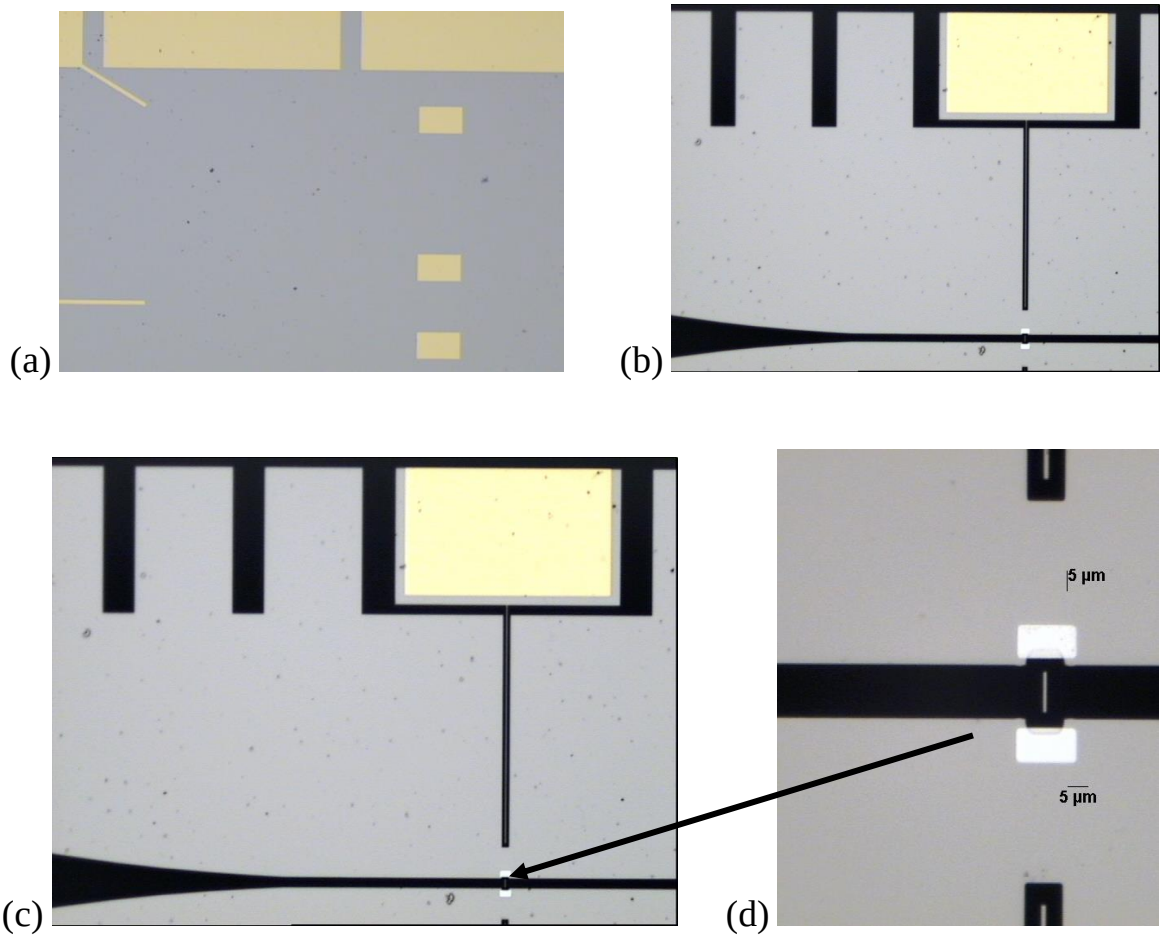

Figure 5.14. New phase switch devices during the fabrication process at different stages. (a) After depositing gold bondpads and contact pads; (b) NbN finlines patterned; (c, d) capacitive layer created as a bottom of flat capacitors, different zooms.

Testing of the capacitively coupled phase switch devices was performed in a HELIOX cryostat at the temperature of 3 K. The IV curve of the devices displayed the typical shape for SIN junctions with a characteristic superconducting gap for NbN. This is an indication that an oxide layer was built between the DC leads and the nanobridge. This could happen due to oxidation of Nb in the air because of possible admixture of Nb in the NbN nanobridge. Another possible reason would be residues of the negative resist left on the surface of NbN due to overheating during the plasma etching of NbN through a resist mask. This issue is less important for the DC coupled devices described in the previous section as in that process no metal layer was deposited on the top of the NbN nanobridge after its patterning. The DC connection was realized by patterning the NbN nanobridge in one layer with the finlines, i. e. no interface was assumed in between.

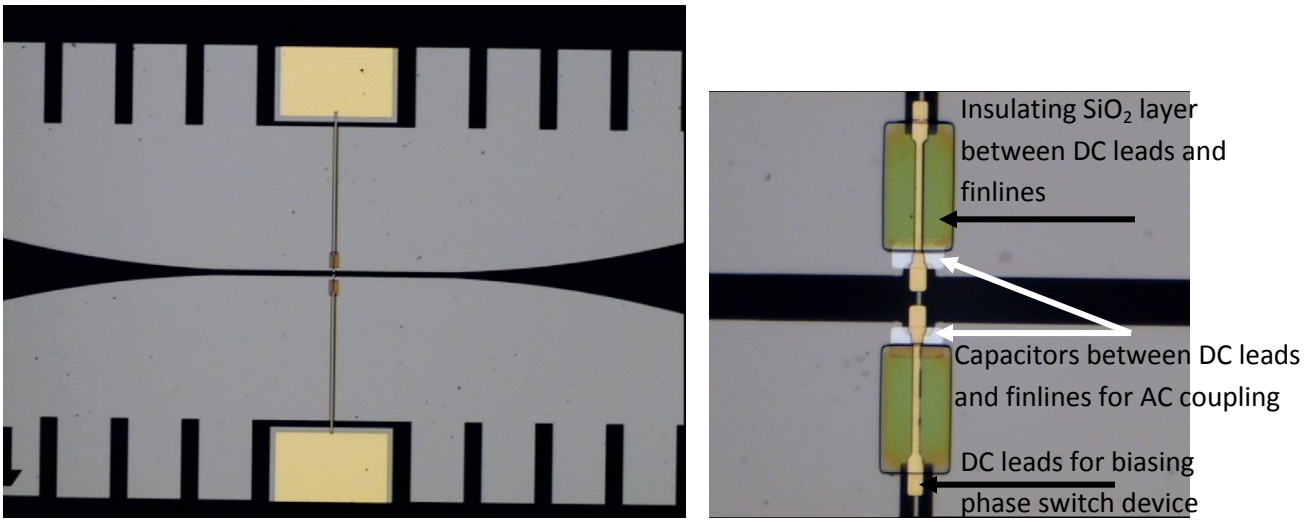

Figure 5.15. Final photo of a phase switch device capacitively coupled to a finline, at different zooms.

5.6. Phase Switches with CEB array

In this section, we will describe a challenging experiment on Phase Switch devices that employs CEB array as the detector of the RF signal after the switching. In the previous experiments, the Phase Switch devices were tested using an SIS detector operating at He temperature or even higher. Hence, the detector was placed in the same waveguide as the phase switch (PS) device or adjoined to it, cooled to the same temperature as PS device. CEB devices however need to be cooled to a much lower temperature than the phase switch devices. Consequently, the CEB device can be neither placed in the same waveguide nor connected thermally to it. CEB must be located at another stage of the cryostat, so-called Cold Stage and cooled down to ~300 mK temperature.

Before mounting the RF block in the cryostat, it was first tested at room temperature using the setup shown in the figure 5.16. A Backward Wave Oscillator (BWO) was used as an RF source in this experiment as well as in the cold experiment described later. The RF signal from the source was focused by a horn onto the input of the waveguide block, also fed by a horn. In this block the phase switch device will be located. At the output of the RF block, the propagated signal was focused by a third horn onto the diode detector, see Figure 5.16.

The signal was detected at the output at frequencies of 200 – 245 GHz and displayed about 4 dB insertion loss. The RF block with the waveguide fabricated according to our design is therefore suitable for switching experiment at these frequencies; the losses are not negligible though.

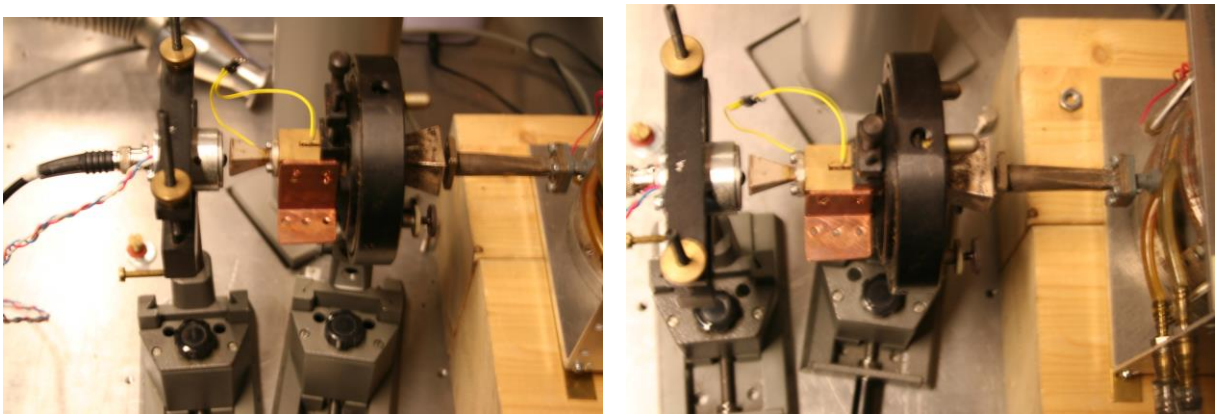

Figure 5.16. The setup for room-temperature calibration, side view and top view.

In the experiment, an array of 64 CEB devices operating at 280 mK was used as the detector for testing of Phase Switch devices operating at 4 K. Consequently, the detector and the device under test could not be placed at the same stage and were kept apart during this experiment. A BWO oscillator was used as the RF power source, shown in Figure 5.17.

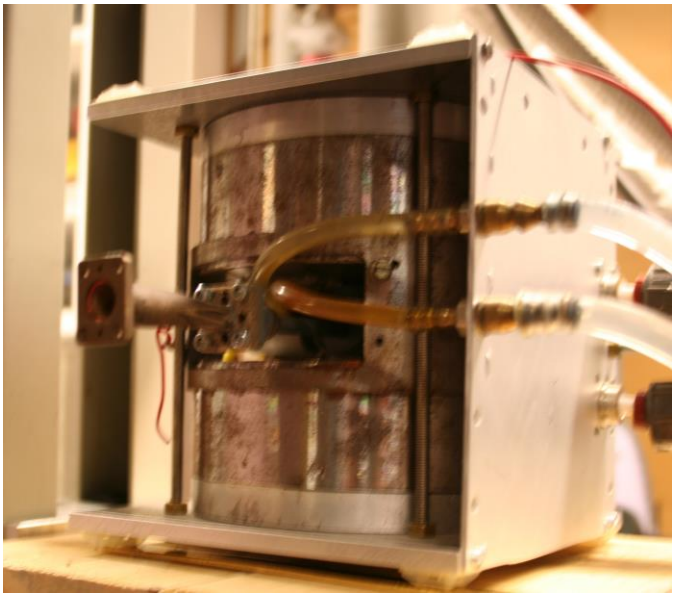

Figure 5.17. The BWO oscillator used as RF source.

The whole setup is shown in Figure 5.18, while Figure 5.19 shows the part of the setup mounted on the cold stage and the 3 K stage in the cryostat.

The response of the CEB array to the toggling of the Phase Switch device is shown in Figure 5.20. It represents the difference in voltage response of the CEB in current-bias mode between the On and Off states of the Phase Switch device. The shape of the voltage response curve is a typical shape of a response of a CEB to the incoming RF power, which confirms that we do observe switching between the open and closed states with the moderate modulation depth of about 1-2 %, which in less than in our previous experiments conducted using SIS and Josephson devices [45, 102].

As can be seen in Figure 5.19, the distance between the RF block and the holder of CEB array is about 0.5 cm, i.e. there is no space in between, either for horn or a lens. The horn available for this experiment was about 5 cm long and cannot be fitted inside the cryostat for this experiment.

As a consequence, the RF matching was worse this time than in previous experiments where the detector was placed either in the same waveguide or just behind it. We estimate the coupling efficiency in this experiment as ~20%. Besides, part of the RF signal could go around the RF block and illuminate the CEB detector directly, which would deteriorate the switching efficiency. Nevertheless, we still observed some switching, as shown in fig. 5.20, which demonstrated the ability of our phase switch device to operate as a part of a complex receiver system and in combination with CEB devices.

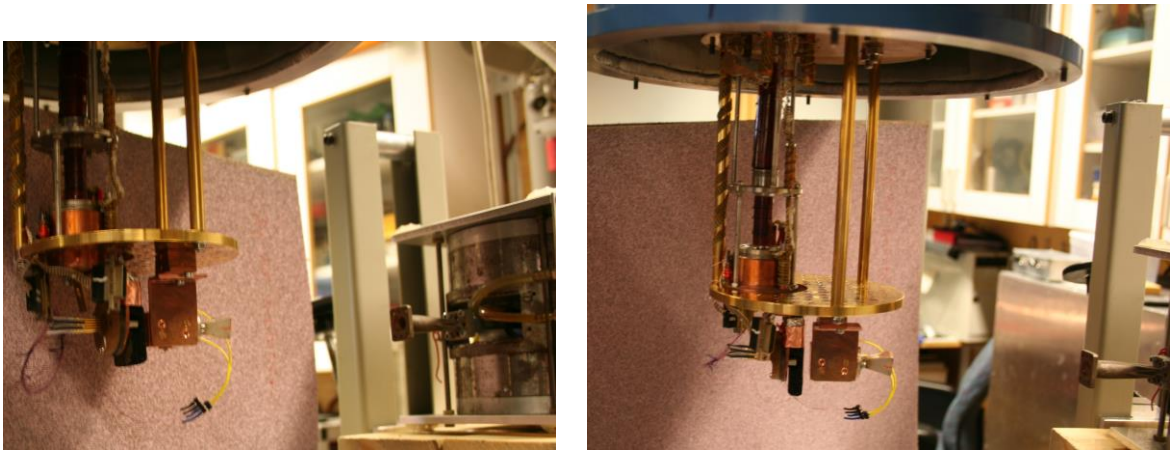

Figure 5.18. Two views of the setup including BWO source outside the cryostat.

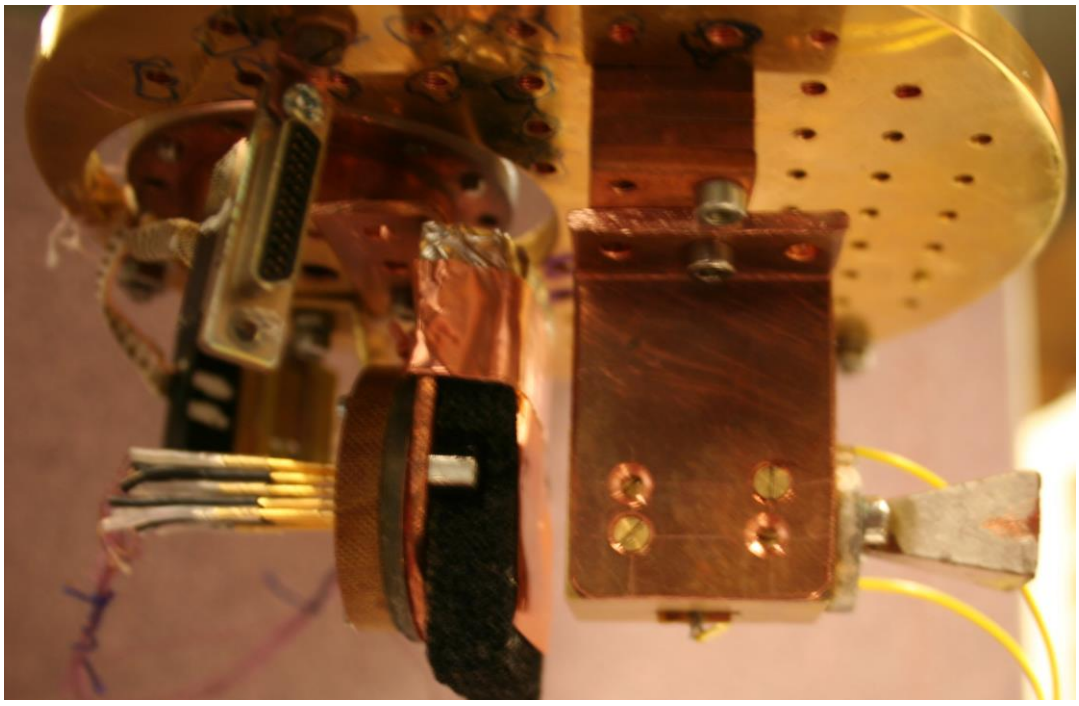

Figure 5.19. The RF block with a horn mounted on the 3 K stage and the CEB device mounted on the millikelvin cold plate and covered by a foil and protected by back absorbing material.

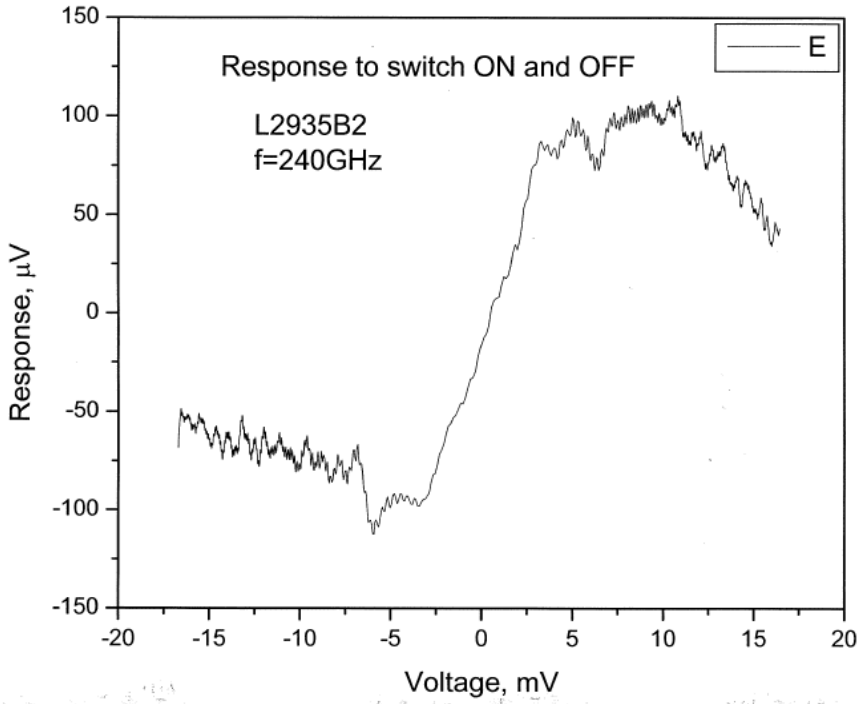

Figure 5.20. The difference in RF response of CEB array between the On and Off states of the phase switch device.

5.7. Conclusions

Planar NbN nano-switches have been designed, fabricated, and tested in collaboration between Chalmers and Oxford University. The author of this thesis designed and fabricated these devices and tested several of those. The switching characteristics have been measured at switching rates of 10 to 100 kHz. The switching speed is well above the response time required for phase modulation in astronomical instrument and is mainly limited by the time constant of the measurement system (~10 μs). Real switching time of a nanobridge could be as short as 30 picoseconds, when not limited by thermal effects. A typical modulation value of about 5 dB was obtained for a signal with a frequency of 195 to 245 GHz in a waveguide. We

believe that the dynamic range was constrained by the kinetic inductance of the nanostrip that reduced impedance mismatch in Closed state and hence deteriorated the switching ability of our devices. Yet, fabricating and running experiments with DC coupled devices was a reasonable choice in that it allowed us to verify the concept of switching the RF signal in the waveguide by shorting the transmission line with a NbN nanostrip.

We have thus demonstrated that the concept of using a superconducting nanostrip to short a transmission line is a feasible approach. The investigated planar phase shift circuits are simple to fabricate and they can be integrated in a planar receiver and replace mechanical switches.

The efficiency of the switching was low in in our experiments, which was mainly due to the geometry of the devices. We expect that modifying the geometry and the design of the test block should improve the results significantly.

New generation NbN phase switch devices with capacitive coupling to finlines were fabricated for better performance. These devices are still under development. Employing devices with capacitively coupled nanostrips should provide higher switching power.

Finally, a phase switch device was successfully tested using a CEB array as a detector, which is a step towards integrated superconducting millimetre-wave receiver systems.

Concluding remarks

In this thesis, we reported our work on the development of detectors based on Superconductor-Insulator-Normal metal (SIN) tunnel junctions, which are to be employed in sub-millimeter astronomical receivers. The detectors presented here are based on absorption of incident photons in a normal metal film and use SIN tunnel junctions to measure a change in the electronic temperature of a normal metal absorber. The readout principle is based on a strong dependence of the tunneling current on the temperature and thus the SIN junction characteristics that depend on the temperature of the absorber. The devices presented in this thesis were fabricated by the author of this thesis using the fabrication procedures that he developed during his DPhil course at Oxford. The devices are designed for millimetre-wave receivers for sensitive measurements in new generations of telescopes.

We examined the concept of the Cold-Electron Bolometer (CEB) as a sensitive millimeter-wave detector employing SIN tunnel junctions to readout changes in the electronic temperature of normal metal and we verified the concept in several different implementations. Namely, the detectors considered here include CEB devices integrated in 97-GHz unilateral finlines and CEBs integrated in other types of planar antennas for quasi-optical coupling, such as log-periodic antennas, 350 GHz double dipole antennas and cross-slot antennas.

Also, the electron cooling which is involved in the CEB operation and provides electro-thermal feedback, was considered in this thesis. The electro-thermal feedback is based on the cooling of the absorber by hottest electrons that escape the system through the tunnel junctions. This makes the saturation power of a CEB well above that of other types of millimeter-wave receivers.

A number of different implementations of CEB devices for efficient detection of electromagnetic signals at millimeter wavelengths were investigated in this thesis. Different fabrication techniques were also developed for manufacturing CEBs and other microwave devices, such as Phase Switches.

We reported the Cold-Electron Bolometer integrated in a 97-GHz finline. This was fabricated using direct-writing of the detector structure, while also depositing the CEB device directly across a unilateral finline onto a planar substrate. Such a fabrication procedure involves the creation of both CEBs and finlines. In this configuration, CEB with SIN tunnel junctions is used for the signal detection, whilst a unilateral finline is used as a simple solution for planar microwave components that can be integrated on the same chip. The CEB device investigated here was manufactured using the trilayer fabrication technology, developed by the author of this thesis. The detector is fed through a waveguide by a horn; the detector testing was performed in a cryostat at 280-315 mK using both an external RF power source and an internal black body source placed inside the cryostat.

We have demonstrated a properly operating CEB device by measuring its performance, including its DC and RF characteristics. First, we measured IV curves at different

temperatures, thus demonstrating the high quality of SIN tunnel junctions and the proper response to the bath temperature. Based on the DC characteristics, we have estimated the dark noise equivalent power for devices in the current biased mode operating at 300 mK, read out by room-temperature JFET electronics, as NEP = $5 \cdot 10^{-16}$ W/Hz$^{1/2}$.

Then, we measured the detector's optical response by focusing an RF signal onto the waveguide input with the horn. We obtained the voltage response to the RF power and analysed the results. The estimated optical NEP reported in this thesis is about ~10^{-16} W/Hz$^{1/2}$ which matches the requirements for CMB polarisation measurements. We have thus demonstrated that the CEB-finline integrated circuit, assembled in a receiver system with a waveguide and a horn, is a feasible design for millimeter-wave detection. To the best of our knowledge, this is the first finline-integrated CEB device in a waveguide ever reported.

The noise performance reported here was measured using the room-temperature amplifier box. As a result, the noise coming from the amplifier dominates the total noise measured. Thus, we expect improved noise performance of CEB when using low-temperature readout electronics. Regarding the fabrication method used, a straightforward and robust technology was chosen for the production of these devices. This was a reasonable choice for developing this experiment, in that it allowed us to demonstrate the full functionality of the CEB detector integrated in a finline. However, our fabrication methods were not optimized in terms of device performance as the trilayer fabrication technology, used for manufacturing these devices, does not allow for a thin and narrow absorber. Thus, the volume of the absorber was not chosen for the best responsivity. Further development of the design using advanced

technologies and readout schemes, including low-temperature readout amplifiers combined with measurements in the voltage-biased mode, should yield future improvements in the device performance.

In this thesis, we also reported CEB devices integrated with other types of planar antennas, used for quasi-optical coupling, as well as the technology development for fabricating SIN junctions and CEB devices. We present CEB devices fabricated using advanced technologies, different to the trilayer process considered before, and integrated with log-periodic, double-dipole and cross-slot antennas. We also measured the CEB performance and analyzed the experimental results.

We first considered the design of the CEB detectors and then presented experimental results on the testing of CEBs comprising a thin Ti film absorber and two SIN junctions integrated in a log-periodic antenna and 350 GHz double dipole antenna. The devices were fabricated using a novel approach for fabricating Ti-TiO_2-Al tunnel junctions, developed by the author of this thesis. This is a simple and efficient technology for fabrication of SIN tunnel junctions between Ti and Al with TiO_2 as an insulating barrier. This is done by depositing of a normal Ti film as a bottom electrode and the superconducting Al film on the top of it after creating a TiO_2 insulating barrier by *ex-situ* oxidation of Ti.

The CEB performance was measured at 300 mK using the hot-cold method and using a black-body source that is heated and controlled by an external current. We reported the results of DC and RF measurements on a Cold-Electron Bolometer deposited across a double dipole antenna and another one fed by a log-periodic antenna on a planar Si substrate. The fabricated

junctions are rather high-ohmic due to a very long oxidation time used for creating tunnel barriers. Shortening the oxidation time and combining it with a proper choice of temperature should allow us to create more low-ohmic tunnel junctions. Thus, more development work is needed to realize low-ohmic junctions that are more suitable for CEB applications.

Our preliminary measurements have yielded NEP ~3×10^{-17} W/Hz$^{1/2}$ which is close to the CMB power level. Improving the design, using series arrays of SIN junctions and improving the readout should yield an NEP level below 1×10^{-17} W/Hz$^{1/2}$.

Therefore, the detector can be a potential candidate for the next generation of space cosmology missions and is also of interest to ground-based astronomical experiments as a result of the simplicity of its integration to planar circuit technology, high saturation power and fast response.

Next, we also reported experimental results on the testing of CEB detectors comprising a non-superconducting thin absorber made of CrO_x/Cr/Al film and an array of SIN tunnel junctions integrated in a planar cross-slot antenna. Each antenna contains two series / parallel arrays of 10 Cold-Electron Bolometers with SIN tunnel junctions integrated in orthogonal ports of the antenna. We also investigated bolometers made of a normal metal absorber and 4 SIN tunnel junctions and integrated in a 4-probe test structure. The CEB devices, integrated in cross-slot antennas, were fabricated using Advanced Shadow Evaporation technology and designed for a balloon-borne telescope project BOOMERANG that is dedicated to the CMB measurements.

The CEB performance was tested in a ^{3}He sorption cryostat HELIOX-AC-V at bath temperatures of 280 to 350 mK and in a dilution refrigerator TRITON down to 50 mK. We first demonstrated that this technology is suitable for detector fabrication by producing high performance IV curves and then presented our experiments on the measurements of the voltage response to the incoming RF power. The optical response was measured using the hot/cold load method by flipping a reflector opposite a blackbody surface inside a 3 K shield. In addition, we investigated electron cooling and demonstrated that it increases the dynamic range of the device.

The reported estimated noise equivalent power in the current biased mode as read out by room temperature electronics is NEP $\sim 2 \cdot 10^{-17}$ W/Hz$^{1/2}$. We also reported a voltage to temperature response of around dV/dT = 8.8 μV/mK for 10 devices in series, voltage to RF power response of $dV/dP = 1 \cdot 10^{8}$ V/W, the dark NEP of $6 \cdot 10^{-18}$ W/Hz$^{1/2}$, and demonstrated the dynamic range over 40 dB measured at the temperature of 280 mK for arrays of cold-electron bolometers integrated in a cross-slot antenna. Moderate electron cooling by 45 to 100 mK was reported. This improves the NEP of the detector and increases the dynamic range.

The measured characteristics approach the requirements for the balloon-borne experiment BOOMERANG and the devices presented could be considered for future balloon and ground-based radio telescope experiments.

The above results reported in this thesis have demonstrated that the CEB device is an operating millimeter-wave detector with high sensitivity and a large dynamic range that

prevents saturation of the system, which can easily be made on planar substrates and integrated into planar antennas.

In this thesis, we also investigated planar NbN phase switch circuits integrated in unilateral back-to-back finlines, operating at 200 - 245 GHz. The phase switch circuits were designed, developed, fabricated, and tested, in order to replace mechanical switches for signals in waveguides. The presented fully planar design allows switching the microwave signal between two branches of a circuit with low losses and high speed.

The reported planar phase shift circuits were fabricated by the author of this thesis and they can be integrated in planar circuits and systems. The phase modulation scheme will be used in high-precision astrophysical experiments such as the investigation of the polarization of the CMB. The scheme will allow to measure Stokes parameters without moving the optics and to improve the sensitivity.

We reported the switching characteristics and demonstrated the switching speed of the device well above the speed required for phase modulation in astronomical instruments. It is mainly limited by the time constant of the measurement system (~10 μs), while the real switching time of a nanobridge is much shorter, about 30 picoseconds, when not limited by thermal effects. We have also measured the switching characteristics using an SIS detector placed in the waveguide with the phase switch circuit and also investigated switching ability at different frequencies, 200-245 GHz.

We reported our attempts to fabricate a phase switch device capacitively coupled to the finline.

In addition, we demonstrated switching between the normal and superconductive states using a CEB array as a detector, with moderate modulation. This experiment confirmed the ability of our phase switch device to operate as a part of a receiver system, as a step towards a fully integrated planar receiver circuit. In the future, the planar design should allow the switch to be integrated into the detector circuit.

The results above have shown that the concept of signal switching using a superconducting nanostrip is a promising technology. While the efficiency of the switching was low in the experiments reported here, this was partly due to the geometry of the devices, and we believe therefore that using capacitively coupled devices or advanced geometries should yield higher switching capability. Layouts with advanced geometries are currently under development.

References

[1] Boon Kok Tan "Development of coherent detector technologies for sub-millimetre wave astronomy observations" DPhil thesis, Oxford University, 2012

[2] S. Shitov, O. Koryukin, Y. Uzawa, et al,"Development of Balanced SIS Mixers for ALMA Band-10". *17th International Symposium on Space Terahertz Technology*, p. 90, 2006.

[3] J. Mather, E. Cheng, R. Eplee, et al., "A preliminary measurement of the cosmic microwave background spectrum by the Cosmic Background Explorer (COBE) satellite". *The Astrophysical Journal Letters*, 354: L37–L40, 1990. doi: 0.1086/185717.

[4] E. Komatsu, J. Dunkley, M. Nolta, et al., "Five-Year Wilkinson Microwave Anisotropy Probe (WMAP) Observations: Cosmological Interpretation". *ArXiv e-prints*, 0803.0547, 2008.

[5] C. North, "Observations of the Cosmic Microwave Background Polarization with Cℓover", DPhil thesis, Oxford University, 2010

[6] F. Piacentini, P. Ade, J. Bock, et al., "A Measurement of the Polarization-Temperature Angular Cross-Power Spectrum of the Cosmic Microwave Background from the 2003 Flight of BOOMERANG". *The Astrophysical Journal*, 647: 833–839, 2006. doi: 10.1086/505557.

[7] A. Readhead, S. Myers, T. Pearson, et al., "Polarization Observations with the Cosmic Background Imager". *Science*, 306: 836–844, 2004. doi: 10.1126/science.1105598.

[8] J. Wu, J. Zuntz, M. Abroe, et al., "MAXIPOL: Data Analysis and Results". *The Astrophysical Journal*, 665: 55–66, 2007. doi: 10.1086/518112.

[9] H. Chiang, P. Ade, D. Barkats, et al., "Measurement of CMB Polarization Power Spectra from Two Years of BICEP Data". *ArXiv e-prints*, 2009.

[10] C. Bischoff, L. Hyatt, J. McMahon, et al., "New Measurements of Fine-Scale CMB Polarization Power Spectra from CAPMAP at Both 40 and 90 GHz". *The Astrophysical Journal*, 684: 771–789, 2008. doi: 10.1086/590487.

[11] E. Leitch, J. Kovac, N. Halverson, et al, "Degree Angular Scale Interferometer 3 Year Cosmic Microwave Background Polarization Results". *The Astrophysical Journal*, 624: 10–20, 2005. doi: 10.1086/428825.

[12] G. Hinshaw, J. Weiland, R. Hill, et al., "Five-Year Wilkinson Microwave Anisotropy Probe Observations: Data Processing, Sky Maps, and Basic Results". *The Astrophysical Journal Supplement Series*, 180: 225–245, 2009. doi: 10.1088/0067-0049/180/2/225.

[13] J. Tauber. "The Planck Mission: Overview and Capabilities for Observing Extended Emission". In: R. Laureijs, K. Leech, & M. Kessler, editor, ISO Beyond Point Sources: Studies of Extended Infrared Emission, 455, ESA Special Publication, p. 185, 2000.

[14] W. Hu and M. White, "A CMB polarization primer". *New Astronomy*, 2: 323–344, 1997. doi: 10.1016/S1384-1076(97)00022-5.

[15] P. Oxley, P. Ade, C. Baccigalupi et al, "The EBEX Experiment" *Proc. SPIE* 5543, 2004.

[16] P. Grimes, G. Yassin, L. Kuzmin, P. Mauskopf, E. Otto et al "Investigation of planar switches for large format CMB polarization Instruments" *Proc. SPIE* 6275, 25, 2006

[17] L. Page, G. Hinshaw, E. Komatsu et al, "Three-year Wilkinson microwave anisotropy probe observations: polarization analysis", *The Astrophysical Journal Supplement Series*, 170: 335, 2007 doi: 10.1086/513699.

[18] G. Yassin, L. Kuzmin, P. Grimes, M. Tarasov, E. Otto, Ph. Mauskopf, "An integrated superconducting phase switch for cosmology instruments" *Physica C* 466, p. 115–123, 2007.

[19] G. Giardino, A. Banday, K. Gorski, et al "Towards a Model of Full-sky Galactic Synchrotron Intensity and Linear Polarisation: A re-analysis if the Parkes data". *Astronomy & Astrophysics*, 387: 82, 2002.

[20] D. Finkbeiner, M. Davis, and D. Schlegel, "Extrapolation of Galactic Dust Emission at 100 microns to Cosmic Microwave Background Radiation Frequencies using FIRAS". *The Astrophysical Journal*, 524: 867, 1999.

[21] L. Piccirillo, P. Ade, M. Audley, et al. "The CℓOVER experiment", *Proc. SPIE* 7020, Millimeter and Submillimeter Detectors and Instrumentation for Astronomy IV, 70201E, 2008; doi: 10.1117/12.788927; http://dx.doi.org/10.1117/12.788927

[22] M. Audley, D. Glowacka, D. Goldie, V. Tsaneva, S. Withington, P. Grimes, C. North et al. "Microstrip-Coupled TES Bolometers for CLOVER". In *Proceedings of the 19th International Symposium on Space Terahertz Technology*, p. 143, Groningen, 2008.

[23] http://astro.uchicago.edu/dasi/

[24] J. Kovac, E. Leitch, C. Pryke et al, "Detection of polarization in the cosmic microwave background using DASI", *Nature* 420, 772-787, 2002. doi: 10.1038/nature01269

[25] G. Yassin, P. Grimes, and S. Sorenson. "Compact optical assemblies for large-format imaging arrays". In *Proceedings of the 16th Int. Symp. on Space THz Tech*., Gothenburg, Sweden, 2005.

[26] P. Grimes, "Design and Analysis of 700 GHz Finline Mixers", PhD thesis, Cambridge University, Cambridge, UK, 2006

[27] I. Robson, W. Holland, SCUBA-2: "The Submillimeter Mapping Machine". In: From Z-Machines to ALMA: (Sub) Millimeter Spectroscopy of Galaxies, 375 *Astronomical Society of the Pacific Conference Series*, 275, 2007.

[28] W. Holland, W. Duncan, and M. Griffin. "Bolometers for submillimeter and millimeter astronomy." In Single-Dish Radio Astronomy: Techniques and Applications, *ASP Conference Proceedings*, 278, 2002.

[29] B. Mazin. "Microwave Kinetic Inductance Detectors", PhD thesis, California Institute of Technology, 2004.

[30] B. Mazin, "Microwave Kinetic Inductance Detectors: The First Decade"
http://web.physics.ucsb.edu/~bmazin/Papers/preprint/LTD13_Mazin2.pdf
13th International Workshop on Low Temperature Detectors – LTD13 July 2009 Stanford

[31] Netherlands Institute for Space Research,
http://www.sron.nl/kid-technology-1942

[32] D. Goldie, M. Audley, D. Glowacka, V. Tsaneva, and S. Withington, "Transition Edge Sensors for bolometric applications: responsivity and saturation". *J. App. Phys*, 103(8): 4509, 2008.

[33] N. Jethava, J. Chervenak; Ari-David Brown, et al. "Development of superconducting transition edge sensors based on electron-phonon decoupling", *Proc. SPIE* 7741, Millimeter, Submillimeter, and Far-Infrared Detectors and Instrumentation for Astronomy V, 774120 2010; doi:10.1117/12.856450; http://dx.doi.org/10.1117/12.856450

[34] M. Audley, D. Glowacka, D. Goldie, et al, "Performance of a Microstrip-coupled TES Imaging Module for CMB Polarimetry", *21st International Symposium on Space Terahertz Technology*, Oxford 2010

[35] D. Glowacka, D. Goldie, S. Withington, "A fabrication process for microstrip-coupled Superconducting Transition Edge Sensors giving highly reproducible device characteristics", *Journal of Low Temperature Physics*, 151, pp. 249‑254, 2008.

[36] E. Otto, M. Tarasov, G. Pettersson, et al "An array of 100 Al-Al_20_3-Cu SIN tunnel junctions in Direct-write trilayer technology" *Supercond. Sci. Technol*. **20** 1155–1158, 2007.

[37] L. Kuzmin, "An Array of Cold-Electron Bolometers with SIN Tunnel Junctions and JFET readout for Cosmology Instruments" *Journal of Physics*: Conference Series (JPCS) EUCAS, Brussels, 2007

[38] E. Otto, M. Tarasov, and L. Kuzmin, "Ti–TiO_2–Al normal metal–insulator–superconductor tunnel junctions fabricated in direct-write technology" *Supercond. Sci. Technol*. **20** 865–869, 2007.

[39] I. Agulo, "Ultrasensitive Cold-Electron Bolometer", PhD thesis, Chalmers University, Göteborg, Sweden, 2007.

[40] L. Kuzmin, "A Superconducting Cold-Electron Bolometer with SIS´ and Josephson Tunnel Junctions" *Journal of Low Temperature Physics*, 151, p. 292-297, 2008.

[41] L. Kuzmin, "Advanced Shadow Evaporation Technique (ASHET) for Large Area Tunnel Junctions". US prepatent , Appl. No. 61/525242, filed August 19, 2011.

[42] L. Kuzmin, K. Olsson, M. Tarasov, S. Mahashabde, L. Tuter, P. de Bernardis, P. Fiadino, G. Yassin, E. Otto, P. Grimes, Ph. Mauskopf, D. Golubev, "Cold-Electron Bolometers with JFET Readout for the CMB polarization measurements" at *Bolometric Interferometry Workshop*, Paris, 2008.

[43] K. Olsson, "Cold Electron Bolometer", Master's Thesis, Chalmers University, 2008

[44] L. Kuzmin . "Capacitively Coupled Hot Electron Microbolometer as Perspective IR and Sub-mm Wave Sensor", Proceeding of the *9th International Symposium on Space Terahertz Technology*, Pasadena, pp 99-103, 1998.

[45] E. Otto, "Direct Write Technology of SIN Tunnel Junctions for Thermometry and Microwave Devices", Licentiate thesis, Chalmers University, Sweden, 2008

[46] L. Kuzmin, G. Yassin, S. Withington, and P. Grimes "An Antenna Coupled Cold-Electron Bolometer for High Performance Cosmology Instruments" *Proc. of the 18th International Symposium on Space Terahertz Technology*, pp. 93-99, Pasadena, 2007.

[47] M. Tarasov, L. Kuzmin, V. Edelman et al, "Optical Response of a Cold-Electron Bolometer Array", *JETP Letters*, 92, No. 6, pp. 416–420, 2010.

[48] G. Burnell, "Quasiparticle and Phonon Transport in Superconducting Particle Detectors", PhD thesis, Cambridge University, 1998.

[49] J. Pekola "Trends in thermometry" *J. Low Temp. Phys*. **135**, 5-6 (2004)

[50] A. Bitterman, "Superconductor detectors for Astronomy", *Superconductor & Cryoelectronics*, 12, No. 2, 17. 1999.

[51] L. Solymar, "Superconductive Tunneling and Applications", Chapman and Hall, London 1972

[52] L. Kuzmin, "Two-Dimensional Array of Cold-Electron Bolometers for Ultrasensitive Polarization Measurements". Radiophisika. Izvestiya VUZov, т. LIV, N8-9, 607 (2011); *Radiophysics and Quantum Electronics,* 2012.

[53] M. Nahum, T. Eiles, J. Martinis, "Electronic microrefrigerator based on a NIS tunnel junction". *Appl. Phys. Lett.,* 65, pp. 3123-3125, 1994

[54] L. Kuzmin, I. Agulo, M. Fominsky, A. Savin, M. Tarasov, "Optimization of the electron cooling by SIN tunnel junctions", *Superconductor Science & Technology* 17 p. 400-405, 2004.

[55] M. Tarasov, L. Kuzmin, N. Kaurova, E. Otto, G. Yassin, and Paolo de Bernardis "Cold-Electron Bolometer Array Integrated with a 350 GHz Cross-Slot Antenna", *21st International Symposium on Space Terahertz Technology*, Oxford, March 2010

[56] L. Kuzmin, "Cold-Electron Bolometer", chapter in: "Bolometers", Edited by A. G. Unil Perera, Published by InTech Janeza Trdine 9, 51000 Rijeka, Croatia, 2012, ISBN 978-953-51-0235-9

[57] J. Bakker, H. Van Kempen, P. Wyder, "Adiabatic demagnetization of ruby and the use of a superconducting tunnel junction thermometer", *Phys. Letts*. 31A, 290, 1970

[58] I. Agulo and L. Kuzmin, "An array of SIN tunnel junctions as a sensitive thermometer," *Supercond. Sci. Technol.* **21,** 2008

[59] L. Kuzmin, P. Mauskopf, D. Golubev, "Superconducting Cold-Electron Bolometers with JFET Readout for OLIMPO Balloon Telescope" *Journal of Physics: Conf. Series (JPCS)* 43 1298, 2006.

[60] L. Kuzmin, "On the concept of a hot-electron microbolometer with capacitive coupling to the antenna," *Physica B* 284-288, 2129, 2000.

[61] L. Kuzmin, "Ultimate cold-electron bolometer with strong electrothermal feedback". *Proc. SPIE*, 5498, p. 349-361, 2004

[62] L. Kuzmin, D. Golubev "On the concept of an optimal hot-electron bolometer with NIS tunnel junctions". *Physica C* 372-376, 378, 2002.

[63] I. Agulo, L. Kuzmin, M. Fominsky, and M. Tarasov "Effective electron micro-refrigeration by superconductor–insulator–normal metal tunnel junctions with advanced geometry of electrodes and normal metal traps" *Nanotechnology* 15 (2004) S224–S228

[64] E. Otto, M. Tarasov, and L. Kuzmin, "Direct-write trilayer technology for Al–Al_2O_3–Cu superconductor-insulator-normal metal tunnel junction fabrication" *J. Vac. Sci. Technol*. B 25 (4), Jul/Aug 2007 p. 1156-1160

[65] S. Sze, "Semiconductor Devices: Physics and Technology" John Wiley & Sons Inc., 1998

[66] JEOL JBX-5DII system : user's manual, www.chalmers.se

[67] N. Ashcroft and N. Mermin (1976). "Solid State Physics."

[68] M. Tinkham. "Introduction to Superconductivity". McGraw-Hill, Inc., Singapore (1996).

[69] D. Golubev, L. Kuzmin and M. Willander, "SIN tunnel junction as a temperature sensor", Part of the SPIE Conference on Photodetectors Materials and Devices IV, San Jose. California, *Proc. SPIE,* Vol 3629, 1999. 0277-786X/99/

[70] G. Donaldson (1967), "Electron tunneling studies of the superconducting state", PhD thesis, University of Cambridge, Cambridge, UK.

[71] D. Golubev, L. Kuzmin, "Nonequilibrium theory of the hot-electron bolometer with NIS tunnel junction", *Journal of Applied Physics*. 89, pp. 6464-6472, 2001.

[72] P. Richards, "Bolometers for infrared and millimeter waves." *Journal of Applied Physics* 76, 1-36, 1994.

[73] S. Golwala, J. Johum, B. Sadoulet, "Noise considerations in low resistance NIS junctions", *Proc. of the 7th International Workshop on Low Temperature Detectors*, pp 64-65, Munich, 1997

[74] J. Mather “Bolometer noise: nonequilibrium theory” *Appl. Opt.* 21, 1125, 1982.

[75] L. Kuzmin, “An Array of Cold-Electron Bolometers with SIN Tunnel Junctions and JFET readout for Cosmology Instruments” *Journal of Physics: Conference Series (JPCS) EUCAS*, Brussels, 2007.

[76] L. Kuzmin, “Array of Cold-Electron Bolometers with SIN Tunnel Junctions for Cosmology Experiments”. *Journal of Physics: Conference Series (JPCS)* 97, p. 012310, 2008.

[77] L. Kuzmin, “A Parallel/Series Array of Cold-Electron Bolometers with SIN Tunnel Junctions for Cosmology Experiments”, *IEEE/CSC & European Superconductivity News Forum*, No. 3, pp 1-9, 2008.

[78] E. Otto, M. Tarasov, P. Grimes, L. Kuzmin, and G. Yassin, “Cold-Electron Bolometer Integrated with a Unilateral Finline”, *21st International Symposium on Space Terahertz Technology*, Oxford, 23-25 March, 2010.

[79] E. Otto, M. Tarasov, P. Grimes, N. Kaurova, H. Kuusisto, L. Kuzmin and G. Yassin, “Finline-integrated cold electron bolometer”, *Proc. SPIE*, June 2010.

[80] C. North, G. Yassin and P. Grimes "Rigorous Analysis and Design of Finline Tapers for High Performance Millimetre and Submillimetre Detectors", *17th Int. Symp. on Space THz Tech.*, 284, 2006.

[81] G. Rebiez, "Millimeter-Wave and Terahertz Integrated Circuit Antennas," *Proceedings of the IEEE*, 80, pp. 1748-1770, No. 11, 1992.

[82] E. Grossman, "Lithographic Antennas for Submillimeter and Infrared Frequencies," *IEEE International Symposium on Electromagnetic Compatibility*, pp. 102-107, 1995, 0-7803-2573-7/95/0000-0018

[83] J. Small, G. Elchinger, A. Javan, et al, "AC Electron Tunneling at Infrared Frequencies: Thin-film M-O-M Diode Structure with Broadband Characteristics", *Applied Physics Letters*, 24, pp. 275-279, 1974.

[84] E. Otto, M. Tarasov, P, Grimes et al “Optical response of Titanium-based Cold-Electron Bolometer”, *Journal Supercond. Sci. Technol*. (SUST), 26, 085020, 2013

[85] Photodetectors Devices, Circuits and Applications, by: S. Donati, Prentice Hall, USA, 2000

[86] http://gs.flir.com/surveillance-products/surveillance-technology/imaging-technotes/IR_Technology_Parameters

[87] M. Van der Vorst, "Integrated Lens Antennas for Submillimetre-wave applications", PhD thesis, Technische Universiteit Eindhoven, 1999.

[88] E. Kosarev A. Shul'man, M. Tarasov, T. Lindström, "Deconvolution problems and superresolution in Hilbert-transform spectroscopy based on AC Josephson effect", *Computer Physics Communications* 151, 171–186, 2003.

[89] B. Karasik, R. Cantor, "Demonstration of high optical sensitivity in far-infrared hot-electron bolometer", *Applied Physics Letters* **98**, 193503, 2011.

[90] M. Tarasov, V. Gromov, G. Bogomolov, E. Otto, L. Kuzmin, "Fabrication and Characteristics of Mesh Band-Pass Filters" *Journal: Instruments and Experimental Techniques*, 2009, 52, No. 1, pp. 74–78, 2009.

[91] D. Porterfield, J. Hesler, R. Densing, et al., "Resonant metal-mesh bandpass filters for the far infrared" *Appl. Opt.*, 33, p. 6046, 1994.

[92] R. Ulrich, "Interference filters for the far infrared," *Appl. Opt.* 7, 1987-1996, 1968.

[93] J. Davis, "Bandpass interference filters for very far infrared astronomy," *Infrared Phys.* 20, 287-290, 1980.

[94] P. Tomaselli, D. Edewaard, P. Gillan, and K. Möller, "Far-infrared bandpass filters from cross-shaped grids," *Appl. Opt.* 20, 1361-1366, 1981.

[95] BOOMERANG - balloon telescope: Measurements of CMB Polarization, http://oberon.roma1.infn.it/boomerang/b2k/

[96] http://www.lbl.gov/Science-Articles/Archive/boomerang-flat.html

[97] http://en.wikipedia.org/wiki/BOOMERanG_experiment

[98] http://cmb.phys.cwru.edu/boomerang/

[99] G. Chattopadhayay, F. Rice, D. Miller, H. LeDuc, and J. Zmuidzinas, "A 530-GHz balanced mixer", *IEEE Microwave Guide Wave Lett.*, 9, pp. 467-469, 1999.

[100] R. Dynes, V. Narayanamurti, J. Garno, "Direct measurement of quasiparticle-lifetime broadening in a strong-coupled superconductor", *Phys. Rev. Lett.*, 41 (21), 1509-1512, 1978.

[101] K. Yoon, P. Ade, D. Barkats et al, "The Robinson Gravitational Wave Background Telescope (BICEP): a bolometric large angular scale CMB polarimeter" *Proc. SPIE* 6275, 62751K-1, 2006.

[102] L. Kuzmin, M. Tarasov, E. Otto et al, "Superconducting Subterahertz Fast Nanoswitch" *JETP Letters*, 86, No. 4, pp. 275–277, 2007.

[103] K. Il'in, M. Lindgren, M. Currie et al, "Picosecond hot-electron energy relaxation in NbN superconducting photodetectors" *Appl. Phys. Lett*. 76, 2752, 2000.

List of publications

E. Otto, M. Tarasov, L. Kuzmin, "*Direct-write trilayer technology for Al-Al203-Cu SIN tunnel junctions fabrication"* J. Vac. Sci. Technol. B **25** (4) Jul/Aug 2007, p. 1156-1160

E. Otto, M. Tarasov, G. Pettersson, D. Gustavsson and L. Kuzmin
"*An array of 100 Al–Al_2O_3–Cu SIN tunnel junctions in direct-write trilayer technology*"
Supercond. Sci. Technol. **20** (2007) 1155–1158

E. Otto, M. Tarasov and L. Kuzmin, "*Ti–TiO_2–Al normal metal–insulator–superconductor tunnel junctions fabricated in direct-write technology*" Supercond. Sci. Technol. **20** (2007) p.865

E. Otto et al., *A Class AB Monolithic CMOS RF Mixer for 2.4 GHz Applications,*
Norchip Conference, November 2000, Turku, Finland.

G. Yassin, L. Kuzmin, P. Grimes, M. Tarasov, E. Otto, and P. Mauskopf
"An Integrated Superconducting Phase Switch for Cosmology Instruments" Physica C 2007

P. Grimes, G. Yassin, L. Kuzmin, P. Mauskopf, E. Otto, M. Jones, and C. North.
"*Investigation of planar switches for large format CMB polarization instruments".*
Proc. SPIE, 6275: 25, 2006.

L. Kuzmin, M. Tarasov, E. Otto, A. Kalabukhov, G. Yassin, P. Grimes, and P. Mauskopf
"Superconducting Subterahertz Fast Nanoswitch" JETP Letters, 2007, Vol. 86, No. 4, pp. 275-7.

E. Otto, M. Tarasov, P. Grimes, L. Kuzmin, and G. Yassin, *"Cold-Electron Bolometer Integrated with a Unilateral Finline"*, 21st International Symposium on Space Terahertz Technology, Oxford, 23-25 March, 2010

E. Otto, M. Tarasov, P. Grimes, N. Kaurova, H. Kuusisto, L. Kuzmin and G. Yassin,
"Finline-integrated cold electron bolometer", *Proc. SPIE*, June 2010.

M. Tarasov, L. Kuzmin, E. Otto, G. Yassin "*Cold-Electron Bolometer Array Integrated with a 350 GHz Cross-Slot Antenna"* 21st International Symposium on Space Terahertz Technology, 23-25 March, 2010

M. Tarasov, V. Gromov, G. Bogomolov, E. Otto, L. Kuzmin, "*Fabrication and Characteristics of Mesh Band-Pass Filters*" Journal: Instruments and Experimental Techniques, 2009, Vol. 52, No. 1, pp. 74–78, 2009.

S. Pelling, E. Otto, S. Spasov et al, "*Electrostatic effects in coupled quantum dot-point contactsingle electron transistor devices*" the Journal of Applied Physics, Vol. **112**, Issue 1, 2012.

E. Otto, M. Tarasov, P, Grimes et al "*Optical response of Titanium-based Cold-Electron Bolometer*", Journal Supercond. Sci. Technol. (SUST). 26 (2013) 085020